Tampere University

ANTTI AHOLA

Quantification of Stem Cell Derived Cardiomyocyte Beating Mechanics using Video Microscopy Image Analysis

Tampere University Dissertations 34

Tampere University Dissertations 34

ANTTI AHOLA

Quantification of Stem Cell Derived Cardiomyocyte Beating Mechanics using Video Microscopy Image Analysis

ACADEMIC DISSERTATION
To be presented, with the permission of
the Faculty Council of Medicine and Health Technologies
of Tampere University,
for public discussion in the auditorium TB109
of the Tietotalo building, Korkeakoulunkatu 1, Tampere,
on 29.3.2019, at 12 o’clock.

ACADEMIC DISSERTATION
Tampere University, Faculty of Medicine and Health Technologies
Finland

Responsible supervisor and Custos	Prof. Jari Hyttinen Tampere University Finland	
Pre-examiners	Prof. Risto Kerkelä University of Oulu Finland	PhD Marko Vendelin Tallinn University of Technology Estonia
Opponent	Dr. Ing. Gunnar Seemann University Heart Center Freiburg · Bad Krozingen Germany	

Cover design: Roihu Inc.

ISBN 978-952-03-1006-6 (print)
ISBN 978-952-03-1007-3 (pdf)
ISSN 2489-9860 (print)
ISSN 2490-0028 (pdf)
http://urn.fi/URN:ISBN:978-952-03-1007-3

PunaMusta Oy – Yliopistopaino
Tampere 2019

ACKNOWLEDGEMENTS

The studies presented in this thesis have been carried out during the years 2010-2018 at BioMediTech and the Faculty of Biomedical Sciences and Engineering, as well as former Department of Electronics and Communications Engineering, and Department of Biomedical Engineering at Tampere University of Technology, Finland.

Firstly, I would like to thank my supervisor, Professor Jari Hyttinen for his scientific guidance and unwavering support in all matters during these years. Working under him has allowed for growth as a researcher, with academic freedom to try and pursue different venues of research, while still providing the vision to keep this thesis project on track. Thank you for providing me with the chance to work in such an exciting field of science. I am very grateful to the thesis pre-examiners, Professor Risto Kerkelä MD, PhD; and Marko Vendelin, PhD for their careful evaluation. They provided valuable comments and constructive feedback, which greatly improved the thesis. I would especially wish to thank Professor Katriina Aalto-Setälä. Throughout the thesis work, she has encouraged me and reminded of the importance of the study, as well as guided my work. This has made me feel like a member of her own research group as well.

I wish to express my gratitude to my former and present colleagues and staff at both Tampere University of Technology and University of Tampere. I have had the privilege of working with so many talented and supportive people, many of whom have become good friends as well. I greatly appreciate the contribution of all my co-authors. In particular I would like to thank Anna Kiviaho, PhD, for the exciting first studies and findings in the field; Eeva Laurila, PhD, for all the shared learning experiences in commercialization endeavors; Markus Honkanen, PhD, for providing me with important technical background and expertise in image-based measurements; Paruthi Pradhapan, MSc, for the great co-operation in development of the analysis tool; and Risto-Pekka Pölönen, MSc, for providing essential understanding of cellular electrophysiology in the later parts of the thesis work and beyond.

The works presented here have been made possible by various sources of funding. I am very grateful for the research grants received from the Finnish Cultural Foundation Pirkanmaa regional fund and Central fund, which represent the largest contribution to this thesis project. In addition, I want to thank for the funding received from the Human Spare Parts projects, funded by EU, Business Finland (former TEKES), Academy of Finland and the Council of Tampere Region as well as grants for finalizing the thesis from Faculty of Biomedical Sciences and Engineering, Tampere University of Technology. I also want to thank Business Finland for the funding related to development of the analysis tool, a project closely related to this thesis topic. Not only did these sources of funding motivate me to continue in this field, but also this thesis work would not have been possible without them.

I warmly thank all my friends and family for continuous support. I cannot express my gratitude enough to my mother Pirjo, my father Kari, and my sister Akira. The love and support you have provided has laid a solid foundation for me to do this work. Finally, I want to thank my wife Reea for the love, care and understanding during the whole thesis work, all the while being a wonderful mother to our children Liina and Tiitus. You all bring love and joy to each and every day of my life.

Tampere, January 2019
Antti Ahola

ABSTRACT

Until recently, the studying of human cardiac cells had been a difficult and to some extent dangerous task due to the risks involved in cardiac biopsies. Induced pluripotent stem cell technology enables the conversion of human adult cells to stem cells, which can be further differentiated to cardiac cells. These cells have the same genotype as the patient from whom they were derived, allowing the studying of genetic cardiac diseases, as well as the cardiac safety and efficacy screening of pharmaceutical agents using human cardiac cells instead of animal cell models. Using the stem cell derived cardiac cells in these studies, however, requires novel and specialized measurement methods for understanding the functioning of these cells.

Long QT syndrome and catecholaminergic polymorphic ventricular tachycardia (CPVT) are genetic cardiac diseases, which can induce deadly arrhythmias. The induced pluripotent stem cell derived cardiac cells allow the studying of these diseases in laboratory conditions. A greater understanding of these diseases is important for prevention of sudden cardiac death, more accurate diagnosis, and development of possible treatment options. In order to understand the functioning of these cells, new methods are sought after. Traditionally, the electrical function of these cells are measured. However, the primary function of the cardiac cells is to beat in order to pump blood for circulation. The methods to quantify this mechanical function, the contraction and relaxation movement of cells, has been in lesser focus.

The main objective of this work is to develop a measurement method, which allows the in vitro quantification of biomechanics of single human cardiac cells using video microscopy. The method uses digital image correlation to determine movement occurring in cardiac cells during contractile movement. The method is implemented in a software tool, which enables the characterization and parametrization of the cardiomyocyte beating function. The beating function itself can be affected by environmental factors, pharmacological agents and cardiac disease.

Here, the quantification of mechanical function is performed using digital image correlation to estimate displacement between subsequent video frames. Velocity vector fields can then be used to calculate signals that characterize the contraction and relaxation movement. We estimate its accuracy in cardiac cell studies using artificial data sets and its feasibility with concurrent electrical measurements. Cardiac diseases are studied by quantifying beating mechanics from Long QT and CPVT specific cell lines. Traditional electrophysiological measurements are used for validation and comparison. The interaction between calcium and contraction is studied with a simultaneous measurement of biomechanics and calcium imaging.

This thesis resulted a new and accessible analysis method capable of measuring cardiomyocyte biomechanics. This method was determined to be non-toxic and minimally invasive, and found capable to be automated for high-throughput analysis. Due to not harming the cells, repeated measurements are enabled. Using the method, we observed for the first time abnormal beating phenotypes in two long QT associated mutations in single cardiomyocytes. Further, we demonstrated a concurrent calcium and motion measurement without background corrections. This provided also evidence that this combined analysis could be particularly useful in some cardiac disease cases. The methods and results shown in the thesis represent key early advances in the field.

The method was implemented in a software tool, which enabled cell biologists to use it different stages of cardiomyocyte studies. Overall, the results of the thesis represent an accessible method of studying cardiomyocyte biomechanics, which improves the understanding of contraction-calcium coupling and paves way for high-throughput analysis of cardiomyocytes in genetic cardiac disease and pharmacological research.

TIIVISTELMÄ

Viime aikoihin asti ihmisen sydämen solujen tutkiminen on ollut vaikeaa ja vaarallista, sillä näytepalojen ottamiseen sydämestä liittyy paljon riskejä. Menetelmä indusoitujen pluripotenttien kantasolujen tuottamiseen sallii aikuisten solujen muuntamisen takaisin kantasolumuotoon, josta ne voidaan vielä erilaistaa sydänsoluiksi. Näillä soluilla on sama geeniperimä kuin potilaalla, josta ne on johdettu. Tämä luo mahdollisuuden tutkia geneettisiä sydänsairauksia, ja sallii lääkeaineiden sydänturvallisuuden ja tehokkuuden tutkimisen käyttäen ihmisen sydänsoluja eläinkokeiden sijaan. Kantasolupohjaisten sydänsolujen käyttäminen näissä tutkimuksissa kuitenkin vaatii uusia ja erityisiä mittausmenetelmiä solujen toiminnan ymmärtämiseksi.

Pitkä QT-syndrooma (LQTS) ja katekolamiiniherkkä polymorfinen kammiotakykardia (CPVT) ovat perinnöllisiä sydänsairauksia, jotka voivat aiheuttaa kuolemaan johtavia rytmihäiriöitä. Indusoiduista pluripotenteista kantasoluista johdettujen sydänsolujen avulla voidaan tutkia näitä sairauksia laboratorio-oloissa. Ymmärtämällä paremmin näitä sairauksia voidaan saavuttaa tarkempia diagnooseja ja kehittää mahdollisia uusia hoitomuotoja sydänperäisten äkkikuolemien estämiseksi. Uusia mittausmenetelmiä tarvitaan, jotta näiden solujen toimintaa voidaan tutkia. Näiden solujen toiminnallisuutta on perinteisesti tutkittu mittaamalla niiden sähköistä toimintaa. Sydänsolujen pääasiallinen tehtävä on kuitenkin mekaaninen: pumpata verta sydämestä verenkiertoon. Tätä solujen supistumista ja rentoutumista mittaavia menetelmiä on tutkittu vähemmän.

Tämän väitöskirjan päämäärä on kehittää mittausmenetelmä, jolla voidaan määrittää yksittäisten ihmisen sydänsolujen biomekaniikkaa in vitro videomikroskopiaa käyttäen. Menetelmä käyttää digitaalista kuvien korrelaatiota määrittämään sydänsoluissa supistusliikkeen aikana tapahtuvan liikkeen. Menetelmää käytetään ohjelmistotyökalussa, jolla voidaan karakterisoida ja parametrisoida sydänsolun syketoimintaa. Syketoimintaan voi vaikuttaa niin ympäristötekijät, lääkeaineet kuin sydänsairaudetkin.

Tässä väitöskirjassa sydänsolujen mekaanista toimintaa mitataan videomikroskopian avulla määrittämällä liikettä videon peräkkäisistä kuvista digitaalista kuvakorrelaatiota käyttäen. Saaduista nopeusvektorikentistä lasketaan supistumista ja rentoutumista kuvaavia signaaleja. Arvoimme sen tarkkuutta sydänsolututkimuksissa käyttäen keinotekoisia tietoaineistoja ja sen soveltuvuutta yhtäaikaisilla sähköisillä mittauksilla. Tutkimme perinnöllisiä sydänsairauksia (LQTS ja CPVT) mittaamalla sykinnän mekaniikkaa yksittäisistä sydänsoluista, jotka ovat johdettu näitä sairauksia kantavien potilaiden kantasolulinjoista. Perinteisiä sähköfysiologisia mittauksia käytetään menetelmän validointiin ja vertailuun. Kalsiumin ja sykinnän vuorovaikutusta tutkitaan yhtäaikaisella biomekaniikan ja kalsiumaineenvaihdunnan mittauksella.

Tämän väitöskirjan tuloksena saatiin aikaan uusi ja helposti lähestyttävä menetelmä sydänlihassolujen biomekaniikan tutkimiseen. Menetelmä ei ole soluille haitallinen ja se vaikuttaa solujen toimintaan perinteisiin menetelmiin verrattuna vain vähän. Se on automatisoitavissa suuria näytemääriä varten. Koska se ei vahingoita soluja, mittaukset voidaan myös toistaa samoilla soluilla. Tätä menetelmää käyttäen havaitsimme ensimmäisinä kahdesta eri LQT1-mutaatiota kantavista potilaista johdetuissa yksittäisissä sydänsoluissa poikkeavia sykintätyyppejä. Lisäksi, osoitimme yhtäaikaisen kalsiumin ja liikkeen mittauksen olevan mahdollinen ilman laskennallisia taustan korjauksia ja havaitsimme, että näin yhdistetystä analyysista voi olla erityistä hyötyä sydänsairauksien tutkimisessa. Väitöskirjassa esitetyt menetelmät ja tulokset edustavat alan tärkeitä ensimmäisiä edistysaskelia.

Tätä menetelmää käytettiin väitöskirjan ohella tehdyssä ohjelmistotyökalussa, jota voidaan käyttää sydänlihassolujen tutkimuksen eri vaiheissa. Väitöskirjan tuloksena syntynyt helposti lähestyttävä menetelmä sallii sydänlihassolujen biomekaniikan analyysin. Sen avulla voidaan myös ymmärtää paremmin supistusliikkeen ja kalsiumin kytkentää. Kokonaisuutena, väitöskirja luo pohjaa sydänlihassolujen suurten näytemäärien analyysille sydänsairauksien ja lääkeaineiden tutkimuksessa.

CONTENTS

ABBREVIATIONS

ADP	adenosine diphosphate
AFM	atomic force microscopy
AP	action potential
APD	action potential duration
ATP	adenosine triphosphate
AV	atrioventricular
BPM	beats per minute
CICR	calcium induced calcium release
CM	cardiomyocyte
CPVT	catecholaminergic polymorphic ventricular tachycardia
DAD	delayed afterdepolarization
EAD	early afterdepolarization
ECG	electrocardiogram
ESC	embryonic stem cell
ESC-CM	embryonic stem cell derived cardiomyocyte
fps	frames per second
GECI	genetically encoded calcium indicator
GEVI	genetically encoded voltage indicator
hiPSC	human induced pluripotent stem cell
hiPSC-CM	human induced pluripotent stem cell derived cardiomyocyte
iPSC	induced pluripotent stem cell
IKr	rapidly activating component of the delayed rectifier potassium current
IKs	slowly activating component of the delayed rectifier potassium current
LQT	long QT
LQTS	long QT syndrome
MAE	mean absolute error
MQD	minimum quadratic difference
PIV	particle image velocimetry

RyR	ryanodine receptor
SA	sinoatrial
SD	standard deviation
SR	sarcoplasmic reticulum
UI	user interface
WT	wild type

ORIGINAL PUBLICATIONS

Publication I	Ahola, A.*, Kiviaho, A. L.*, Larsson, K., Honkanen, M., Aalto-Setälä, K. & Hyttinen, J. 2014. Video image-based analysis of single human induced pluripotent stem cell derived cardiomyocyte beating dynamics using digital image correlation. Biomedical Engineering Online, 13:39. **
Publication II	Ahola, A.*, Pradhapan P.*, Laurila E., Aalto-Setälä, K. & Hyttinen, J. 2014. Motion Analysis Method for Determining Cardiomyocyte Beating Properties Based on Digital Image Correlation and Templates. Proceedings of Computing in Cardiology, 41:1137-1140.
Publication III	Kiviaho, A. L., Ahola, A., Larsson, K., Penttinen, K., Swan, H., Pekkanen-Mattila, M., Venäläinen, H., Paavola, K., Hyttinen, J. & Aalto-Setälä, K. 2015. Distinct electrophysiological and mechanical beating phenotypes of long QT syndrome type 1-specific cardiomyocytes carrying different mutations. International Journal of Cardiology Heart & Vasculature, 8:19-31. **
Publication IV	Ahola, A., Pölönen, R.-P., Aalto-Setälä, K. & Hyttinen, J. 2018. Simultaneous Measurement of Contraction and Calcium Transients in Stem Cell Derived Cardiomyocytes. Annals of Biomedical Engineering, 46:148.

* These authors contributed equally to this work.

** Publication has been previously included in the doctoral dissertation "Long QT Syndrome -specific Cardiomyocytes Derived from Induced Pluripotent Stem Cells: From cell lines to disease models" by Anna Kiviaho in BioMediTech Institute, University of Tampere, Finland, 2014.

1 INTRODUCTION

Cardiovascular diseases present a major cause of mortality and chronic disability in the world [1]. Greater understanding of the heart, cardiac diseases and cardiac function paves way for new and more efficient options for treatment and prevention of cardiac disease. Studying the functioning of cardiac cells has previously been difficult due to the high risks involved in cardiac biopsies. These studies have become considerably easier with the advent of induced pluripotent stem cells, which allow the derivation of patient specific cardiac cells from somatic cells from a number of tissue types, such as skin or blood samples, and culturing them in laboratory conditions towards cardiomyocytes [2,3]. These patient specific cell lines retain the same genotype as the cell donor, making it possible to study the cells in laboratory conditions. Analyzing *in vitro* cellular disease models derived from carriers of genetic cardiac diseases can help to understand the disease mechanisms and assess the risk of individuals developing symptoms. As the first symptom of such disease, for instance long QT syndrome, can be sudden cardiac death, it is difficult for a physician to evaluate possible treatments for an otherwise asymptomatic carrier of the gene defect.

In pharmaceutical studies, it is essential to determine the adverse effects of pharmaceutical agents as early as possible, since drug discovery and development is expensive and the costs are increasing at a rapid annual rate [4]. Cardiac side effects are among the leading causes of drug market withdrawal [5,6]. Cancer drugs in particular have a greater risk of affecting cardiac function [7]. Stem cell derived cardiomyocytes have provided alternatives to animal testing, which not only causes suffering for the animals, but is also time consuming and expensive. Further, the results obtained with animal models do not necessarily translate well to the human physiology due to differences in species [8]. Thus, there exists a substantial need in drug research to develop new, effective methods capable of screening large numbers of substances for abnormal cardiac function. Eliminating substances which cause adverse effects, in as early phase as possible shortens the drug development time and lowers the related expenses.

Previously, the in-vitro analysis of cardiomyocytes has focused mainly on the electrophysiological measurements, such as patch clamp, microelectrode arrays and calcium imaging [9]. While these methods provide a detailed and accurate view on cardiomyocyte functionality, they are typically either invasive - such as patch clamp, toxic – such as calcium imaging, or do not provide detailed information on single cells, as has previously been the case with microelectrode arrays. In addition, they do not describe the primary function of cardiac cells – contraction and relaxation processes which pump blood through the circulatory system.

The biomechanical side of the cardiomyocyte function has been less in focus, partly due to the lack of easily implementable *in vitro* methods. These mechanobiological measurements have been previously done using methods such as atomic force microscopy [10] and mechanical transduction platforms, such as microposts [11]. However, they are not typically well suited for high-throughput applications as they are labor intensive or require specific measurement platforms. The quantification of the beating motion *in vitro* from video microscopy has been demonstrated briefly to provide information on the cardiomyocyte biomechanics without using labels or probes in live cell imaging, or without external instrumentation [12].

The general aim of the thesis is to develop a video microscopy-based method capable of characterizing the cardiomyocyte biomechanics on a single dissociated cell level, and to quantify the abnormal biomechanics observed in cell models of genetic cardiac diseases. At the time of the beginning of the study, adult and embryonic stem cell derived cardiomyocytes had been studied using similar methods. Induced pluripotent stem cell derived cardiomyocytes, however, had not yet been characterized, and we were among the first to measure the biomechanics of these cells using video image microscopy. These cells have immature cellular physiology, which influences their contractile function [13]. During the course of the thesis work, video microscopy analyses of cardiomyocytes were conducted also by different groups in addition to us [12,14–18]. In their studies, they analyzed the effects of various different pharmacological agents on cardiomyocyte beating using video microscopy based methods. Different software tools have also been developed by these groups. Thus, the field of study presented in this thesis was – and still is – a topical subject and very pertinent to the understanding of cardiomyocytes. Based on our findings and the results obtained by the other groups, video microscopy based methods can be regarded as a feasible option for high-throughput analysis of cardiomyocytes.

The main, and start hypothesis regarding the thesis is that stem cell derived cardiomyocyte beating mechanics can be quantified accurately on a single cell level with video-based methods, specifically minimum quadratic difference based particle image velocimetry. In this thesis, we aim to study the feasibility of calculating velocity vector fields from consecutive video frames to determine contraction and relaxation, and validate the method using artificial data sets and concurrent electrophysiological measurements, such as patch clamp and calcium imaging. Patch clamp represents the gold standard in cellular electrophysiological measurements, whereas calcium imaging provides a view on cellular calcium exchange, a key aspect of contraction. We aim to assert that video-based analysis of cardiomyocyte biomechanics combined with other measurement methods can provide a detailed and comprehensive view on the cardiomyocyte functionality.

The validation of the video measurement is done using healthy control cell lines and artificial data by assessing the results in conjunction with traditional electrophysiological measurements of cardiomyocytes. Based on the visual observation of abnormal mechanical manifestations in cardiomyocytes derived from disease specific stem cell lines, we hypothesize that the method can be used for characterizing different beating phenotypes rising from abnormal electrical function in genetic cardiac disease. Long QT syndrome and CPVT are studied using the developed method: cardiomyocytes derived from patient specific stem cell lines are measured and characterized. The obtained results are again compared with results obtained using traditional electrophysiological measurements. During the studies, the question of optimal recording parameters and requirements for videos became a topical subject as the method accuracy depends greatly on the recording of video microscopy data. We hypothesize that using multiple comparable data sets with different variables of interest the effect could be quantified. High quality video recordings were performed and by gradually decreasing the measurement length and frame rate, different data sets were obtained. We aim to answer if a concurrent contraction-calcium measurement without fluorescence corrections can be achieved using the method to increase the understanding of cardiomyocyte calcium-contraction coupling. A measurement is performed in a setting consisting of alternating frames of fluorescence imaging and brightfield microscopy, allowing the measurement of both signals individually and together to achieve this aim. In addition to these aims, a software tool is developed alongside the research for biologists to use in assessing cardiomyocyte biomechanics in different stages of research.

Together, these objectives will allow us to demonstrate the feasibility of video microscopy-based analysis of cardiomyocyte biomechanics *in vitro*.

2 REVIEW OF LITERATURE

2.1 Anatomy of the human heart and cardiac cells

The human heart contracts and relaxes periodically to pump blood in the blood vessels of the circulatory system. This pumping action delivers blood to and from all the body. The human circulatory system consists of two parts. In the systemic circulation, oxygenated blood and nutrients are transferred to tissues and organs in arteries, and metabolism waste products are transferred out of them in veins. In pulmonary circulation, carbon dioxide is released in the lungs and oxygen enters the blood.

The heart is a muscular organ, covered by a protective pericardial sac. The heart consists of four chambers: left and right atria, and left and right ventricles, with the left and right halves of the heart separated by septum. The blood flow within the heart is controlled by valves, located between the atria and ventricles on both sides and between the atria and main blood veins. The heart wall consists of three layers: myocardial, pericardial and endocardial layers, depicted in Figure 1. Myocardium forms the main layer consisting of groups of spirally oriented cardiac muscle fibers. This layer performs the main function of the heart, being capable of contracting and relaxing. Pericardium represents the outermost layer, which protects the heart. It consists of a fibrous layer and a serous layer, which in turn consists of parietal layer, pericardial cavity, and visceral layer, known as epicardium. The innermost layer, endocardium is layer of connective tissue, which lines the heart chambers and covers the valves. [19]

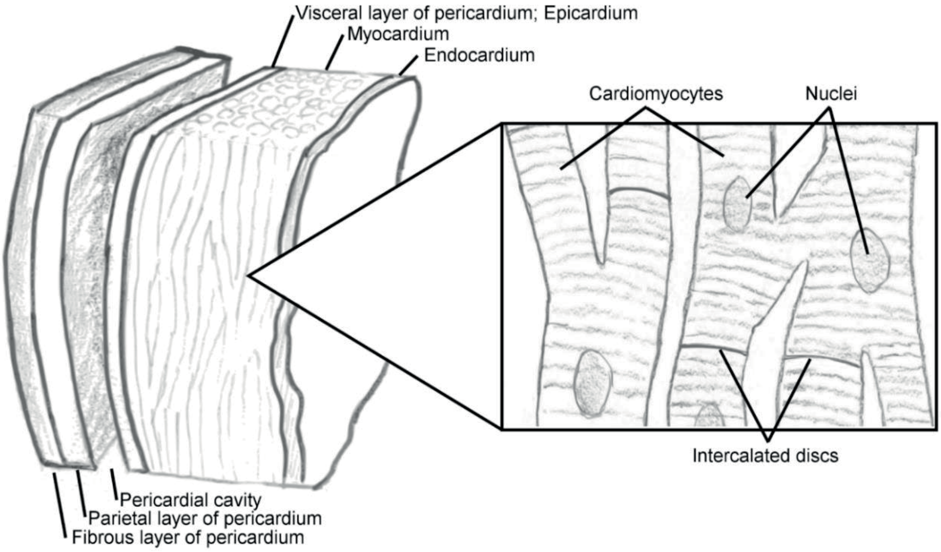

Figure 1. An illustration of the anatomy of heart wall and myocardial tissue. The heart is covered with a protective pericardial sac consisting of fibrous and serous layers. The serous layer is composed of a parietal and a visceral layer, which surround the pericardial cavity. Myocardium performs the contractile function of the heart. Endocardium lines the inner surface of the heart. The myocardial tissue contains cardiomyocytes, striated cardiac muscle cells that may contain up to two nuclei, connected to each other by intercalated discs.

Adult mammalian cardiac tissue in myocardium illustrated in Figure 1 consists of numerous cell types. Striated cardiac muscle cells - cardiomyocytes (CM) – account for 70-85 % of heart volume, while still representing only 25-35% of the number of cells in the heart. The composition of non-myocyte cell population, consisting of fibroblasts, endothelial cells, leukocytes, smooth muscle cells and pericytes, has been a point of debate. Previously, cardiac fibroblasts had been considered the largest group. However, this view has been challenged recently by Pinto et al., who showed that endothelial cells are the most numerous non-myocyte cell type. [20,21]. Typically, a ventricular CM is 50-150 μm long and 10-20 μm wide whereas atrial CMs are slightly smaller [22]. The cells contain 1-2 nuclei and a proportionally large number of mitochondria. The bulk of the cell consists a bundle of long myofibril strands, which create the contractile force. Adjacent CMs are connected to each other longitudinally via intercalated discs, native only to cardiac muscle cells. The discs contains three intercellular junctions: desmosomes, adherens junctions and gap junctions. Additionally, the discs contain proteins such as Coxsackie virus and adenovirus receptor (CAR) protein, Claudin-5, and zonula occludens-1, which are associated with tight junctions, intercellular junctions associated with epithelial cells [23]. Desmosomes keep the cells from detaching from each other during contraction. Adherens junctions transmit power between adjacent cells, and serve as end points for myofibrils. Gap junctions can transport ions, and thus serve as the electrical connection between each CM, allowing the cells to function together in a *syncytium*. The CAR protein in CMs facilitates the propagation of excitation from atrium to ventricle. [19,23–25] Figure 2 illustrates the organization of the cell organelles.

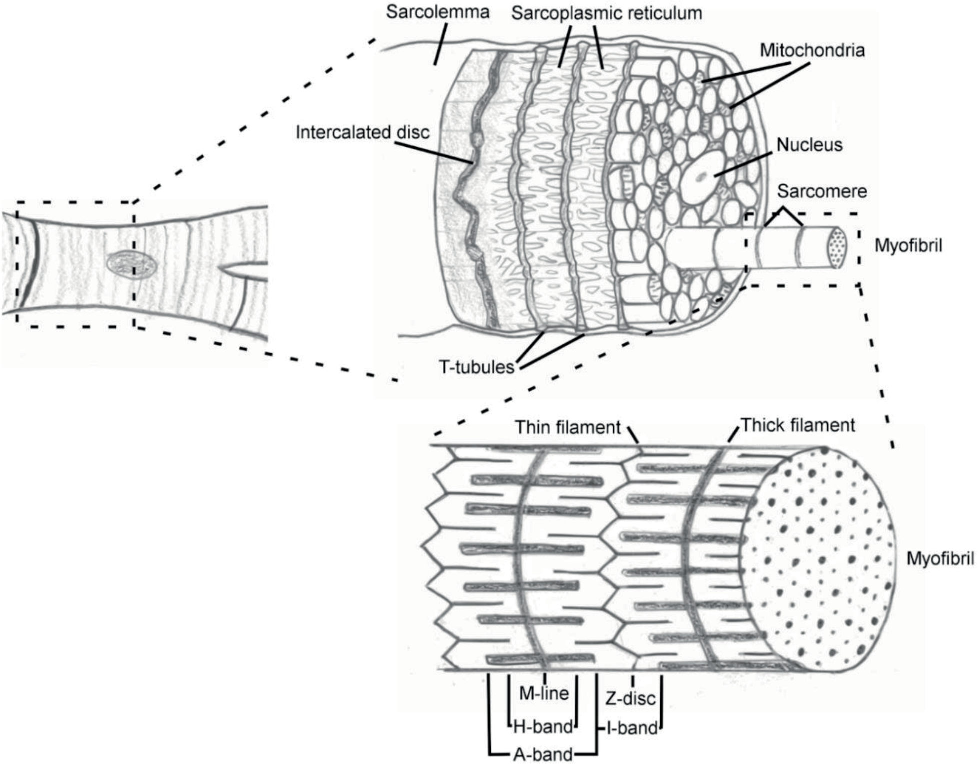

Figure 2. An illustration of cardiac cell and its structure at different magnifications. The bundle of myofibril strands is encapsulated by the sarcolemma and connected to another cell via the intercalated disc. The cells have a high number of mitochondria. A single myofibril consists of multiple sarcomeres connected by Z-discs. The sarcomeres are composed of thin and thick filaments.

Each myofibril strand consists of sarcomeres, longitudinal units connected in series with each other. Sarcomeres are separated from each other by Z-discs, to which they are anchored. In addition to the structural task, Z-discs are involved in sensing stretching and in signaling [26]. Each sarcomere can further be divided into thin actin and thick myosin filaments, forming the basic contractile unit of the cell, as illustrated in Figure 2. The thick filaments (approximately 1.5 μm in length) are surrounded on six sides by thin filaments (approximately 1 μm in length). A thick filament consists of two myosin heavy chains (MHC) and two myosin light chains (MLC 1 and MLC 2). Thin filaments consist of actin polymers, tropomyosin and troponin (with its subunits troponin C, I and T). [22,25] Together, these form sarcomere lines, bands and zones, determined based on microscopy in contracted and relaxed states. A-band indicates the location of thick filaments, I-band indicates the location of thin filaments without overlapping thick filaments, H-zone the subregion of A-band with no overlapping thin filaments, M-line the center of A-band, and Z-disc at the ends of thin filaments (and sarcomeres). At Z-discs, the thin filaments are separated by actin binding protein α-actinin. M-line serves to hold together the thick filaments. A third filament, titin, is a giant protein that connects the Z-disc with the M-line, holding the structure together. It also has spring like properties, which help the cell to return to its relaxed state. [26] The process of contraction and force generation is described in 2.2.4.

2.2 Cardiac electrophysiology and mechanobiology

2.2.1 Electrical activity of the whole heart

In order for the different areas of the heart to contract and relax in unison, a mechanism of rapid activation is required. CMs can be roughly divided into pacemaker cells, which spontaneously create electrical activity and work cells, which generate the force. The electrical activity consisting of depolarization and repolarization of the cell membranes normally begins in pacemaker cells in sinoatrial (SA) node. Being the fastest of the excitatory cells, the SA node sets the beating rhythm for the whole heart. The activity then propagates through gap junctions between cells, through the atria to the atrioventricular (AV) node. The AV node delays the propagation of the impulse, in order for the atria to contract before the ventricles. From the AV node, the impulse spreads to AV bundle, which serves as an electrical connection between the atria and the ventricles. Next, the activity splits to left and right bundle branches, which go along the setup all the way to the apex of the heart, reaching finally the Purkinje fibers. The fibers are long strands of few myofibrils, which spread the impulse throughout the ventricles. While SA node acts as the primary pacemaker, AV node and the ventricular system can act as accessory pacemakers in the case of SA failure or AV block. [24]

The electrophysiological functioning of the whole heart can be measured and monitored using electrocardiogram (ECG). Typically used 12-lead ECG is recorded to measure the action potentials of the atrial and ventricular CMs on the surface of the body using electrodes. In an ECG trace, the resting membrane potentials of the CMs are represented as the baseline, with each deviation is denoted with a letter, as illustrated in Figure 3. [27]

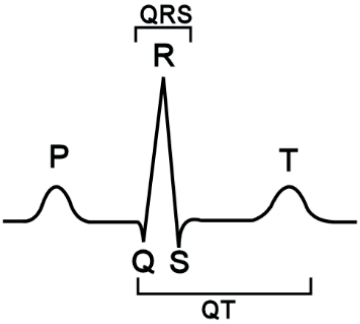

Figure 3. Normal ECG, with deviations from baseline defined with specific letters. P wave denotes the atrial depolarization, QRS complex the depolarization of ventricles and T wave the repolarization of ventricles. QT time signifies the time from ventricular depolarization to ventricular repolarization.

P wave denotes the depolarization of the atrial cells. The potential of atrial repolarization is typically too low to be detected using with surface electrodes, even if the depolarization of ventricles was delayed. The following Q, R and S waves form the QRS complex, which represents the depolarization of ventricles. The ventricular repolarization can be seen on ECG, and is represented by the T wave. [22,27,28]

The main time intervals of interest between waves are PQ, ST and QT –intervals. The PQ –interval is mostly due to the slow conduction in AV node. During ST segment, the ventricular CMs are depolarized. The QT interval is the period from the beginning of ventricular depolarization to the end of ventricular repolarization [24]. As the intervals change as a function of heart rate, a measure of corrected QT (QTc) interval is calculated to normalize it using one of several methods, such as Bazett's formula and Fridericia's formula, where the QT interval is divided by the square or cubic root, respectively of the preceding interval of R peaks in seconds. [29]

2.2.2 Cardiac action potential

On a cellular level, this electrical propagation process is established with cardiac action potential (AP). During an AP, the cell goes through different phases, during which different ions flow through the cellular membrane via ion channels. The most important ions related to cardiac action potential are sodium, potassium and calcium. With no activity, there is an electrical potential difference, transmembrane potential between the inside and the outside of the cell, called the resting potential. The shape and magnitude of the AP depend on which region of the heart the CM is located, as illustrated in Figure 4.

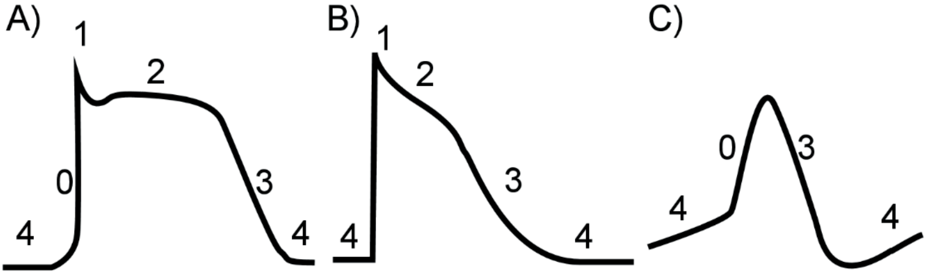

Figure 4. The phases of cardiac action potential waveforms in A) ventricular cells, B) atrial cells and C) pacemaker cells. The ventricular-type CMs exhibit a more square-shaped AP with a long plateau phase, whereas the shape of atrial AP is triangular. The shape of AP in pacemaker cells do not feature the same phases as the atrial and ventricular APs, such as the high peak associated with phase 1.

The phases for an AP in atrial and ventricular CMs are described in detail below. [30,31]

Phase 4. The cell is at the resting potential (about -90 mV), maintained by different ion pumps and mechanisms working against the electrochemical gradient, and the inward rectifying K^+ current I_{K1} due to K^+ ions leaving the cell. The Na^+ and Ca^{2+} channels remain closed.

Phase 0. An action potential reaches the cell and when the transmembrane potential reaches the threshold potential (about -75 mV) it starts rapidly depolarizing due to the activation of rapid inward Na^+ current through voltage-gated Na^+ channels. The rectifying K^+ channels close, stopping I_{K1}.

Phase 1. The early repolarization begins, due to the closing of rapid voltage-gated Na^+ channels and opening of transient outward K^+ channel current, composed of transient outward current I_{to1} and in atria, the ultra-rapid current I_{Kur}. This causes the transmembrane potential to decrease, creating a notch in the AP. The depolarization of the membrane activates the voltage-gated L-type Ca^{2+} channels.

Phase 2. Transmembrane potential reaches a plateau phase, due to the inward flow of Ca^{2+} ions I_{CaL} through L-type Ca^{2+} channels and the delayed outward rectifier K^+ current, composed of currents flowing through the rapidly (I_{Kr}) and slowly (I_{Ks}) activating K^+ channels, balancing out each other.

Phase 3. When the voltage dependent L-type Ca^{2+} channels close, the delayed outward K^+ currents dominate, starting the repolarization of the cell. The L-type Ca^{2+} channels inactivate mainly due to the release of Ca^{2+} from SR. Inward rectifying current I_{K1} opens (at about -20 mV), and the cell finally reaches its resting membrane potential and returns to phase 4.

The APs in human SA node, AV node and other excitatory system CMs are less steep in contrast to atrial and ventricular CMs: the pacemaker AP is more triangular in shape, as they are missing phases 1 and 2 and the associated rapid membrane voltage changes. In addition, phase 4 is not stable as they are constantly depolarizing due to the influx of N+ as an effect of various currents. The process is described below in phases:

Phase 4. As the cell is hyperpolarized at the end of repolarization, the pacemaker current channel (I_f, funny current) opens, playing a major role in the initiation of the depolarization along with slow T-type Ca^{2+} channels. This depolarization brings the cell to a threshold potential and eventually reaches phase 0 by itself, or alternatively, when an external depolarization reaches the cell.

Phase 0. The cell membrane reaches threshold potential at about -40mV, which opens L-type Ca^{2+} channels, further depolarizing the membrane as more Ca^{2+} ions flow in.

Phase 3. As the inward Ca^{2+} current reverses the transmembrane potential, K^+ leakage channels open, increasing the outward K^+ currents. L-type Ca^{2+} channels close. This causes the cell to repolarize and return to its unstable resting potential.

The pacemaking I_f current can also be activated by cyclic nucleotides, allowing the cell to depolarize faster than its intrinsic rhythm. [32,33]

2.2.3 Excitation-contraction coupling

Cardiac excitation-contraction coupling is the process, in which electrical stimulus is relayed to mechanical contraction. The main driving force for contraction of a CM is the influx of Ca^{2+} ions through L-type Ca^{2+} channels during phase 2 of the AP. Ca^{2+} concentrations are maintained by the electrochemical gradient and L- and T-type voltage dependent Ca^{2+} channels, located near sarcolemmal-sarcoplasmic reticulum (SR) junctions. The influx of Ca^{2+} causes SR - smooth endoplasmic reticulum in myocytes for regulating Ca^{2+} ion concentration in cytoplasm - to further release Ca^{2+} into intracellular matrix in a process known as calcium-induced calcium release (CICR) through ryanodine receptors (RyR). This interaction increases the local concentration of Ca^{2+}, which regulates further influx of Ca^{2+}. The free Ca^{2+} binds to the protein troponin C within actin filaments, causing the contraction to occur. In order for the cell to return to relaxed state, it is necessary for the intracellular Ca^{2+} ion concentration to decline, allowing the bound Ca^{2+} to dissociate from troponin. Due to the concentration gradient, adenosine triphosphate (ATP) is required for removing Ca^{2+} from cytosol. The pathways involved lowering the concentration are Ca^{2+}-ATPase in SR, Na^+/Ca^{2+} exchange and Ca^{2+}-ATPase in sarcolemma, and Ca^{2+} uniport in mitochondria. During diastolic depolarization, oscillatory local SR Ca^{2+} release events occur. Thus, in addition to the ionic currents, Ca^{2+} released from SR spontaneously participates in the pacing of the cell. It has been shown that these release events are independent of the membrane potential, indicating that there is a Ca^{2+} clock that participates in the initiation of the AP. [34,35]

In CICR, the amount of released Ca^{2+} is greater than the triggering influx of Ca^{2+} in humans. The ratio of the released Ca^{2+} and the amount of Ca^{2+} due to influx is a measure of excitation-contraction coupling efficiency. [36,37] A number of proteins, such as RyR, related to excitation-contraction coupling are located in the vicinity of transverse tubules, or T-tubules, which are small infoldings of the surface membrane. While the majority of T-tubules are near Z-discs, T-tubules form an extensive system which has branching tubules in both axial and transverse directions of the CM. This tubular network is essential to the spatially and temporally synchronous release of Ca^{2+} in the cell. [38]

2.2.4 Force production and contractility

The myosin-actin interaction in force generation is explained in a cross-bridge cycle model, which refined the original sliding filament theory. In the cross-bridge model, the proteins involved in the process undergo a number of conformational changes in a cycle. When the cell is relaxed, tropomyosin is bound to actin, inhibiting myosin from binding to actin. When Ca^{2+} molecules bind to troponin C in actin filaments, tropomyosin changes its position so that myosin binding sites are revealed, allowing myosin to bind to the thin filament. Myosin segments with attached adenosine diphosphate (ADP) and phosphate molecules move to bind with an actin binding sites, releasing the phosphate molecules. Myosin then spends the ADP to generate a power stroke, which pulls the actin filament. This increases the overlap of thick and thin filaments, decreasing the sarcomere length. The myosin segment can then bind ATP, which allows myosin and actin to detach. ATP is subsequently broken down in hydrolysis to ADP and a phosphate molecule, and myosin returns to its resting position. Relaxation requires ATP, as actin remains bound to myosin. This cycle repeats itself as long as a required Ca^{2+} concentration is present in the cell, keeping the tropomyosin-troponin complex from inhibiting myosin binding. [39]

The force expressed by the CM is dependent on the Ca^{2+} bound to troponin C, which in turn is dependent on the total Ca^{2+} ion concentration, i.e. free intracellular Ca^{2+} and the buffered Ca^{2+} is further dependent on the amplitude and duration of the Ca^{2+} transient, the number of myofilaments that can participate in contraction, their sensitivity to Ca^{2+}, as well as the strength of Ca^{2+} binding [40]. As a myofilament is stretched, it becomes more sensitive to Ca^{2+} and creates a stronger contraction. Further, sensitivity can be increased by caffeine and drugs. Sensitivity of force generation to Ca^{2+} concentration can decrease under certain conditions, such as ischemia, as the process needs ATP and is dependent on the energy available. Thus, the dependence of force on Ca^{2+} ion concentration is not linear. [41] The force is also dependent on the overlap ratio of thick and thin filaments, which determines the sarcomere length, and the aforementioned factors. Optimally, the sarcomere length is about 2.2 μm, with lower or higher distances decreasing the strength of contraction. [39] Along with the intracellular Ca^{2+} concentration, the rate at which Ca^{2+} ions detach from troponin C regulates the relaxation of the cell. As the Ca^{2+} pumps require energy to function, fluctuations in ATP levels can slow down the process. [22] Methods used in measuring CM contractility are presented in section 2.7.

2.3 Cardiac arrhythmias on cellular level

2.3.1 Abnormal electrophysiological phenomena in cardiac cells

The mechanisms of cardiac arrhythmias related to single cells can be divided into two categories: disorders in impulse formation and disorders in impulse conduction. Whereas the disorders in impulse formation occur mostly at cellular level, the disorders in impulse conduction occur predominantly at macro level, including issues such as blocks in conduction and impulse reentry. Impulse formation disorders include altered normal automaticity, abnormal automaticity and triggered activity. Altered normal automaticity may occur when another pacemaker site takes priority over SA node. Abnormal automaticity occurs when non-pacemaker cells reach their threshold potential without a stimulus, for example due to an increase in extracellular K^+ or changes in K^+ channel activity. Triggered activity includes abnormal electrical activity that occurs after an initial impulse has already been generated within the cell. [42,43]

Triggered activity is the underlying mechanism behind most ventricular arrhythmias. It can be divided into early afterdepolarizations (EAD) and delayed afterdepolarizations (DAD). EADs are depolarizing oscillations occurring during AP plateau at potential higher than -30mV (phase 2) or late repolarization at lower potentials (phase 3), whereas DADs occur after a full repolarization. If an EAD or DAD is sufficiently large and brings the membrane potential to a threshold, it may result in a spontaneous AP referred to as triggered activity. [42,44]

During the plateau phase in AP, membrane potential is maintained by the balance of inward and outward currents. A number of different factors can change ionic balance and bring forth arrhythmic events, with the major currents being L-type Ca^{2+} current and Na^+-Ca^{2+} -exchanger current. Typically, EADs may occur when the AP is prolonged in such a way that the voltage-dependent calcium current through L-type Ca^{2+} channels can recover from inactivation and cause another upstroke. In the repolarization phase 3, the EADs may occur due to a reduced K^+ influx, or due to partially recovered Na+ current. In ECG, this can be seen as QT prolongation, associated with long QT (LQT) syndrome (LQTS). When sustained, EADs can lead to Torsade de Pointes, a ventricular tachyarrhythmia. [42,45,46]

The mechanism behind DADs is closely related to cellular Ca^{2+} loading. In an abnormal case, spontaneous RyR2 opening during diastole causes a transient inward current, primarily (and possibly solely in humans) due to the activation of the Na^+-

Ca^{2+} exchanger. If the current is large enough, it may cause a DAD. [47] There are various conditions which may increase the probability of RyR2 opening, including an overload of Ca^{2+} within SR [48,49]. Ca^{2+} overloading can be facilitated by digitalis, β-adrenergic receptor stimulation by catecholamines and low extracellular K^+ [50]. In catecholaminergic polymorphic ventricular tachycardia (CPVT), the mutations may increase the probability of RyR channel opening, causing DADs and arrhythmias. The abnormality of Ca^{2+} exchange has only limited effect on excitation-contraction coupling, as the patients do not suffer from arrhythmias in baseline conditions. As the release process of Ca^{2+} from SR is auto-regulated, compensatory mechanisms are capable of normalizing the coupling. When the auto-regulation cannot compensate sufficiently, abnormalities in the form of DADs and arrhythmias become more apparent. [51]

LQTS and CPVT are two genetic cardiac diseases studied in this thesis, described in 2.3.2 and 2.3.3. Cellular models of these diseases are described in section 2.4.5.

2.3.2 Long QT syndrome

LQTS is an inherited or acquired cardiac disorder. It is typically characterized by lengthening of the QT interval and T wave abnormalities on ECG. It represents an elevated risk for Torsade de Pointes, syncope, and sudden cardiac death. [52]

LQTS is caused by genetic or acquired factors [53]. In its congenital form, there are three major (LQT1-LQT3) and 10 minor (LQT4-LQT13) LQTS susceptibility genotypes. Additionally, there are three genotypes with atypical LQTS or multisystem disorders associated with prolonged QT time. [54] The three major genotypes (KCNQ1, KCNH2 and SCN5A, respectively) account for the greatest majority (75-90%) of all LQTS cases [55,56]. Normally, a QTc interval is less than 440 ms in males and 450 ms in females. In LQTS, the interval is defined to be greater than 450-460 ms in males and 460-470 ms in females, depending on classification of borderline cases [54,57]. Usually, arrhythmias are associated with a QT interval of 500 ms. [57]

In LQT1, the most common subtype of LQTS, the gene KCNQ1 responsible for the encoding the primary subunit of the Kv7.1 channel protein is mutated. The subunit generates the slowly activating component of the delayed rectifier K^+ current I_{Ks}. Its proper function is essential to the shortening of the QT interval in increased heart rates, as a reduction in the current reduces the repolarization capacity of the cell. In the KCNQ1 sequence, hundreds of different LQTS causing mutations have been found, and the number is growing [58]. In this thesis, two Finnish founder mutations G589D and ivs7-2A>G, located at the C-terminal domain of KCNQ1, are considered. The loss-of-function mutation in KCNQ1 can thus cause cardiac events during physical or emotional stress when the heart rate is high. [54]

2.3.3 Catecholaminergic polymorphic ventricular tachycardia

CPVT is an inherited cardiac disorder. Its typical characteristics include stress-induced bidirectional and polymorphic ventricular tachycardia in structurally healthy heart. It may cause syncope and sudden death at a young age, with a 30-35% mortality rate when untreated. The resting ECG for CPVT patients is normal and alterations can only be seen during exercise or intense emotion [59–61]. During exercise, premature ventricular contractions may occur, followed by bidirectional or polymorphic ventricular tachycardia.

There are a number of CPVT subtypes, with the number of types being a matter of debate. Initially, autosomally dominant RyR encoding gene RYR2 in chromosome 1q42-q43 was recognized as a cause of CPVT phenotype. [60,62,63] As previously described in 2.2.3, RyR encodes a Ca^{2+} release channel in SR. CPVT has been also shown to be caused by a mutation in the autosomally recessive calsequestrin 2 encoding gene CASQ2, which serves as a Ca^{2+} store in SR [64]. Later, a mutation in gene TRDN, responsible for encoding triadin - a transmembrane protein in SR - has been shown to cause CPVT [65]. Another cause of CPVT has been shown to be a mutation in the gene CALM1 which encodes calmodulin, an accessory protein of RyR [66]. RYR2 mutation represents the most common subtype of CPVT.

2.4 Stem cells

2.4.1 Stem cell hierarchy and classification

Unlike somatic cells, stem cells are cells capable of differentiating into specialized cells and proliferating almost indefinitely. Their potency differs depending on the phase of development. The most potent stem cells, *totipotent* stem cells, can be found in fertilized oocytes and the first few days of the embryonic development. They can differentiate into all cells of the organism, including extraembryonic structures such as the placenta. Later in blastocyst phase, the cells can be divided into two categories:

the outer trophoblast cells and the inner cells. The stem cells of the inner cell mass can differentiate into all cell types of the actual embryo, and thus they are called *pluripotent* stem cells *(PSC)*. In adults, stem cells are *multipotent* and can repair damage by replacing dead and lost cells based on their location, e.g. small intestinal stem cells can differentiate into the principal cell types of its epithelium: paneth, goblet, absorptive columnar and enteroendocrine cells. Previously, it was believed the cells could only become more differentiated, and thus lose their potency. In the last decade, it has been shown to be possible to induce pluripotency in cells and thus caution should be exercised with strict classification of these cells. [67–69]

Due to their properties, PSCs have various applications in regenerative medicine, understanding diseases and drug studies. First human embryonic stem cell (ESC) lines in 1998 from the blastocyst inner cell mass [70]. However, there are various ethical and moral issues with the derivation of PSC lines from oocytes and embryos [71].

The ethical issues were circumvented using an alternative solution to procuring PSCs: somatic cells were reprogrammed to regain their pluripotent state, first in mice [69] and then in human cells [72,73], resulting in induced pluripotent stem cells (iPSC). In the study by Takahashi et al., four transcription factors (OCT3/4, SOX2, KLF4, and c-MYC) were introduced to a colony of adult human dermal fibroblasts using retroviral transfection [72]. In the study by Yu et al., another set of four transcription factors (OCT4, SOX2, NANOG, and LIN28) were cloned into a lentiviral vector and used to induce pluripotency [73]. As the iPSCs are adult cells that have been made pluripotent, they allow the generation of individual- and patient specific cell lines [72,73].

2.4.2 Stem cell induction

There are a number of main factors that have an effect on the induction: the transcription factors, the methods used to deliver the factors to cells, the original cell type and culturing conditions [74]. There have been various alternative approaches to inducing pluripotency, with different efficiencies and advantages [75].

As the first two studies by Takahashi *et al.* and Yu *et al.* showed, variation in the transcription factors used in inducing pluripotency is possible. It has further been shown, that the combination of the aforementioned six transcription factors increases efficiency [76]. The factors required for inducing pluripotency are dependent on the cell type, as endogenous gene expression can be used to compensate: for example, melanocytes express Sox2 endogenously and thus ectopic Sox2 is not needed [77]. Further, by only using OCT4 human neural stem cells can be converted to iPSCs [78]. Small molecule compounds present an option for altogether replacing the factors. Instead of introducing exogenous genes into cells, small molecule compounds are used. The number of required genes had previously been reduced using the compounds, but Oct4 remained necessary up until Hou *et al.* managed to chemically induce pluripotency using only 7 small molecule compounds in mice [79,80]. Entirely small molecule based reprogramming for human cells remains yet to be discovered.

Retro- and lentiviruses were used in the first iPSC studies for transferring the transcription factors. The delivery method has been shown to affect the differentiation [81]. Additionally, when using the more efficient integrative methods, there is a risk of integrating viral transgenes into the genome of the cell and ultimately resulting in tumorigenicity. The use of other viral delivery methods, such as adenoviruses or sendai viruses, is less efficient, but does not have the risk of integration [82,83]. Further, non-integrative methods have been shown to produce iPSCs with greater resemblance to fully reprogrammed pluripotent state [75].

Non-viral methods include using plasmids [84], minicircle vectors [85], RNA and proteins such as cell-penetrating peptides [86]. Although plasmids do not require sophisticated laboratories, further studies are needed to improve their efficiency. Minicircle vectors have a greater efficiency, but when compared to other non-integrating methods, they require technology that is more complicated. Synthetic RNA based methods are efficient, non-integrating and non-mutagenic, but the RNAs are difficult to generate in laboratories. Although protein based methods would provide control over the reprogramming procedure, they have thus far had problems with efficiency and production and it is not definitely known, if they can be used for adult cells. [79]

The first human iPSC studies were done using dermal fibroblasts [72,73]. After that, a multitude of cell types have been used for deriving human iPSCs, including hematopoietic, amniotic fluid, adipose, dental pulp and urinary cells [74]. The reprogramming efficiency differs between cell types, as keratinocytes have been shown to be 100 times more efficient than skin fibroblasts, and reprogramming time was two times faster [87]. Additionally, the induced cells may retain epigenetic memory, which may affect the direction in which they eventually differentiate, favoring their original cell type. For example, iPSCs derived from blood cells differentiate easier towards hematopoietic cells [81]. This behavior can be eliminated by continuous passaging of the cell line and suggests that iPSCs can lose their inherited characteristics over time [88].

Reprogramming efficiency and quality can be improved by optimizing the culturing conditions. By introducing growth factors, such as fibroblast growth factor or human leukemia inhibitory factor, differentiation can be inhibited and long-term culturing enabled. Hypoxia has been shown to increase the efficiency [74,89].

2.4.3 Cardiomyocyte cell cultures and cell lines

Studying CMs *in vitro* had been until recently, a daunting task. A cardiac biopsy is a risky procedure, and maintaining the colony is challenging as the cells start to dedifferentiate [90]. Previously, CMs have been differentiated from human ESC lines, which provided not only a powerful tool for studying CM development and function, but also for using them in pharmacological testing [91]. With the discovery of iPSCs, it became possible to create human iPSC (hiPSC) lines and thus individual-specific CMs [3]. This advance has sparked the creation of a multitude of disease models based on specific cell lines, paving way for individualized medicine in the treatment of genetic cardiac diseases. [92,93]

Differentiation of PSCs to CMs can be induced using different methods: co-culturing with mouse visceral endoderm-like (END-2) stromal cells, embryoid body differentiation in suspension and 2D monolayer differentiation [94]. The first beating CMs are observed on day 7 after induction of differentiation and a maximum is reached on days 12-14. Aggregates provide a larger number of CMs, whereas monolayers allow the monitoring of individual cells. [95]

2.4.4 Differences between stem cell derived and mature cardiomyocytes

While the PSC derived CMs (PSC-CMs) are similar to CMs in a developing heart, in that they express the same proteins, behave electrically similarly and display other promising characteristics, the derived CMs do not have the same morphological and functional characteristics of primary adult CMs under current culturing conditions. These differences originate from mainly environmental factors: in vivo, the cells experience organized mechanical and electrical stress, as well as humoral factors. [96] This in total results in a contractile behavior that is different from adult CMs [97]. Table 1 lists key differences between PSC-CMs and adult CMs.

The differences are numerous. The CMs vary in size, with PSC-CMs being significantly smaller. Size is significant, as it has an effect on impulse propagation, depolarization rate and contractile force. By measuring membrane capacitance, which is directly proportional to cell surface area, human ESC derived CMs (ESC-

CMs) have been reported to have a capacitance of 17.5 pF, whereas adult ventricular CMs have a capacitance of approximately 150 pF. [98] The shape of the CMs is different as well: whereas adult CMs are elongated and aligned, in vitro CMs are flat and round [3]. Their sarcomeric structure is immature and the sarcomeres are shorter [13]. In 2D-cultures, they have few, or no T-tubules which are essential to a coordinated contraction [99]. Their mitochondria are long and slender and either clustered near the nucleus or situated near the cell boundaries as opposed to being regularly distributed [100].

A distinct difference in electrophysiology is that PSC-CMs beat spontaneously, whereas adult CMs do not. A likely explanation for this can be the combination of the funny current I_f - absent in adult CMs but present in the developing heart and PSC-CMs - and a reduced inward rectifier K^+ current [101]. The latter also contributes to an approximately 30 mV higher resting membrane potential [9]. PSC-CMs also have a reduced number of Nav1.5 and L-type Ca^{2+} channels, which contribute to the slower AP upstroke velocity and reduced AP plateau phase [101]. There have been studies with differing results considering the handling of Ca^{2+} and the use of intracellular Ca^{2+} stores, suggesting that the variability may be dependent on the maturity status of the cell [102].

The electrophysiological differences have been studied also with *in silico* models, which have indicated the cells to be more sensitive of blocks of L-type Ca^{2+} channels and inward rectifier K^+ current [103]. The models further highlight their greater tendency for arrhythmic events than adult CMs [104]. The contractile force of a cell depends on not only the cell characteristics, but also on the underlying substrate and the measurement technique. In general, however, the force output is not as high as in adult cells. On single cell level, the contraction force measured from PSC-CMs has been measured to be in the 10^{-9} N range [11,105] whereas for adult rat CMs, the force has been in the 10^{-6} N range [106]. The contractile force itself is influenced by multiple factors presented here.

Table 1. Key differences between PSC-CMs and mature CMs related to electromechanical activity. Modified and appended from [102].

Parameter		Human PSC-CM	Mature
Morphology	Cell shape	Flat, round	Elongated
	Membrane capacitance	17.5 pF	150 pF
Sarcomeres	Structure	Disorganized	Highly organized
	Length	1.6 μm	2.2 μm
T-tubules		Few/none	Yes
Mitochondria	Distribution	Irregular, clustered	Regular
Electrophysiology	Spontaneous APs	Yes	Only pacemaker cells
	Resting membrane potential	-60 mV	-90 mV
	AP upstroke velocity	50 V/s	250 V/s
	Repolarization reserves	Reduced	Normal
	Na^+/Ca^{2+} exchanger	Overexpression	Normal
	I_{K1} current	Reduced	Normal
	I_f current	Large	Only pacemaker cells
Ca^{2+} handling		Stage dependent	Mature
Contractile force		10^{-9} N range	10^{-6} N range

There has been evidence to support the idea that the PSC-CMs are capable of maturing to resemble adult CMs [13]. Various techniques have been presented to promote this maturation of the human PSC cells. In addition to longer time in culture [13,101], different approaches such as electrical stimulation [107–109], mechanical stretching [110–112], 3-dimensional scaffolding [113], topographical cues [114,115] and biochemical cues [116,117] have been tested. From drug testing perspective, the feasibility of using iPSC derived CMs has been debated due to their immature state [118,119]. More mature CMs may represent better the adult heart and thus they would be preferable. For transplantation purposes, however, immaturity is preferred to the adult phenotype [102,120].

2.4.5 iPSC derived cardiomyocyte disease models

As iPSC derived CMs carry their original genotype, they provide a platform for culturing and analysis of patient specific CMs *in vitro*. The number of cell models for different diseases has greatly increased, allowing the development of *in silico* models. Recently developed hiPSC models of inherited cardiac arrhythmias have been reviewed by Shinnawi and Gepstein [121], as well as Chunbo and colleagues [122].

In LQTS, for example, the subtypes LQT1 [123], LQT2 [92] and LQT3 [124,125] have been developed and characterized. These LQTS cell models have demonstrated APD and field potential duration prolongation, spontaneous EADs, differences in ion channel currents and impaired rate adaptation of APDs. Positive results in inhibiting abnormal function have been obtained using various substances, such as beta blockers, beta antagonists, Ca^{2+} channel blockers and K^+ channel enhancers. [121]

As with LQTS, human iPSC derived CMs (hiPSC-CMs) from patients with CPVT can serve as *in vitro* disease models. A number of models for different mutations have been created: a RYR2 model [93,126] and a CASQ2 model [127]. These cell models have exhibited EADs and DADs in adrenergic stimulation, higher diastolic Ca^{2+} levels and higher CICR. Rescue of function in the cell models has been achieved using dantrolene, beta agonists, CAMKII inhibitors and Ca^{2+} channel agonists. [121] In addition to the restoring of function in cell models, dantrolene response similarity in cell models and patients has been evaluated [128].

2.5 Electrophysiological in vitro cardiomyocyte studies

2.5.1 Patch clamp

Patch clamp technique refers to a number of experiment setups, where a glass micropipette, filled with a solution similar to intracellular content, is brought to contact with the cell membrane to measure the electrical activity of the cell against another reference electrode. It is considered to be a gold standard for ion channel measurements [129] and has been used in studies since 1949 in its earliest form with the invention of glass microelectrodes [130]. The method was expanded in later studies, with patch clamp method developed in 1976 [131]. It allows the studying of ion channels even in single cells. There are several configurations for measurements, which have different uses: cell-attached, inside-out, outside-out, whole-cell and perforated patch modes. Cell-attached mode serves as a starting point for the other measurement configurations. [129,132]

In the cell-attached mode, the pipette is placed against the cell surface and suction is applied. This creates a strong electrical seal in the range of gigaohms, allowing the measurement of single ion channels now inside the pipette. While it provides a physiological measurement environment, it does not allow intracellular changes. If the pipette is then withdrawn quickly, the patch of membrane is torn from the cell, making it possible to study the cell membrane by manipulating the solution inside the pipette. This is referred to as *inside-out* technique. Alternatively, if suction is applied to destroy the membrane and the pipette is pulled away, the membrane should reseal to make the membrane intracellular side face the pipette solution. This is referred to as *outside-out* technique. In *whole-cell* configuration, suction is again applied to destroy the membrane patch, making the cell interior come in contact with the pipette solution. This process, however, dilutes the cytoplasm. The dilution effect is reduced in *perforated-patch* configuration, where the cell membrane is not ruptured. Instead, channel forming compounds such as fungicides are inserted in the pipette. These agents form channels in the cell membrane, and allow small ions flow through. [132,133]

The measurements can then be done in two configurations: voltage clamp and current clamp. Voltage clamp refers to a measurement, where the membrane voltage is held constant and the current is being measured, whereas current clamp refers to a study where the voltage is being measured when current is held constant. The activity of ion channels can be determined by measuring current flowing through a patch. When the voltage across the membrane is held constant, changes in membrane resistance – opening and closing of ion channels – will result in a change in current. The activity of ion channels in the patch can be measured by measuring the current while manipulating the opening conditions of ion channels, such as voltage and ligands. For studying a specific channel, the other currents are blocked using specific ion channel blockers or by eliminating the ions in question. The opening and closing of channels can then be seen as small changes in the transmembrane current. [132,133]

Patch clamp provides a way to measure cardiac APs and calculate different measures for classifying them. In addition to membrane potentials and slopes, AP duration (APD) has been a commonly used metric for characterization. Different APD measures, such as APD at 90% of amplitude (APD90) and 50% (APD50) have been calculated. These have then been used for categorization of PSC CMs to either nodal, atrial or ventricular [123,134–136]. This approach has, however, been recently debated, as seeding densities may affect the AP morphology and that it should not be used for categorization [137,138]. Despite the debate, it is agreed that patch clamp recordings of CM electrophysiological parameters are the most accurate way to study APs. Further, it is uncontested that potassium current and resting membrane potentials remain important measures [139].

While patch clamp is commonly done manually, automated systems exist. Manual patch clamp is not well suited for high throughput analysis, as it is work intensive and its use requires extensive training. Recent advancements in automated patch clamp has made its use in drug screening applications more feasible due to possibility for higher throughputs. Manual patch clamp, however, remains necessary in research applications including ion channel studies, cell populations with mixed cell types and differentiated cells, such as iPSCs and ESCs. [129,134]

2.5.2 Microelectrode arrays

In vitro microelectrode array (MEA) refers to a typically 2-dimensional electrode arrangement, which can measure the electrical activity of tissues and cell cultures, and stimulate them electrically. Typically, the cells to be studied are placed on top of the electrode grid in a culture well. The activity of each electrode can be measured, showing the field potential changes of the culture. Such arrays have been in used since 1972 [140]. They have been a mainstay in CM studies [92,141–143] due to their non-invasive nature, capability for long-term measurements and the possibility to stimulate and record from different sites [144,145].

MEA provides an alternative to more complex techniques, such as patch clamp, as less manual work and expertise is required [146]. However, MEAs are not very well suited towards single cell studies, as the electrodes themselves and the distances between electrodes are large compared to single cells. Further, the electrical coupling between the electrodes and cells is not optimal. [147]

2.6 Optical fluorescence methods

2.6.1 Fluorescent dyes

Fluorescence is used in cellular studies to tag certain proteins and molecules for imaging. Here, potentiometric dyes, and calcium dyes in particular are examined.

Potentiometric dyes allow the measurement of the cell membrane potential by optical measurements. These dyes bind to the cell membrane and they change their optical properties - fluorescence or absorption - based on the alterations of the electrical field on cell membrane. This method provides high-resolution spatial measurements of the membrane potential, enabling the studying of phenomena such repolarization patterns. Fluorescent dyes are the most sensitive probes, as they provide the highest signal-to-noise ratio. Their fluorescence changes linearly with membrane potentials. The setup consists of a light source to excite the fluorescent reporters, optical filters, optics, a photodetector, and data acquisition hardware. [148,149]

The most commonly used potentiometric fluorescent dyes in cardiac measurements are aminonaphthylethenylpyridinium (ANEP) dyes, di-4-ANEPPS, di-8-ANEPPS and RH237. For a 100 mV change in membrane potential, their fluorescence changes by 10%. [148]

Fluorescent calcium indicators provide a way to visualize and measure the Ca^{2+} fluctuations within the cell, in a similar fashion as voltage indicators. The Ca^{2+} indicator fluorophores bind to free Ca^{2+} ions within the cell and emit fluorescent light, which can then be detected with a similar setup as with voltage indicators described above. [148,150] There are a number of different chemical Ca^{2+} indicator dyes, which have different properties. The dyes can be divided in two categories: single wavelength (non-ratiometric) and ratiometric dyes. The single wavelength dyes (such as Fluo-3, Calcium Green-1) emit the same excitation and emission wavelengths independent of their binding status. This is advantageous, when multiple fluorescent compounds are used as no spectral overlap will occur. In general terms, the more $Ca^{2}+$ is present, the brighter the signal. Ratiometric dyes (such as Fura-2 and Indo-1) not only change their intensity, but shift their emission or excitation peak when they bind to Ca^{2+}. This allows a precise measurement of intracellular Ca^{2+} concentration by the ratio of excitation and emission amplitudes. While it requires a greater wavelength spectrum, it helps counteract effects such as uneven dye loading, dye leakage, photobleaching and cell volume changes [150]. While ratiometric dyes provide more precise results, quantitative calcium recordings have been shown to be possible with single wavelength dyes as well [151].

The fluorescent dyes, however, suffer from different degrees of cytotoxicity and may induce electrophysiological changes in the cells [152,153]. The phototoxicity results from free radical production by the excited states of the dyes, due to excitation with the UV light [154]. These effects, along with bleaching of the probe molecules – the photo-induced chemical destruction of fluorescence – severely limit the use of in short-term measurements [153]. For voltage-sensitive dyes, di-4-ANEPPS has not been widely used for single cells due to imminent phototoxicity [148], with RH237 having similar levels of phototoxicity [149]. While di-8-ANEPPS is less phototoxic, the time window for recordings is still limited. [153,155] There have been different approaches to counteract the effects, but in general a greater signal-to-noise ratio lead to greater photodynamic damage [156]. In addition, the dyes are compartmentalized and extruded from the cells during the measurement, and precise targeting is difficult [157,158]. In addition, they have been shown to affect the cell stiffness and adhesion [159]. As the Ca^{2+} indicators bind to free Ca^{2+}, they also serve as Ca^{2+} buffers. While a higher concentration of the dye would produce a greater signal, it would also have an effect on the Ca^{2+} kinetics of the cell. Further, the dyes have different speeds with which they bind to Ca^{2+} [150].

In cardiac studies, Ca^{2+} imaging has been widely used due to the importance of Ca^{2+} in the CM biomechanics. In fact, the role of CICR in excitation-contraction coupling was discovered by using fluorescent calcium probes [160]. It has been used e.g. in hiPSC-CM functionality assessments [161,162], assessment of drug effects using hiPSC models [163,164] and characterization of diseases [93,165,166].

2.6.2 Genetically encoded fluorescent probes

A number of issues related to dyes can be circumvented by introducing fluorescent genetically encoded fluorescent probes to the cells. For potentiometric measurements, genetically encoded voltage indicators (GEVI) were initially used in 1997 [167], and the method has been applied recently in various studies with different cell types [168,169]. Further, these indicators have been tested in hIPSC-CMs as well [170,171]. In addition to longer studies, GEVIs make it possible to target specific cells and the uptake in cells is more homogeneous [169]. Most GEVIs are not without cardiotoxic effects, as they may affect the myocardial structure and function [172]. With the recently developed VSFP2.3, no evidence for cardiotoxicity has been found [169].

For Ca^{2+} imaging, the same approach can be use as Ca^{2+} indicator proteins can be genetically encoded to cells. When compared to Ca^{2+} sensitive dyes, the GECI have a substantially lower signal-to-noise ratio due to their 10-times higher resting baseline fluorescence, and inferior kinetics and ion selectivity [173,174]. Recent studies with genetically encoded fluorescent dyes have shown their high potential in CM studies [171,175]. However, there have been results indicating that the genetic probes may interfere with the Ca^{2+} release activity of the cells [176].

2.7 Mechanical analysis

2.7.1 Atomic force microscopy

Initially when discovered in 1986, atomic force microscopy (AFM) was developed for analyzing 3D nanoscale features of solid materials with very high resolution and sensitivity [177]. It has since been used in various biomedical studies as well.

In AFM, a sharp probe is descended on top of the surface to be measured. AFM then measures all forces occurring between the probe and the surface by attaching the probe to a cantilever, which acts as a spring. The sample is then scanned in x-y plane and the bending or deflection of the cantilever is measured e.g. using a piezoelectric actuator or lately, a laser beam to cover the entire sample to be measured [177,178]. AFM can be used in different imaging modes. In the most commonly used mode, contact mode, the probe is in mechanical contact with the sample. The deflection of cantilever is kept constant and measured using a feedback loop. There is a risk of damaging the sample, and there is no constant zero force reference level. In dynamic modes, the probe is not in contact with the sample, but oscillates near its resonance frequency. Typically, amplitude of oscillation is the measured parameter, although frequency and phase can be measured as well. Jumping mode is a combination of the contact and dynamic mode: the probe is moved in and out of contact, which retains a zero force reference point. [179]

In CM studies, the topographical mapping of the cell is not always necessary, as the biomechanics of contraction and relaxation are temporal in nature. As the cell beats, its surface movement can be detected using AFM. Due to its high sensitivity, it has been widely used in CM studies. It has been used to determine the contractile behavior [10,180] as well as measure the relation between force and calcium concentration using a concurrent Ca^{2+} fluorescence imaging and AFM [181]. In studies using hIPSC-CMs, AFM has been used to study the mechanobiological properties of single CMs and characterize cells derived from patients with dilated cardiomyopathy [182], and the contraction-relaxation parameters of CMs with different compounds [183].

2.7.2 Mechanical transduction methods

Mechanical transduction has a long history of measuring cellular forces. The first method was based on optically measuring the bending of fine glass filaments by cells [184,185]. Methods such as using microelectromechanical systems [186] and viscous loading [187] have been proposed. However, new methods have been in demand as the instrumentation for these methods has been difficult and obtaining exact results has not been straightforward.

A force measuring technique was proposed by Tan and colleagues in 2003. They developed a platform where cells are seeded on top of a microarray of elastomeric microposts, allowing the studying of mechanical interactions between cells and substrates. The deflection of each micropost is measured to characterize contractile force, velocity and power. The method has high spatial resolution and it can be used in conjunction with other methods, such as immunofluorescence. Tan and colleagues used bovine pulmonary artery smooth muscle cells [188]. Rodriguez and colleagues used microposts extensively in their studies of hIPSC-CMs. The effect of substrate stiffness, extracellular matrix and tri-iodo-L-thyronine has been studied. The contact between the cell and microposts may have an effect on the cell membrane and thus the cell function. [11,189,190]

Wilson et al. measured rat skeletal muscle contractile function using cells plated on silicon cantilever chips [191]. The chip platform consists of multiple cantilevers, which can be used to measure the force and the spatial coordinates of the beating. Human ESC-CMs were later studied using the same method by Stancescu et al. from the same research group [192]. Goßmann et al. developed a method, where monolayers hiPSC-CMs were grown on thin silicone membranes. As the CMs beat, the membrane moves up and down. The pressure beneath the membrane is measured using a pressure sensor and the tension calculated from the deflection [193].

Yin and colleagues presented a method of measuring contractile force using magnetic beads in 2005. Their approach is based on attaching a magnetic bead to one end of a CM. When the cell beats, the bead moves with the cell. An external magnetic field can then be used to have the cell contract under different force loads. They studied a rat chronic ischemic cardiomyopathy model. [194] The effect of dynamic loads has also been studied by Iribe and colleagues in 2007 using a pair of piezo translator -positioned carbon fibers. The relation between force and length was studied in ventricular guinea pig CMs [195].

2.7.3 Traction force microscopy

Traction force microscopy is an indirect measurement of contractility and force of adherent cells using elastic substrate embedded with microbeads. The method was pioneered by Harris and colleagues in 1980 [196]. From a general point of view, a reference force microscopy image, or “null force” image, is taken before seeding of cells. When the cells are seeded on top of a suitable substrate, the cells exert their force on the substrate. Its deformation and subsequent measured movement of the microbeads from a second image is used to compute the traction force after the cells are detached from the surface. By using the reference image and the second image, traction fields can be calculated by measuring individual bead movement or by applying different displacement analysis methods, such as particle image velocimetry (PIV), described in more detail in section 2.8.2. [197] The force by itself is not quantifiable from displacement alone, but can be inferred from the mechanical properties of the system. The substrates used in traction force microscopy can be assumed to have linear and isotropic properties, as well as to be incompressible. With the substrate stress-strain properties known, the inverse problem of elastic theory can be calculated using inverse Boussinesq formulation. Alternatively, if high quality 3D imaging is available, the stress tensor can be calculated directly from the image data. [198,199]

2.7.4 Impedance assays

Impedance assay platforms are non-invasive and label-free method of analyzing CM functionality. The assays consist of electrodes embedded to the bottom of cell culture wells. CMs are seeded and attached to the wells and a weak alternating current is applied between the electrodes. The cells in between act as insulators and restrict the flow of current between the electrodes. CM beating causes small changes in the range of 0.1% in the cellular impedance. These fluctuations can be measured, enabling the beating analysis of CM monolayers. [200] While impedance is an electrical property, impedance assays measure the mechanical function – the movement of cells over electrodes [201].

The method has been used recently in studying cardiotoxicity. The xCELLigence Real-Time Cell Analysis Cardio platform was developed and validated with mouse ESC-CMs, hiPSC-CMs and neonatal rat CMs [202]. Responses to drugs and various arrhythmic agents were tested on mouse ESC-CMs [203], hIPSC-CMs were analyzed in the presence of compounds [204]. The sensitivity of the method provides a challenge, as the sensitivity is highly dependent on electrode distance and layout [205].

2.8 Video based motion estimation

2.8.1 Method classification

Determining change between two consecutive visual states forms the basis of motion estimation. Motion can occur due to movement of either the measured object or the observer, in 2D or 3D. The purpose of motion estimation is to measure the movement using visual methods and quantifying it. While measuring the movement of macroscopic objects is somewhat trivial, measuring the movement, or flow, of liquids has been a relevant question for ages in engineering. In its most primitive form, flow can be visualized by following a floating object in a stream. In image-based measurements, movement in 3D is projected to a 2D plane, creating an ill-posed problem.

Motion estimation methods can be roughly divided in two categories: optical flow methods and feature tracking methods. Optical flow methods use the changes in spatio-temporal pixel intensity values in determining motion, whereas the feature-based methods use specific features such as corners, templates and color tones to match features between frames. [206] Optical flow methods can be further divided into differential techniques, block matching, energy-based techniques and phase-based techniques [207]. Block matching method is focused on in this study. Feature based methods are typically used in video compression: although the calculations are performed faster, they have lower accuracy [208].

2.8.2 Block matching background

Only in the past 40 years has it been actually feasible to quantify accurately the fluid velocities in multiple points. The study in question, particle image velocimetry (PIV) means the "accurate, quantitative measurement of fluid velocity vectors at a very large number of points simultaneously", as well defined by R. J. Adrian [209]. Typically, in a PIV measurement, the planar or volumetric flow being measured is seeded with tracer particles that follow the flow. These tracer particles are then illuminated twice within a short time period and the images are recorded. The displacement of the seeder particles can then be calculated from the obtained images by dividing the recording into small interrogation areas for block matching. For each of these interrogation areas, a local displacement vector is calculated using statistical methods. It is assumed that the particles in an interrogation window move homogeneously. As per definition of velocity, the first derivative of position with respect to time, the displacement vector and the known time interval between the frames is used to calculate the velocity vector for each interrogation window, resulting in a velocity vector field between the two frames [210]. Due to the application of block matching in the context of CM analysis as opposed to flow dynamics, the technical background of PIV measurement methods - including seeding of gases/liquids, light sources, optics and sensors along with the necessary model corrections related to these factors - is not presented here. Additionally, only single exposure PIV processing methods are presented, as double exposure is not relevant for CM studies. A more focused view on PIV methods can be found in the review article Fundamentals of digital particle image velocimetry [211] and the book Particle Image Velocimetry: A Practical Guide by Raffel *et al* [210].

In a digital grayscale image, each picture element, or pixel, is assigned an integer value: a higher pixel value indicates a brighter element. As previously mentioned, the recordings are divided into interrogation areas of size M*N, or preferably N^2. In general, a degree of similarity is calculated for an interrogation window in the first image with a number of interrogation windows in the second image to match the block [212] at a specified search distance. The windows may overlap each other, and in most algorithms an overlap of 50% is used [213]. This process generates a degree of similarity matrix, which shows a composition of peaks, as shown in Figure 5. The signal peaks in the figure illustrate the locations with the highest cross-correlation factor, surrounded by noise. A key issue in a successful block matching evaluation relies on whether the signal peak is higher than the noise peaks. [209]

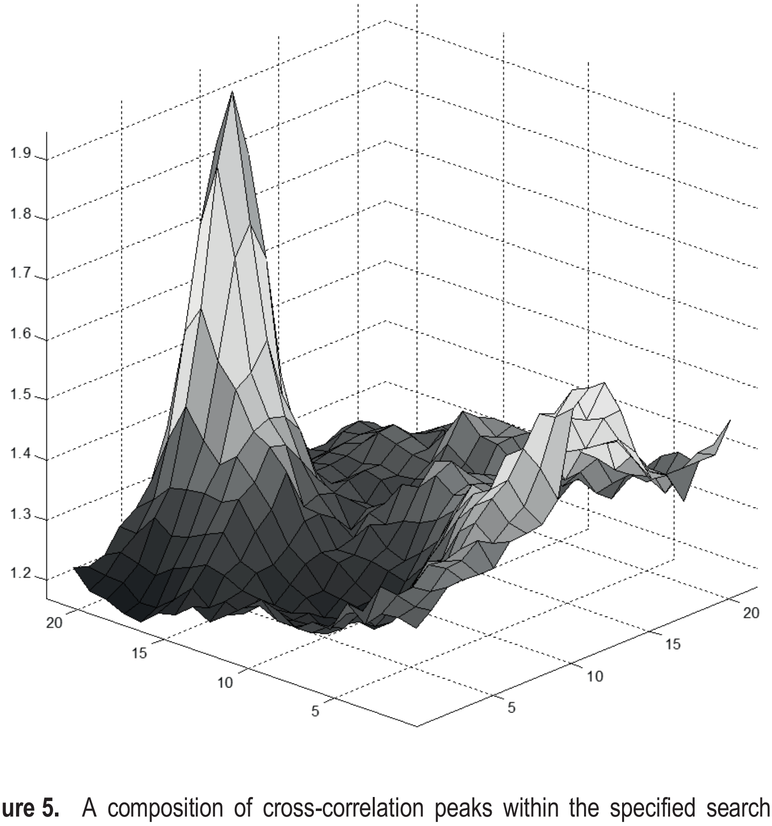

Figure 5. A composition of cross-correlation peaks within the specified search distance in a PIV recording. The highest correlation peak represents the most likely location of displacement.

A number of algorithms using cross-correlation in one form or another have been developed for evaluating the recordings. The digital implementations of a few commonly used ones are presented here. In its simplest form, cross-correlation (ϕ_A) can be defined for the consecutive images f and g as:

$$\phi_A(m,n) = \sum_{i=1}^{M}\sum_{j=1}^{N} f(i,j)g(i+m,j+n)$$

Here, f and g represent the gray value intensities in the interrogation window of size M x N pixels, with (m,n) representing the offset required for matching. Due to the direct multiplication of values, the correlation of the matching area may have a smaller value than bright spots with high intensity value. This concern has been taken into account in another cross-correlation measure (ϕ_B) where the mean gray value of each interrogation area is reduced, as shown below:

$$\phi_B(m,n) = \frac{1}{(M-m)(N-n)}\sum_{i=1}^{M-m}\sum_{j=1}^{N-n}\left[f(i,j)-\bar{f}\right]\left[g(i+m,j+n)-\bar{g}\right]$$

The values $\bar{f}$ and $\bar{g}$ indicate the mean values for images f and g, respectively. The denominator applies to the overlapping area of the interrogation windows. Ultimately, it is divided by the overlapping area of the interrogation window. The last step can be left out to achieve another measure of correlation (ϕ_C).

Mean absolute error (MAE) method tries to find the best degree of similarity by minimizing the error in absolute differences of gray value distributions. The function can be defined as following:

$$D(m,n) = \frac{1}{MN}\sum_{i=1}^{M}\sum_{j=1}^{N}\left|f(i,j)-g(i+m,j+n)\right|$$

In 1996, Gui and Merzkirch proposed a new method, based on minimizing the quadratic differences of matrices to find the degree of similarity, namely minimum quadratic difference (MQD) method [214]. MQD is also known as mean squared error, least squares matching or sum of squared differences [215]. Using this approach, the displacement D(m,n), where the maximum similarity can be found, is described as below:

$$D(m,n) = \frac{1}{MN}\sum_{i=0}^{M-1}\sum_{j=0}^{N-1}[f(i,j) - g(i+m, j+n)]^2$$

The performance of these different methods have been evaluated, and the results indicate that the latter two produce the best results. Fei, Gui and Merzkirch found the correlation based measures (ϕ_A, ϕ_B and ϕ_C) to have lower accuracy than the error-based measures, with MQD algorithm to provide the most accurate values [216]. Ghanbari found MAE to be marginally more accurate than MQD [212].

Due to the images being discrete, the resulting displacements are limited by the pixel count in the interrogation windows. In order to increase the accuracy of displacement estimation, interpolation methods are used to achieve sub-pixel accuracy. Once a motion vector with integer precision accuracy has been calculated, fractional positions around the first estimate is are calculated and considered. Bilinear interpolation is commonly used in deriving the fractional pixel values due to its simplicity and robustness, but higher-order polynomial functions are used for greater accuracy. However, the process of searching the matching block again in interpolated image data is computationally expensive. A combination of block matching and optical flow method without interpolation has been presented as an alternative. [217]

Typically, the raw vector field data is not without errors. There may be spurious vectors of unusual magnitude, missing vectors and background Gaussian noise. Thus, post-processing of the vector field data is often required before analysis of the results. The errors may be evident when compared with neighboring vectors, but correcting them without human pattern recognition ability may be difficult. [218] Various different methods, such as global histogram operator and dynamic mean value operator have been used for validation [210].

2.8.3 Cardiomyocyte contractility studies

Traditionally, video-based CM contractile motion analysis has been conducted by measuring the movement of the cell extremities or sarcomere length [219–221] or measuring the intensity variations during beating with fast Fourier transform [222]. In its simplest form, the length of CMs are measured while relaxed and contracted.

While not an immediately intuitive solution due to its primary use in flow dynamics, PIV/image correlation analysis has been used in CM studies in the past decade. These methods had only been applied in few applications or in minor roles concerning cell dynamics until recently, regarding cell migration and wound healing process with fibroblasts, estimation of motion in hemicochlear preparates and only later with CMs [223–225]. Even though the cell environment is not seeded with particles, as opposed to traction force microscopy presented in 2.7.3, the PIV methods are capable of determining the cellular deformations due to differing cell textures. Typically, CM deformations during cell beating resulting from contraction and relaxation is recorded with a camera and a phase contrast or brightfield microscope. A suitable motion detection is then applied to quantify the motion in the videos to obtain a beating signal.

In terms of use in cellular studies, analysis of video microscopy has the advantage of not requiring probes or tracer substances. The cells are, however, still subject to visible light – a condition the cells are not exposed to *in vivo*. While white light per se has not been shown to produce immediately obvious adverse effects to the cells, it has potential for phototoxicity if the light sources do not carefully exclude near ultraviolet/infrared frequencies. [226]

A number of groups have developed video microscopy based methods [12,14,16,17,222,227–231], presented in Table 2. The block matching methods are most commonly used. A wide range of cardioactive substances have been studied, including autonomic agents, ion channel blockers and other pharmaceuticals. Varying frame rates (frames per second, fps) have been used. The directionality of CM contraction has been in focus only by some groups. The typical measured parameters include beating frequency, durations of contraction and relaxation, total duration of mechanical activity, time from baseline to peak, displacement and magnitude. The characteristics of wild type cardiomyocyte biomechanics have not been widely reported, with the effect of substances being more in focus.

Table 2. Recent key publications regarding video microscopy analysis of CMs, and their analysis features.

Publication	Method [fps]	Cell culture	Substances studied	Parameters	Measured characteristics
Kamgoué et al. (2009) [12]	Block matching (cross-correlation) [9 fps]	Adult rat CM (single)	-	Displacement, time from baseline to peak.	Contraction/relaxation cycle 2.05 s. Time to maximum contraction 0.57 s, 0.33 s.
Hossain et al. (2010) [222]	Variation in total pixel intensities [30 fps]	Mouse ESC derived CM	Caffeine hydrate, p-hydroxyphenylacetamide, calcium chloride dehydrate	Amplitude, frequency Motion direction detection	-
Hayakawa et al. (2012) [14]	Block matching (MAE) [14, 125 fps]	Neonatal rat CM (monolayer)	E-4031, dl-sotalol, terfenadine, 18-beta-flycyrrhetinic acid, 1-heptanol, acetylcholine, epinephrine, propranolol	Frequency, maximum velocities of contraction and relaxation, peak width	-
Liu et al. (2012) [228]	Demons registration with principal component analysis [15-30 fps]	Nondescript (single, populations)	-	Motion direction detection	-
Chen et al. (2014) [229]	Horn-Schunk optical flow [7, 20 fps]	Human ESC derived CMs (sheet)	E-4031, isoprenaline	Duration, frequency, synchronicity, orientation, acceleration Motion direction detection: polar coordinates	Contractile duration 1.16+/-0.06 s, 1.13+/-0.03 s
Hayakawa et al. (2014) [227]	Block matching (MAE) [150 fps]	Human iPSC derived CMs (monolayer)	Isoproterenol, E-4031, verapamil	Velocity, deformation distance, total duration, frequency	Peak contraction speed 8-15 µm/s, peak relaxation speed 4-10 µm/s
Huebsch et al. (2015) [16]	Block matching (MAD) [14 fps]	Human iPSC derived CMs (sheet)	Isoproterenol	Velocity, frequency Motion direction detection: beating centers	Peak contraction velocity 80 µm/s, peak relaxation velocity 35 µm/s
Maddah et al. (2015) [230]	Relative correlation of intensity vectors [50 fps]	Human iPSC derived CMs. (monolayer, sphere, single)	Norepinephrine, cisapride, quinidine, verapamil, E-4031, sotalol, nifedipine, aspirin	Frequency, duration	-
Lee et al. (2015) [17]	Horn-Schunk optical flow [15.6, 8.6 fps]	Human iPSC derived CMs	E-4031, verapamil, blebbistatin	Duration, frequency, amplitude, time from peak to baseline, time from baseline to peak, area under curve Motion direction detection	-
Ribeiro et al. (2017) [231]	Block matching (cross-correlation) [30 fps]	Human iPSC derived CMs (single)	Caffeine, isoproterenol, omecamtiv mecarbil	Average displacement, velocity, spatial asynchronicity, temporal asynchronicity Motion direction detection	Contraction 1.09 µm, 0.78 µm; peak relaxation velocity 3.78 µm/s, 2.87 µm/s; peak contraction velocity 6.85 µm/s, 3.53 µm/s

In 2009, Kamgoué and colleagues calculated intracellular strain fields from single adult and neonatal rat CMs. A cross-correlation measure was calculated for the image pairs and the propagation of strain waves and shortening of CMs was quantified. Additionally, they developed a test set of artificial images to verify the method. In essence, they were among the first to apply image correlation analysis to single CMs. [12]

Hayakawa and colleagues developed a method for extracting CM beating parameters and assessing wave propagation in neonatal rat CM monolayers. The monolayers were imaged using phase-contrast microscopy with a frame rate of 125 fps. For vector calculation, MAE was used. Additionally, they performed simultaneous Ca^{2+} measurements and studied the effect of several drugs and agents that influence the beating. K^+ channel blockers (E-4031, dl-sotalol, terfenadine), gap junction inhibitors (18-β-glycyrrhetinic acid, 1-heptanol), autonomic agents (acetylcholine, epinephrine) and propranolol were applied. [14] They later expanded their studies with hIPSC-CMs using the same method, and compared the findings with traction force microscopy, field potential measurements and Ca^{2+} imaging. They found the video microscopy to correlate well with force development and showed that effect of different compounds can be detected using video imaging. [227] The method had later been used in a software tool by Sala and colleagues, used in characterization of LQT and hypertropic cardiomyopathy. They studied the effect of isoprenaline and nifedipine on contraction amplitude, as well as relaxation and contraction duration. [232]

Liu and colleagues introduced a real-time automatic CM analysis method and characterized the beating signal by studying its spectral properties [228]. Their cell data consisted of dense CM populations and single CMs. The cellular background was not reported. As opposed to PIV methods, they used Thirion's demons image matching method [233] for the generation of the vector fields. In short, the demon based algorithm tries to align objects by non-rigid models and estimating their deforming force vectors. In their later work [18], they improved their method by addressing the problems related to accuracy of motion estimation and that the method assumed CMs to be connected and beat with the same pattern. They developed a method, which segmented images into clusters that have differing beating characteristics.

Chen and colleagues demonstrated the use of an integrated platform in CM studies with optical methods. They aligned clusters of CMs using shrink-wrap film and assessed their beating parameters. In addition, they applied E-4031 and isoprenaline to evaluate the performance of the platform. They studied H9 human

ESC-CMs, recorded their beating at 7 fps and 20 fps, and analysed their beating using a correlation based open-source software built by Sun and colleagues [234]. A number of characteristics were calculated: duration, frequency, synchronicity, orientation and acceleration of contractions. As opposed to previously presented methods evaluating the magnitudes of vectors, they assessed the recorded series of images with categorical values in a grid to determine areas beating together. [229] The method was later used in conjunction with machine learning methods to show the feasibility of automated high-throughput drug effect analysis. hIPSC-CM response to E-4031, verapamil and blebbistatin was assessed. [17]

Huebsch and colleagues applied a block matching algorithm to analyze hIPSC-CMs. In their method, MAE is used to generate the vector fields from 14 fps videos. They defined beating centers as regions where the motion originates by calculating the net movement toward and away from a smaller selected subregion. A beating center is a region where the difference between inward movement and outward movement is maximized. They validated the results of the motion analysis by electrophysiological methods. In one set, motion analysis was conducted with a concurrent MEA measurement. In another test set, a concurrent patch clamp measurement was done. In addition, they analyzed the Ca^{2+} flux using GECI GCaMP6f and performed motion analysis on the videos. Further, they assessed the CM response to isoproterenol with the developed method. [16]

Maddah and colleagues presented a CM analysis platform based on video microscopy and image analysis [230] using a method they developed earlier [15]. Their analysis pipeline consists of recording CM cultures with a camera on 24 fps acquisition and segmenting them to regions of beating cells, non-beating cells and background. The beating signal is formed by calculating a correlation coefficient of the frames with respect to a resting-state reference image. Finally, the signals are characterized and regions are clustered to identify areas with similar and differing beating characteristics. Additionally, they characterized CM drug response using cisapride and norepinephrine. In the later study, regular hIPSC-CMs and GECI line (GCaMP) IPSCs were analysed using the platform. They also performed comparisons with existing methods: video analysis was applied simultaneously with patch clamp. Additionally, they performed test sets with video analysis followed by calcium imaging, using quinidine and blebbistatin. They also expanded on their previous study of drug responses by adding E-4031, verapamil, sotalol, nifedipine and aspirin, in addition to the ones mentioned earlier.

Ribeiro and colleagues used cross-correlation based block matching to analyze hIPSC-CMs. The aim was to analyze the effect of cell shape and substrate properties to contractility. They used micropatterned surfaces to shape the CMs to more physiological form. They found these factors to increase cellular mechanical output. In addition, directed calcium flow, mitochondrial distribution, more mature electrophysiology and T-tubule formation were found to increase contractility. [231]

3 AIMS OF THE STUDY

The aim of the study was to develop a non-invasive video-based analysis method for characterizing CM biomechanics and to assess its functionality and performance.

This involved validation of the tool, conducting comparative studies and evaluating relevant biological problems using the method. To reach this goal, the following study aims were prepared.

1. Develop a tool for quantifying hiPSC-CM beating dynamics in vitro, assess the imaging protocol and determine the method accuracy using artificial data sets (Studies I, II)

2. Compare and validate the measurement results with patch clamp, calcium imaging and microelectrode arrays (Studies I, III, IV)

3. Demonstrate the use of the method on diseased cells using LQT1 and CPVT disease specific hiPSC-CMs, determine beating phenotypes between populations and compare them with respective electrical phenotypes (Studies III and IV)

4. Perform simultaneous contraction and calcium imaging measurements (Study IV)

5. Develop a software tool for use in cardiomyocyte studies (Studies I-IV)

4 MATERIALS AND METHODS

4.1 Generation of stem cell lines

The iPSC cell lines used in the studies were generated in BioMediTech, University of Tampere with permission from the ethical committee of Pirkanmaa Hospital District (R08070). Written consent for the research was also obtained from all the skin biopsy donors.

The cell lines used in the studies are listed in Table 3, along with the mutations. The wild type (WT) cell lines UTA.40602.WT and UTA.04607.WT are treated as control cell lines in the studies. The LQT1 is studied using two founder mutations of the KCNQ1 gene with two cell lines each: G589D (also referred to as KCNQ1-FinA: UTA.00208.LQT1 and UTA.00211.LQT1 – here in brief LQT1A) and ivs7-2A>G (also referred to as KCNQ1-FinB: UTA.00102.LQT1 and UTA.00118.LQT1 – here in brief LQT1B). CPVT is studied using two mutations of RYR2 gene with one cell line each: exon 3 deletion (UTA.05605.CPVT – here in brief CPVTa) and V4653F (UTA.05404.CPVT – here in brief CPVTb).

Table 3. Cell lines and mutations used in each of the studies.

Cell line	Mutation	Referred to as	Study
UTA.04602.WT	None (WT)	WT/Control	I, II, III, IV
UTA.04607.WT	None (WT)	WT/Control	I, III
UTA.00208.LQT1	KCNQ1-FinA: G589D	LQT1A	III
UTA.00211.LQT1	KCNQ1-FinA: G589D	LQT1A	III
UTA.00102.LQT1	KCNQ1-FinB: ivs7-2A>G	LQT1B	III
UTA.00118.LQT1	KCNQ1-FinB: ivs7-2A>G	LQT1B	III
UTA.05605.CPVT	RYR2: exon 3 deletion	CPVTa	IV
UTA.05404.CPVT	RYR2: V4653F	CPVTb	IV

The WT cell lines were established from primary dermal fibroblasts obtained with a skin biopsy from a healthy 55-year-old female. The LQT1 patient with G589D mutation is a 46-year-old female and the one with ivs7-2A>G mutation a 51-year-old female. Both patients were on β-blocker medication. The CPVT patients were described in an earlier study [163]. The obtained primary fibroblasts were cultured under fibroblast culturing conditions. The WT and disease specific iPSC lines were established using lentiviral infection, followed by retroviral infection. The full protocol of establishing the iPSC cell lines has been described earlier [69,92].

4.2 Cardiomyocyte differentiation and characterization

The hiPSCs were differentiated into CMs by co-culturing with murine visceral endoderm-like (END-2) cells (Humbrecht Institute, Utrecht, The Netherlands). After a minimum of 14 days, beating colonies were dissociated mechanically, treated with collagenase A (Roche Diagnostics, Mannheim, Germany) and plated on 0.1 % gelatin. In studies I-III, the dissociated cells were plated on standard cell culture multi-well plates and in Study IV, the CMs were plated on glass coverslips.

4.3 Video-image based contraction analysis

Analysis of the video data represents the core part of the study.

4.3.1 Video recordings

Beating cells were identified visually using a microscope and spontaneous beating was recorded on video without pacing. In the studies I and III, a Nikon Eclipse TS100 phase contrast microscope (Nikon Corporation, Japan) and an OPTIKA DIGI-12 digital video camera (OPTIKA Microscopes, Italy) were used. The duration of recorded videos was 30-60 seconds, with a 720x480-pixel resolution, 30 fps. In Study II, IGV-B1620 (IMPERX, FL, USA) was used with Nikon Eclipse TS100 phase contrast microscope (Nikon Corporation, Japan) to record videos at 60 and 120 fps. Study IV included similar video recordings, but overall featured a more complex imaging protocol, described in 4.4.3.

4.3.2 Video analysis process

During this thesis project, a video analysis method and software tool was gradually developed and improved. In brief, the method uses particle image velocimetry based block matching method for calculation of velocity vector fields from consecutive video frames. It uses a beating focus point based approach, defined in detail later in this section, for determining directional components from the vector fields and calculates beating signals, characterizing the motion of the cell.

The flowchart of the analysis is illustrated in Figure 6. As the method was developed during and between the individual studies, several phases shown were not present and used at first, as they had not yet been developed and were instead done manually.

<table>
<tr><th colspan="2">1. PIV calculation from video</th></tr>
<tr><td colspan="2">Manually set window size and analysis region for MQD based motion estimation</td></tr>
<tr><th colspan="2">2. Region of interest selection</th></tr>
<tr><td>Manual (I, III)</td><td>Texture-based ROI estimation on grayscale entropy, object size and distribution of grayscale values (II, IV)</td></tr>
<tr><th colspan="2">3. Beating focus estimation</th></tr>
<tr><td>Manually based on visual observation (I, III)</td><td>Based on velocity vector field gradient at maximum contraction velocity and estimated location (II, IV)</td></tr>
<tr><th colspan="2">4. Directional signal calculation</th></tr>
<tr><td colspan="2">Radial and tangential components based on beating focus point and ROI (I-IV)</td></tr>
<tr><th colspan="2">5. Signal peak detection</th></tr>
<tr><td colspan="2">Based on inter-peak distance and magnitude, possible signal filtering (II, IV)</td></tr>
<tr><th colspan="2">6. Template calculation</th></tr>
<tr><td colspan="2">Correlation-based averaging (II, IV)</td></tr>
<tr><th colspan="2">7. Signal parametrization of contraction and relaxation</th></tr>
<tr><td>Manual (I, III)</td><td>Automatic determination of contraction and relaxation start and end points (II, IV)</td></tr>
<tr><th colspan="2">8. Generation of results</th></tr>
<tr><td colspan="2">Result summary and upload to database (IV)</td></tr>
</table>

Figure 6. The stages of video analysis process with the development of automation and other features, and their use in studies. While the indicated features were present during the studies mentioned, the features were not all used for the indicated studies. For instance, the online database was not used in deriving results in Study IV.

The overall analysis flow starts from the recorded video of cardiomyocyte beating. The block matching window size and the analysis region are set manually (stage 1). This allowed the calculation of velocity vector fields for multiple cells within the same video. Although determining a proper window size and analysis region could be made automatic, setting these manually enabled flexible use in different applications. After the analysis, the cells were segmented semi-automatically using a texture-based algorithm using greyscale entropy, cell size and the distribution of greyscale values within the analysis region (stage 2). Within these segmented cells, the beating focus point was estimated based on the velocity vector gradient within the cell during a contraction (stage 3). Based on the ROI and the beating focus point, the directional signals are calculated (stage 4). Signal peaks are then detected based on estimated peak distance, and frequency and magnitude distribution of the signal. Possible signal lowpass filtering is applied to facilitate peak detection (stage 5). An averaged waveform template is calculated based on a set correlation factor (stage 6): the signal is divided into beat cycles, and the template is initiated with a beat cycle, and the rest of the beat cycles are either averaged or discarded depending on the correlation with the initiated template, as presented by Pradhapan and colleagues [235]. The template or the whole signal is then parametrized to extract the start- and end-points of contraction and relaxation movement (stage 7). A summary of the results is then provided, and uploaded to a result database (stage 8).

4.3.2.1 Image velocimetry

In the studies, MATLAB PIV toolbox mpiv was used to calculate velocity vector fields between video frames using MQD method [236]. The analysis methodology was developed iteratively between the studies and while the underlying mechanics stay the same, the method has become more refined.

Adjacent sub-window overlap ratio of 0.5 was used. A default sub-window size of 32 pixels was used and vector resolution was improved with recurrent calculation, reducing the window size by half. Choosing an optimal sub-window size depends on the image resolution, cell size and the desired resolution of the velocity vector field. The calculated vector fields typically were not complete as stray vectors were eliminated. Median filter was applied to the vector field and it corrected using kriging interpolation to determine missing vectors. Finally, the field was smoothed using a weighted 3x3 kernel as a low-pass filter. An example of a velocity vector field determined from cardiomyocyte contraction is shown in Figure 7.

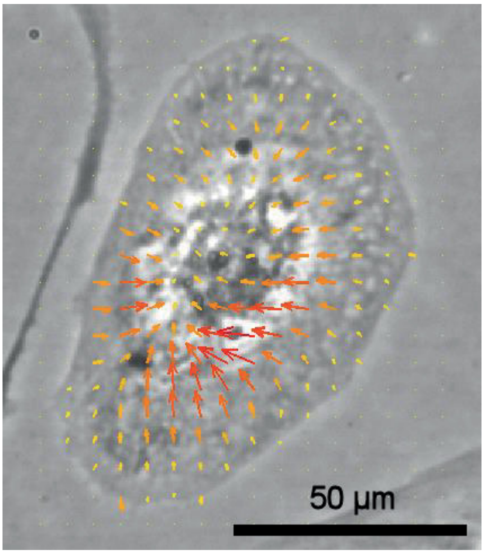

Figure 7. A velocity vector field measured during a CM contraction. In contrast to an adult CM with a primary axis of contraction, hiPSC-CMs typically have more fusiform beating patterns directed towards the center of the cell.

The parameters related to maximum possible displacement and stray vector elimination threshold were subject to small alterations depending on the cell/cell cluster size and application.

4.3.2.2 Derivation of beating signals

Beating signals were calculated from velocity vector fields. While the time axis for the signals is easily defined due to frame rate, a meaningful measure of movement magnitude is not easily accessible and dependent on the camera and the measurement optics. Here, the absolute magnitude of motion was not deemed interesting due to a number of reasons: the cell sizes varied, their maturity was not constant resulting in fusiform beating patterns, the cells were not uniformly attached to the culture plates and ultimately the fundamental question of how to select the region of interest properly remained unanswered.

First, a region of interest was determined. During the first studies, it was selected manually based on observed motion. Later on, semiautomatic methods including texture segmentation based on local entropy were used to determine the cell location and the textures that typically exhibit movement within a cell. Due to the differences in contractile behavior and morphology between mature CMs and human iPSC derived CMs, the cells did not have predetermined directionality in their beating. The fusiform beating behavior caused the contraction to head towards the center of the cell from all directions. In order to differentiate the directional components between contraction and relaxation, a beating focus point was determined. At first, it was determined manually and later automatized by determining velocity vector field gradient maxima.

In order to quantify the fusiform nature of beating, the region of interest was divided to eight sectors around the beating focus point. The velocity vectors in that region were divided to radial and tangential components. In the studies I and III, the division to components was done with respect to the midline of the sector whereas in studies II and IV, with respect to their individual location vector. The division is illustrated in Figures 8A and B, respectively.

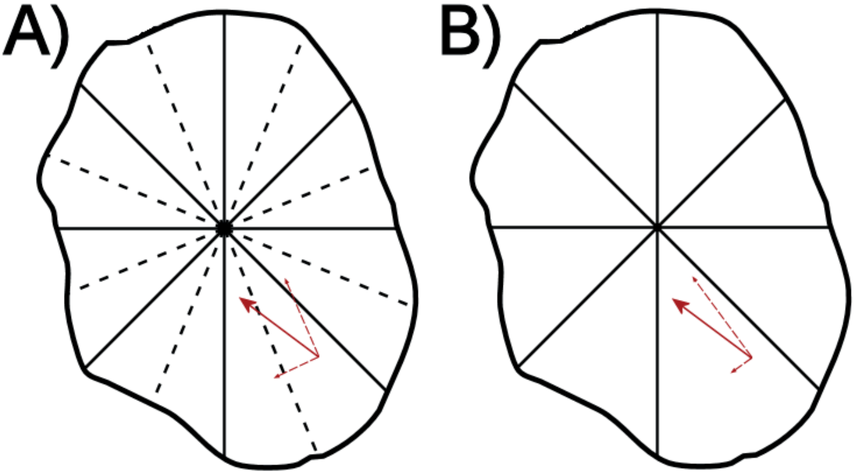

Figure 8. The sector division approaches used in studies for determining radial and tangential components of motion. Approach A) uses sector midline as a reference, whereas approach B) uses the location vector of each individual vector.

With this process, 16 different beating signals were formed – two from each of the eight sectors. The radial signals represent the movement towards and away of the beating focus point, and tangential signals the movement perpendicular to that. The positive and negative signs for the signals were not set consistently.

4.3.2.3 Signal post-processing

When possible, the signals were used unfiltered. This was done to preserve the signal shapes with as much detail as possible, as the signal/noise distribution was not immediately known. In studies I and IV, motion signals integrals with respect to time were calculated. This way the resulting displacement signals could be compared with other measurement modalities. In Study II, the signals were filtered using a 20-point Gaussian window. In Study IV, the signals were first filtered using zero-phase digital filtering with a third order Butterworth lowpass filter at normalized 0.25 frequency. The baseline was corrected with linear detrending.

4.3.2.4 Signal characterization

In order to characterize the motion signal, time characteristics of different phases were determined: duration of contraction (phase 1), duration when cell stays contracted (phase 2) and duration of relaxation (phase 3). In addition, the duration when the cell is relaxed was measured. As the analysis continued, it became apparent that an additional phase 4 was required for the parameterization due to motion observed after relaxation. Phase 5 indicated the duration cell remained relaxed. The phases are illustrated in Figure 9.

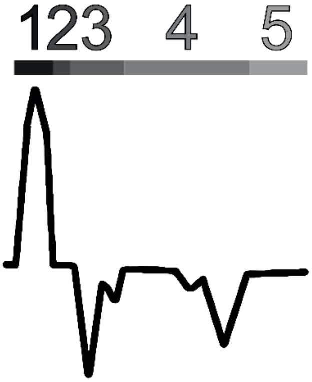

Figure 9. An illustration of the beating motion signal featuring all specified phases. Phase 1 indicates the cell is contracting, phase 2 the duration cell remains contracted, phase 3 the cell relaxes, phase 4 the motion after the first relaxation peak, and phase 5 when cell remains relaxed. In healthy control-type cells, typically only phases 1, 3 and 5 were present.

4.3.2.5 Correlation based averaged waveform templates (II and IV)

Averaged waveform templates were calculated to determine parameters characterizing the cell beating. These templates were calculated using a method presented by Pradhapan and colleagues [235].

The template was first initialized by selecting a beat at measurement mid-point. Cross-correlation with the other beats was then measured. The beats with a minimum cross-correlation value of 0.8 or greater were selected and averaged, to remove waveforms that visually did not correspond well to the template. The templates were synchronized based on the peak of contraction velocity. This process allowed the rejection of erroneous beats and more consistent averaging. The cross-correlation value was lowered in Study IV to 0.5 to disregard only the most erroneous peaks due to the lower number of total beats. The effect of frame rate and the number of beats was examined in Study II, as described in 4.3.3.

4.3.3 Artificial data sets (I and II)

Artificial data sets were included in studies I and II. In Study I, a still frame of a CM was distorted to produce a video imitating a beating CM. Pinch and spherize filter [237] was used to generate distortion fields of varying magnitudes to a region of interest. In essence, each point of the region of interest was mapped to a virtual half-sphere and a new distance to the beating focus point was set based on the desired distortion factor. The known distortion field was then compared with the results obtained using video analysis. The effect of noise to the analysis was further tested: speckle noise of different variances was applied to the images, the resulting videos were analyzed and the analysis result correlation calculated. Speckle noise was selected because sporadic appearances of bright and dark pixels presents a challenge for PIV. The noise was calculated using the equation below, where J represents the resulting image, I represents the original image, V the set variance and I_R the random noise between values -0.5 and 0.5, using a mean of 0.

$$J = I + \sqrt{12V} I I_R$$

In Study II, the effect of sampling frequency to the formation of templates was examined. As described in 4.3.1, videos at 120 fps were recorded. The videos were decimated to 60 fps and 40 fps by omitting frames to create videos with lower framerates. The videos were then analyzed using the present method, and the resulting templates were resampled for comparing templates formed with different templates.

4.4 Reference in vitro measurements

In addition to the video image-based method, the cells were analyzed using measurements that quantify their electrical and ionic activity. The measurements were conducted both concurrently and asynchronously with the video-based analysis method. The results were used to determine cellular phenotypes in both control and disease-specific genotypes, as well as compare the biomechanical signals with signals from electrical and ionic activity measurements.

4.4.1 Patch clamp measurements (I and III)

Patch clamp measurements were conducted in Study I and III. In Study I, patch clamp was used as a reference method for simultaneous measurement with video measurements in two single CMs. Standard current clamp configuration was used in perforated patch mode to measure CM action potentials while recording light transmission video. TTL synchronization pulses were used to synchronize the video data with current clamp data and compare the obtained video signal with the membrane potential signal. Similarly in Study III, the same measurement mode was used to record action potentials for both simultaneous and standalone measurements. Action potential characteristics (APD90, APD50 and APA) were measured to determine whether the cells were ventricular-, atrial- or nodal-like. In addition, patch clamp was used simultaneously with video imaging to compare the electrical and mechanical phenotypes of WT and LQT specific cells.

LQT-specific CM electrophysiology was studied by blocking delayed rectifying K^+ currents in ventricular-type CMs, mimicking the LQTS conditions with abnormal K^+ current dynamics. The slowly activating component I_{Ks} was blocked using JNJ303 at 300 nM concentration. The rapidly activating component I_{Kr} was blocked using E-4031 at 100 nM. APs were measured at baseline, exposure and after wash-out.

The action potentials were recorded using Axon Axopatch 200B (Molecular Devices, CA, USA) patch clamp amplifier, connected via AD/DA Digidata 1440 (Molecular Devices, CA, USA) to an acquisition computer, digitally sampled at 20 kHz and filtered at 5 kHz using a low pass Bessel filter. In concurrent video measurement, ANDOR iXon 885 CCD camera (Andor Technology, Belfast, Northern Ireland) was used.

4.4.2 Calcium imaging (III)

Ratiometric calcium imaging was used in Study III to assess the Ca^{2+} handling in LQT-type cells. The CMs were plated on glass coverslips and loaded with 4 µM Fura-2 AM (Life Technologies Ltd, UK). Andor iXon 885 CCD camera and inverted Olympus X71 microscope were used in imaging. Camera was synchronized with Polychrome V light source to excite the cells at 340 nm and 380 nm wavelengths. The emission was detected at 505 nm. The 15 s recordings were categorized by amplitude stability, arrhythmias due to multiple peaks and smaller amplitude events.

4.4.3 Concurrent calcium imaging and video measurements (IV)

Study IV involved a simultaneous measurement of calcium and video imaging. To determine the feasibility of measuring motion from a video with calcium fluorescence, a protocol for alternating between measurement modalities was devised, as described below. The CMs were plated on glass coverslips and loaded with 4 µM Fluo-4 AM (Life Technologies Ltd, UK). Two light sources, Polychrome V and Olympus TH4-200, were used to create four different lighting profiles as shown in Figure 10.

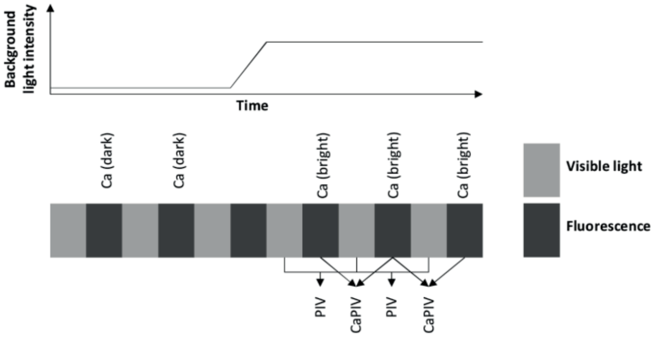

Figure 10. Concurrent calcium and video measurement lighting profiles. The fluorophore excitation was synchronized with the video recording so the frames alternated between fluorescent imaging and only visible light. Mid-recording the background light intensity was increased to obtain transmission video images with visible light. Four different signals were calculated: PIV from the transmission frames, CaPIV from the fluorescent frames, Ca(dark) from the fluorescence frames without background light and Ca(bright) with fluorescent light. Image from Study IV.

Two imaging channels were used: Andor iXon 885 CCD camera was used in imaging and was synchronized with Polychrome V light source to excite calcium at 488 nm every other frame while the other frame remained unilluminated. TH4-200 light source was used mid-measurement to apply the background light, while still being able to discern calcium fluctuations. Olympus IX71 inverted microscope was used in the measurement. Both fluorescence and video signals were recorded through Olympus U-MF2 Alexa 488 bandpass filter cube (excitation 470-495, emission 525/50 nm). Frame rates and resolutions varied; frame rates of 46-114 fps were acquired, resulting in 23-57 fps per channel.

The process generated four different signals from the same region of interest: calcium transient signal with and without illumination (Ca (bright) and Ca (dark), respectively), and PIV signal with and without calcium excitation (PIV and CaPIV, respectively). Motion signals were measured as described in 4.3.2.2. The motion signals were integrated with respect to time to produce contraction signals, and linear detrending was used to correct the baseline.

Both calcium and contraction signals were characterized by determining parameters describing waveform widths and amplitudes. Durations at percentages of the maximum peak height were defined for 10 %, 25 %, 50 %, 80 % and 90 %, as shown in Figure 11A. The time difference between contraction and calcium peaks were measured by calculating the time difference between the maximum rates of change in both onset and offset of each waveform, as illustrated in Figure 11B. To assess the effect of fluorescence to motion signal magnitude, symmetric mean absolute percentage error was calculated between PIV and CaPIV peaks for all signals.

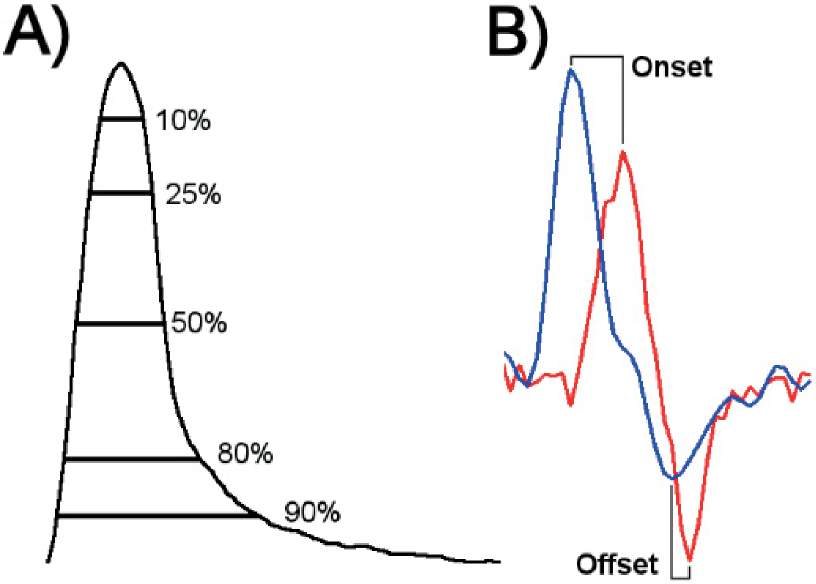

Figure 11. Parameters calculated in concurrent measurement of calcium and contraction. A) Duration parameters defined at 10%, 25%, 50%, 80% and 90% of maximum peak height. B) Time differences between maximum rates of change in calcium (blue) and contraction (red) signals. The time interval is defined positive when contraction follows calcium. The signals are scaled and fitted for illustration. Figure A is adapted from Study IV.

4.5 Statistical analysis

The statistical analysis was performed using MATLAB R2014a. In Study I and II, mean values and standard deviations (SD) were calculated for the determined parameters. In Study III, two-sample t-test was used in comparing two individual experiments and one-way ANOVA was used when comparing multiple experiments. Baseline and drug effect were compared using paired sample t-test. Standard error of mean was used in place of standard deviation. In Study IV, a two-sample t-test was used to determine the statistical difference between the measurement modalities. Linear regression was used and coefficient of determination was calculated in mapping parameters against each other. To demonstrate the variability of the cells, population SD was calculated instead of sample SD. Symmetric mean absolute percentage error was used in determining differences in velocity magnitudes. In all studies, p-values below 0.05 were considered significantly different.

Here in this thesis, additional measures of standard error of mean are calculated to make comparisons easier between the studies.

4.6 Analysis tool interface development

The tool was to be used both as standalone and as augment to other studies. Cell biologists actively participated in determining the tool capabilities and suggesting features. As such, it was subject to constant changes when new needs rose. Initially, the software was little more than a processing script to extract beating signals. Manual work was required to extract signal parameters. During a study, the tool had typically gone through a number of adaptations many of which were not implemented in the study at question, as it would have required repeated re-analyses of the same data.

The aim of the software tool was to provide a means for biologists to use contraction analysis as a low threshold method. For this purpose, a graphical user interface (UI) was to be developed to make the use of the tool convenient and intuitive. Semiautomatic operation was considered necessary for providing users with control over the analysis, while keeping the user experience streamlined and the interface uncluttered.

A number of requirements was set for the tool, and other features were added along the way. The software was to analyze cells one at a time by determining cell location, region of interest and beating focus point. It was to calculate the velocity vector signals for all sectors and represent them for the user. In addition, it was to calculate the waveform templates and calculate time intervals characterizing the signal. The user was to be able to upload the results of the analysis to an online database and generate result reports in PDF format.

5 RESULTS

The results presented here are divided in categories: the results from the validation of the method on artificial data and on control-type cells, results from patient specific cells, and finally the video analysis tool resulting from the study.

5.1 Video analysis method validation

5.1.1 Cardiomyocyte beating velocity signal characterization (I-IV)

The MQD method estimates where a certain windowed region has moved between the two frames, resulting the distance and direction for each window. Using the protocol described in 4.3.2-4.3.2.3, signals characterizing the CM beating were obtained.

The method enabled successful quantification of beating from cells where the beating resulted in movement of cell textures and the moving area was large enough to support 16x16 windowing. Movement consisting of primarily Z-directional movement manifested itself as changes of pixel brightness in the cell. Without X/Y-directional movement, measuring the motion was difficult and occasionally impossible. While the changes in pixel intensity are visible to human eye, it was not detectable using the PIV block matching method. These cell videos were not included in the analysis.

The beating signal shows the motion magnitude on an arbitrary scale. For illustration, the magnitude is shown linearly normalized to 0-1 interval. A typical beating signal is shown in Figure 12. The signal illustrates the contraction cycle of the cell with two peaks in opposite directions: a contraction and the relaxation.

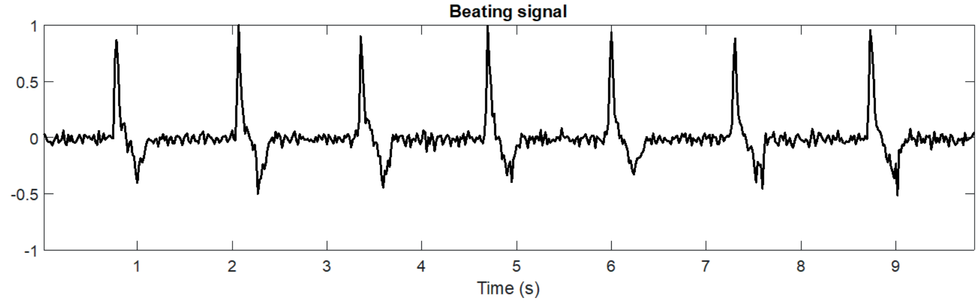

Figure 12. A typical beating signal as a function of time. An upward peak represents contraction and a downward peak relaxation. Zero level represents the baseline, with amplitude normalized to maximum contraction velocity.

5.1.2 Validation of movement (I)

To validate the method, artificial video data using a known displacement field set was created, a protocol described in 4.3.3. Correlation coefficients between the signals obtained from artificial data and the known displacement velocity was calculated. The results varied between sectors and directions, with mean value of 0.95 for all sectors. The extent of contraction was not uniform from the beating focus point, as the cell was not uniformly round. Correlation of entire signals with differing amplitudes results in lower correlation figures. However, as the changes were done for each frame, measures such as time to peak and transient widths would not have shown any differences.

The effect of noise to the measurement was tested using speckle noise. The correlation between the set displacement field and the one measured with different variances was calculated for three sectors to cover different parts of the cell. Figure 13 illustrates the decline of mean correlation to the known motion with respect to noise level as maximum percentage change in pixel intensity. In essence, a 0.003 variance resulted in maximum pixel value changes of ± 10 % and 0.015 variance changes of ± 22 %.

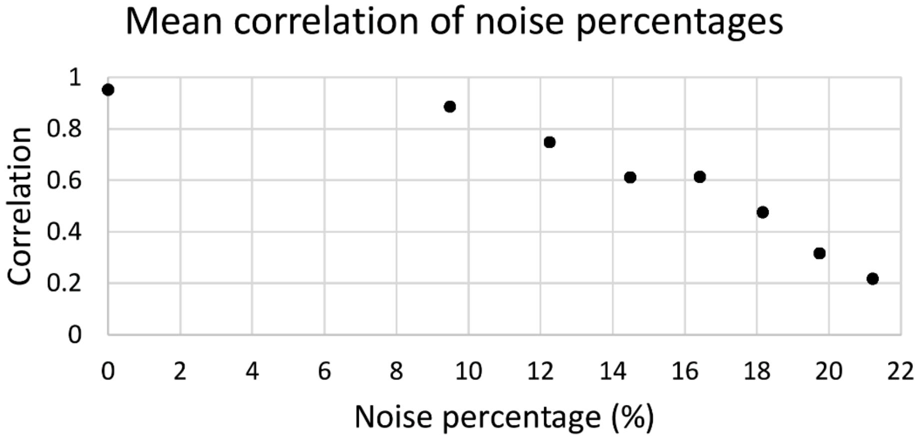

Figure 13. Mean correlation of variances as a function of speckle noise percentage. A correlation of 0.9 level can be achieved even at 9 % noise percentage level. Data adapted from Study I.

As a reference, the pixel value fluctuation in a typical video recording was measured from a 300 frame recording used in Study I, in an area without cells. The values were found to be between ± 0.4-0.6 %.

5.1.3 Template building (II)

In Study II, the effect of frame rate and number of samples to forming the templates was studied as described in 4.3.2.4 and 4.3.3. The original 120 fps videos and the derived videos decimated to 60 fps and 40 fps videos were analyzed using templates. The correlation of template signals from 60 fps and 40 fps videos with resampled template signals from 120 fps videos were calculated. Halving the framerate to 60 fps decreased the mean correlation in the measured cells in three sectors to 0.97, and dividing into three to 40 fps decreased it to 0.95. The correlations between resampled 120 fps templates and 40 fps templates was found to be poor in two videos. The effect was found in videos with higher frame rate.

The effect of number of beats to the template quality was assessed visually. Starting at 20 beats, the number of beats included in the calculation of the templates were decreased one by one. It was determined that the signal quality remained similar until 12 beats (60 % of the beats) were included. At six beats (30 %), the template quality was visibly poor in comparison with the original.

5.1.4 Concurrent video and patch clamp measurement (I)

In the concurrent video and patch clamp measurement, described in 4.4.1, the contraction velocity signal was integrated with respect to time to obtain position data. It was compared with the current clamp data to measure the time difference between AP and contraction peaks. The time difference of all beats in the measurement consisting of control cells in Study I was found to be 306 ms with a 40 ms SD, which is in line with a later study [232], as well as with previously reported values for rabbit ventricular myocytes [41].

5.1.5 Effect of fluorescence on video measurement accuracy (IV)

Brightfield video and calcium imaging was recorded in subsequent video frames. This procedure allowed the near-simultaneous assessment of the accuracy of the MQD based PIV method in the presence of fluorescent dyes. Transient duration parameters at widths 10, 25, 50, 80 and 90 % did not show any statistically significant differences between the signals measured in the presence of absence of fluorescent dyes, as can also be seen in Figure 14. As stated in 5.1.1, assessing the absolute magnitude of motion does not necessarily offer relevant information due to the difficulty of inter-cell comparison. However, the magnitude of motion of the same cell can be compared. When comparing the velocity amplitudes of the signals with and without fluorescence in all recordings involved in the study, a 5 % symmetric mean absolute percentage error was found.

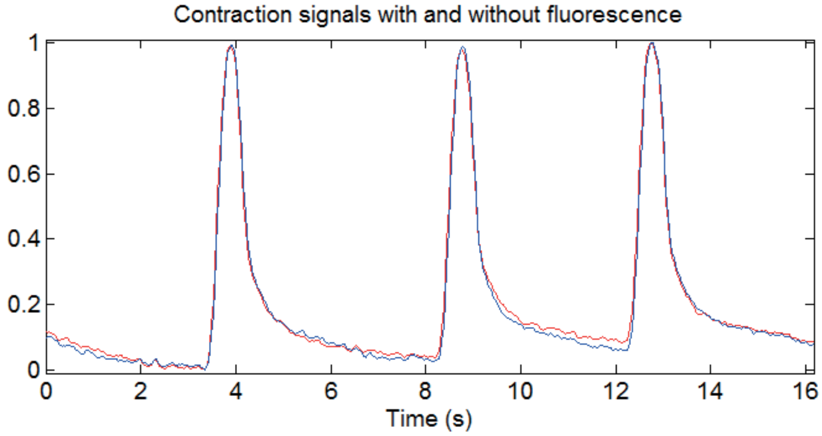

Figure 14. Typical contraction signals with and without fluorescence. Blue shows the signal in the presence of fluorescence and red the signal in its absence.

5.1.6 Contraction-calcium dynamics measurement

Due to the negligible differences in video measurement accuracy caused by fluorescence, contraction and calcium could be measured simultaneously. A typical signal from a concurrent measurement is shown in Figure 15, with calcium shown in blue and contraction in red. Contraction follows calcium with a delay and the contraction transient has a steeper fall than that of calcium, a finding that can also be interpreted from previous studies [16].

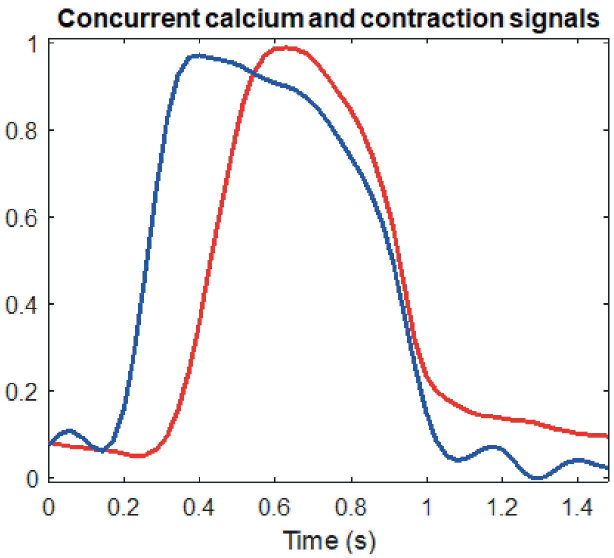

Figure 15. A typical calcium and contraction transient pair in a concurrent measurement scaled to fit on an arbitrary magnitude scale. Calcium shown in blue and contraction in red.

The contraction and calcium transients were characterized using peak width parameters as described in 4.4.3. The signals were obtained from brightfield video frames with fluorescent calcium present. The peak width parameters in WT cells are shown in Figure 16.

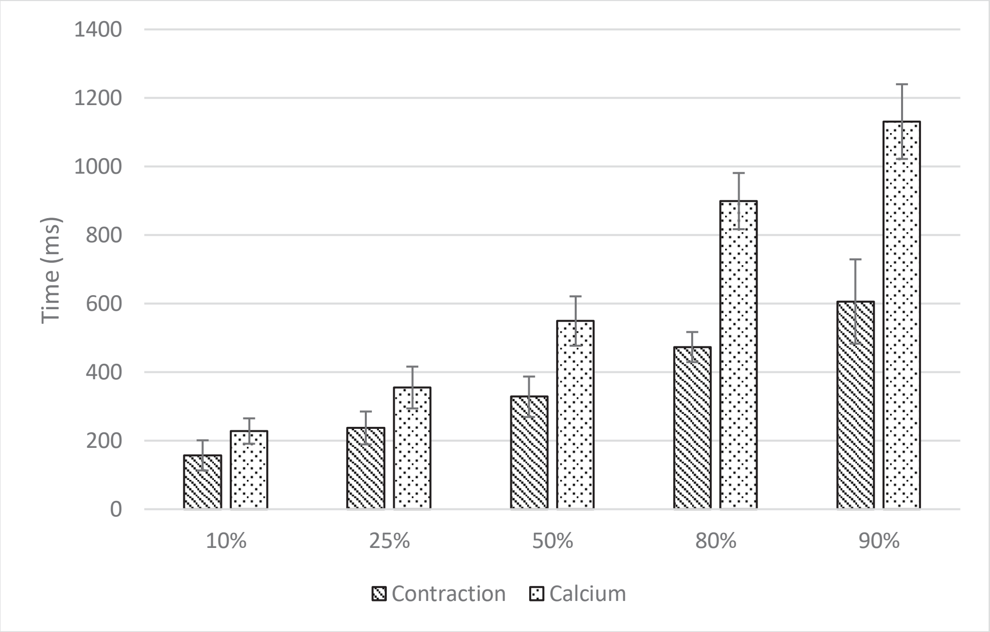

Figure 16. Fridericia beat rate corrected contraction and calcium transient characterization parameters at 10 %, 25 %, 50 %, 80 % and 90 % of the peak height maximum in WT cells. The transients at the peak 10 % have nearly the same width. The error bars show standard error of mean. The mid-transient 50 % values show a greater disparity as calcium transient width reaches 600 ms – a near-baseline value for contraction. Data adapted from Study IV.

5.2 Cell line specific studies

5.2.1 Motion signal characterization of wild type cardiomyocytes (I)

Motion signals obtained from wild-type cells were analyzed in Study I. The measured time parameter values were measured as such, without regard to beating rate. In our later study [171], Fridericia QT correction was used to account for different beating frequencies. When the same correction is applied to the results of Study I, the phase durations are easier to be compared with previously reported results, as the effect of different beating rate is decreased. Here, the results of the Study I are presented as QT-corrected and shown in Table 4.

Table 4. Beating frequency corrected phase durations in WT cells. Data adapted from Study I.

Cell (n = 13)	Beats per minute (BPM)	Phase 1 (ms)	Phase 2 (ms)	Phase 3 (ms)	Phases 1-3 (ms)
1	12.0	264	0	334	609
2	18.2	282	0	411	693
3	22.8	232	0	322	554
4	23.6	264	1	328	592
5	24.1	121	0	149	270
6	24.6	317	6	397	720
7	26.0	135	0	262	397
8	26.3	171	10	451	632
9	29.1	177	0	250	427
10	36.5	226	1	274	501
11	41.8	192	3	262	456
12	43.1	245	0	323	569
13	66.3	216	7	326	549
Mean	27.3	218.9	1.7	313.6	536.1
SD	9.1	60.2	3.1	82.2	124.9
SME	2.6	17.4	0.9	23.7	34.7

5.2.2 LQT patient specific cardiomyocytes (III)

5.2.2.1 Motion signal characterization

Typically, the relaxation movement followed the contraction movement with a delay of 0-2 frames in Study I, indicating a delay of 0-67 ms with 30 fps in individual beats. However, already a visual observation of LQT-type cells can reveal atypical beating behavior when compared to wild type cells. In LQT1A (G589D mutation) type cells, the cell stayed contracted for a prolonged time before relaxing. The LQT1B (ivs7-2A>G mutation) type cells exhibited similar behavior, but also included twitching motion after the cell had seemingly relaxed. This behavior in mechanical phenotype was previously unreported and was a new finding. As described earlier, an additional phase 4 indicating the incomplete relaxation was required to characterize the beating.

Typical signal waveforms of both LQT phenotypes were presented in Study III. Here, integrated waveforms of both are illustrated as well in Figure 17, showing how the previously reported waveforms relate to the integrated contraction curves used in later studies. While the characterizations “relaxation duration” and “incomplete relaxation" seem misleading when considering the integrated contraction signal, the unintegrated motion signal represents better the actual visual observation.

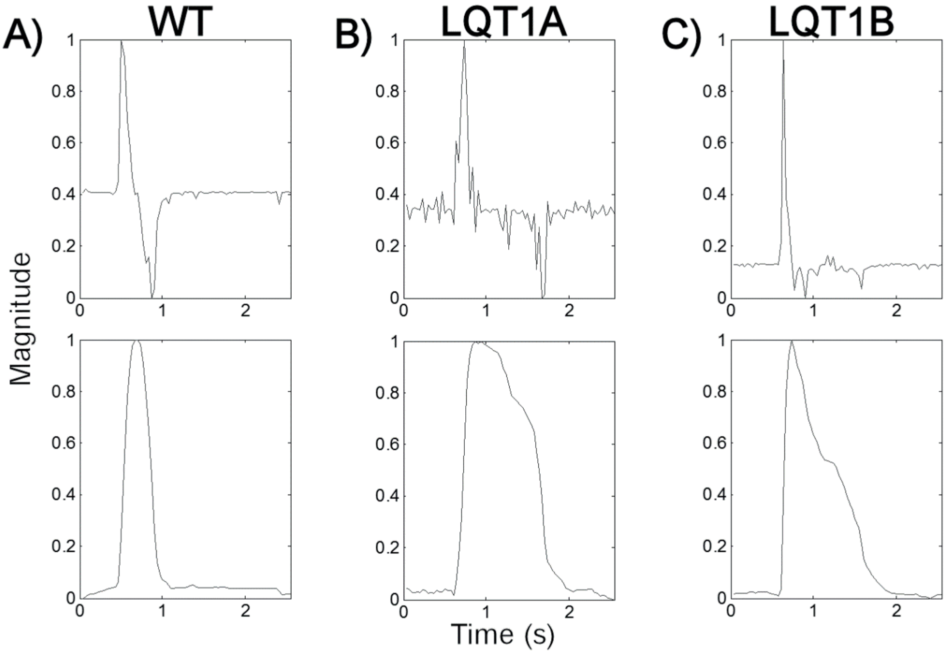

Figure 17. Typical WT and LQT motion signals (above) and integrated contraction signals (below). Subfigures A-C represent the beating signals from WT, LQT1A and LQT1B cells, respectively. LQT1A cells exhibit a prolonged interval between contraction peak and relaxation peak in motion signal when compared to WT, where relaxation occurs shortly after contraction. LQT1B cells show multiple, smaller relaxation-associated peaks.

In Study III, the WT cell lines used as control cells did not exhibit abnormal behavior. 17/24 CMs of type LQT1A exhibited phase 2, with two of these cells exhibiting also phase 4. Phase 2 was present also in LQT1B type cells (17/25), although its duration was not as long as in LQT1A type cells. 15 out of these 17 exhibited phase 4. Control-type beating patterns were seen in the remaining cells of both LQT-specific cell lines. These results of these time parameters were presented in Study III similarly as in Study I without beat rate correction. Table 5 illustrates the durations of the phases with Fridericia beat rate correction.

Table 5. Durations of beat phases in wild type, G589D and ivs7-2A>G genotypes in milliseconds, ± standard error of mean. Both control-like and abnormal beating phenotypes were observed in the patient specific cell lines. (*) indicates $p<0.05$ and (**) $p<0.001$ in two-way t-tests. Data adapted from Study III.

		Phase 1 (ms)	Phase 2 (ms)	Phase 3 (ms)	Phase 4 (ms)	Phases 1-4 (ms)
Control (n = 11)	Normal	220 ± 18	3 ± 1	320 ± 15	0	543 ± 40
G589D (n = 7)	Normal	223 ± 24	12 ± 4	285 ± 12	0	520 ± 36
(n = 17)	Abnormal	204 ± 20	132 ± 22*	256 ± 21	26 ± 25	620 ± 61
ivs7-2A>G (n = 8)	Normal	188 ± 23	4 ± 2	288 ± 31	0	480 ± 54
(n = 17)	Abnormal	228 ± 25	35 ± 11	301 ± 21	254 ± 41**	818 ± 64

5.2.2.2 Electrophysiological measurements

In addition to the mechanical phenotype, the LQT phenotype was studied using patch clamp and calcium imaging in Study III. The APD50s in LQT1A- and LQT1B-type ventricular-like CMs were 458.5 ± 57.4 ms and 416.1 ± 221 ms, respectively. When compared to control-type ventricular-like CMs, APD50 was 291.8 ± 21.5 ms, indicating a statistically significant difference, as was expected. In LQT1A type cells, spontaneous EADs were detected, but not in LQT1B type cells or WT cells. In calcium imaging, LQT1A type cells exhibited more severe abnormalities. Both disease genotypes displayed double peaks and small amplitude arrhythmias in calcium transients more than in WT cells. Calcium transients from LQT1A type cells had more double peaks, small amplitude arrhythmias as well as longer calcium transient duration than those from LQT1B type cells. Typical signals from the measurements are shown in Figure 18.

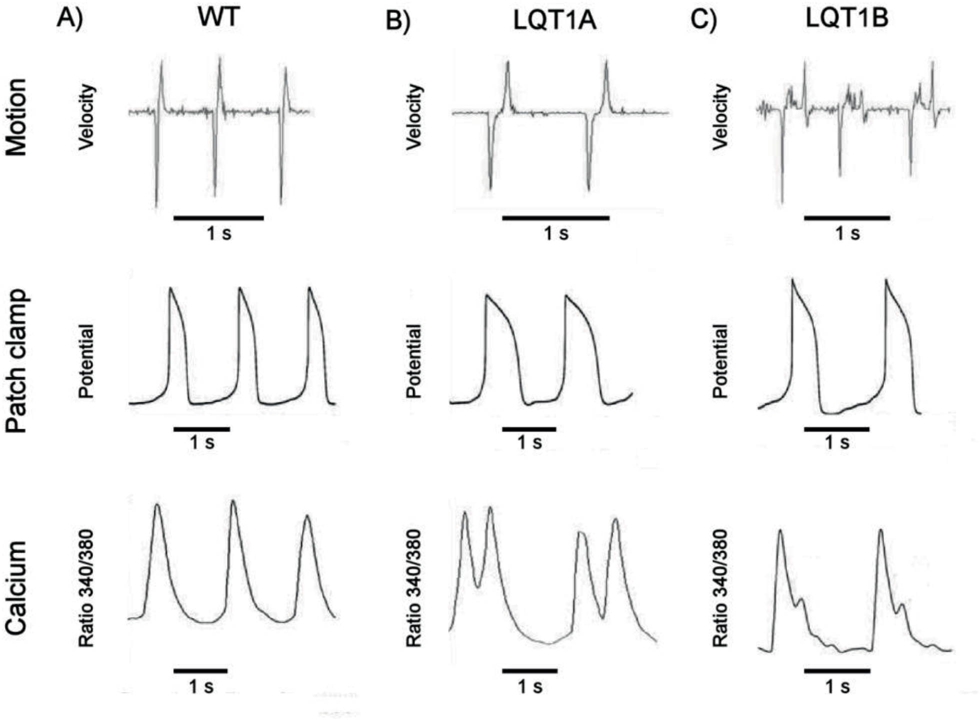

Figure 18. Typical motion signals (top row), patch clamp recordings (middle row) and calcium transients (bottom row) from A) WT cells, B) LQT1A and C) LQT1B cells measured from different cells in non-simultaneous measurements. The most typical abnormality in LQT1A cells were prolonged contraction in motion signal and double peaks in calcium signal. In LQT1B, the most typical abnormality were interrupted relaxation in motion signal and spikes in calcium transient. The action potentials in both LQT1A and LQT1B were prolonged. Image adapted from Study III.

The effect of K^+ channel blockers was studied on WT and LQT1 type cells using patch clamp and calcium imaging. JNJ303, an I_{Ks} blocker, had a prolongation of APD50 and APD90 in WT cells (31% and 28%, respectively). However, it had little effect on LQT1A type cells (7.7% and 8.7%, respectively) and no effect on LQT1B type cells. The effect was reversible with wash-out. E-4031, an I_{Kr} blocker, prolonged APD50 and APD90 in WT cells (30% and 74%, respectively). No EADs were detected. In LQT1A type cells, the APDs were significantly prolonged (70% and 314%). In LQT1B type cells, the prolongation effect was even larger (412% and 771%). While the APDs were recovered by wash-out, the maximum diastolic potential was only partially recovered.

5.2.3 Simultaneous measurement of motion and calcium in CPVT cells (IV)

Using the protocol described in 4.4.3, two CPVT lines were characterized with concurrent motion and calcium measurements. Widths of integrated motion signals, i.e. contraction signals, and calcium transient widths were calculated from all lines. The resulting values are listed in Table 6, and an example of the transients are illustrated previously in Figure 15.

Table 6. Beating rate corrected motion and calcium signal parameters. Mean transient widths at different peak heights ± SD. Data adapted from Study IV.

	Motion			Calcium		
	WT (ms)	**CPVTa (ms)**	**CPVTb (ms)**	**WT (ms)**	**CPVTa (ms)**	**CPVTb (ms)**
10%	157 ± 54	208 ± 109	150 ± 54	228 ± 77	239 ± 90	156 ± 98
25%	236 ± 84	289 ± 116	222 ± 114	355 ± 102	390 ± 149	237 ± 157
50%	328 ± 115	389 ± 145	297 ± 129	549 ± 140	531 ± 176	341 ± 174
80%	473 ± 138	581 ± 109	414 ± 102	899 ± 232	707 ± 202	457 ± 202
90%	606 ± 230	857 ± 302	536 ± 166	1132 ± 302	860 ± 267	527 ± 273

When compared to WT, CPVTa and CPVTb motion and calcium transients appear to be similar in width. Although not directly comparable, the values for WT 90% are similar to the results obtained in studies I and III. The values characterizing WT calcium transient at 90% in Study III, however, were nearly 500 ms lower than the non-BPM corrected ones obtained in Study IV, indicating a large variability in the cells.

The means of contraction related parameters did not show statistically significant differences between cell lines even without BPM correction, although CPVTa came close in 80%-90% parameters ($p<0.1$). In calcium related parameters, CPVTb showed statistically significant differences in 25%-90% parameters with BPM correction with background light on and 50%-90% without background light, while the calcium parameters not corrected for BPM only showed differences in 80%-90% parameters. Statistically significant differences were found between the corresponding contraction parameters and calcium parameters in WT, but not in CPVTa or CPVTb, even when adjusted for BPM.

Linear regression was used to assess the similarity of the different measured signals. The coefficient of determination (R^2) was used as a measure to characterize signal similarity using the BPM correction. The results are listed in Table 7.

Table 7. Coefficients of determination in linear regression of the measured characteristics in all signal pairs.

	PIV / CaPIV				PIV / Ca(bright)				CaPIV / Ca(bright)		
	WT	**CPVTa**	**CPVTb**		**WT**	**CPVTa**	**CPVTb**		**WT**	**CPVTa**	**CPVTb**
10%	0.98	1.00	0.99	**10%**	0.70	0.07	0.40	**10%**	0.73	0.07	0.50
25%	0.94	0.99	1.00	**25%**	0.70	0.50	0.94	**25%**	0.69	0.50	0.94
50%	0.97	0.99	1.00	**50%**	0.58	0.65	0.77	**50%**	0.56	0.59	0.77
80%	0.97	0.81	0.98	**80%**	0.46	0.04	0.55	**80%**	0.47	0.01	0.51
90%	0.54	0.99	0.88	**90%**	0.53	0.09	0.30	**90%**	0.56	0.05	0.21

	Ca(bright) / Ca(dark)				PIV / Ca(dark)				CaPIV / Ca(dark)		
	WT	**CPVTa**	**CPVTb**		**WT**	**CPVTa**	**CPVTb**		**WT**	**CPVTa**	**CPVTb**
10%	0.91	0.89	0.46	**10%**	0.55	0.08	0.97	**10%**	0.55	0.08	0.99
25%	0.93	0.77	0.85	**25%**	0.63	0.54	0.89	**25%**	0.58	0.55	0.85
50%	0.93	0.97	1.00	**50%**	0.46	0.66	0.78	**50%**	0.42	0.60	0.77
80%	0.95	0.95	0.99	**80%**	0.36	0.03	0.60	**80%**	0.37	0.01	0.59
90%	0.92	0.80	0.98	**90%**	0.49	0.00	0.37	**90%**	0.50	0.00	0.25

High coefficients were found in categories representing the same type of measurement, i.e. PIV/CaPIV and Ca(bright)/Ca(dark). There was a limited connection between calcium and motion in WT and CPVTb, and overall a poor connection in CPVTa. As the Ca(dark) measurements were not concurrent with Ca(bright) and motion measurements, the coefficients are typically smaller than for concurrent measurements due to variability between waveforms.

Mean time differences between calcium and contraction maximum rise and fall velocities were calculated to assess the synchronicity of calcium and motion. Beating rate correction was used. The mean time differences and standard error of means for the three cell lines used are listed in Table 8.

Table 8. Mean time differences between maximum onset and offset rates of motion and calcium transients ± standard error of mean for the three cell lines.

	Onset (ms)	Offset (ms)
WT	109 ± 20	24 ± 15
CPVTa	159 ± 29	20 ± 34
CPVTb	70 ± 23	63 ± 17

Positive value indicates calcium transient reaching its maximum velocity in onset and offset before motion. One CPVTa-line cell showed contraction reaching its maximum fall velocity after calcium. This behavior was not seen in other cells.

Although the differences between cell lines are not statistically significant, the values show signs of dissimilar contraction-calcium coupling dynamics. CPVTa has differing values based on results presented in Tables 7 and 8, where the possible disconnection between contraction and calcium modalities manifested itself as differing transient shapes and time differences.

5.3 Video analysis tool

The method was used in a video analysis tool, developed during the course of the studies. It is based on the MATLAB implementation of the method. A graphical UI was developed and using MATLAB deploytool, an implementation of the software enabled biologists and researchers studying cardiomyocytes to use it in their studies.

At first, the analysis method was first ran from MATLAB command line as a combination of scripts. A UI was developed as the need for more analyses increased and the tool was to be used by other researchers, with background mainly in biology. A processing queue of videos made it easier and faster to handle large numbers of samples. After processing the videos, for analyzing vector field results the option of selecting the region of interest either manually or automatically using texture-based filtering was created. Similarly, an option for either manual selection or gradient-based selection was devised for beating focus point.

The UI enabled easy viewing of all 16 signals, as shown in Figure 19 illustrating the UI. The signal could be cropped to exclude portions with shaking or other undesirable portions to facilitate parametrization. The parametrization could be done either automatically by using the template method based on the signal peaks, or manually by selecting points of interest from the signal. The results of the analysis could then be saved to a report. For storing analysis results, an online database with a web-based UI was acquired. The database was set up to categorize the results by saving key metadata of the results: date of recording, time, plate index, cell line, genetic background, drug and concentration, data on cell environment, date of analysis, analysis operator and software version, as well as a packed video with its own metadata including duration.

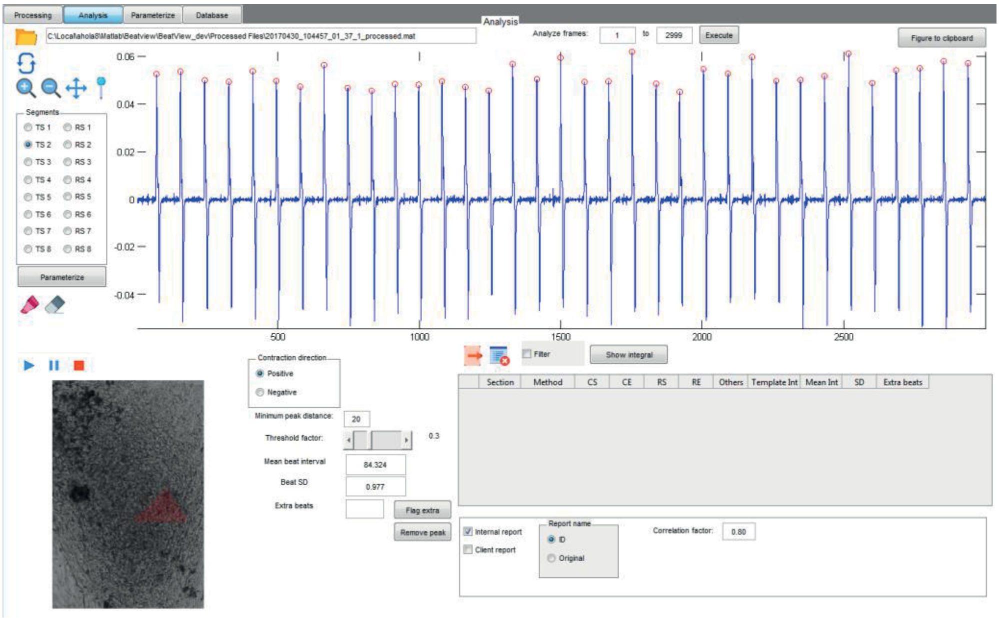

C:\Local\ahola8\Matlab\Beatview\BeatView_dev\Processed Files\20170430_104457_01_37_1_processed.mat

Analyze frames: 1 to 2999

Segments: ● TS 2

Contraction direction: ● Positive ○ Negative

☐ Filter

Minimum peak distance: 20

Threshold factor: 0.3

Mean beat interval: 84.324

Beat SD: 0.977

Extra beats:

☑ Internal report

☐ Client report

Report name: ● ID ○ Original

Correlation factor: 0.80

Figure 19. Video analysis tool UI. The user can view measured signals from different areas of the cell. The software uses peak detection algorithms for initializing parametrization. The user can view the signal simultaneously with the video, crop the signal, adjust various settings, such as modify the peak detection settings, flag extra peaks, and remove recording artefacts such as vibration.

The web-based UI allowed reviewing of results and signals, searching with filters for results and downloading them. It also enabled uploading of original videos after directly recording, making it simple to link the analysis results directly to the original video and allowing multiple analyses of the same original recording.

For the purpose of calculation speed, a C++ version of the calculation of vector fields was developed. It has support for the use of NVIDIA parallel computing model CUDA, which allows the use of graphics processing units in calculation of the vector fields, which is computationally the most intensive task. The process shortened the time required for analysis drastically, as the velocity vector field calculation is computationally the most demanding task.

6 DISCUSSION

The aim of this thesis was to develop a novel method and tool for quantifying CM contraction-relaxation biomechanics using video microscopy. Its accuracy and functionality was validated and an analysis tool using the method was devised. The results obtained and shown in 5.1.1 and 5.1.2 show that the analysis method, based on block matching motion estimation, can quantify the beating of single dissociated CMs. The motion estimation from brightfield and phase contrast videos is non-invasive, non-destructive and label-free. In addition, it is easy to perform and can be automated. The method can be used either standalone or as a complement to other studies. When complementing traditional electrophysiological measurements, it can be used either simultaneously or separately. Video analysis combined with methods such as patch clamp, calcium imaging and MEAs, form a comprehensive view on CM functionality. The resulting tool can be used in quantifying cardiomyocyte biomechanics in research use, determine drug responses in pharmaceutical studies and characterize genetic cardiac diseases.

6.1 Video microscopy based quantification of contraction

6.1.1 Method development

The method uses PIV-based block matching algorithm to estimate the motion in videos recorded using brightfield microscopy. It calculates velocity vector fields from the video frames and determines signals characterizing the beating of the CMs. The tool and method was constantly subject to changes, starting from the comparably primitive first versions to the late stages. In addition to the development and use of the method, the UI and user experience required attention. For publications, a version of the analysis tool had to be fixed and the study performed using this version for processing of results and writing the publications, even if the method had been considerably improved meanwhile. This was seen in Study III, which was performed at the same time as Study I, but published later than Study II. The reason for the publication dates is that Study III required Study I to be published, as the analysis method had not been reviewed and accepted by a journal focusing on technology. Before submitting the first study to a journal, a patent application was filed in December 2012.

The decision of dividing the signals to tangential/radial motion was done specifically to analyze hiPSC-CMs, which typically have an immature sarcomere structure. In contrast to adult cardiomyocytes, the beating is fusiform and there is no specific contraction axis. Thus, the radial and tangential axes can provide specific information on the timing of movement in different directions. The version used in Studies I and III used a sector midline approach for deriving the directional signals, and the tangential/radial motion based on a manually selected beating focus point. The obtained results were consistent with visually observed beating. However, the method as such was not very sophisticated and it was changed in Studies II and IV to calculate the velocity components against a unit vector from its location to the beating focus point. This change has an effect on the results, although subjective observations deemed it minor (data not shown). However, we did not study its magnitude in detail. As the motion direction is determined based on the focus point, the method is sensitive to erroneous focus point detection. If the focus point is off, the transients may have small erroneous peaks as motion related to relaxation may be detected as motion away from focus point instead of motion towards focus point. Determining the beating focus point was a novel approach, one which was later also used in another study by Huebsch and colleagues [16]. The division to radial and tangential signals was important, as the twisting of the cells were not present in all sectors similarly. Chen and colleagues noted the vector directions to provide greater temporal and spatial resolution, especially regarding more complex beating patterns [229]. The incomplete relaxation motion shown in cell line with mutation ivs7-2A>G was not evident in all sectors and directions. This was also highlighted in Study II, where the relaxation movement of the cell began earlier in some parts of the cell than others. Therefore, simple averaging over all sectors or analyzing all areas at the same time may not be optimal. In general terms, high signal-to-noise ratio in motion signals are obtained from cell areas with high density of vectors with high magnitude. Thus, detection and recognition of abnormal motion is challenging, if it occurs in areas with low magnitude of motion.

6.1.2 Estimation of accuracy

The artificial beating video developed in Study I was a step towards defining the accuracy of the method. The radial symmetry of the pinch filter produced a feasible approximation of the beating motion. The motion analysis results from the analyzed video with distortion were similar in shape to the actual distortion, but there were differences in magnitudes. The sector division around the center point produced regions of interest of different sizes and the distortion field extended outside the region of interest. Producing a more extensive test set would also allow comparing different block matching methods. Test images had been used previously by Kamgoué and colleagues to determine the accuracy of their algorithm for measuring CM contraction. They estimated the measured velocity vector field to have a maximum error of 15 % from the known displacement field [12].

The effect of speckle noise to the artificial data set was determined to be a feasible estimate to assess the noise resistance of the method. The type of noise was selected based on its perceived difficulty for PIV. The granular nature of speckle noise indeed does challenge the method - while the method was in some sectors capable of handling even high variance noise, in some sectors the quality decreased greatly. In retrospect, a test with Poisson type noise would have been more informative as it would better mimic conditions present in low-light imaging – simulating a more typical imaging problem. In the study, the magnitude of noise variance was not an easily accessible metric: a seemingly small 0.003 variance already indicated ± 10 % changes in pixel intensity. Comparing the re-calculated results shown in 5.1.2 with the typical noise level of ± 0.4-0.6 % measured during a recording shows the method to perform well even under noisy conditions, and only lose accuracy under excessively high noise levels.

6.1.3 Video analysis prerequisites

In studies I and III, the videos were recorded using 30 fps. As the frequency corresponds to 33 ms per frame and the entire beat may last only 200 ms, every data point is significant in determining signal shape. Thus, it was important to study the conditions that provide a good basis for analysis with the method. Study II examined the possibility of using correlation-based averaged templates in contraction signals. These templates provided a way of producing one-glance signals by using selective averaging based on correlation. The template method was used in Study II to answer the question of required frame rate and the number of beats necessary for creating a reliable template. Both factors influence the quality of the template, and thus the reliability of the measurement. We found that for templates, going lower than 60 fps or 12 beats in a signal started to reduce the quality of the template, as indicated in 5.1.3. In later scrutiny of the results it was found that the resampling of high fps templates and matching with lower fps templates had induced an error in the calculation. This error was due to the template formation process: the number of frames included in the template before the contraction peak was not modified correctly for different frame rates. This resulted in substantially worse correlations for the frame rate comparisons, as the total number of frames included in a template relies on the beating rate. Thus, the results regarding the frame rate in Study II should be approached with caution: lower frame rates perform better than the obtained results would indicate.

While the approach of using correlation to compare the quality of templates was a reasonable approach, it did not give a very solid foundation to make conclusions. However, the study provided us guidelines for further studies. On the other hand, in Study IV the findings related to frame rate were not followed stringently due to practical reasons related to the study aims and equipment at hand. Furthermore, in this study, the minimum correlation was set much lower, effectively turning cross-correlation templates into simple averaging as only the most erroneous peaks were disregarded. Also, due to the prevalent double peaks in data, the maximum rate of change was deemed a more suitable metric for synchronizing the templates than the contraction peak. Nevertheless, despite the low framerate in the studies I and III, we were able to establish statistically significant differences between cell lines.

Huebsch and colleagues found 14 fps to be sufficient for determining CM baseline function by comparing against a recording with 100 fps [16]. The measured parameters did not include separate contraction and relaxation times, as the analysis was more focused on the beating rate. They did note the low fps to underestimate the movement speeds. Sala and colleagues suggest frame rate of 70 fps or more for detailed analysis [232]. The other research groups listed in Table 2 in 2.8.3 have typically either used frame rates below 30 fps and even below 15 fps, or very high frame rates up to 150 fps.

Based on our studies, we could obtain meaningful measurement data with 20 fps in Study IV. Despite the erroneous results obtained in Study II regarding the template quality and frame rate, suggestions regarding the frame rate can be derived from the cell characterization in studies I and III, shown in 5.2.1 and 5.2.2.1. In these studies, the frame rate was 30 fps, and the borderline abnormal beating behavior had average durations in the range of 30 ms. As this is effectively the duration of one frame at 30 fps, the accuracy and reliability of results would benefit greatly from a doubled frame rate of 60 fps, or more. As the error in Study II regarding template creation caused the templates to contain extra baseline frames, the comparisons produced strictly worse results than what correct calculations would provide. This is partly confirmed by the frame rates used by other research groups: frame rates in range of 15-30 have been used regularly as shown in Table 2. Although our studies did not include pharmaceutical studies, it is reasonable to suggest that high time resolution is meaningful when comparing effects of pharmaceutical substances on the same cells. Frame rates of >100 fps have been used in this context, as shown in Table 2.

A key aspect of a successful measurement of motion relies on the obtained image quality. Captured video data, when uncompressed, represents gigabytes of data. If the videos are compressed with lossy frame-by-frame algorithms, the quality of the videos may suffer, and the analysis results become less reliable. In particular, high JPEG compression may induce a checkerboard pattern, referred to as Gibb's phenomenon, which may drastically affect the PIV measurement. For best results, lossless video compression is recommended. [238]

6.1.4 Concurrent measurements with other modalities

The effectiveness of video analysis was determined by using it alongside other measurement methods. Video analysis was used concurrently with patch clamp in Study I, where it served as a validation with gold standard of cellular electrophysiology to show the procession of AP to contraction. The signals were recorded simultaneously to measure the time difference between peaks. To our best knowledge, this was the first combined measurement of patch clamp and video microscopy motion analysis of hiPSC-CMs. The video based method was capable of measuring the contractile activity even though the pipette was blocking a large part of the cell area. Inserting the pipette visually dampened the beating slightly, but the exact effect was not measured. A time difference of 306 ± 40 ms SD between the peaks of PC and motion signal was detected, as indicated in section 5.1.4. The developed method fared well, as the results show similar delay as previously reported for rabbit ventricular myocytes. Later in a similar study using video microscopy analysis and patch clamp by Sala and colleagues, a time difference in the same range was obtained [232].

In Study III, the calcium measurements and contraction measurements were done separately. A concurrent measurement of calcium and contraction on the LQT phenotype would have provided a more detailed view on the disease. For this purpose, it was important to determine a way to measure them simultaneously. Study IV implemented a concurrent motion measurement with calcium imaging. Similar studies had previously been done by Hayakawa and colleagues, and Huebsch and colleagues. The former group separated phase contrast and fluorescence images by evaluating the oscillation minima of the fluorescence intensity. The latter group normalized pixel intensity within subwindows to induce tracking of textures rather than intensities. [14,16]. We showed that using MQD, the measurement can be done directly without such corrections with high accuracy, with only a minor difference in baseline, as demonstrated in Study IV and section 5.1.5. Part of the observed error, especially related to the signal peak height between the motion signals from brightfield and combined brightfield-calcium imaging, can be explained by the time difference between the frames with and without fluorescence. The lowest frame rate for the individual channels was 23 fps, indicating a nearly 22 ms difference between brightfield and combined brightfield-calcium imaging. If the cells used in the study had had faster contraction mechanics, the frame rate effect would have been even greater. With a higher frame rate, a more detailed view on the differences between imaging systems would be obtained.

The photobleaching of fluorophores in a simultaneous measurement can affect the measurement. As we were performing a simultaneous measurement, this was not a core research question in this study. The phototoxicity effects should be considered when using the method for measuring contraction-calcium dynamics, and a more detailed study with different background light levels would be essential.

6.1.5 Signal parameterization

At the onset of the first studies, little was known on the hiPSC-CM beating characteristics. Furthermore, the parameters to measure from the signals were not established. The observed differences in beating between dissociated WT and LQT specific CMs formed the basis of signal interpretation: WT cells were observed to relax shortly after contraction, and prolonged contraction present in LQT specific CMs was determined to be abnormal. Thus, our first parametrization only differentiated between contraction and relaxation, and more parameters were required. We added parameters regarding contraction-relaxation delay and incomplete relaxation to account for the LQT abnormality. Later, we characterized the motion using contraction signal, the integral of motion with respect to time. It enabled easier comparison between different modalities, such as calcium imaging and patch clamp.

As there was considerable variation of beating rate between the measurements in studies I-IV, the contraction and relaxation times were not easy to compare. To facilitate the evaluation of the results, Fridericia QT correction was applied to all results here. While generally used for clinical QT correction, it provided more uniform results that allowed greater comparability, as shown in 5.2.1 where we reanalyze the results of Study I using the correction. A beat rate correction is necessary, as the APD and Ca^{2+} transient durations in CMs are rate-dependent and thus the contraction duration, which depends on these functions, is rate dependent as well. This effect can be seen when comparing the results of Study I and III to Table 4 and Table 5, respectively. The corrected results demonstrated better the control/disease phenotype when comparing the time parameters, especially when considering the sum of phases I-IV. While the beat rate corrections, developed for ECG interpretation, do appear to function with single cells, it is likely they are not optimally suited for single cell motion studies. The correction to beat duration has been previously used in video microscopy contraction analysis by us [171], and by Maddah and colleagues [230].

6.2 Cellular studies

6.2.1 LQT phenotype

Study III presented the characteristics of LQT-specific CMs with two mutations. The mutations expressed different mechanical and electrophysiological phenotypes, as shown in 5.2.2.1. The LQT1A (G589D mutation) mechanical phenotype showed a prolonged duration between the contraction and relaxation movements in contrast to the wild type cells as expected in LQT genotype. In LQT1B (ivs7-2A>G mutation) phenotype, the prolongation was present in some cells, but the more pronounced difference was seen in the incomplete relaxation sequence, where it manifested as a twitching motion in relaxation. These differences in beating behavior when compared to WT cells were previously reported only on whole heart level, where the prolonged APD resulted in prolonged regional ventricular contraction [239]. However, the twitching motion related to LQT1B type cells had not previously been reported.

These effects were seen typically in dissociated single cells or clusters of 2-3 cells, and their beating patterns were atypical: the contractile motion was not always directed towards a single point. The motion was twisting and fusiform. Combined with the 20x magnification, small resolution and a 16x16 window size, measuring these cells was not a simple task. In addition, the way cells are adhered to the plates can affect the results, as a loose cell edge may increase the motion in some areas. Yet, signals that matched the visually observed phenomenon were able to be determined and the results were evident even when averaged over three different sectors, reducing the bias of manual selection.

In LQT1A cells, the duration of interval between contraction and relaxation was measured from the end of contraction movement and start of relaxation movement. The velocities in contraction ending and relaxation beginning are small, making the question of determining these points relevant for accurate characterization. It can be argued what constitutes as a prolongation between the two time points, when it can be difficult to determine the point of zero movement from a noisy signal and thus the duration of the actual interval. However, the parameters were measured manually using the same criteria by the same observer. A repeated study on the same cell lines with a camera with higher frame rate could present a better view on the subject. The twitching motion in LQT1B cells was considered as incomplete relaxation. In effect, the cell relaxed in two phases in the video recordings. For LQT1B there was less room for interpretation than for LQT1A, as the mean pause between the relaxation movements was as long as 12 frames. However, defining the exact frames in a noisy recording was subjective, and thus created a source of error.

The Ca^{2+} transients measured from LQT type cells had abnormalities consisting of double or more peaks, as well as spikes with small amplitude, as shown in Figure 18 in 5.2.2.2. These effects were seen in WT cells as well, although they were more prevalent in LQT type cells. In LQT-type cells, these effects were more pronounced in LQT1A cells, which exhibited both features. In LQT1B, small upward spikes during calcium transient were the more prevalent than the double peaks. These spikes are a less pronounced feature than the double peaks. In both LQT-type mutations, the cell lines showed significantly prolonged APs in patch clamp study. EADs were present in 5/30 of the LQT1A-type cells, but not in the LQT1B-type.

Although the APD prolongation was more severe in LQT1A type cells than in LQT1B type cells, inducing the prolonged state of contraction, the latter were more susceptible for ion channel blockers, as shown in 5.2.2.2. These factors may be associated with the interrupted relaxation sequence. Mechanically, the LQT1B type cells seemed to exhibit more problems in the beating behavior due to the presence of both prolongation of contraction-relaxation interval and the incomplete relaxation. The patients from which the cell lines were derived exhibited similar clinical long QT symptoms, although the LQT1B patient did have a longer QTc time. It could thus be possible for the heart to have mechanisms that compensate for the phenotypes of the cell models. In addition, the abnormal beating behavior was not present in all of the cells, which could indicate that the healthier cells compensate for the abnormal ones when beating in syncytium. It could also mean that the prolongation has more symptomatic effects. When considering the recalculated contraction profiles in section 5.2.2.1, the calcium transients are more in line with the contraction waveforms. They show the LQT1A-specific cells to have more drastic abnormality in waveform than LQT1B, when compared to WT cells, which supports findings in patch clamp and calcium imaging that showed longer APD and double peaks, respectively. However, the total mechanical activity times calculated from the onset of contraction to the end of incomplete relaxation were longer in LQT1B than in LQT1A. It is uncertain if the activity is related to EADs manifesting themselves as aftercontractions, as EADs were not detected with patch clamp in LQT1B. However, patch clamp is by design an invasive measurement and thus it may affect the behavior of cells by disrupting activity that can be detected using other methods. The mechanical phenotype of LQT1 has later been analyzed also by Sala and colleagues [232] using the method presented by Hayakawa and colleagues [14,227]. In their study, the disease phenotype was visible as prolonged duration of contraction, similarly as our findings indicated in LQT1A-type cells [232]. They did not report LQT1B-type behavior. Aftercontractions similar to the ones we detected, however, have been reported by Nguyen and colleagues in studies involving dofetilide, a hERG channel blocker, where the compound caused aftercontractions and prolongation of total mechanical activity [240].

6.2.2 Contraction-calcium dynamics

In Study IV, we found the contraction to follow the calcium transient after a short delay, as expected. Contraction and calcium appear to have a close association, as was shown in 5.1.6 and 5.2.3. The motion and calcium signals showed independent behavior, which indicates that they provide complementary information. Although they share characteristics due to calcium inducing the contraction, a study that uses both modalities can give a more thorough view on cellular function. The measured onset- and offset-times indicate that there is considerable variation between the cells. Although the calcium and contraction measurements were done from the same region of the cell, the measured motion is a product of the local calcium driven motion and the deformation of the cell driven by other regions of the cell, which are both affected by the way the cells are adhered to the well plate. Thus, these aspects do not affect the calcium signal and the contraction signal in the same way.

The study implies that previously recorded calcium imaging data can be analyzed afterwards for determining the contraction movement. This enables revisiting previous studies to gain information on the calcium-contraction coupling, and how abnormal calcium transients translate to contractility.

6.2.3 CPVT phenotype

The CPVT phenotype was analyzed in Study IV as a demonstration of the simultaneous calcium-contraction measurement. Two different mutations were considered: exon 3 deletion (CPVTa) and V4653F mutation (CPVTb) in RYR2 gene. Unfortunately, the number of videos recorded was small and the video durations were short, as this study was not the main aim of the cell measurements performed by our collaborators. Despite the low sample size, the results did indicate towards CPVT not displaying an abnormal biomechanical phenotype at baseline conditions. This result is in agreement with previous studies, where the abnormal electrophysiological phenotype is revealed only when the beating rate is increased. A difference was discovered in linear regression of near-baseline calcium/contraction parameters for the cell line carrying the exon 3 deletion mutation. This difference would indicate a greater disconnection between calcium and contraction mechanics. This is in line with the exon 3 deletion mutation having a more severe clinical outcome than the V4653F mutation [163]. However, due to the limitations of the number of the cells and recorded videos, and the absence adrenergic stimulation, we cannot obtain a solid foundation for this conclusion and a more detailed Study is required.

6.2.4 The effect of cell culture and dissociated to single cells

In our studies, dissociated CMs were used. The abnormal beating behavior was present in LQT specific CMs, and there is reason to expect dissociated CMs to exhibit more LQTS type behavior: DAD/EADs might not cause arrhythmias as the neighboring cells may act as current sinks [36].

While the prolonged contraction was deemed abnormal in dissociated CMs, the contraction time for monolayers and large clusters appears to be longer for control cells [241] when compared to our results with dissociated single cells. Therefore, the parameters for abnormality depend on the cell culture. Further, the delay indicating the time when the cell stays contracted, could be characteristic to more mature cells, as it could be a feature of stronger sarcomere cooperation. Thus, sensitivity in studies with dissociated CMs may be higher than with larger clusters or monolayers, as the more complex structures form a very different electrical and mechanical environment, which likely equalizes intercellular differences. Due to these reasons, foresight is advised when comparing analysis results of CM biomechanics from different cultures.

Even though single cells are more sensitive to displaying abnormal behavior, it is unclear whether dissociated cells are the optimal choice for drug testing or if larger populations should be used, due to myocardium acting as a syncytium. Further considerations include cardiac 3D structures, which have shown to exhibit functional differences in cultures [242]. Based on our observations, dissociated cells appear to offer greater sensitivity for characterizing LQTS as healthy nearby cells can overcome the abnormality in other cells. Greater sensitivity of dissociated cells has been reported by other groups as well [243]. Nevertheless, monolayers and large clusters can be analyzed as well using the method. They may have multiple beating areas and by extension, multiple focus points and can thus provide multiple signals. Further, the beating areas may be asynchronous and the interplay of contractile activity at their boundaries is a candidate for future research.

6.3 Feasibility of video analysis in different studies

6.3.1 General cardiomyocyte studies

The video analysis tool provides an easily accessible tool for CM studies. These studies typically involve using a microscope, as the beating of CMs is an integral part of their function. Thus, recording a video of this beating motion is a low effort procedure, as the cells are already being observed visually. As discovered in Study I, the camera requirements for recording a video are low: a camera attached to the microscope ocular suffices and smartphone video recording capability has been suggested to be sufficient [232]. When the analysis of recorded video data is easily available, the motion analysis provides relevant data on cellular biomechanics and functionality can be linked with any CM study. Video analysis can also be used to monitor the cells in long-term cultures, when cameras are incorporated in culturing environment.

6.3.2 Genetic cardiac disease studies

We demonstrated the characterization of CM beating abnormalities caused by LQTS in Study III and found different mechanical beating phenotypes. By analyzing CMs derived from individuals with genetic cardiac disease, in addition to motion abnormalities, the ratio of abnormally beating cells to control-like cells could provide a metric for assessing the status of the patient. Single dissociated CMs appear to provide greater sensitivity in detecting abnormal cell behavior. For this purpose, video analysis is a suitable method due to its non-invasive nature and good enough resolution to analyze such cells. Electrophysiological measurements would be required for more accurate results on normally beating cells, but abnormally beating cells alone would indicate susceptibility for arrhythmias.

6.3.3 Pharmaceutical studies

Video analysis method can be a feasible platform for drug screening in CM cultures. In contrast to more invasive analysis methods, the effect of the drug can be interpreted without interference from measurement agents. In addition, the method can be automated and it is scalable, paving way for high throughput screening. The method is well suited for early-phase safety assays, where the substances that cause abnormal beating can be omitted from more labor extensive electrophysiological studies. Due to their method of operation, cancer drugs in particular would benefit from the screening of abnormal mechanical function.

While not included in this thesis, we have used the method in these studies to analyze the effect of E-4031 on the contraction duration parameters, as well as the contraction intensity and showed that motion analysis could detect dose-dependent decrease of magnitude from 30 nM level onwards [171]. One of the key advantages of video analysis is that due to the possibility of repeated measurements in long term cultures, toxicity related to long term drug exposure can be detected [244].

Human iPSC derived CMs have the potential to decrease the number of animal experiments required in drug discovery. Further, there are a number of differences between human CM physiology and animal models. [245] New methods, such as the one presented in this thesis, make these hiPSC-CM models more feasible to use and in turn make drug discovery more ethical. The results of Study IV could also be applied animal studies, decreasing the number of animals required, as contraction could be measured directly from calcium data. This translates into reduced costs and more ethical research.

6.3.4 Previous video analysis use

In addition to the publications included in this thesis, the tool has been used in a number of studies and master's theses, with the name BeatView and CellVisus. Optogenetic dyes have been assessed simultaneously with contraction measurement by Björk, Ojala and colleagues [171]. CM functionality was measured in development of a fluorimetric oxygen sensor by Välimäki and colleagues [246]. The imaging and measurement capability of a portable live-cell imaging system was demonstrated with a CM measurement by Rajan and colleagues [247]. The impact of indirect temperature control for the portable imaging system on CM functionality was assessed by Mäki and colleagues [248].

6.4 Video analysis tool

The software tool developed during the presented studies was built in several stages, depending on the needs of the studies performed and the needs of the users. The resulting tool presented in 5.3 has been evaluation in various development stages and in use by cell biologists in Tampere University Heart Group since 2013 in its different forms. It allows the users to measure the cellular function prior to studies that are more laborious. Recently, it has also been used as a standalone method, as mentioned in 6.3.4.

The use of the developed online database in gathering results ultimately leads to vast amounts of data characterizing the cardiomyocyte biomechanics. The possibility of filtering the experiments, data and results based on selected criteria enables pooling of results from different studies. As the database also saves the original videos and software version numbers, the database can be used to recalculate the data using newer software versions. The web-based interface enables directly uploading video recordings from measurement computers, subsequent easy downloading on analysis computers and the linking of the recordings with results.

The current stage of automation in the software removes user-induced bias in parametrization of the signals. However, as unsupported arrhythmias and beating characteristics emerge, user intervention is required. With the use of the result database, the software can be modified to better parameterize the signals as defined by the researchers with most experience on the specific arrhythmias.

Barring unsupported arrhythmias requiring user interaction, the overall analysis process duration depends largely on the computer processing power. Changing the analysis process from MATLAB-based mpiv to the in-house developed C++ version using CUDA cut the processing times drastically. Due to this development in computing power, even real-time analysis can be achieved with typical imaging resolutions on desktop computers with dedicated graphics cards that support CUDA.

The software is currently closed source. Its licensing terms are currently in internal discussion.

6.5 Study limitations and biasing factors

In contrast to other methods, video analysis requires actual movement from cells. Thus, the beating motion may be a biasing factor as only cells with visible beating were selected for the analysis. The calcium cycling required for calcium imaging may still be present even if the beating motion is weak, or nonexistent. The cells have to be sufficiently strong to beat in the first place, ignoring the weaker cells. As the CM induction process generates mixtures of subtypes: atrial, ventricular and nodal, there may be a bias towards a specific type of cells in the video recording selection process. Unfortunately, the most accurate methods for determining chamber specificity from CMs are with microelectrodes, and patch clamp the only measurement capable of determining the ionic activity. Thus far, the possibility of determining chamber specificity of CMs using contractility has not been studied. Further, the question of cell density is relevant also in this regard: there has been debate and doubt cast on its effect on determining the chamber specificity of cells based on their action potential morphology in single cells [137–139]. This complicates the use of MEAs in conjunction with video analysis, as MEAs are not well suited towards measuring single cells.

In studies I and III, the parametrization was done manually by the same observer, using the same criteria. However, the analyst had *a priori* information on the cell genotype, thus allowing room for possible bias. The effect of this bias is not believed to be large, as visual observations by another analyst in these studies on the percentages of abnormally beating cells were in agreement with the parametrizations of the beating signals. The method produces a number of signals from different areas of the cell. Selecting the areas and signals for further analysis and parametrization is not obvious due to cell attachment and the fusiform nature of beating of the stem cell derived CMs. In studies I and III, three signals from three sectors were selected and the parameters calculated from those were averaged. In studies II and IV, no abnormal beating behavior was detected, which is why this averaging was not done. Typically, the subjectively highest quality signals were the ones with largest motion, as they showed the highest signal-to-noise ratio.

While the method itself is non-invasive, the cells are stressed by the measurement due to light needed for the video recording. However, in regular video recording, no high intensity light is applied and thus the effect is minimal. However, there has not been extensive research on the effects of long-term low intensity light or pulsed lighting. We did recognize the effect of laboratory lighting from fluorescent tubes in the video analysis, as the overall lighting of the room with a window changed during the day (data not shown). The effect was not substantial or systematic enough for a full report, but it is a factor that should be taken into account when comparing results from different laboratories in detail.

All the studies suffered from small sample sizes. This diminished the importance of Study IV in particular, where the analysis of CPVT cell line was severely limited and was used only for demonstration. While only few cells were analyzed in Study II, the focus of that study was in the technique itself. The sample size also affected the nature of studies that could be performed, as they limited the possibilities to analyze further the parameters: for instance, we were not able to look into the intensity of contraction. With small sample size, the effect of cell adhesion plays a large role in contraction intensity and population-wide differences could be masked by differences between individual cells. With larger cell populations, we could also have taken the cell adhesion points into account, as suggested in master of science thesis by Muhonen in 2016 [249].

6.6 Future aspects and studies

The work opens new venues of CM research. As the process of video recording and the entire video analysis procedure can be automated, the functionality of the cells could be measured periodically in incubators during their lifetime, and report the gathered statistics directly to researchers. The technology could also be implemented in microscopy stations, which could monitor the functionality of the cells in real time while any CM microscopy study is conducted, and inform the operator if the cells exhibit abnormal behavior. As the method can be used in conjunction with other measurement modalities, such as Ca^{2+} and voltage indicators, the scientific community can gain a more complete view on the CM functionality on a single cell level, as already demonstrated by us [171].

The biomechanics of other genetic cardiac diseases remain unexplored, as well as the effect of pharmaceutical agents on their biomechanical phenotype. A future study of motion-calcium coupling in CPVT cells should include adrenergic stimulation to induce arrhythmias. As the arrhythmias in LQT specific cell lines were detected using the method, it is a reasonable assumption that arrhythmias related to CPVT can be detected as well. In addition, a study of motion-calcium coupling in LQT cells could help understand the differing phenotypes.

7 SUMMARY AND CONCLUSIONS

The aim of the thesis was to develop a video image-based analysis method for analyzing cardiomyocyte biomechanics, and to use it to characterize genetic cardiac disease. The following conclusions can be made based on the results of the studies.

1. Cardiomyocyte video analysis in general, and the developed tool in particular, enables an accessible way to assess the biomechanics of cardiomyocytes. Video analysis provides an easy and fast way for cell biologists and scientists to determine biomechanical functional characteristics of the cells as a standalone method, or as a way to augment other types of measurements.
2. Video image analysis has a number of advantages beneficial to high throughput applications, important for pharmaceutical research. The process described here requires little user interaction, allowing future full automation. The method uses no labels, is non-toxic and minimally invasive, allowing repeated measurements of the same cells at different time points.
3. The biomechanical phenotype of long QT syndrome cell in human induced pluripotent stem cell derived cardiomyocytes was studied using the method. For the first time, abnormal mechanical beating was discovered and measured on a single cell level. Two different long QT genotypes exhibit differing characteristics in beating as well as calcium cycling and electrical properties.
4. While the beating signals recorded with low frame rates can be parametrized, low frame rate and low number of beats will result in error in averaging of signals and the loss of detail. Especially for studies where small changes and the function of the same cell is followed, a high frame rate would allow better discrimination.
5. Concurrent calcium-contraction measurement without additional image corrections allows the simultaneous ionic and motion analysis, and also the analysis of contraction from previously recorded calcium imaging data, given enough fluorescence to ensure visibility of the cell.

6. CPVT cells exhibit normal beating phenotype in baseline conditions. Further research is needed to confirm or reject the preliminary findings in this thesis related to disconnection of contraction and calcium transients near baseline.

These conclusions signify that video microscopy-based measurements of cardiomyocytes have feasible future applications in cardiomyocyte studies and in pharmaceutical research, as they provide a minimally invasive and high-throughput capable complement to electrophysiological methods.

REFERENCES

1. Roth, G. A. *et al.* Global, Regional, and National Burden of Cardiovascular Diseases for 10 Causes, 1990 to 2015. *J. Am. Coll. Cardiol.* **70:** 1–25 (2017).
2. Ohnuki, M., Takahashi, K. & Yamanaka, S. Generation and characterization of human induced pluripotent stem cells. *Curr. Protoc. Stem Cell Biol.* **Chapter 4:** Unit 4A.2 (2009).
3. Zhang, J. *et al.* Functional cardiomyocytes derived from human induced pluripotent stem cells. *Circ. Res.* **104:** (2009).
4. DiMasi, J. A., Grabowski, H. G. & Hansen, R. W. Innovation in the pharmaceutical industry: New estimates of R&D costs. *J. Health Econ.* **47:** 20–33 (2016).
5. McNaughton, R., Huet, G. & Shakir, S. An investigation into drug products withdrawn from the EU market between 2002 and 2011 for safety reasons and the evidence used to support the decision-making. *BMJ Open* **4:** (2014).
6. Onakpoya, I. J., Heneghan, C. J. & Aronson, J. K. Post-marketing withdrawal of 462 medicinal products because of adverse drug reactions: a systematic review of the world literature. *BMC Med.* **14:** 10 (2016).
7. Suter, T. M. & Ewer, M. S. Cancer drugs and the heart: importance and management. *Eur. Heart J.* **34:** 1102–1111 (2013).
8. van der Worp, H. B. *et al.* Can Animal Models of Disease Reliably Inform Human Studies? *PLOS Med.* **7:** e1000245 (2010).
9. Hoekstra, M., Mummery, C. L., Wilde, A. A. M., Bezzina, C. R. & Verkerk, A. O. Induced pluripotent stem cell derived cardiomyocytes as models for cardiac arrhythmias. *Front. Physiol.* **3:** 346 (2012).
10. Chang, W.-T., Yu, D., Lai, Y.-C., Lin, K.-Y. & Liau, I. Characterization of the mechanodynamic response of cardiomyocytes with atomic force microscopy. *Anal. Chem.* **85:** 1395–1400 (2013).
11. Rodriguez, M. L. *et al.* Measuring the Contractile Forces of Human Induced Pluripotent Stem Cell-Derived Cardiomyocytes With Arrays of Microposts. *J. Biomech. Eng.* **136:** 510051–5100510 (2014).
12. Kamgoué, A., Ohayon, J., Usson, Y., Riou, L. & Tracqui, P. Quantification of cardiomyocyte contraction based on image correlation analysis. *Cytom. Part A* **75:** 298–308 (2009).
13. Lundy, S. D., Zhu, W. Z., Regnier, M. & Laflamme, M. A. Structural and functional maturation of cardiomyocytes derived from human pluripotent stem cells. *Stem Cells Dev* **22:** 1991–2002 (2013).
14. Hayakawa, T. *et al.* Noninvasive Evaluation of Contractile Behavior of Cardiomyocyte Monolayers Based on Motion Vector Analysis. *Tissue Eng. Part C Methods* **18:** 21–32 (2012).
15. Maddah, M. & Loewke, K. Automated, Non-Invasive Characterization of Stem Cell-Derived Cardiomyocytes from Phase-Contrast Microscopy. In *Medical Image Computing and Computer-Assisted Intervention -- MICCAI 2014. Lecture Notes in Computer Science* (eds. Golland, P., Hata, N., Barillot, C., Hornegger, J. & Howe, R.) **8673:** 57–64 (Springer International Publishing, 2014).

16. Huebsch, N. *et al.* Automated Video-Based Analysis of Contractility and Calcium Flux in Human-Induced Pluripotent Stem Cell-Derived Cardiomyocytes Cultured over Different Spatial Scales. *Tissue Eng. Part C. Methods* **21:** 467–479 (2015).
17. Lee, E. K., Kurokawa, Y. K., Tu, R., George, S. C. & Khine, M. Machine learning plus optical flow: A simple and sensitive method to detect cardioactive drugs. *Sci. Rep.* **5:** 11817 (2015).
18. Liu, X. & Padfield, D. Motion-Based Segmentation for Cardiomyocyte Characterization. In *Spatio-temporal Image Analysis for Longitudinal and Time-Series Image Data. STIA 2012. Lecture Notes in Computer Science* (eds. Durrleman, S., Fletcher, T., Gerig, G. & Niethammer, M.) **7570:** 137–146 (Springer Berlin Heidelberg, 2012).
19. Malmivuo, J. & Plonsey, R. Bioelectromagnetism - Principles and Applications of Bioelectric and Biomagnetic Fields. (1995).
20. Camelliti, P., Borg, T. K. & Kohl, P. Structural and functional characterisation of cardiac fibroblasts. *Cardiovasc. Res.* **65:** 40–51 (2005).
21. Pinto, A. R. *et al.* Revisiting Cardiac Cellular Composition. *Circ. Res.* **118:** 400–409 (2016).
22. Heikkilä, J. *et al. Kardiologia*. (Kustannus Oy Duodecim, 2008).
23. Lisewski, U. *et al.* The tight junction protein CAR regulates cardiac conduction and cell–cell communication. *J. Exp. Med.* **205:** 2369–2379 (2008).
24. Marieb, H. & Hoehn, K. *Human anatomy and physiology*. (Pearson Benjamin Cummings, 2007).
25. Sarantitis, I., Papanastasopoulos, P., Manousi, M., Baikoussis, G. & Apostolakis, E. The Cytoskeleton of the Cardiac Muscle Cell Basic morphology of the cardiac muscle cell. *Hell. J. Cardiol. HJC @BULLET Hell. J Cardiol* **367:** 367–379 (2012).
26. Epstein, N. D. & Davis, J. S. Sensing Stretch Is Fundamental. *Cell* **112:** 147–150 (2003).
27. Becker, D. E. Fundamentals of Electrocardiography Interpretation. *Anesth. Prog.* **53:** 53–64 (2006).
28. Childers, R. Atrial repolarization : its impact on electrocardiography. *J. Electrocardiol.* **44:** 635–640 (2011).
29. Funck-Brentano, C. & Jaillon, P. Rate-corrected QT interval: techniques and limitations. *Am. J. Cardiol.* **72:** 17B–22B (1993).
30. Grant, A. O. Cardiac ion channels. *Circ. Arrhythmia Electrophysiol.* **2:** 185–194 (2009).
31. Nerbonne, J. M. & Kass, R. S. Molecular physiology of cardiac repolarization. *Physiol Rev.* **85:** 1205–1253 (2005).
32. DiFrancesco, D. Pacemaker Mechanisms in Cardiac Tissue. *Annu. Rev. Physiol.* **55:** 455–472 (1993).
33. Pinnell, J., Turner, S. & Howell, S. Cardiac muscle physiology. *Contin. Educ. Anaesth. Crit. Care Pain* **7:** 85–88 (2007).
34. Vinogradova, T. M. *et al.* Rhythmic ryanodine receptor Ca2+ releases during diastolic depolarization of sinoatrial pacemaker cells do not require membrane depolarization. *Circ. Res.* **94:** 802–809 (2004).
35. Maltsev, V. A. & Lakatta, E. G. Normal heart rhythm is initiated and regulated by an intracellular Calcium clock within pacemaker cells. *Heart. Lung Circ.* **16:** 335–348 (2007).
36. Bers, D. M. Calcium cycling and signaling in cardiac myocytes. *Annu. Rev. Physiol.* **70:** 23–49 (2008).
37. Lakatta, E. G. Intracellular Ca2+ cycling is a general regulator of how fast and how strong the heart beats. *Dialogues Cardiovasc. Med.* **15:** 253–278 (2010).
38. Brette, F. & Orchard, C. T-Tubule Function in Mammalian Cardiac Myocytes. *Circ. Res.* **92:** 1182–1192 (2003).
39. Barnett, V. A. Cardiac Myocytes. In *Handbook of Cardiac Anatomy, Physiology, and Devices* (ed. Iaizzo, P. A.) 113–121 (Humana Press, 2005).

40. Eisner, D. A., Caldwell, J. L., Kistamás, K. & Trafford, A. W. Calcium and Excitation-Contraction Coupling in the Heart. *Circ. Res.* **121:** 181–195 (2017).
41. Bers, D. M. Cardiac excitation–contraction coupling. *Nature* **415:** 198–205 (2002).
42. Gaztañaga, L., Marchlinski, F. E. & Betensky, B. P. Mechanisms of Cardiac Arrhythmias. *Rev. Española Cardiol. (English Ed.* **65:** 174–185 (2012).
43. Antzelevitch, C. & Burashnikov, A. Overview of Basic Mechanisms of Cardiac Arrhythmia. *Card. Electrophysiol. Clin.* **3:** 23–45 (2011).
44. Khan, R. Identifying and understanding the role of pulmonary vein activity in atrial fibrillation. *Cardiovasc. Res.* **64:** 387–394 (2004).
45. Maruyama, M. *et al.* Genesis of Phase-3 Early Afterdepolarizations and Triggered Activity in Acquired Long QT Syndrome. *Circ. Arrhythm. Electrophysiol.* **4:** 103–111 (2011).
46. Weiss, J. N., Garfinkel, A., Karagueuzian, H. S., Chen, P.-S. & Qu, Z. Early Afterdepolarizations and Cardiac Arrhythmias. *Heart Rhythm* **7:** 1891–1899 (2010).
47. Pogwizd, S. M., Schlotthauer, K., Li, L., Yuan, W. & Bers, D. M. Arrhythmogenesis and Contractile Dysfunction in Heart Failure: Roles of Sodium-Calcium Exchange, Inward Rectifier Potassium Current, and Residual β-Adrenergic Responsiveness. *Circ. Res.* **88:** 1159–1167 (2001).
48. Venetucci, L. A., Trafford, A. W. & Eisner, D. A. Increasing Ryanodine Receptor Open Probability Alone Does Not Produce Arrhythmogenic Calcium Waves: Threshold Sarcoplasmic Reticulum Calcium Content Is Required . *Circ. Res.* **100:** 105–111 (2007).
49. Fink, M., Noble, P. J. & Noble, D. Ca(2+)-induced delayed afterdepolarizations are triggered by dyadic subspace Ca(2+) affirming that increasing SERCA reduces aftercontractions. *Am. J. Physiol. - Hear. Circ. Physiol.* **301:** H921–H935 (2011).
50. Tse, G. Mechanisms of cardiac arrhythmias. *J. Arrhythmia* **32:** 75–81 (2016).
51. Priori, S. G. & Chen, S. R. W. Inherited dysfunction of Sarcoplasmic Reticulum Ca(2+) Handling and Arrhythmogenesis. *Circ. Res.* **108:** 871–883 (2011).
52. Hedley, P. L. *et al.* The genetic basis of long QT and short QT syndromes: A mutation update. *Hum. Mutat.* **30:** 1486–1511
53. Khan, I. A. Long QT syndrome: Diagnosis and management. *Am. Heart J.* **143:** 7–14 (2002).
54. Giudicessi, J. R. & Ackerman, M. J. Genotype- and Phenotype-Guided Management of Congenital Long QT Syndrome. *Curr. Probl. Cardiol.* **38:** 417–455 (2013).
55. Tester, D. J. & Ackerman, M. J. Genetics of Long Qt Syndrome. *Methodist Debakey Cardiovasc. J.* **10:** 29–33 (2014).
56. Schwartz, P. J., Crotti, L. & Insolia, R. Long-QT syndrome from genetics to management. *Circ. Arrhythmia Electrophysiol.* **5:** 868–877 (2012).
57. Kaye, A. D., Volpi-Abadie, J., Bensler, J. M., Kaye, A. M. & Diaz, J. H. QT interval abnormalities: risk factors and perioperative management in long QT syndromes and Torsades de Pointes. *J. Anesth.* **27:** 575–587 (2013).
58. Zhang, T. *et al.* LQTS Gene LOVD Database. *Hum. Mutat.* **31:** E1801–E1810 (2010).
59. Coumel, P., Fidelle, J. & Lucet, V. Catecholamine-induced severe ventricular arrhythmias with Adams-Stokes syndrome in children: report of four cases. *Br. Heart J.* 28–37 (1978).
60. Swan, H. *et al.* Arrhythmic disorder mapped to chromosome 1q42-q43 causes malignant polymorphic ventricular tachycardia in structurally normal hearts. *J. Am. Coll. Cardiol.* **34:** 2035–2042 (1999).
61. Postma, A. V *et al.* Catecholaminergic polymorphic ventricular tachycardia: RYR2 mutations, bradycardia, and follow up of the patients. *J. Med. Genet.* **42:** 863–870 (2005).
62. Priori, S. G. *et al.* Mutations in the Cardiac Ryanodine Receptor Gene (hRyR2) Underlie Catecholaminergic Polymorphic Ventricular Tachycardia. *Circulation* **103:** 196–200 (2001).

63. Laitinen, P. J. *et al.* Mutations of the cardiac ryanodine receptor (RyR2) gene in familial polymorphic ventricular tachycardia. *Circulation* **103:** 485–490 (2001).

64. Lahat, H. *et al.* A missense mutation in a highly conserved region of CASQ2 is associated with autosomal recessive catecholamine-induced polymorphic ventricular tachycardia in Bedouin families from Israel. *Am. J. Hum. Genet.* **69:** 1378–1384 (2001).

65. Roux-Buisson, N. *et al.* Absence of triadin, a protein of the calcium release complex, is responsible for cardiac arrhythmia with sudden death in human. *Hum. Mol. Genet.* **21:** 2759–2767 (2012).

66. Nyegaard, M. *et al.* Mutations in Calmodulin Cause Ventricular Tachycardia and Sudden Cardiac Death. *Am. J. Hum. Genet.* **91:** 703–712 (2012).

67. Wobus, A. M. & Boheler, K. R. Embryonic Stem Cells : Prospects for Developmental Biology and Cell Therapy. 635–678 (2005).

68. Alison, M. & Islam, S. Attributes of adult stem cells. *J. Pathol.* **217:** 144–160 (2009).

69. Takahashi, K. & Yamanaka, S. Induction of Pluripotent Stem Cells from Mouse Embryonic and Adult Fibroblast Cultures by Defined Factors. **2:** 663–676 (2006).

70. Thomson, J. A. *et al.* Embryonic Stem Cell Lines Derived from Human Blastocysts. **282:** 1145–1148 (1998).

71. Lo, B. & Parham, L. Ethical Issues in Stem Cell Research. *Endocrine Reviews* **30:** 204–213 (2009).

72. Takahashi, K. *et al.* Induction of Pluripotent Stem Cells from Adult Human Fibroblasts by Defined Factors. 861–872 (2007).

73. Yu, J. *et al.* Induced Pluripotent Stem Cell Lines Derived from Human Somatic Cells. *Science (80-.).* **318:** 1917–1920 (2007).

74. Brouwer, M., Zhou, H. & Nadif Kasri, N. Choices for Induction of Pluripotency: Recent Developments in Human Induced Pluripotent Stem Cell Reprogramming Strategies. *Stem Cell Rev.* **12:** 54–72 (2016).

75. Liu, Y., Cheng, D., Li, Z., Gao, X. & Wang, H. The gene expression profiles of induced pluripotent stem cells (iPSCs) generated by a non-integrating method are more similar to embryonic stem cells than those of iPSCs generated by an integrating method. *Genet. Mol. Biol.* **35:** 693–700 (2012).

76. Liao, J. *et al.* Enhanced efficiency of generating induced pluripotent stem (iPS) cells from human somatic cells by a combination of six transcription factors. **18:** 600–603 (2008).

77. Utikal, J., Maherali, N., Kulalert, W. & Hochedlinger, K. Sox2 is dispensable for the reprogramming of melanocytes and melanoma cells into induced pluripotent stem cells. *J. Cell Sci.* **122:** 3502–3510 (2009).

78. Kim, J. B. *et al.* Oct4-Induced Pluripotency in Adult Neural Stem Cells. *Cell* **136:** 411–419 (2009).

79. Deng, X. *et al.* Non-Viral Methods For Generating Integration-Free , Induced Pluripotent Stem Cells. *Curr. Stem Cell Res. Ther.* **10:** 153–158 (2015).

80. Hou, P. *et al.* Pluripotent Stem Cells Induced from Mouse Somatic Cells by Small-Molecule Compounds. *Science (80-.).* **341:** 651–654 (2013).

81. Kim, K. *et al.* Epigenetic memory in induced pluripotent stem cells. *Nature* **467:** 285–290 (2010).

82. Stadtfeld, M., Nagaya, M., Utikal, J., Weir, G. & Hochedlinger, K. Induced Pluripotent Stem Cells Generated Without Viral Integration. *Science (80-.).* **322:** 945–949 (2008).

83. Fusaki, N., Ban, H., Nishiyama, A., Saeki, K. & Hasegawa, M. Efficient induction of transgene-free human pluripotent stem cells using a vector based on Sendai virus, an RNA virus that does not integrate into the host genome. *Proc. Jpn. Acad. Ser. B. Phys. Biol. Sci.* **85:** 348–362 (2009).

84. Okita, K., Nakagawa, M., Hyenjong, H., Ichisaka, T. & Yamanaka, S. Generation of Mouse Induced Pluripotent Stem Cells Without Viral Vectors. *Science (80-.).* **322:** 949–953 (2008).
85. Jia, F. *et al.* A Nonviral Minicircle Vector for Deriving Human iPS Cells. *Nat. Methods* **7:** 197–199 (2010).
86. Kim, D. *et al.* Generation of Human Induced Pluripotent Stem Cells by Direct Delivery of Reprogramming Proteins. *Cell Stem Cell* **4:** 472–476 (2009).
87. Aasen, T. *et al.* Efficient and rapid generation of induced pluripotent stem cells from human keratinocytes. *Nat Biotech* **26:** 1276–1284 (2008).
88. Polo, J. M. *et al.* Cell type of origin influences the molecular and functional properties of mouse induced pluripotent stem cells. *Nat Biotech* **28:** 848–855 (2010).
89. Iida, K. *et al.* Hypoxia-enhanced Derivation of iPSCs from Human Dental Pulp Cells. *J. Dent. Res.* **92:** 905–910 (2013).
90. Mitcheson, J. S., Hancox, J. C. & Levi, A. J. Action potentials, ion channel currents and transverse tubule density in adult rabbit ventricular myocytes maintained for 6 days in cell culture. *Pflügers Arch.* **431:** 814–827 (1996).
91. Kehat, I. & Kenyagin-Karsenti, D. Human embryonic stem cells can differentiate into myocytes with structural and functional properties of cardiomyocytes. *J. Clin. Invest.* **108:** 363–364 (2001).
92. Lahti, A. L. *et al.* Model for long QT syndrome type 2 using human iPS cells demonstrates arrhythmogenic characteristics in cell culture. *Dis. Model. Mech.* **5:** 220–230 (2012).
93. Kujala, K. *et al.* Cell model of catecholaminergic polymorphic ventricular tachycardia reveals early and delayed afterdepolarizations. *PLoS One* **7:** e44660 (2012).
94. Batalov, I. & Feinberg, A. W. Differentiation of Cardiomyocytes from Human Pluripotent Stem Cells Using Monolayer Culture: Supplementary Issue: Stem Cell Biology. *Biomark. Insights* **10s1:** BMI.S20050 (2015).
95. Eschenhagen, T., Mummery, C. & Knollmann, B. C. Modelling sarcomeric cardiomyopathies in the dish: from human heart samples to iPSC cardiomyocytes. *Cardiovasc. Res.* **105:** 424–438 (2015).
96. Dell'Era, P. *et al.* Cardiac disease modeling using induced pluripotent stem cell-derived human cardiomyocytes. *World J. Stem Cells* **7:** 329–42 (2015).
97. Xi, J. *et al.* Comparison of contractile behavior of native murine ventricular tissue and cardiomyocytes derived from embryonic or induced pluripotent stem cells. *FASEB J.* **24:** 2739–2751 (2010).
98. Zhu, W.-Z. *et al.* Neuregulin/ErbB Signaling Regulates Cardiac Subtype Specification in Differentiating Human Embryonic Stem Cells. *Circ. Res.* **107:** 776–786 (2010).
99. Lieu, D. K. *et al.* Absence of transverse tubules contributes to non-uniform Ca(2+) wavefronts in mouse and human embryonic stem cell-derived cardiomyocytes. *Stem Cells Dev.* **18:** 1493–1500 (2009).
100. Gherghiceanu, M. *et al.* Cardiomyocytes derived from human embryonic and induced pluripotent stem cells: comparative ultrastructure. *J. Cell. Mol. Med.* **15:** 2539–2551 (2011).
101. Sartiani, L. *et al.* Developmental changes in cardiomyocytes differentiated from human embryonic stem cells: a molecular and electrophysiological approach. *Stem Cells* **25:** 1136–44 (2007).
102. Yang, X., Pabon, L. & Murry, C. E. Engineering adolescence: Maturation of human pluripotent stem cell-derived cardiomyocytes. *Circ. Res.* **114:** 511–523 (2014).
103. Paci, M., Hyttinen, J., Rodriguez, B. & Severi, S. Human induced pluripotent stem cell-derived versus adult cardiomyocytes: an in silico electrophysiological study on effects of ionic current block. *Br. J. Pharmacol.* **172:** 5147–5160 (2015).

104. Koivumäki, J. T. *et al.* Structural Immaturity of Human iPSC-Derived Cardiomyocytes: In Silico Investigation of Effects on Function and Disease Modeling. *Frontiers in Physiology* **9:** 80 (2018).

105. Kita-Matsuo, H. *et al.* Lentiviral Vectors and Protocols for Creation of Stable hESC Lines for Fluorescent Tracking and Drug Resistance Selection of Cardiomyocytes. *PLoS One* **4:** e5046 (2009).

106. Korte, F. S., Herron, T. J., Rovetto, M. J. & McDonald, K. S. Power output is linearly related to MyHC content in rat skinned myocytes and isolated working hearts. *Am. J. Physiol. Heart Circ. Physiol.* **289:** H801-12 (2005).

107. Chan, Y.-C. *et al.* Electrical Stimulation Promotes Maturation of Cardiomyocytes Derived from Human Embryonic Stem Cells. *J. Cardiovasc. Transl. Res.* **6:** 989–999 (2013).

108. Serena, E. *et al.* Electrical stimulation of human embryonic stem cells: cardiac differentiation and the generation of reactive oxygen species. *Exp. Cell Res.* **315:** 3611–3619 (2009).

109. Kujala, K. *et al.* Electrical field stimulation with a novel platform: Effect on cardiomyocyte gene expression but not on orientation. *Int. J. Biomed. Sci.* **8:** 109–120 (2012).

110. Salameh, A. *et al.* Cyclic Mechanical Stretch Induces Cardiomyocyte Orientation and Polarization of the Gap Junction Protein Connexin43. *Circ. Res.* **106:** 1592–1602 (2010).

111. Shimko, V. F. & Claycomb, W. C. Effect of mechanical loading on three-dimensional cultures of embryonic stem cell-derived cardiomyocytes. *Tissue Eng. Part A* **14:** 49–58 (2008).

112. Mihic, A. *et al.* The effect of cyclic stretch on maturation and 3D tissue formation of human embryonic stem cell-derived cardiomyocytes. *Biomaterials* **35:** 2798–2808 (2014).

113. Chen, Y. *et al.* Three-dimensional poly-(ε-caprolactone) nanofibrous scaffolds directly promote the cardiomyocyte differentiation of murine-induced pluripotent stem cells through Wnt/β-catenin signaling. *BMC Cell Biol.* **16:** 22 (2015).

114. Wang, P.-Y., Yu, J., Lin, J.-H. & Tsai, W.-B. Modulation of alignment, elongation and contraction of cardiomyocytes through a combination of nanotopography and rigidity of substrates. *Acta Biomater.* **7:** 3285–3293 (2011).

115. Heidi Au, H. T., Cui, B., Chu, Z. E., Veres, T. & Radisic, M. Cell culture chips for simultaneous application of topographical and electrical cues enhance phenotype of cardiomyocytes. *Lab Chip* **9:** 564–575 (2009).

116. Foldes, G. *et al.* Modulation of human embryonic stem cell-derived cardiomyocyte growth: a testbed for studying human cardiac hypertrophy? *J. Mol. Cell. Cardiol.* **50:** 367–376 (2011).

117. Lee, Y.-K. *et al.* Triiodothyronine promotes cardiac differentiation and maturation of embryonic stem cells via the classical genomic pathway. *Mol. Endocrinol.* **24:** 1728–1736 (2010).

118. Knollmann, B. C. Induced Pluripotent Stem Cell–Derived Cardiomyocytes: Boutique Science or Valuable Arrhythmia Model? *Circ. Res.* **112:** 969–976 (2013).

119. Khan, J. M., Lyon, A. R. & Harding, S. E. The case for induced pluripotent stem cell-derived cardiomyocytes in pharmacological screening. *Br. J. Pharmacol.* **169:** 304–317 (2013).

120. Rajala, K., Pekkanen-Mattila, M. & Aalto-Setälä, K. Cardiac Differentiation of Pluripotent Stem Cells. *Stem Cells Int.* **2011:** 1–12 (2011).

121. Shinnawi, R. & Gepstein, L. iPCS Cell Modeling of Inherited Cardiac Arrhythmias. *Curr. Treat. Options Cardiovasc. Med.* **16:** (2014).

122. Chunbo, Y. *et al.* Concise Review: Cardiac Disease Modeling Using Induced Pluripotent Stem Cells. *Stem Cells* **33:** 2643–2651 (2015).

123. Moretti, A. *et al.* Patient-Specific Induced Pluripotent Stem-Cell Models for Long-QT Syndrome. *N. Engl. J. Med.* **363:** 1397–1409 (2010).
124. Terrenoire, C. *et al.* Induced pluripotent stem cells used to reveal drug actions in a long QT syndrome family with complex genetics. *J. Gen. Physiol.* **141:** 61–72 (2013).
125. Paci, M., Passini, E., Severi, S., Hyttinen, J. & Rodriguez, B. Phenotypic variability in LQT3 human induced pluripotent stem cell-derived cardiomyocytes and their response to antiarrhythmic pharmacologic therapy: An in silico approach. *Hear. Rhythm* **14:** 1704–1712 (2017).
126. Itzhaki, I. *et al.* Modeling of catecholaminergic polymorphic ventricular tachycardia with patient-specific human-induced pluripotent stem cells. *J. Am. Coll. Cardiol.* **60:** 990–1000 (2012).
127. Novak, A., Barad, L., Lorber, A., Itskovitz-Eldor, J. & Binah, O. Modeling Catecholaminergic Polymorphic Ventricular Tachycardia using Induced Pluripotent Stem Cell-derived Cardiomyocytes. *Rambam Maimonides Med. J.* **3:** e0015 (2012).
128. Kiviaho, A. L. *et al.* Distinct electrophysiological and mechanical beating phenotypes of long QT syndrome type 1-specific cardiomyocytes carrying different mutations. *IJC Hear. Vasc.* **8:** 19–31 (2015).
129. Yajuan, X., Xin, L. & Zhiyuan, L. A Comparison of the Performance and Application Differences Between Manual and Automated Patch-Clamp Techniques. *Curr. Chem. Genomics* **6:** 87–92 (2012).
130. Ling, G. & Gerard, R. W. The normal membrane potential of frog sartorius fibers. *J. Cell. Comp. Physiol.* **34:** 383–396 (1949).
131. Neher, E. & Sakmann, B. Single-channel currents recorded from membrane of denervated frog muscle fibres. *Nature* **260:** 799–802 (1976).
132. Ogden, D. & Stanfield, P. Patch clamp techniques for single channel and whole-cell recording. In *Microelectrode techniques, The Plymouth workshop handbook* (ed. Ogden, D.) 53–78 (Company of Biologists, 1994).
133. Kornreich, B. G. The patch clamp technique: Principles and technical considerations. *J. Vet. Cardiol.* **9:** 25–37 (2007).
134. Scheel, O. *et al.* Action Potential Characterization of Human Induced Pluripotent Stem Cell–Derived Cardiomyocytes Using Automated Patch-Clamp Technology. *Assay Drug Dev. Technol.* **12:** 457–469 (2014).
135. Itzhaki, I. *et al.* Modelling the long QT syndrome with induced pluripotent stem cells. *Nature* **471:** 225–229 (2011).
136. Honda, M., Kiyokawa, J., Tabo, M. & Inoue, T. Electrophysiological Characterization of Cardiomyocytes Derived From Human Induced Pluripotent Stem Cells. *J. Pharmacol. Sci.* **117:** 149–159 (2011).
137. Du, D. T., Hellen, N., Kane, C. & Terracciano, C. M. Action Potential Morphology of Human Induced Pluripotent Stem Cell-Derived Cardiomyocytes Does Not Predict Cardiac Chamber Specificity and Is Dependent on Cell Density. *Biophys. J.* **108:** 1–4 (2015).
138. Giles, W. R. & Noble, D. Rigorous Phenotyping of Cardiac iPSC Preparations Requires Knowledge of Their Resting Potential(s). *Biophys. J.* **110:** 278–280 (2016).
139. Kane, C., Du, D. T. M., Hellen, N. & Terracciano, C. M. The Fallacy of Assigning Chamber Specificity to iPSC Cardiac Myocytes from Action Potential Morphology. *Biophys. J.* **110:** 281–283 (2016).
140. Thomas, C. A., Springer, P. A., Loeb, G. E., Berwald-Netter, Y. & Okun, L. M. A miniature microelectrode array to monitor the bioelectric activity of cultured cells. *Exp. Cell Res.* **74:** 61–66 (1972).
141. Kehat, I., Gepstein, A., Spira, A., Itskovitz-Eldor, J. & Gepstein, L. High-Resolution Electrophysiological Assessment of Human Embryonic Stem Cell-Derived

Cardiomyocytes: A Novel In Vitro Model for the Study of Conduction. *Circ. Res.* **91:** 659–661 (2002).

142. Riedel, M. *et al.* Functional and Pharmacological Analysis of Cardiomyocytes Differentiated from Human Peripheral Blood Mononuclear-Derived Pluripotent Stem Cells. *Stem Cell Reports* **3:** 131–141 (2014).
143. Pekkanen-Mattila, M. *et al.* Substantial variation in the cardiac differentiation of human embryonic stem cell lines derived and propagated under the same conditions—a comparison of multiple cell lines. *Ann. Med.* **41:** 360–370 (2009).
144. Whitson, J., Kubota, D., Shimono, K., Jia, Y. & Taketani, M. Multi-Electrode Arrays: Enhancing Traditional Methods and Enabling Network Physiology. In *Advances in Network Electrophysiology: Using Multi-Electrode Arrays* (eds. Taketani, M. & Baudry, M.) 38–68 (Springer US, 2006).
145. Egert, U., Banach, K. & Meyer, T. Analysis of Cardiac Myocyte Activity Dynamics with Micro-Electrode Arrays. In *Advances in Network Electrophysiology: Using Multi-Electrode Arrays* (eds. Taketani, M. & Baudry, M.) 274–290 (Springer US, 2006).
146. Stett, A. *et al.* Biological application of microelectrode arrays in drug discovery and basic research. *Anal. Bioanal. Chem.* **377:** 486–495 (2003).
147. Braeken, D. *et al.* Local electrical stimulation of single adherent cells using three-dimensional electrode arrays with small interelectrode distances. *2009 Annual International Conference of the IEEE Engineering in Medicine and Biology Society* 2756–2759 (2009).
148. Herron, T. J., Lee, P. & Jalife, J. Optical Imaging of Voltage and Calcium in Cardiac Cells & Tissues. *Circ. Res.* **110:** 609–623 (2012).
149. Fast, V. G. Recording Action Potentials Using Voltage-Sensitive Dyes. In *Practical Methods in Cardiovascular Research* (eds. Dhein, S., Mohr, F. W. & Delmar, M.) 233–255 (Springer Berlin Heidelberg, 2005).
150. Paredes, R. M., Etzler, J. C., Watts, L. T., Zheng, W. & Lechleiter, J. D. Chemical calcium indicators. *Methods* **46:** 143–151 (2008).
151. Maravall, M., Mainen, Z. F., Sabatini, B. L. & Svoboda, K. Estimating intracellular calcium concentrations and buffering without wavelength ratioing. *Biophys. J.* **78:** 2655–2667 (2000).
152. Novakova, M. *et al.* Effects of voltage sensitive dye di-4-ANEPPS on guinea pig and rabbit myocardium. *Gen. Physiol. Biophys.* **27:** 45–54 (2008).
153. Rohr, S. & Salzberg, B. M. Multiple site optical recording of transmembrane voltage (MSORTV) in patterned growth heart cell cultures: assessing electrical behavior, with microsecond resolution, on a cellular and subcellular scale. *Biophys. J.* **67:** 1301–1315 (1994).
154. Ram, D. & Richard, C. Cell damage and reactive oxygen species production induced by fluorescence microscopy: effect on mitosis and guidelines for non-invasive fluorescence microscopy. *Plant J.* **36:** 280–290 (2003).
155. Schaffer, P., Ahammer, H., Muller, W., Koidl, B. & Windisch, H. Di-4-ANEPPS causes photodynamic damage to isolated cardiomyocytes. *Pflugers Arch.* **426:** 548–551 (1994).
156. Efimov, I. & Salama, G. The Future of Optical Mapping is Bright: RE: Review on: “Optical Imaging of Voltage and Calcium in Cardiac Cells and Tissues” by Herron, Lee, and Jalife. *Circ. Res.* **110:** e70–e71 (2012).
157. Pérez Koldenkova, V. & Nagai, T. Genetically encoded Ca2 + indicators: Properties and evaluation. *Biochim. Biophys. Acta - Mol. Cell Res.* **1833:** 1787–1797 (2013).
158. Song, L., Hennink, E. J., Young, I. T. & Tanke, H. J. Photobleaching kinetics of fluorescein in quantitative fluorescence microscopy. *Biophys. J.* **68:** 2588–2600 (1995).
159. Lulevich, V., Shih, Y.-P., Lo, S. H. & Liu, G. Cell tracing dyes significantly change single cell mechanics. *J. Phys. Chem. B* **113:** 6511–6519 (2009).

160. Fabiato, A. & Fabiato, F. Use of chlorotetracycline fluorescence to demonstrate Ca2+-induced release of Ca2+ from the sarcoplasmic reticulum of skinned cardiac cells. *Nature* **281:** 146–148 (1979).

161. Itzhaki, I. *et al.* Calcium Handling in Human Induced Pluripotent Stem Cell Derived Cardiomyocytes. *PLoS One* **6:** e18037 (2011).

162. Lee, Y.-K. *et al.* Calcium Homeostasis in Human Induced Pluripotent Stem Cell-Derived Cardiomyocytes. *Stem Cell Rev.* **7:** 976–986 (2011).

163. Penttinen, K. *et al.* Antiarrhythmic Effects of Dantrolene in Patients with Catecholaminergic Polymorphic Ventricular Tachycardia and Replication of the Responses Using iPSC Models. *PLoS One* **10:** e0125366 (2015).

164. Yazawa, M. *et al.* Using iPS cells to investigate cardiac phenotypes in patients with Timothy Syndrome. *Nature* **471:** 230–234 (2011).

165. Spencer, C. I. *et al.* Calcium Transients Closely Reflect Prolonged Action Potentials in iPSC Models of Inherited Cardiac Arrhythmia. *Stem Cell Reports* **3:** 269–281 (2014).

166. Herron, T. J., Milstein, M. L., Anumonwo, J., Priori, S. G. & Jalife, J. Purkinje Cell Calcium Dysregulation Is the Cellular Mechanism that Underlies Catecholaminergic Polymorphic Ventricular Tachycardia. *Heart Rhythm* **7:** 1122–1128 (2010).

167. Siegel, M. S. & Isacoff, E. Y. A genetically encoded optical probe of membrane voltage. *Neuron* **19:** 735–741 (1997).

168. Kralj, J. M., Douglass, A. D., Hochbaum, D. R., Maclaurin, D. & Cohen, A. E. Optical recording of action potentials in mammalian neurons using a microbial rhodopsin. *Nat Meth* **9:** 90–95 (2012).

169. Chang Liao, M.-L. *et al.* Sensing Cardiac Electrical Activity With a Cardiac Myocyte--Targeted Optogenetic Voltage Indicator. *Circ. Res.* **117:** 401–412 (2015).

170. Leyton-Mange, J. S. *et al.* Rapid Cellular Phenotyping of Human Pluripotent Stem Cell-Derived Cardiomyocytes using a Genetically Encoded Fluorescent Voltage Sensor. *Stem Cell Reports* **2:** 163–170 (2014).

171. Björk, S. *et al.* Evaluation of Optogenetic Electrophysiology Tools in Human Stem Cell-Derived Cardiomyocytes. *Frontiers in Physiology* **8:** 884 (2017).

172. Huang, W.-Y., Aramburu, J., Douglas, P. S. & Izumo, S. Transgenic expression of green fluorescence protein can cause dilated cardiomyopathy. *Nat Med* **6:** 482–483 (2000).

173. Hires, S. A., Tian, L. & Looger, L. L. Reporting neural activity with genetically encoded calcium indicators. *Brain Cell Biol.* **36:** 69–86 (2008).

174. Mank, M. & Griesbeck, O. Genetically Encoded Calcium Indicators. *Chem. Rev.* **108:** 1550–1564 (2008).

175. Shinnawi, R. *et al.* Monitoring Human-Induced Pluripotent Stem Cell-Derived Cardiomyocytes with Genetically Encoded Calcium and Voltage Fluorescent Reporters. *Stem Cell Reports* **5:** 582–596 (2015).

176. Lock, J. T., Parker, I. & Smith, I. F. A comparison of fluorescent Ca(2+) indicators for imaging local Ca(2+) signals in cultured cells. *Cell Calcium* **58:** 638–648 (2015).

177. Binnig, G., Quate, C. F. & Gerber, C. Atomic Force Microscope. *Phys. Rev. Lett.* **56:** 930–933 (1986).

178. Dufrêne, Y. F. Atomic Force Microscopy, a Powerful Tool in Microbiology. *J. Bacteriol.* **184:** 5205–5213 (2002).

179. Moreno-Herrero, F., Colchero, J., Gomez-Herrero, J. & Baro, A. M. Atomic force microscopy contact, tapping, and jumping modes for imaging biological samples in liquids. *Phys. Rev. E. Stat. Nonlin. Soft Matter Phys.* **69:** 31915 (2004).

180. Domke, J., Parak, W. J., George, M., Gaub, H. E. & Radmacher, M. Mapping the mechanical pulse of single cardiomyocytes with the atomic force microscope. *Eur. Biophys. J.* **28:** 179–186 (1999).

181. Liu, Y. *et al.* In situ mechanical analysis of cardiomyocytes at nano scales. *Nanoscale* **4:** 99–102 (2012).
182. Liu, J., Sun, N., Bruce, M. A., Wu, J. C. & Butte, M. J. Atomic force mechanobiology of pluripotent stem cell-derived cardiomyocytes. *PLoS One* **7:** e37559 (2012).
183. Pesl, M. *et al.* Atomic force microscopy combined with human pluripotent stem cell derived cardiomyocytes for biomechanical sensing. *Biosens. Bioelectron.* **85:** 751–757 (2016).
184. Yoneda, M. Force Exerted by a Single Cilium of Mytilus Edulis. *J. Exp. Biol.* **39:** 307–317 (1962).
185. Canaday, P. G. & Fay, F. S. An ultrasensitive isometric force transducer for single smooth muscle cell mechanics. *J. Appl. Physiol.* **40:** 243–246 (1976).
186. Lin, G., Pister, K. S. J. & Roos, K. P. Surface micromachined polysilicon heart cell force transducer. *Journal of Microelectromechanical Systems* **9:** 9–17 (2000).
187. Kent, R. L. *et al.* Contractile function of isolated feline cardiocytes in response to viscous loading. *Am. J. Physiol.* **257:** H1717-27 (1989).
188. Tan, J. L. *et al.* Cells lying on a bed of microneedles: An approach to isolate mechanical force. *Proc. Natl. Acad. Sci.* **100:** 1484–1489 (2003).
189. Han, S. J., Bielawski, K. S., Ting, L. H., Rodriguez, M. L. & Sniadecki, N. J. Decoupling Substrate Stiffness, Spread Area, and Micropost Density: A Close Spatial Relationship between Traction Forces and Focal Adhesions. *Biophys. J.* **103:** 640–648 (2012).
190. Yang, X. *et al.* Tri-iodo-L-thyronine Promotes the Maturation of Human Cardiomyocytes-Derived from Induced Pluripotent Stem Cells. *J. Mol. Cell. Cardiol.* **72:** 296–304 (2014).
191. Wilson, K., Das, M., Wahl, K. J., Colton, R. J. & Hickman, J. Measurement of Contractile Stress Generated by Cultured Rat Muscle on Silicon Cantilevers for Toxin Detection and Muscle Performance Enhancement. *PLoS One* **5:** 1–11 (2010).
192. Stancescu, M. *et al.* A phenotypic in vitro model for the main determinants of human whole heart function. *Biomaterials* **60:** 20–30 (2015).
193. Goßmann, M. *et al.* Mechano-Pharmacological Characterization of Cardiomyocytes Derived from Human Induced Pluripotent Stem Cells. *Cell. Physiol. Biochem.* **38:** 1182–1198 (2016).
194. Yin, S. *et al.* Measuring Single Cardiac Myocyte Contractile Force via Moving a Magnetic Bead. *Biophys. J.* **88:** 1489–1495 (2005).
195. Iribe, G., Helmes, M. & Kohl, P. Force-length relations in isolated intact cardiomyocytes subjected to dynamic changes in mechanical load. *Am. J. Physiol. - Hear. Circ. Physiol.* **292:** H1487–H1497 (2007).
196. Harris, A. K., Wild, P. & Stopak, D. Silicone rubber substrata: a new wrinkle in the study of cell locomotion. *Science* **208:** 177–179 (1980).
197. Wang, J. H. C. & Lin, J. S. Cell traction force and measurement methods. *Biomech. Model. Mechanobiol.* **6:** 361–371 (2007).
198. Schwarz, U. S. & Soine, J. R. D. Traction force microscopy on soft elastic substrates: A guide to recent computational advances. *Biochim. Biophys. Acta* **1853:** 3095–3104 (2015).
199. Franck, C., Maskarinec, S. A., Tirrell, D. A. & Ravichandran, G. Three-Dimensional Traction Force Microscopy: A New Tool for Quantifying Cell-Matrix Interactions. *PLoS One* **6:** e17833 (2011).
200. Peters, M. F., Lamore, S. D., Guo, L., Scott, C. W. & Kolaja, K. L. Human stem cell-derived cardiomyocytes in cellular impedance assays: bringing cardiotoxicity screening to the front line. *Cardiovasc. Toxicol.* **15:** 127–139 (2015).
201. Böttrich, M., Tanskanen, J. M. A. & Hyttinen, J. A. K. Lead field theory provides a powerful tool for designing microelectrode array impedance measurements for biological cell detection and observation. *Biomed. Eng. Online* **16:** 85 (2017).

202. Xi, B. *et al.* Functional Cardiotoxicity Profiling and Screening Using the xCELLigence RTCA Cardio System. *J. Assoc. Lab. Autom.* **16:** 415–421 (2011).
203. Abassi, Y. A. *et al.* Dynamic monitoring of beating periodicity of stem cell-derived cardiomyocytes as a predictive tool for preclinical safety assessment. *Br. J. Pharmacol.* **165:** 1424–1441 (2012).
204. Scott, C. W. *et al.* An Impedance-Based Cellular Assay Using Human iPSC-Derived Cardiomyocytes to Quantify Modulators of Cardiac Contractility. *Toxicol. Sci.* **142:** 331–338 (2014).
205. Tervonen, A. & Hyttinen, J. *Sensitivity Distribution of Electrical Impedance Epithelial Measurement Systems BT - EMBEC & NBC 2017*. In (eds. Eskola, H., Väisänen, O., Viik, J. & Hyttinen, J.) 623–626 (Springer Singapore, 2018).
206. Philip, J. T., Samuvel, B., Pradeesh, K. & Nimmi, N. K. *A comparative study of block matching and optical flow motion estimation algorithms*. In *2014 Annual International Conference on Emerging Research Areas: Magnetics, Machines and Drives (AICERA/iCMMD)* 1–6 (2014).
207. Barron, J. L., Fleet, D. J. & Beauchemin, S. S. Performance of optical flow techniques. *Int. J. Comput. Vis.* **12:** 43–77 (1994).
208. Strzodka, R. & Garbe, C. *Real-time motion estimation and visualization on graphics cards*. In *IEEE Visualization 2004* 545–552 (2004).
209. Adrian, R. J. Twenty years of particle image velocimetry. *Exp. Fluids* **39:** 159–169 (2005).
210. Raffel, M., Willert, C., Wereley, S. & Kompenhans, J. *Particle Image Velocimetry: A Practical Guide.* (Springer Berlin Heidelberg, 2007).
211. Westerweel, J. Fundamentals of digital particle image velocimetry. *Meas. Sci. Technol.* **8:** 1379–1392 (1997).
212. Ghanbari, M. The cross-search algorithm for motion estimation. *IEEE Trans. Commun.* **38:** 950–953 (1990).
213. Willert, C. E. & Gharib, M. Digital particle image velocimetry. *Exp. Fluids* **10:** 181–193 (1991).
214. Gui, L. C. & Merzkirch, W. A method of tracking ensembles of particle images. *Exp. Fluids* 465–468 (1996).
215. Wieneke, B. & Provost, R. DIC Uncertainty Estimation from Statistical Analysis of Correlation Values. In *Advancement of Optical Methods in Experimental Mechanics, Volume 3* 125–136 (Springer International Publishing, 2014).
216. Fei, R., Gui, L. & Merzkirch, W. Comparative study of correlation-based PIV evaluation methods. *Mach. Graph. Vis.* **8:** 571–578 (1999).
217. Chan, S. H., Võ, D. T. & Nguyen, T. Q. *Subpixel motion estimation without interpolation*. In *2010 IEEE International Conference on Acoustics, Speech and Signal Processing* 722–725 (2010).
218. Hart, P. D. PIV error correction. *Exp. Fluids* **29:** 13–22 (2000).
219. Steadman, B. W., Moore, K. B., Spitzer, K. W. & Bridge, J. H. B. A video system for measuring motion in contracting heart cells. *IEEE Transactions on Biomedical Engineering* **35:** 264–272 (1988).
220. Tameyasu, T., Toyoki, T. & Sugi, H. Nonsteady motion in unloaded contractions of single frog cardiac cells. *Biophys. J.* **48:** 461–465 (1985).
221. Mukherjee, R., Crawford, F. A., Hewett, K. W. & Spinale, F. G. Cell and sarcomere contractile performance from the same cardiocyte using video microscopy. *J. Appl. Physiol.* **74:** 2023–2033 (1993).
222. Hossain, M. M. *et al.* Non-invasive characterization of mouse embryonic stem cell derived cardiomyocytes based on the intensity variation in digital beating video. *Analyst* **135:** 1624–1630 (2010).

223. Germain, F., Doisy, A., Ronot, X. & Tracqui, P. Characterization of cell deformation and migration using a parametric estimation of image motion. *IEEE Trans. Biomed. Eng.* **46:** 584–600 (1999).
224. Cai, H., Richter, C.-P. & Chadwick, R. S. Motion Analysis in the Hemicochlea. *Biophys. J.* **85:** 1929–1937 (2003).
225. Kaikkonen, L. *et al.* p38α regulates SERCA2a function. *J. Mol. Cell. Cardiol.* **67:** 86–93 (2014).
226. Frigault, M. M., Lacoste, J., Swift, J. L. & Brown, C. M. Live-cell microscopy – tips and tools. *J. Cell Sci.* **122:** 753 LP-767 (2009).
227. Hayakawa, T. *et al.* Image-based evaluation of contraction-relaxation kinetics of human-induced pluripotent stem cell-derived cardiomyocytes: Correlation and complementarity with extracellular electrophysiology. *J. Mol. Cell. Cardiol.* **77:** 178–191 (2014).
228. Liu, X., Iyengar, S. G. & Rittscher, J. Monitoring cardiomyocyte motion in real time through image registration and time series analysis. *IEEE Int. Symp. Biomed. Imaging From Nano to Macro* 1308–1311 (2012).
229. Chen, A. *et al.* Integrated platform for functional monitoring of biomimetic heart sheets derived from human pluripotent stem cells. *Biomaterials* **35:** 675–683 (2014).
230. Maddah, M. *et al.* A Non-invasive Platform for Functional Characterization of Stem-Cell-Derived Cardiomyocytes with Applications in Cardiotoxicity Testing. *Stem Cell Reports* **4:** 621–631 (2015).
231. Ribeiro, A. J. S. *et al.* Multi-Imaging Method to Assay the Contractile Mechanical Output of Micropatterned Human iPSC-Derived Cardiac MyocytesNovelty and Significance. *Circ. Res.* **120:** 1572–1583 (2017).
232. Sala, L. *et al.* MUSCLEMOTION: A Versatile Open Software Tool to Quantify Cardiomyocyte and Cardiac Muscle Contraction In Vitro and In Vivo. *Circ. Res.* **122:** e5–e16 (2018).
233. Thirion, J.-P. Image matching as a diffusion process: an analogy with Maxwell's demons. *Med. Image Anal.* **2:** 243–260 (1998).
234. Sun, D., Roth, S. & Black, M. J. Secrets of optical flow estimation and their principles. *Computer Vision and Pattern Recognition (CVPR), 2010 IEEE Conference on* 2432–2439 (2010).
235. Pradhapan, P., Kuusela, J., Viik, J., Aalto-Setälä, K. & Hyttinen, J. Cardiomyocyte MEA Data Analysis (CardioMDA) – A Novel Field Potential Data Analysis Software for Pluripotent Stem Cell Derived Cardiomyocytes. *PLoS One* **8:** 1–11 (2013).
236. Nobuhito, M. & Kuang-An, C. Introduction to MPIV. User reference manual, 14p. (2003). Available at: http://www.oceanwave.jp/softwares/mpiv/.
237. Kroon, D.-J. Pinch and Spherize filter. MathWorks File Exchange (2009). Available at: http://se.mathworks.com/matlabcentral/fileexchange/22573-pinch-and-spherize-filter.
238. Humphreys, W. M. & Naguib, A. M. Comparative Study of Image Compression Techniques for Digital Particle Image Velocimetry. *AIAA J.* **40:** 1026–1036 (2002).
239. Haugaa, K. H. *et al.* Transmural Differences in Myocardial Contraction in Long-QT SyndromeClinical Perspective. *Circulation* **122:** 1355–1363 (2010).
240. Nguyen, N. *et al.* Adult human primary cardiomyocyte-based model for the simultaneous prediction of drug-induced inotropic and pro-arrhythmia risk. *Frontiers in Physiology* **8:** 1073 (2017).
241. Burridge, P. W. *et al.* Human induced pluripotent stem cell–derived cardiomyocytes recapitulate the predilection of breast cancer patients to doxorubicin-induced cardiotoxicity. *Nat. Med.* **22:** 547 (2016).
242. Soares, C. P. *et al.* 2D and 3D-Organized Cardiac Cells Shows Differences in Cellular Morphology, Adhesion Junctions, Presence of Myofibrils and Protein Expression. *PLoS One* **7:** e38147 (2012).

243. Matsa, E. *et al.* Drug evaluation in cardiomyocytes derived from human induced pluripotent stem cells carrying a long QT syndrome type 2 mutation. *Eur. Heart J.* **32:** 952–962 (2011).

244. Abi-Gerges, N. *et al.* Preservation of cardiomyocytes from the adult heart. *J. Mol. Cell. Cardiol.* **64:** 108–119 (2013).

245. Karakikes, I., Ameen, M., Termglinchan, V. & Wu, J. C. Human induced pluripotent stem cell-derived cardiomyocytes: insights into molecular, cellular, and functional phenotypes. *Circ. Res.* **117:** 80–88 (2015).

246. Välimäki, H. *et al.* Fluorimetric oxygen sensor with an efficient optical read-out for in vitro cell models. *Sensors Actuators B Chem.* **249:** 738–746 (2017).

247. Rajan, D. K. *et al.* A portable live-cell imaging system with an invert-upright-convertible architecture and a mini-bioreactor for long-term simultaneous cell imaging, chemical sensing and electrophysiological recording. *IEEE Access* **6:** 11063–11075 (2018).

248. Mäki, A.-J. *et al.* A Portable Microscale Cell Culture System with Indirect Temperature Control. *SLAS Technol.* (2018).

249. Muhonen, V. Image based analysis for cardiomyocyte motion and cell adhesion. Master of Science Thesis, Tampere University of Technology, Tampere, Finland (2016).

PUBLICATIONS

PUBLICATION
I

Video image-based analysis of single human induced pluripotent stem cell derived cardiomyocyte beating dynamics using digital image correlation

Ahola, A., Kiviaho, A. L., Larsson, K., Honkanen, M., Aalto-Setälä, K. & Hyttinen, J.

Biomedical Engineering Online (2014), 13:39
https://doi.org/10.1186/1475-925X-13-39

Ahola *et al. BioMedical Engineering OnLine* 2014, **13**:39
http://www.biomedical-engineering-online.com/content/13/1/39

BioMedical Engineering OnLine

RESEARCH Open Access

Video image-based analysis of single human induced pluripotent stem cell derived cardiomyocyte beating dynamics using digital image correlation

Antti Ahola[1*†], Anna L Kiviaho[2†], Kim Larsson[2], Markus Honkanen[3], Katriina Aalto-Setälä[2,4,5] and Jari Hyttinen[1]

* Correspondence: antti.l.ahola@tut.fi
†Equal contributors
[1]Computional Biophysics and Imaging Group, Department of Electronics and Communications Engineering, and BioMediTech, Tampere University of Technology, Tampere, Finland
Full list of author information is available at the end of the article

Abstract

Background: The functionality of a cardiomyocyte is primarily measured by analyzing the electrophysiological properties of the cell. The analysis of the beating behavior of single cardiomyocytes, especially ones derived from stem cells, is challenging but well warranted. In this study, a video-based method that is non-invasive and label-free is introduced and applied for the study of single human cardiomyocytes derived from induced pluripotent stem cells.

Methods: The beating of dissociated stem cell-derived cardiomyocytes was visualized with a microscope and the motion was video-recorded. Minimum quadratic difference, a digital image correlation method, was used for beating analysis with geometrical sectorial cell division and radial/tangential directions. The time series of the temporal displacement vector fields of a single cardiomyocyte was computed from video data. The vector field data was processed to obtain cell-specific, contraction-relaxation dynamics signals. Simulated cardiomyocyte beating was used as a reference and the current clamp of real cardiomyocytes was used to analyze the electrical functionality of the beating cardiomyocytes.

Results: Our results demonstrate that our sectorized image correlation method is capable of extracting single cell beating characteristics from the video data of induced pluripotent stem cell-derived cardiomyocytes that have no clear movement axis, and that the method can accurately identify beating phases and time parameters.

Conclusion: Our video analysis of the beating motion of single human cardiomyocytes provides a robust, non-invasive and label-free method to analyze the mechanobiological functionality of cardiomyocytes derived from induced pluripotent stem cells. Thus, our method has potential for the high-throughput analysis of cardiomyocyte functions.

Keywords: Cardiomyocyte mechanic functionality, Velocity vector analysis, Minimum quadratic difference method

Introduction

The withdrawal of drugs already on the market is most commonly due to cardiac side effects. Cardiac safety analyses are currently done using animals as model organisms and/or ectopic expression of single ion channels in non-cardiac human cells [1]. These applications do not provide an optimal platform to explore the conditions in human cardiac cells. Unfortunately, human cardiomyocytes (CMs) have been very challenging to study, since the myocardial biopsy is a high-risk procedure and primary CMs dedifferentiate quickly and stop beating in cell culture conditions. Also, the available methods to measure the functionality of a cardiomyocyte (CM) are challenging and do not provide high throughput.

Moreover, recent developments in stem cell technology, namely the invention of induced pluripotent stem (iPS) cells, have increased the need for new methods to characterize cells derived from iPS cells. iPS cells can be obtained from any individual by reprogramming already differentiated mature cells such as skin fibroblasts into a pluripotent state [2]. Therefore, by using iPS cells it is possible to obtain genetically defined human pluripotent cells that can be differentiated into the cell type of interest, for example CMs [3]. Recently, it has been shown that human iPS cell-derived CMs have proper electrophysiological properties and assays using these cells can provide a reliable alternative to preclinical in vitro testing [4].

The functional measurement of single CMs has traditionally been laborious and time consuming. There are a few tools available for the study of the electrical properties of individual cells. Patch clamp is a commonly used method for analyzing the functionality of single CMs, but this technique requires special, relatively expensive instrumentation, and laborious manual work that requires highly skilled personnel [5]. Microelectrode arrays (MEA) provide a platform for the analysis of larger aggregates of cells with less manual work. Due to the dimensions of the electrodes and the distances between the electrodes, however, they are not suited for single cell functionality studies [6]. Voltage sensitive dyes such as di-8-ANEPPS provide one solution for the analysis of single CMs. This method, however, is based on fluorescence imaging and the dyes interact with some ion channels, e.g. the product of the human Ether-à-go-go-Related Gene (hERG), and thus potentially alter the electrophysiological properties of the cells [7].

The electrical functionality of single CMs does not directly reveal the mechanical properties of the cells. Atomic force microscopy (AFM) can be used to quantify the mechanical properties of CMs, e.g. force. However, AFM is not well suited for long-term measurements because it interferes with the cell [8]. Cellular electric impedance measured with well plate integrated electrodes is also used to measure the beating characteristics of cardiomyocytes [9]. The spatial resolution of the method is, however, not high enough to study the movements within the cell in detail. High-speed video microscopy can be used to obtain information from the beating cycle. Such methods quantify the movement of single CMs with no intervention. By analyzing the movements of the cells, it is possible to receive data from the mechanobiological functionality of the cell and to combine the data with electrical measurements to understand electro-mechanical coupling. Traditional video-based CM analysis methods [10,11] may not, however, be optimal for the study of single iPS cell-derived CMs. The sarcomere structure of iPS cell-derived CMs is not fully organized [12] and, therefore, their beating is less uniform with no main contraction direction. Thus, better methods are required that are robust in the detection of movement signals from these types of cells.

Here, we propose a robust, non-invasive method for the analysis of the beating dynamic of single CMs with no clear axis of contraction by using recorded microscope videos. The method is based on digital image correlation (DIC), more specifically its subtype the minimum quadratic difference (MQD) method that has been developed mainly for particle image velocimetry (PIV). Further, we use sectorial derivation of movement directions. The aim is to provide detailed physical information on the dynamics and timing of the contraction and relaxation of stem cell-derived CMs. The previous methods used to analyze video data [10,11] are not well suited for the analysis of heterogeneous beating. Our method is specifically aimed towards the use of CMs derived from iPS cells. We present validation tests of the method using artificial displacement images and current clamp recordings from human iPS cell-derived CMs. Since the CMs derived from the cell line used here have not previously been fully characterized, we also briefly provide the biological characterization data.

Materials and methods

Ethics statement

The study was approved by the Ethical Committee of the Pirkanmaa Hospital District (R08070). A written informed consent from participants has been obtained.

Cell culture

Primary fibroblasts were obtained from skin biopsy and cultured under fibroblast culturing conditions: Dulbecco's modified eagle medium (DMEM, Lonza, Switzerland) containing 10% FBS, 2 mmol/l L-glutamine and 50 U/ml penicillin/streptomycin. 293FT-cells (Invitrogen, CA, USA) were maintained similarly with 1% non-essential amino acids (NEAA, Cambrex, NJ, USA). Plat-E-cells (Cell Biolabs, CA, USA) and irradiated or mitomysin C (Sigma-Aldrich, MO, USA) treated mouse embryonic fibroblast (MEF, Millipore, MA, USA) cells were cultured in the same conditions but without antibiotics. iPS cells were cultured with MEF cells as feeders in KSR-medium: knockout (KO)-DMEM (Invitrogen) containing 20% KO-serum replacement (KO-SR, Invitrogen), NEAA, L-glutamine, penicillin/streptomycin, 0.1 mmol/L 2-mercaptoethanol, and 4 ng/ml basic fibroblast growth factor (bFGF, R & D Systems Inc., MN, USA).

iPS cells

iPS cell lines were established from the dermal fibroblasts of a 55 year old female using lentivirus infection followed by retrovirus infection into the fibroblasts. The following cells, plasmids and reagents were used: 293FT-cells, Plat-E-cells, pLenti6/UbC/mSlc7a1-vector (Addgene, MA, USA), ViraPower™ Packaging Mix (Invitrogen), Lipofectamine™ 2000 (Invitrogen), pMX retroviral vector (hOCT3/4, hSOX2, hKLF4 or hc-MYC, Addgene), and Fugene 6 (Roche Diagnostics, Germany). The full and detailed protocol has been described earlier [2,13]. Two iPS cell lines from the same individual were used for the studies: UTA.04602.WT and UTA.04607.WT.

Characterization of iPS cells

Reverse transcription polymerase chain reaction (RT-PCR). Total RNA was collected from the iPS cells at passage 6 and purified with a NucleoSpin RNA II -kit

(Macherey-Nagel, Germany). cDNA conversion was carried out with a high-capacity cDNA RT -kit (Applied Biosystems, CA, USA) using 200 ng of RNA. RT-PCRs were carried out with Dynazyme II (Finnzymes Oy, Finland) using 1 μl of cDNA as a template and 5 μM primers. As positive controls for exogenous primers, PCR was also carried out using the transfected plasmids (hOCT3/4, hSOX2, hKLF4, and hc-MYC) as templates. Primers and reaction conditions for iPS cell characterization [2] and PCR-primers for different germ layer markers [13] have been described earlier. β-actin and glyceraldehyde 3-phosphate dehydrogenase (GAPDH) were used as housekeeping control genes. **Immunocytochemistry for pluripotency.** iPS cells at passage 8 were fixed with 4% paraformaldehyde (PFA, Sigma-Aldrich) and stained with anti-Oct3/4 (1:400, R & D Systems), anti-TRA1-60 (1:200, Millipore), anti-Sox2, anti-Nanog, anti-SSEA4, and anti-TRA1-81 (all 1:200, Santa Cruz Biotechnology, CA, USA). The secondary antibodies (1:800, Invitrogen) were Alexa-Fluor-568-donkey-anti-goat-IgG, Alexa-Fluor-568-goat-anti-mouse-IgM, or Alexa-Fluor-568-donkey-anti-mouse-IgG. Vectashield mounting medium with DAPI (4′,6-diamidino-2-phenylindole, Vector Laboratories Inc., CA, USA) was used to stain nuclei. **Karyotype analysis.** A commercial company (Medix laboratories, Finland) defined the karyotypes of the iPS cell lines by using G-banding chromosome analysis according to standard protocol. **Formation of embryoid bodies (EBs).** EBs were cultured without feeder cells in EB-medium (KO-DMEM with 20% fetal bovine serum (FBS), NEAA, L-glutamine and penicillin/streptomycin) without bFGF for 5 weeks. RNA isolation and reverse transcription from the EBs was performed as described above. The expression of markers characteristic of ectoderm, endoderm, and mesoderm development in EBs was determined using RT-PCR (see above).

Cardiac differentiation and characterization

CM differentiation was performed by co-culturing iPS cells together with END-2-cells. END-2-cells were cultured as described earlier [14]. To initiate CM differentiation, undifferentiated iPS cell colonies were dissected mechanically into aggregates containing a few hundred cells and placed on the top of Mitomycin C -treated END-2 cells in KSR-culture medium without fetal bovine serum, serum replacement, or basic fibroblastic growth factor. Ascorbic acid (Sigma-Aldrich) was also added into the medium with a final concentration of 2.92 mg/ml [15]. The differentiating cell colonies were monitored by microscopy daily and the medium was changed after 5, 8, and 12 days of culturing. After 14 days, the 10% SR was added to the medium and ascorbic acid was no longer used. **RT-PCR for cardiac markers.** RNA was collected from beating cardiac cells and transcribed into cDNA as described for the pluripotent cells above. The reverse transcription polymerase chain reaction (RT-PCRs) were also carried out in a way similar to that of the pluripotency markers and primers of cardiac markers that have been described earlier [13]. **Immunocytochemical staining.** The spontaneously beating areas of the colonies were mechanically excised and treated with collagenase A (Roche Diagnostics) as described by Mummery et al. [14]. Seven days after dissociation, the cells were fixed with 4% paraformaldehyde for immunostaining with anti-cardiac-troponin-T (1:1500, Abcam, MA, USA), anti-α-actinin (1:1500, Sigma-Aldrich), anti-myosin-heavy-chain (MHC, 1:100, Millipore), anti-atrial-myosin-light-chain (MLC2a, 1:300, Abcam), and anti-ventricular-myosin-light-chain (MLC2v, 1:150, Abcam). The secondary antibodies (1:800, Invitrogen) were Alexa-Fluor-568-donkey-anti-goat-IgG, Alexa-Fluor-568-coat-anti-mouse-IgG, Alexa-Fluor-488-donkey-anti-rabbit, and Alexa-Fluor-488-donkey-anti-mouse. Vectashield mounting medium with DAPI was used to stain the nuclei. Dissociated CMs were prepared for video recording in the same way as for immunocytochemical staining.

Video microscopy

Videos of the dissociated spontaneously beating single CMs were recorded using video microscopy. Both iPS cell lines were used in the recordings and they gave identical results. Thirteen CMs were video-recorded for 30 s at 30 frames per second under sterile conditions. The CMs were visualized using a Nikon Eclipse TS100 (Nikon Corporation, Japan) microscope and monochrome 8 bit videos were acquired with an Optika DIGI-12 (Optika Microscopes, Italy) camera mounted on the microscope. Additionally, two CMs were videoed and their concurrent action potentials were acquired with current clamp measurement for combined functionality verification. In this series, a high resolution 14 bit Andor XION 885 (Andor Technology, UK) camera mounted on an Olympus IX51 (Olympus Corporation, Japan) microscope was used. Transmission images were acquired for 60 s at 50 frames per second using TILLvisION (TILL photonics GmbH, Germany).

Digital image correlation analysis

The term DIC refers to methods that acquire images and perform analysis for full-field shape, deformation and/or motion measurements [16]. The images are divided into small sub-regions where the grayscale values are cross-correlated between the consecutive image frames to provide a displacement map that indicates the movements of the scene [16]. Standard cross-correlation analysis emphasizes bright pixels due to the multiplication of intensity values [16]. In CM images, however, all image pixels regardless of their grayscale value can contribute to the motion analysis. Therefore, the weighting of bright pixels in the standard cross-correlation analysis is a clear disadvantage. In this study, we removed this disadvantage by using the MQD method [17] that puts equal weight to all image pixels. Additionally, MQD has been shown to be more accurate than other PIV evaluation methods based on correlation [18]. The MQD method was originally developed to evaluate PIV recordings. It uses a least-square principle to obtain the velocity vector field across the image based on two consecutive video frames [16]. Image sub-regions (i, j) are compared between the consecutive image frames (I_1 and I_2) using the function (1):

$$\mathrm{S}_{\mathrm{i,j}}(\mathrm{dx},\mathrm{dy}) = \sum_{x=-N/2}^{N/2}\sum_{y=-N/2}^{N/2}\left[I_1(i+x,j+y)-I_2(i+x+dx,j+y+dy)\right]^2, \tag{1}$$

where x and y are the indices to the pixels inside the sub-region of size [N, N]. The sub-region in the second frame I_2 is shifted in x- and y-directions by dx, dy to obtain a value at point (dx, dy) in the quadratic difference map $S_{i,j}$ of sub-region (i, j). The computational ranges of dx and dy can be freely selected to match the application. The location of the minimum value in $S_{i,j}$ reveals the medial displacement of the scene inside the sub-region (i, j). Due to small displacements between CM frames, the necessary sub-pixel accuracy in displacement estimation is obtained by sub-pixel fitting on the minimum value (dx, dy) in $S_{i,j}$ with a 1-dimensional 3-point Gaussian interpolation fitting function (2) to determine the correlation peak [19].

$$\Delta x = \frac{\ln(S(dx-1,dy)) - \ln(S(dx+1,dy))}{2[\ln(S(dx+1,dy)) - 2\ln(S(dx,dy)) + \ln(S(dx-1,dy))]},$$

$$\Delta y = \frac{\ln(S(dx,dy-1)) - \ln(S(dx,dy+1))}{2[\ln(S(dx,dy+1)) - 2\ln(S(dx,dy)) + \ln(S(dx,dy-1))]} \tag{2}$$

Cardiomyocyte analysis with MQD

Single CMs recorded on video were manually segmented for MQD analysis. The non-moving parts of the cell were cropped outside of the region of interest to decrease processing time and noise. To obtain a cell-specific coordinate system for the beating analysis, the beating focus point of the cell is selected by visual approximation from the video and the region of interest is divided into 8 sectors, each comprising a 45-degree sector from the beating focus (Figure 1A). This enables the analysis of the inconsistent beating patterns of iPS-derived CMs. For each velocity vector in a sector, two dot products are calculated. First with regard to the center line of the sector, to calculate the approximate radial component, and second with regard to the normal of the center line, to calculate the approximate tangential component (Figure 1B). The centerline normals pointing towards sectors 1–4 were selected for sectors 1–4, and the normals pointing towards 5–8 for sectors 5–8. For each sector, the sum of these vector components was calculated. In total, 16 different signals, 8 radial and 8 tangential signals, were obtained from a video.

The analysis was conducted using open source Matlab algorithm mpiv [20]. A 16×16 px subwindow size with a 0.5 overlap ratio was used. The resulting vectors were smoothed using a median filter. Possible stray vectors were determined and removed if the vector was outside the range of 2.5 times the standard deviation from the mean value. Kriging interpolation was used to assign values for vectors that did not have applicable values. Finally, weighting was used to smooth the vector field using a 3 × 3 kernel $\begin{matrix} 1 & 2 & 1 \\ 2 & 4 & 2 \\ 1 & 2 & 1 \end{matrix}$ as a low-pass filter.

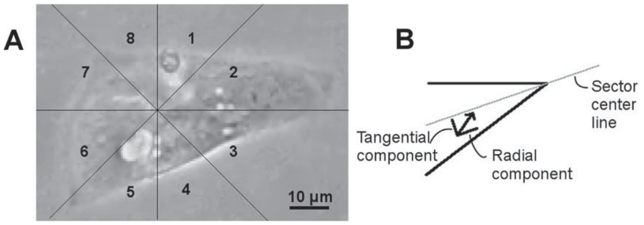

Figure 1 Beating analysis framework. A: The cell is divided into 8 sectors, each being of 45°, with the center point being at the observed beating focus point of the cell. The sectors are numbered in a clockwise manner. **B**: The radial and tangential components of the velocity vectors in each sector are calculated with regard to the sector centerline going through the beating focus point.

Data verification

The proposed beating analysis was verified using artificial displacement images. We modified still CM images so that they modeled the displacement of the pixels during CM beating with known displacement. An image distortion filter [21] was modified and used on a CM image to create artificial distortions that resembled the various stages of a beating iPS cell-derived CM with no main contraction axis. The resulting images were analyzed using the MQD method. Figure 2 illustrates the effect of the artificial distortion on an even grid image and on a CM image.

The artificial images for the video were constructed by stretching the cell with the distortion γ. Each point (x, y) in the original image within a set radius from the determined beating focus was mapped onto a virtual half-sphere of radius R, and a new distance X to the beating focus point was set-based on the desired distortion factor γ, as done in the original image distortion filter.

With this method, an image of a cell was modified with varying values of γ and combined to a video to get artificial cell data resembling that of a beating cell. Artificial images were created using 5 different γ values: −1, −2, −4, −7, and −10. The video was created from a total of 51 frames representing two beats that comprised 10 still frames, 5 frames with decreasing γ values, 5 frames with increasing γ values, 11 still frames, 5 frames with decreasing γ values, 5 frames with increasing γ values, and finally 10 still frames. Figure 2A shows an unmodified, original image of the cell and Figure 2B an image distorted using the explained method with γ = −10. The values of X define the displacement that can be compared with the results of the MQD analysis due to symmetry.

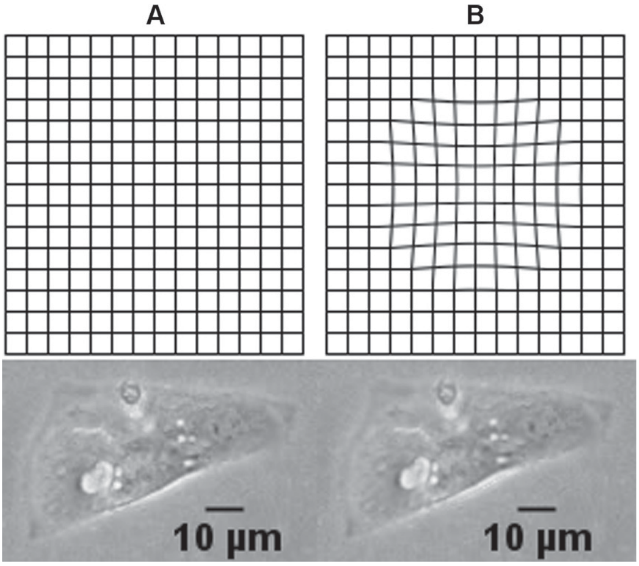

Figure 2 Artificial data set created from a cardiomyocyte image. An even grid and a cardiomyocyte image are shown to illustrate the effect of the artificial deformation that was used to create the data set. **A**: An even grid and a cardiomyocyte image without the artificial deformation. **B**: An even grid and a cardiomyocyte image with the described deformation applied, γ = 10.

Noise resistance testing

The noise resistance of the proposed method was tested by adding multiplicative speckle noise to each frame of the generated artificial video data that was obtained from modifying a CM image, as explained above. The cell size was 6796 pixels. Speckle noise was added to each image using the equation $J = I + \sqrt{12 * V} * I * I_r$, where I is the original image, J is the resulting image, V is variance and I_r is uniformly distributed random noise between values −0.5 and 0.5, with mean of 0. 8. The following noise variances were used: 0, 0.03, 0.05, 0.07, 0.09, 0.011, 0.013, and 0.015.

Beating analysis of cardiomyocytes

The analysis was carried out for the 13 CMs recorded on video. The time required for each phase of beating was measured: the contraction, the time it stayed contracted, the relaxation time, and the time it stayed relaxed. The beating frequency was also measured.

Current clamp measurement

To further verify the findings, the proposed video analysis was conducted from video data recorded from iPS cell-derived CMs with concurrent current clamp measurement. Action potentials were recorded using the Axopatch 200B patch clamp amplifier connected to an acquisition computer via AD/DA Digidata 1440 (Molecular devices, USA). The measurement was carried out at room temperature in gap free mode using the standard current clamp configuration in perforated patch mode. The HEPES (4-(2-hydroxyethyl)-1-piperazineethanesulfonic acid)-based extracellular perfusate for current clamp recordings comprised (in mmol/l): 143 NaCl, 5 KCl, 1.8 $CaCl_2$, 1.2 $MgCl_2$, 5 glucose, and 10 HEPES. The pH was adjusted to 7.4 with NaOH and the osmolarity set to 300 ± 2 mOsm (Gonotec, Osmomat 030, Labo Line Oy, Finland). The intracellular solution comprised (in mmol/l): 122 $KMeSO_4$, 30 KCl, 1 $MgCl_2$, and 10 HEPES. KOH was used to set pH to 7.15 and the osmolarity was set to 295 ± 2 mOsm. Amphotericin B (Sigma-Aldrich) was used as a membrane perforation agent and was dissolved in dimethyl sulfoxide to a final concentration in the patch pipette of 0.24 mg/ml. Current-clamp recordings were digitally sampled at 20 kHz and filtered at 5 kHz using the lowpass Bessel filter on the recording amplifier.

Combining current clamp and video analysis

TTL synchronization pulses (1 pulse per frame) were delivered by the digital signal processor-driven imaging control unit (programmed in TILLvisION) to synchronize the transmission frames and current clamp data sampling. The pulses and current clamp data were concurrently sampled using 2 channels in current clamp. The video data obtained simultaneously with the current clamp measurement was processed using the proposed method.

Results

Characterization of induced pluripotent stem cells

The generated iPS cells were first characterized by the morphology of the cell colonies and the individual cells that exhibited similar characteristics to those of human embryonic stem cells: compact and round in shape (Figure 3A), defined edges and distinct cell borders (Figure 3B). The iPS cells also expressed endogenous pluripotent marker genes at the

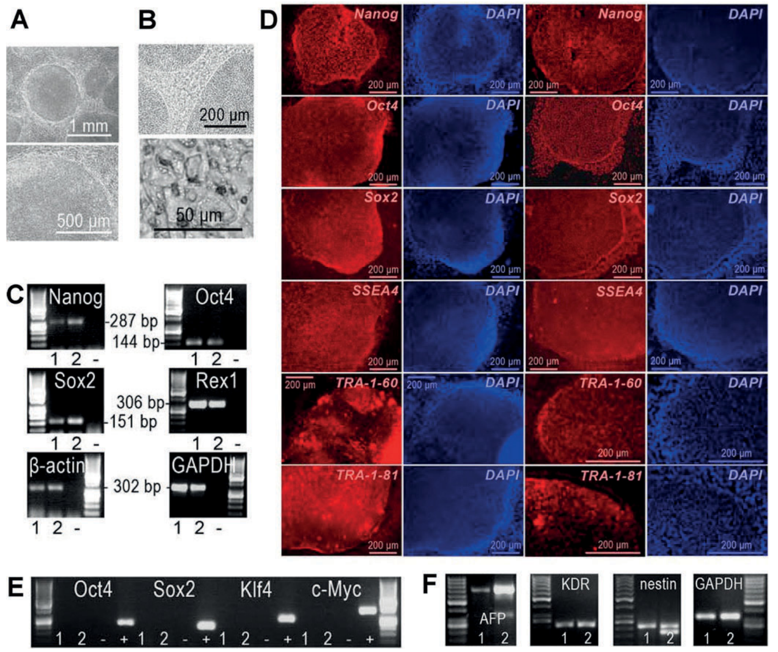

Figure 3 Characterization of iPS cells for their pluripotency. Number 1 represents the cell line UTA.04602.WT and 2 the line UTA.04607.WT. **A**: iPS cells formed typical colonies for pluripotent stem cells that are rather compact and round in shape. **B**: The iPS cell colonies typically had well defined edges and distinct cell borders, and the iPS cells had a high nucleus to cytoplasm -ratio and a large nucleoli characteristic for stem cells. **C**: Endogenous pluripotency gene expression was studied using RT-PCR. Nanog, Oct4, Sox2 and Rex1 were all expressed at mRNA level in the iPS cells. β-actin and GAPDH were used as housekeeping control genes for both endogenous and exogenous markers. **D**: The expression of pluripotency genes was also studied at the protein level by immunocytochemical staining. The iPS cell expressed several markers for the pluripotent state: Nanog, Oct4, Sox2, SSEA4, TRA-1-60, and TRA-1-81 (all in red). Pictures in the left panel are from the line UTA.04602.WT and the ones on the right side are from UTA.04607.WT. Blue in all pictures indicates the DAPI staining of nuclei. **E**: Using RT-PCR, it was shown that all the transgenes were silenced in the iPS cells. Negative control is marked with "-" and positive control with "+". **F**: Embryoid body (EB) -assay was used to define the pluripotency of the iPS cells *in vitro*. Markers for all three germ layers were detected from the EBs formed from both cell lines. Alpha-fetoprotein (AFP) was used as a marker for endoderm, kinase insert domain receptor (KDR, also known as vascular endothelial growth factor receptor 2 (VEGFR-2) was used as a marker for mesoderm and nestin was used as an ectoderm marker. GAPDH was used as an endogenous control gene.

mRNA level that was shown by RT-PCR (Figure 3C). The expression of pluripotency genes also at the protein level was demonstrated by the immunocytochemical staining of different markers for pluripotent stem cells (Figure 3D). On the other hand, transgene expression was turned off in the iPS cells (Figure 3E). To confirm the pluripotent state of the iPS cells, an EB formation assay was carried out. The cells from the EBs were shown to express marker genes from all three germ layers: endoderm, ectoderm, and mesoderm (Figure 3F). The generated cell lines were also analyzed for their karyotypes and were both found to be normal (Figure 4A and B).

Characterization of the cardiomyocytes differentiated from iPS cells

Generated iPS cells were differentiated into spontaneously beating CMs that expressed different cardiac markers. Using RT-PCR, it was shown that troponin T (TNTT2),

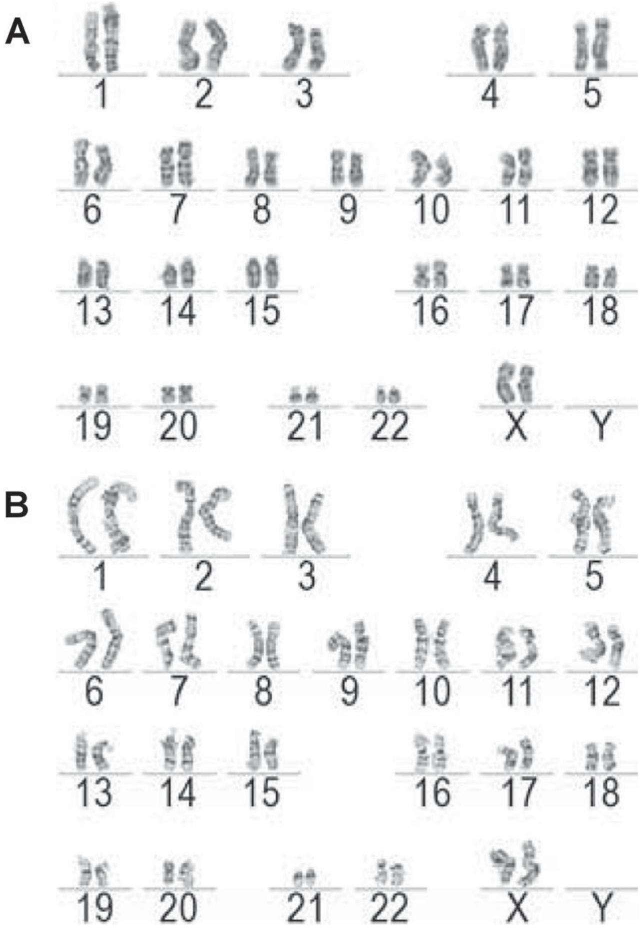

Figure 4 Karyotype analysis from iPS cells. A & **B**: The lines were verified for normal karyotypes (G: UTA.04602.WT and H: UTA.04607.WT).

MLC2v, MLC2a, connexin-43 (Cx-43), myosin heavy chain (MYH7), hERG, and GATA4 were expressed in the cells (data not shown for hERG and GATA4) (Figure 5A). The expression of cardiac marker genes at the protein level was also confirmed (Figure 5B). With immunocytochemical staining, it was also shown that both atrial and ventricular cells were present among the iPS cell-derived CMs (data not shown). The electrical properties of the iPS cell-derived CMs were also characterized using a microelectrode array that revealed that the cell aggregates exhibited appropriate beating rates and field potentials (Figure 5C and D).

Beating signals of iPS cell-derived CMs

The method was applied on iPS-derived CMs to obtain beating signals. One such signal that shows two beats is shown in Figure 6A. For radial components, contraction was

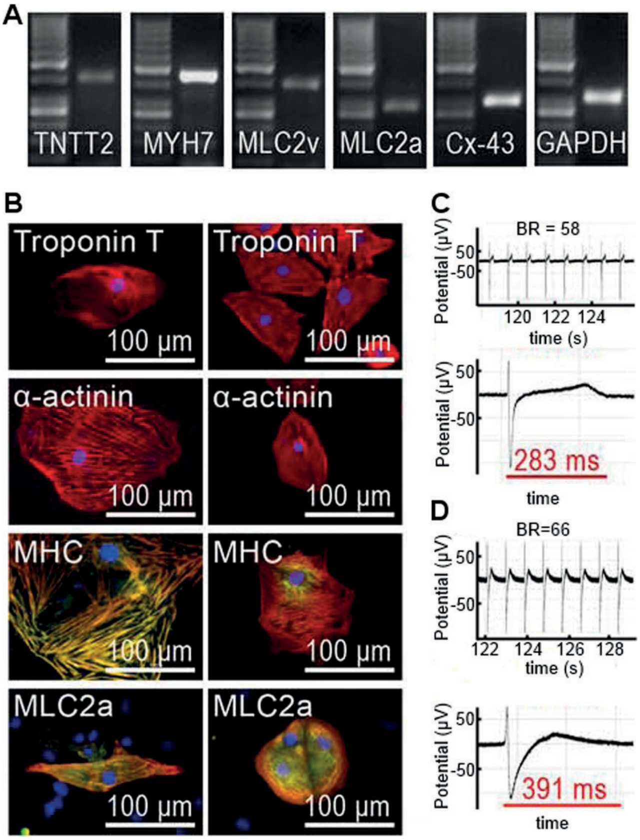

Figure 5 Cardiomyocytes differentiated from the iPS cells. A: Several cardiac markers were discovered using RT-PCR indicating their expression at mRNA level. Data from UTA.04602.WT is shown here. **B**: By immunocytochemical staining it was shown that the iPS cell-derived cardiac cells express proteins specific for cardiomyocytes. Cardiac troponin T, α-actinin, myosin heavy chain (MHC) and atrial myosin light chain 2 (MLC2a) were detected from the cells. The pictures on the left side are from the line UTA.04602.WT and the pictures on the right side are from UTA.04607.WT. In the pictures showing MHC and MLC2a with green fluorescent, red indicates troponin T and in all pictures DAPI staining of nuclei is seen in blue. **C** & **D**: A micro electrode array (MEA) was used to define the electrical properties of the iPS cell-derived cardiomyocytes. The beating rates (BR) and field potential durations (FPD) of cell aggregates were evaluated (B: UTA.04602.WT, BR = 58, FPD = 283 ms and C: UTA.04607.WT, BR = 66, FPD = 391 ms).

defined negative (Figure 6A II) and relaxation positive (Figure 6A III). Figure 6B illustrates a typical signal.

From the 13 measured cells, the time parameters of the different phases of the beating were calculated from the sum displacement signal using the proposed method. The phases were the following: contraction, time the cell was contracted, relaxation, and the time the cell was relaxed. The average values of three analysis signals for each cell were calculated. The results for each cell measurement are presented in Table 1.

Figure 6C shows all 16 velocity signals obtained from one of the measured cells.

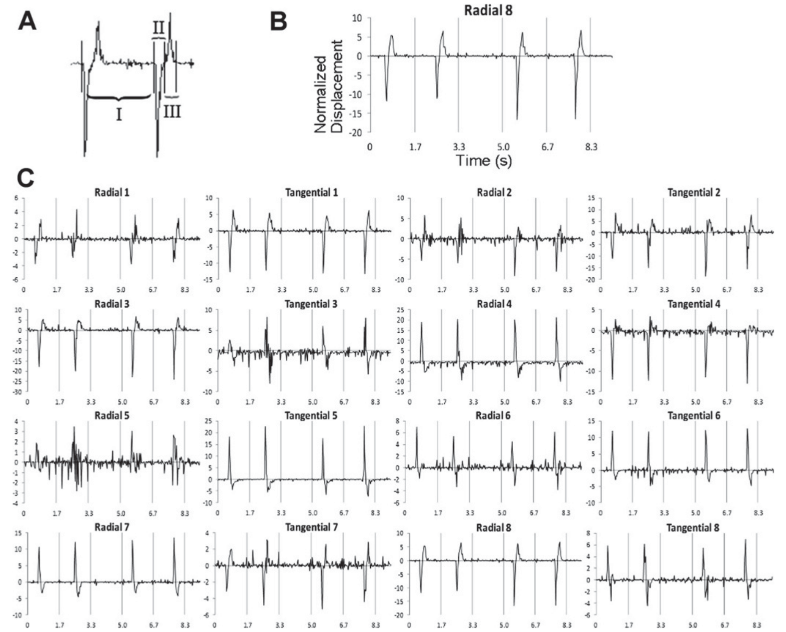

Figure 6 The beating signals obtained from an iPS cell-derived CM. A: The classification of beating phases. The time between each individual beat is marked with I. Contraction movement is defined as negative movement (marked with II) and relaxation movement as positive (marked with III). **B**: An enlarged image of the sector 8 radial component. **C**: The beating signals of each sector obtained from one of the measured CMs. For various sectors, the contraction seems to push certain areas away from the perceived beating focus point. This results in an upward peak in lieu of a downward peak due to the fusiform nature of the beating. While most sectors produce a signal of high quality, sectors such as radial 5 have too little movement to generate a well-formed displacement signal.

Method verification using artificial displacement images

The DIC analysis results created using artificial displacement images are illustrated in Figure 7. The figure shows (A) the division of the cell into analysis sectors, (B) the displacement vector field during the contraction phase, (C) the known displacement velocity, and (D) the results of the DIC analysis (red) shown with the known displacement velocity (blue). The average correlation coefficient between the known displacement field and the analysis results for all 16 signals was 0.9525.

For noise resistance testing, 8 videos with speckle noise were created using different noise variances. The proposed analysis was applied to these videos. For each video, 3 segments were chosen. The average correlation between the resulting signals and the known displacement was calculated as a function of noise variance. The results for three different sectors are shown in Table 2. Example images of different noise levels are shown in Figure 8A-D.

Comparison with current clamp recording

Spontaneously beating iPS cell-derived CMs had the characteristics of ventricular- type cells. The cells were beating individually and not part of a larger beating cell cluster.

Table 1 Multiple cell analysis

Cell	Frequency (bpm)	Contraction (ms)	Contracted (ms)	Relaxation (ms)	Relaxed (ms)
1	12.03	451	18	571	3949
2	18.20	419	0	612	2265
3	22.78	321	0	444	1868
4	23.64	360	1	447	1730
5	24.12	164	0	202	2122
6	24.56	427	8	535	1472
7	25.98	179	0	346	1784
8	26.34	225	13	594	1446
9	29.13	225	0	318	1517
10	36.45	267	1	324	1053
11	41.82	216	3	295	921
12	43.13	274	30	361	727
13	66.34	209	7	315	373

Results obtained from multiple cell analysis. The times of the different beating phases in milliseconds and the corresponding beats per minute (bpm) were measured from 13 cells.

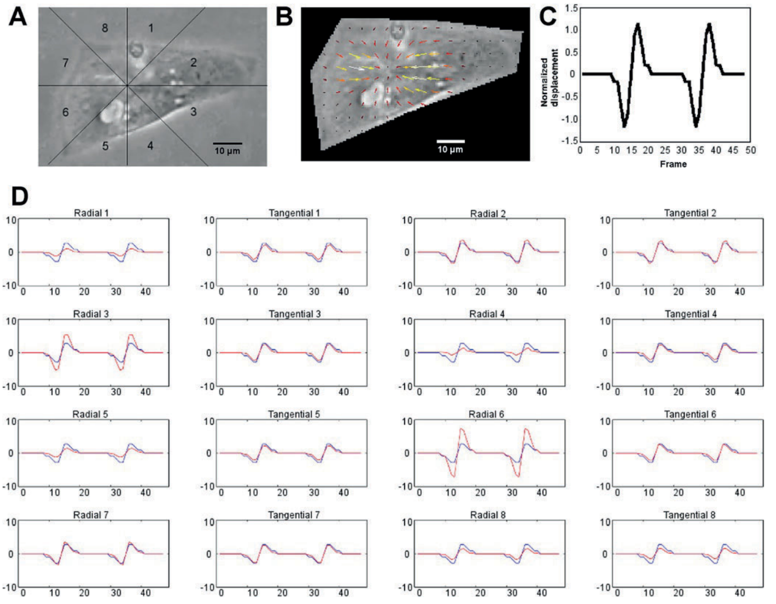

Figure 7 Comparison of measured and known motion signals in different sectors. A CM image was modified using image-processing methods with varying parameters to create a video resembling the contraction and relaxation of the cell. In the upper row are illustrated **A**: the sector division, **B**: the velocity vector field during the contraction, and **C**: the known displacement velocity. Since the artificial displacement has circular symmetry, a horizontal cross-sectional displacement is shown. **D**: The proposed method was applied to the video data and the signal marked with red was obtained. A blue signal illustrates the known displacement field.

Table 2 Analysis result correlation with known displacement

	Radial component 1		Radial component 3		Radial component 5	
Noise variance	**AVG**	**SD**	**AVG**	**SD**	**AVG**	**SD**
0	0.964	0.000	0.952	0.000	0.939	0.000
0.003	0.922	0.034	0.956	0.005	0.781	0.150
0.005	0.761	0.111	0.950	0.013	0.532	0.152
0.007	0.480	0.364	0.926	0.076	0.359	0.389
0.009	0.490	0.177	0.894	0.050	0.456	0.209
0.011	0.423	0.342	0.671	0.310	0.334	0.228
0.013	0.183	0.385	0.441	0.250	0.325	0.324
0.015	0.259	0.335	0.435	0.440	−0.041	0.410

The average correlations (AVG) of the analysis results with the known displacement field and their standard deviations (SD). Noise with variances ranging from 0 to 0.015, with example images shown in Figure 6A-D, was added to video frames that comprised the artificial displacement images of a cardiomyocyte. The average correlation of 8 videos between the analysis results and the known displacement was determined, along with the standard deviation.

The velocity vector data was integrated with respect to time in order to obtain position data, and compared with the current clamp data to see the relationship between the mechanical and electrical activity. The time between the peaks of electrical activity and mechanical activity was calculated from the synchronized data.

The DIC signal onset occurred after the action potential onset and the action potential declined earlier. Figure 9 shows both signals from one of the recorded cells in the same graph. The basic action potential parameters for the recorded cell are listed in Table 3. The time difference between the peaks of action potentials and the maximum displacement was 306 ms with a 40 ms standard deviation. The result is in line with previously reported values [22].

Discussion

We developed a microscope video analysis method to provide accurate and detailed information on the beating motion dynamics of single CMs, especially those derived from stem cells. We observed that our DIC-based methods are promising for the study of

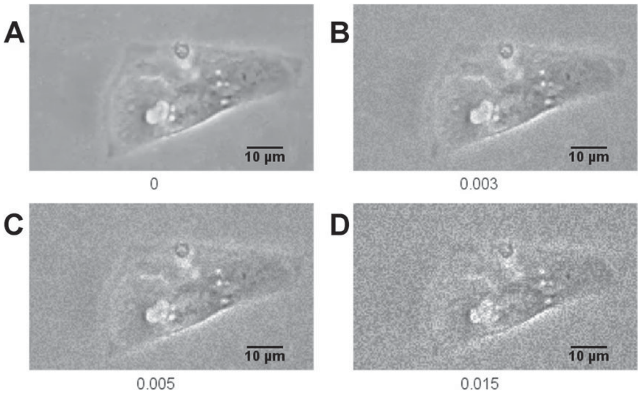

Figure 8 Assessment of the effect of noise on video beating analysis. Varying degrees of speckle noise variance were added to a video for testing noise resistance. **A-D**: Example images for four noise variance levels are shown: 0, 0.003, 0.005, and 0.015.

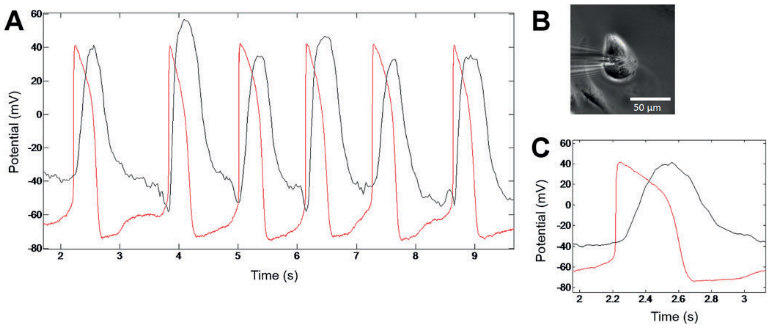

Figure 9 Combined current clamp and displacement data for a cell. A: Concurrent action potential and displacement signal, integrated with respect to time from the movement data obtained from the video data, are plotted in the same figure. The action potential data is shown in red and the movement data in black. For current clamp data, the potential in mV is shown, whereas for movement data, the y-axis is arbitrary. **B**: Image from the video data used for the analysis of a CM being recorded with current clamp. **C**: An enlarged part of the signal showing the time difference between the action potential and the displacement signal.

the mechanical functions of CMs because they enable the cell geometry-based beating parameters of cells to be calculated. Previously, DIC had been used for the analysis of cell cultures [11] and the morphogenesis of the heart and changes in blood flow during embryogenesis [23]. The displacement vector analysis approach has also been used for the analysis of the motion of living embryos [24]. In these *in vivo* studies, fluorescent particles were injected into the embryos and the motion of the particles inside the heart was analyzed. Our method does not require the invasion of the cell or the use of an artificial tracer and can be used for detailed single cell analysis.

DIC was found to be a viable complement to electrical studies in CM research. In this study, we demonstrated that MQD can be successfully used to analyze single beating CMs. Further, dividing the cell into sectors and calculating the radial and tangential signals for different parts of the cell provides a way to derive basic cell motion directions and thus motion signals related to cell geometry. This enabled the robust detection of all movements. This is especially important for iPS cell-derived CMs that do not beat as uniformly as fully matured native CMs. As also shown here, the beating does not have a main contraction axis and the beating shows fusiform characteristics.

In comparison to other similar methods that analyse contraction [10,11], our analysis that uses a sector approach is advantageous for iPS cell-derived CMs that lack the well-organized structure of mature native cells. Our results show that the eight sectors and directional components provide signals that can be used to analyze the mechanical behavior of an IPS cell-derived CM. Because it does not depend on mathematical estimators such as the principal components of motion vectors, the method is simple and

Table 3 Action potential parameters

Unpatched (bpm)	Patched (bpm)	Vmax (dV/dT)	APD10 (ms)	APD50 (ms)	APD90 (ms)	APA (mV)
39	42.52	43.08	97.67	279.53	371.00	116.30

CM action potential parameters in current clamp experiment. Beats per minute (bpm) for unpatched and patched cells are listed. Maximal rise velocity (Vmax), action potential durations at 10%, 50% and 90% of repolarization (APD10, APD50, and APD90, respectively), and action potential amplitude (APA) are listed.

robust. In our method dividing the cell into sectors depends on the visual selection of the beating focus point. While this approach allows flexibility in analysis, it could result in a source of user based error. As the optimal selection of the beating focus point is not inherently clear, automated methods for beating focus point detection well warranted.

Our results indicate that our method provides a reliable signal, and the results of the simulated data show that the method performs well in challenging noise conditions. The sector analysis withstood noise very well and provided high correlation figures compared to simulated movements. In addition, the speckle noise applied in the noise resistance provides a good approximation of video noise. The simulation results indicate that our method is also applicable with relatively low quality video data and that the standard cameras used in microscopes are capable of producing video data that can be used for reliable motion analysis.

We used current clamp, considered as a gold standard for the analysis of single CMs [25] as a reference method to verify the timing of beating. The region of interest for the analysis was partly hampered by the patch pipette that blocked a large part of the view to the cell. Still, the mechanical behavior of the beating cells, which corresponded to electrical activity measured with current clamp, could be detected with the MQD method with good accuracy. Furthermore, we observed that the beating of the cell during the patching was noticeably weaker indicating that patching can alter the function. Thus, non-invasive and non-label methods such as those presented here are well warranted for the detailed functional analysis of CMs.

Some issues should be taken into account when making the video recordings and the motion analysis. For example, the cells in our test were of varying sizes and, despite our best efforts, the video focus was not uniform for all cells. In some videos, noise in the recording and video packing artifacts caused noise in the motion analysis signal. This was especially observed for the cells that had weak beating, videos that were slightly out of focus, and cells that had a uniform surface pattern. The calculated contraction and relaxation times for different cells were, however, similarly proportioned despite the noise. Based on these findings, it can be stated that high quality recordings are not required. Since the method creates the signal based on the moving patterns inside the cell, it can also provide a good signal when the cell is attached to the surface and the outline does not move.

In many cases, the dissociated CMs are attached to the bottom of the culture plate in such a way that the outline of the cell does not move and the movement can only be seen by observing the moving patterns inside the cell. Some cells, however, also had a moving outline. As a result, the cells have varying and fusiform movement patterns. However, our method was able to derive the movement dynamics of all these cells by using the cell geometry-based sectorial and directional summation of the PIV vectors. The sectorial approach has specific benefits for the analysis of cells such as stem cell-derived CMs with varying and inhomogeneous movement patterns inside the cells or with a lack of a main axis of contractility. Due to these reasons, quantifying the extent of the contraction or contractility of the dissociated CMs derived from iPS cells, e.g. in pixels per time unit or movement in micrometers, is not meaningful.

Conclusions

MQD analysis using a sector approach provides a novel way for the non-invasive and non-labeled function analysis of the biomechanics of CMs, especially those derived from stem cells. Motion analysis in general has clear advantages over other existing methods: it requires very little training for personnel, it does not require external hardware apart from a microscope and a video camera, it can be used for high throughput screening, and it is non-invasive and label-free. Motion analysis can also reveal information that is beyond the electrical properties and ion movements of the cardiac cells such as actual biomechanical timing and possible intracellular motion defects. Motion analysis is, therefore, an important addition to any electrical study. Moreover, the motion analysis method may provide an important addition to the traditional way of studying cell functionality, especially the actual mechanical movement, namely the timing of contraction and relaxation of CMs. Our method is especially designed to provide robust motion information from fusiform inhomogeneously beating dissociated CMs derived from stem cells.

In conclusion, these capabilities in conjunction with improved stem cell technologies that produce patient specific cell lines make the proposed system a good candidate for high throughput drug screening, safety analysis, and the basic studies of cardiac diseases using stem cell-derived CMs.

Abbreviations

AFP: Alpha-fetoprotein; AFM: Atomic force microscopy; APA: Action potential amplitude; APD: Action potential duration; AVG: Average correlation; bFGF: Basic fibroblast growth factor; BR: Beating rate; CM: Cardiomyocyte; Cx-43: Connexin-43; DAPI: 4′,6-diamidino-2-phenylindole; DIC: Digital image correlation; DMEM: Dulbecco's modified eagle medium; EB: Embryoid body; FBS: Fetal bovine serum; FPD: Field potential duration; GAPDH: β-actin and glyceraldehyde 3-phosphate dehydrogenase; HEPES: 4-(2-hydroxyethyl)-1-piperazineethanesulfonic acid; hERG: Human ether-à-go-go-related gene; iPS: Induced pluripotent stem; KDR: Kinase insert domain receptor; KO: Knockout; KO-SR: Knockout serum replacement; KSR: Knockout serum replacement -medium; MEA: Micro electrode array; MEF: Mouse embryonic fibroblast; MHC: Myosin-heavy-chain; MLC2a: Atrial myosin light chain; MLC2v: Ventricular myosin light chain; MQD: Minimum quadratic difference; MYH7: Myosin heavy chain; NEAA: Non-essential amino acids; PFA: Paraformaldehyde; PIV: Particle image velocimetry; RT-PCR: Reverse transcription polymerase chain reaction; SD: Standard deviation; TNTT2: Troponin T; VEGFR-2: Vascular endothelial growth factor receptor 2.

Competing interests

A patent application concerning the method has been filed. There are no other conflicts of interests.

Authors' contributions

AA developed and tested the method, analyzed the videos, modeled the artificial beating and drafted the manuscript. AK conducted the iPS cell production, CM differentiation and characterization, recorded the videos, and drafted the applicable parts of the manuscript. She also observed the need for the method. KL conducted the patch clamp experiment and drafted the applicable parts of the manuscript. MH participated in conception of the method and assisted with manuscript drafting. KA-S and JH participated in the development of the method, the design and coordination of the study, and helped to draft the manuscript. KA-S also participated in formulating the original necessity for the method. All authors read and approved the final manuscript.

Acknowledgements

We would like to thank Prof. Mummery (Hubrecht Institute, Utrecht, The Netherlands) for providing the END-2 cells for co-culturing.
This study was funded partly by personal research grants from Finnish Cultural Foundation, Pirkanmaa Regional Fund; Tampere Graduate Program in Biomedicine and Biotechnology, Institute of Biomedical Technology, University of Tampere, Finland; Stemfunc project funded by the Academy of Finland (decision number 122947); Human spare parts project funded by Finnish Funding Agency for Technology and Innovation (TEKES); Finnish Foundation for Cardiovascular Research; Pirkanmaa hospital district (EVO).

Author details

[1]Computional Biophysics and Imaging Group, Department of Electronics and Communications Engineering, and BioMediTech, Tampere University of Technology, Tampere, Finland. [2]Heart Group, BioMediTech, University of Tampere, Tampere, Finland. [3]Pixact Oy, Postitorvenkatu 16, FI-33840 Tampere, Finland. [4]Heart Hospital, Tampere University Hospital, Tampere, Finland. [5]Medical School, University of Tampere, Tampere, Finland.

Received: 23 September 2013 Accepted: 1 April 2014
Published: 7 April 2014

References

1. Pollard C, Valentin JP, Hammond T: **Strategies to reduce the risk of drug-induced QT interval prolongation: a pharmaceutical company perspective.** *Br J Pharmacol* 2008, **154:**1538–1543.

2. Takahashi K, Tanabe K, Ohnuki M, Narita M, Ichisaka T, Tomoda K, Yamanaka S: **Induction of pluripotent stem cells from adult human fibroblasts by defined factors.** *Cell* 2007, **131:**861–872.
3. Zhang J, Wilson GF, Soerens AG, Koonce CH, Yu J, Palacek SP, Thomson JA, Kamp TJ: **Functional cardiomyocytes derived from human induced pluripotent stem cells.** *Circ Res* 2009, **104:**e30–e41.
4. Harris K, Aylott M, Cui Y, Louttit JB, McMahon NC, Sridhar A: **Comparison of electrophysiological data from human-induced pluripotent stem cell-derived cardiomyocytes to functional preclinical safety assays.** *Toxicol Sci* 2013, **134:**412–426.
5. Brüggemann A, Stoelzle S, George M, Behrends JC, Fertig N: **Microchip technology for automated and parallel patch-clamp recording.** *Small* 2006, **2:**840–846.
6. Braeken D, Huys R, Jans D, Loo J, Severi S, Vleugels F, Borghs G, Callewaert G, Bartic C: **Local electrical stimulation of single adherent cells using three-dimensional electrode arrays with small interelectrode distances.** *Conf Proc IEEE Eng Med Biol Soc* 2009, **2009:**2756–2759.
7. Novakova M, Bardonova J, Provaznik I, Taborska E, Bochorakova H, Paulova H, Horky D: **Effects of voltage sensitive dye di-4-ANEPPS on guinea pig and rabbit myocardium.** *Gen Physiol Biophys* 2008, **27:**45–54.
8. Liu J, Sun N, Bruce MA, Wu JC, Butte MJ: **Atomic force mechanobiology of pluripotent stem cell-derived cardiomyocytes.** *PLOS ONE* 2012, **7:**e37559.
9. Peters MF, Scott CM, Ochalski R, Dragan YP: **Evaluation of cellular impedance measures of cardiomyocyte cultures for drug screening applications.** *Assay Drug Dev Technol* 2012, **10:**525–532.
10. Hayakawa T, Kunihiro T, Dowaki S, Uno H, Matsui E, Uchida M, Kobayashi S, Yasuda A, Shimizu T, Okano T: **Noninvasive evaluation of contractile behaviour of cardiomyocyte monolayers based on motion vector analysis.** *Tissue Eng Part C* 2012, **18:**21–32.
11. Kamgoué A, Ohayon J, Usson Y, Riou L, Tracqui P: **Quantification of cardiomyocyte contraction based on image correlation analysis.** *Cytometry A* 2009, **75:**298–308.
12. Xi J, Khalil M, Shishechian N, Hannes T, Pfannkuche K, Liang H, Fatima A, Haustein M, Suhr F, Bloch W, Reppel M, Saric T, Wernig M, Jänisch R, Brockmeier K, Hescheler J, Pillekamp F: **Comparison of contractile behavior of native murine ventricular tissue and cardiomyocytes derived from embryonic or induced pluripotent stem cells.** *FASEB J* 2010, **24:**2739–2751.
13. Lahti AL, Kujala VJ, Chapman H, Koivisto AP, Pekkanen-Mattila M, Kerkelä E, Hyttinen J, Kontula K, Swan H, Conklin BR, Yamanaka S, Silvennoinen O, Aalto-Setälä K: **Model for long QT syndrome type 2 using human iPS cells demonstrates arrhythmogenic characteristics in cell culture.** *Dis Model Mech* 2012, **5:**220–230.
14. Mummery C, Oostwaard DW, Doevendans P, Spijker R, van den Brink S, Hassink R: **Differentiation of human embryonic stem cells to cardiomyocytes: role of coculture with visceral endoderm-like cells.** *Circulation* 2003, **107:**2733–2740.
15. Takahashi T, Lord B, Schulze PC, Fryer RM, Sarang SS, Gullans SR, Lee RT: **Ascorbic acid enhances differentiation of embryonic stem cells into cardiac myocytes.** *Circulation* 2003, **107:**1912–1916.
16. Sutton MA, Orteu JJ, Schreier HW: *Image Correlation for Shape, Motion and Deformation Measurements.* New York: Springer-Verlag; 2009.
17. Gui L, Merzkirch W: **A method of tracking ensembles of particle images.** *Exp Fluids* 1996, **21:**465–468.
18. Gui L, Merzkirch W: **Comparative study of the MQD method and several correlation-based PIV evaluation methods.** *Exp Fluids* 2000, **28:**36–44.
19. Willert C, Gharib M: **Digital particle image velocimetry.** *Exp Fluids* 1991, **10:**181–193.
20. Mori N, Chang KA: **Introduction to MPIV.** http://www.oceanwave.jp/softwares/mpiv/.
21. Kroon DJ: **Pinch and Spherize Filter.** http://www.mathworks.com/matlabcentral/fileexchange/22573.
22. Bers DM: *Excitation-contraction Coupling and Cardiac Contractile Force – Second Edition.* Dordrecht, The Netherlands: Kluwer Academic Publishers; 2001.
23. Ohn J, Tsai HJ, Liebling M: **Joint dynamic imaging of morphogenesis and function in the developing heart.** *Organogenesis* 2009, **5:**248–255.
24. Lu J, Pereira F, Fraser S, Gharib M: **Three-dimensional real-time imaging of cardiac cell motions in living embryos.** *J Biomed Opt* 2008, **13:**014006.
25. Kornreich B: **The patch clamp technique: principles and technical considerations.** *J Vet Cardiol* 2007, **9:**25–37.

doi:10.1186/1475-925X-13-39
Cite this article as: Ahola *et al.*: Video image-based analysis of single human induced pluripotent stem cell derived cardiomyocyte beating dynamics using digital image correlation. *BioMedical Engineering OnLine* 2014 **13**:39.

PUBLICATION
II

Motion Analysis Method for Determining Cardiomyocyte Beating Properties Based on Digital Image Correlation and Templates

Ahola, A., Pradhapan P., Laurila E., Aalto-Setälä, K. & Hyttinen, J.

Proceedings of Computing in Cardiology (2014), 41:1137-1140

Motion Analysis Method for Determining Cardiomyocyte Beating Properties Based on Digital Image Correlation and Templates

Antti Ahola[1§], Paruthi Pradhapan[1§], Eeva Laurila[2], Katriina Aalto-Setälä[2,3], Jari Hyttinen[1]

[1]Computational Biophysics and Imaging Group, Department of Electronics and Communications Engineering, and BioMediTech, Tampere University of Technology, Tampere, Finland
[2]Heart Group, BioMediTech, University of Tampere, Tampere, Finland
[3]Heart Hospital, Tampere University Hospital, Tampere, Finland
[§]Authors with equal contribution

Abstract.

Video-based analysis of cardiomyocytes provides a non-invasive and label-free method of analyzing their beating characteristics. Here, we aim to demonstrate that defining averaged signal templates can improve the determination of cardiomyocyte beating characteristics.

Video recordings of human iPSC derived cardiomyocytes were performed. Beating patterns from different sectors of the cell were calculated from displacement vector fields using our in-house developed digital image correlation based video analysis method. A cross-correlation template based average waveform was computed for individual cell sectors, representing their beating characteristics. We also studied the effect of video sampling frequency and video duration on template formation to optimize the recording process.

By comparing the average waveforms from different sectors, we observed the fusiform nature of iPSC derived cardiomyocytes. Our results indicate that using templates allows minimizing measurement time. However, then the sampling frequency should be at least 60 Hz, for high quality single cell dynamics.

To conclude, the sector approach is beneficial for analysis of iPSC derived cardiomyocytes. Also, the presented methods improve the parameterization of the signal.

1. Introduction

The development of induced pluripotent stem cells (iPSC) has opened new avenues for in-vitro modelling of disease conditions and drug screening. With the advent of these new applications, there is an increased need for novel analysis methods. We have shown before [1] that video-based microscopy measurements provide a feasible, non-invasive and label-free method for measuring beating dynamics of human iPSC derived cardiomyocytes (CMs). As the sarcomeric structure of iPSC derived CMs is not fully organized [2], the displacement of cell is far from the uniform beating of the mature CM and thus traditional methods are not well suited for them.

Analyzing the mechanical functionality of single CMs has traditionally been a laborious and time consuming task. Atomic force microscopy and cellular electric impedance methods can be used to quantify the mechanical properties of the cells, but they are not well suited for long term measurements with high spatial resolution. Video-based methods provide a non-invasive way of analyzing CM beating dynamics. We have previously presented a digital image correlation (DIC) method [1] for the analysis of single CMs.

The aim of this study is to demonstrate the use of template matching in signals obtained by video analysis of CMs. We have shown that cross-correlation based template matching accurately and consistently determines differences in beating properties of CMs [3]. In this study, our aim is to establish inter-sector differences in the beating dynamics by comparing average waveforms from video-based displacement data of various sectors. Further, the optimal sampling frequency parameters and measurement time for video recording are studied. While the method by itself is suitable for long term measurements, in laboratory use CMs cannot be kept out of an incubator for extended periods of time. Therefore it is important to minimize the recording time so that the cell condition remains the same throughout the measurement, while still obtaining as much information on the beating as possible.

In this article, we intend to demonstrate that the combination of our previously reported sector approach of video analysis with template matching algorithm can provide additional information on the beating dynamics of iPSC derived CMs.

2. Materials and methods

2.1. Ethics statement

This study was approved by the ethical committee of Pirkanmaa Hospital District (R07080).

2.2. Cell culture

All iPSC lines used in this study were prepared as described by Lahti et al. and Takahashi et al. [4, 5]. The CM differentiation and dissociation were performed by using the previously described protocols [1, 6]. Briefly, the iPS cells were co-cultured with END-2 cells to induce cardiac differentiation, and after a minimum of 14 days, the spontaneously beating colonies were mechanically excised and treated with collagenase A (Roche Diagnostics, Mannheim, Germany). The dissociated CMs were plated and on 2 cm^2 wells on standard cell culture multi-well plates and cultured for 2-14 days for video recording.

2.3. Video recording

CM beating was recorded using a Nikon (Nikon, Tokyo, Japan) Eclipse TS100 inverted microscope with an attached heating plate, and an IMPERX (Boca Raton, FL, USA) B1620 camera. A single, dissociated beating cell was visually selected and recorded at 60 frames per second (fps) or 120 fps. In total, six videos were recorded and further analyzed.

2.4. Digital image correlation analysis

The recorded videos were processed applying DIC to provide beating signals, as described by Ahola et al. [1]. Velocity vector fields were obtained by calculating the displacement between each subsequent video frame. The cell area was divided to 8 sectors, with the center being the visually approximated beating focus point. In contrast to the previously published method [1], the radial and tangential components for each velocity vector were calculated based on their location with respect to the beating focus point. The cell area was segmented semi-automatically, using segmentation based on thresholding and manual selection, to reduce analysis of areas with little to no movement.

The sum of the radial components of each sector was calculated to provide a signal representing the radial displacement in that area of the CM. Tangential displacement was calculated similarly. This process generates in total 16 beating signals from each cell. Each signal was then filtered using a 20-point Gaussian window. For the analysis in this paper, we chose the signals with highest quality. An example of such signal is illustrated in Figure 1a.

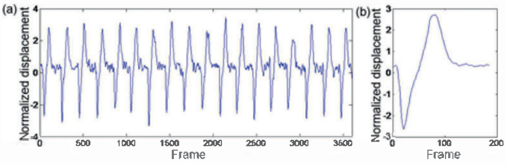

Figure 1: Cardiomyocyte beating signals. a) A beating signal as a function of frames. The magnitude of the beating illustrates the normalized displacement of the sector. The downward peak represents the contraction and the upward peak the relaxation. b) An average waveform template calculated from the signal in a). The template starts from the onset of the contraction. The template baseline after relaxation shows the mean interval between beats.

2.5. Template setup

A template based cross-correlation analysis was implemented to identify the beats that closely resembled the beating pattern in individual sectors. This method has been presented earlier for determining field potential durations from electrical signals of CMs plated on microelectrode arrays in a software that can be found online (http://www.biomeditech.fi/CardioMDA/)[3]. In this study, we applied the template matching method to compute an average waveform for individual sectors of the CM using video recordings. The template was initialized using the beat complex occurring at the half-way point of the total recording. Cross-correlation is then performed for the vector field signal against the selected template. The correlation coefficient measures the degree of similarity between the template and each beat complex identified from the vector field. It is computed as the sum of the products of corresponding pair of points from the two complexes within a specific time window. The cut-off for correlation coefficient was set such that all beat complexes whose resemblance to the template is greater than or equal to 80% were selected for averaging. This average waveform represents the general beat morphology of all the beats in the vector field. Figure 1b shows an example of an averaged waveform, calculated from the signal in Figure 1a.

The average waveforms from different sectors were then compared to determine differences in beating patterns between individual sectors.

2.6. Analysis parameter optimization

A test set for analyzing the effect of sampling frequency on the optimal parameters for template analysis was created. Four 120 fps videos were decimated to 60 fps and 40 fps. The videos were then analyzed using DIC analysis to create beating signals. From these signals, average waveform templates were calculated for the signals with low noise characteristics. Templates from 120 fps videos were downsampled to match those from low fps videos in order to calculate correlation between the averaged waveforms from original and decimated videos. The templates were shifted temporally so that the contraction happens in both templates at the same time in order to make comparisons more valid.

Additionally, we calculated templates for the 120 fps videos by reducing the number of beats, one beat at a time from the end of the signal. This allowed us to study the effect of decreasing video recording time.

3. Results

3.1. Template matching

The beating signal templates from different sectors of the same cell were compared with each other. The templates were synchronized with the contraction peak.

Figure 2 shows the templates calculated from two cells, recorded with 60 fps, displaying the differences in beating dynamics across the cell. Figure 2a illustrates a case in which contraction and relaxation occur similarly in measured sectors. In Figure 2b, relaxation occurs at a different time in all three sectors. This further illustrates the fusiform nature of the cell.

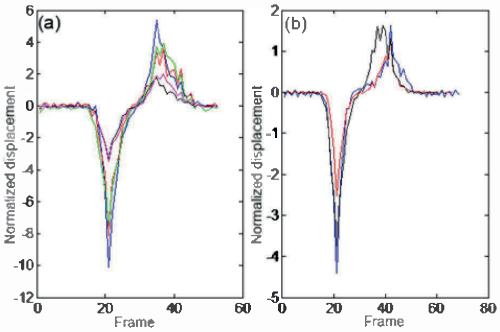

Figure 2: Templates calculated from different sectors of two cells. a) The beating characteristics of the cell are similar in all measured sectors – both contraction and relaxation last a similar time in all sectors. b) The beating characteristics of the cell differ from each other. The relaxation of the cell begins first in the sector marked with black, continues to sector marked with red and finally reaches the sector marked with blue.

3.2. Effect of frame rate

The effect of video frame rate on the quality of the template formation was studied using decimated videos. The correlations between the original template and the template calculated from decimated videos were calculated, and the results are shown in Table 1. Downsampling to 40 fps reduced the quality of the template drastically for two of the cells beating at higher frequencies, rendering the templates unusable.

Table 1. Correlations of the templates calculated from fps decimated videos with the templates from 120 fps videos. Forming a template for 40 fps decimated videos was not possible for cells 2 and 3, due to their higher beating rate.

Cell	bpm	Sector	60 fps	40 fps
1	10	1	0.972	0.939
		2	0.979	0.950
		3	0.986	0.958
2	19.5	1	0.968	N/A
		2	0.960	N/A
		3	0.971	N/A
3	12.5	1	0.970	N/A
		2	0.951	N/A
		3	0.960	N/A
4	9	1	0.984	0.962
		2	0.965	0.935
		3	0.975	0.953

3.3. Effect of the number of beats in template

The effect of the number of beats on the template formation was studied by repeatedly removing the last beat from the calculated video signal. The degradation of the template can be seen in Figure 3.

The beating was recorded at 120 fps for 120 seconds. During this time, the cell beat 20 times. The calculated templates show marginal reduction in quality at 50%, and a significant reduction at 30% of the number of beats. To obtain a functional template, at least 12 beats should be included in the signal.

4. Discussion

We demonstrated the use of averaged waveforms as a basis of determining CM beating behaviour. While the signals obtained using the method previously presented by Ahola et al [1] present well the beating of the cell, a more concise form of presentation is necessary for recognizing beating characteristics with one glance. In this study, we presented that applying the template matching method makes it easier to compare the results obtained both from different cells, and from different areas of the same cell.

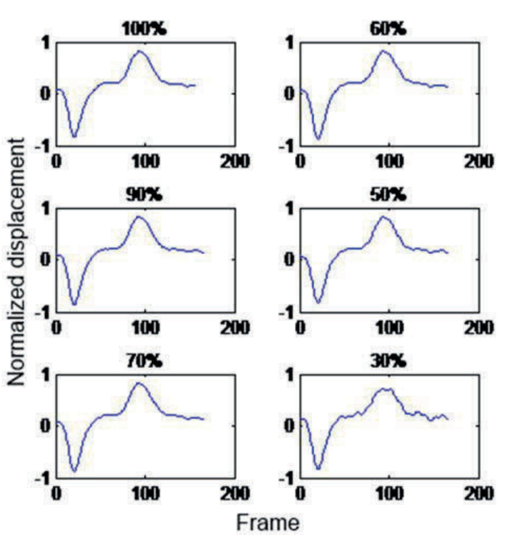

Figure 3: Templates calculated with reduced beat count. The quality of the template remains similar until 60%, after which is starts degrading.

Using the template based video analysis can further help understand the mechanobiological functions of the CMs. In the case of iPS cell derived CMs, the beating behaviour is not as uniform as it is with native, adult CMs. The sectorial approach along with templates will help understand the fusiform nature of the beating.

Our results on the optimization of the analysis parameters provide insight into setting guidelines for the recording process of the video analysis. The results on the frame rate indicate that 60 fps provides a reasonable sampling rate, while the results with 40 fps are often unusable with templates. We suggest that with this method, the sampling rate should be prioritized. At least 60 fps should be used. The sampling rate should be higher with cells beating at high frequencies. Further, the signal should contain at least 12 beats to provide templates that represent best the whole beating signal.

While the test set provided results in the range of 9-19.5 bpm, a larger test set with would be required to draw conclusions about recording protocols for cells beating with higher frequencies.

For this study, the cells were selected to have diverse backgrounds. The cells used in the study were from different individuals and as a result, different cell lines. Additionally, the cell age was different when measured from both differentiation and dissociation. Because of this, our cell material has a more comprehensive interpretation on iPSC derived CMs. As the results were consistent, we ascertain that our method does not depend on the cell culture technique.

Our motion analysis method, therefore, has potential to provide valuable information for different disease models and drug development studies.

Acknowledgements

We would like to thank Prof. Mummery (Hubrecht Institute, Utrecht, The Netherlands) for providing the END-2 cells for co-culturing.

This work was partially funded by a personal research grant from Finnish Cultural Foundation Pirkanmaa Regional Fund and Human spare parts project funded by Finnish Funding Agency for Technology and Innovation (TEKES).

References

[1] Ahola A, Kiviaho AL, Larsson K, Honkanen M, Aalto-Setälä K, Hyttinen J. Video image-based analysis of single human induced pluripotent stem cell derived cardiomyocyte beating dynamics using digital image correlation. Biomed Eng Online 2014; 13:39.

[2] Xi J, Khalil M, Shishechian N, Hannes T, Pfannkuche K, Liang H et al. Comparison of contractile behavior of native murine ventricular tissue and cardiomyocytes derived from embryonic or induced pluripotent stem cells. FASEB J 2010; 24:2739-2751.

[3] Pradhapan P, Kuusela J, Viik J, Aalto-Setälä K, Hyttinen J. Cardiomyocyte MEA Data Analysis (CardioMDA) – A Novel Field Potential Data Analysis Software for Pluripotent Stem Cell Derived Cardiomyocytes. PLoS One 2013;8:e73637.

[4] Lahti AL, Kujala VJ, Chapman H, Koivisto AP, Pekkanen-Mattila M, Kerkelä E et al. Model for long QT syndrome type 2 using human iPS cells demonstrates arrhythmogenic characteristics in cell culture. Dis Model Mech 2012; 5:220-230.

[5] Takahashi K, Tanabe K, Ohnuki M, Narita M, Ichisaka, Tomoda K et al. Induction of pluripotent stem cells from adult human fibroblasts by defined factors. Cell 2007; 131:861-872.

[6] Mummery C, Oostwaard DW, Doevendans P, Spijker R, van den Brink S, Hassink R et al. Differentiation of human embryonic stem cells to cardiomyocytes: role of coculture with visceral endoderm-like cells. Circulation 2003; 107:2733-2740.

Address for correspondence.

Antti Ahola
Department of Electronics and Communications Engineering
Tampere University of Technology
Finn-Medi 1 L 4, Biokatu 6
FI-33520 Tampere, Finland
antti.l.ahola@tut.fi

PUBLICATION
III

Distinct electrophysiological and mechanical beating phenotypes of long QT syndrome type 1-specific cardiomyocytes carrying different mutations

Kiviaho, A. L., Ahola, A., Larsson, K., Penttinen, K., Swan, H., Pekkanen-Mattila, M.,
Venäläinen, H., Paavola, K., Hyttinen, J. & Aalto-Setälä, K.

International Journal of Cardiology Heart & Vasculature (2015), 8:19-31
https://doi.org/10.1016/j.ijcha.2015.04.008

IJC Heart & Vasculature 8 (2015) 19–31

Contents lists available at ScienceDirect

IJC Heart & Vasculature

journal homepage: http://www.journals.elsevier.com/ijc-heart-and-vasculature

Distinct electrophysiological and mechanical beating phenotypes of long QT syndrome type 1-specific cardiomyocytes carrying different mutations

Anna L. Kiviaho [a,*,1], Antti Ahola [b,1], Kim Larsson [a,1], Kirsi Penttinen [a,1], Heikki Swan [c,1], Mari Pekkanen-Mattila [a,1], Henna Venäläinen [a,1], Kiti Paavola [a,1], Jari Hyttinen [b,1], Katriina Aalto-Setälä [a,d,1]

[a] University of Tampere, BioMediTech, School of Medicine, Tampere, Finland
[b] Tampere University of Technology, Department of Electronics and Communications Engineering, BioMediTech, Tampere, Finland
[c] Heart and Lung Center, Helsinki University Central Hospital, University of Helsinki, Helsinki, Finland
[d] Heart Center, Tampere University Hospital, Tampere, Finland

ARTICLE INFO

Article history:
Received 8 April 2015
Accepted 16 April 2015
Available online 25 April 2015

Keywords:
Long QT syndrome
Induced pluripotent stem cell
Arrhythmia
Patch clamp
Calcium imaging
Digital image correlation

ABSTRACT

Background: Long QT syndrome (LQTS) is associated with increased risk of ventricular arrhythmias and cardiac arrest. LQTS type 1 (LQT1), the most prevalent subtype of LQTS, is caused by defects of slow delayed rectifier potassium current (I_{Ks}) that lead to abnormal cardiac repolarization. Here we used pluripotent stem cell (iPSC)-technology to investigate both the electrophysiological and also for the first time the mechanical beating behavior of genetically defined, LQT1 specific cardiomyocytes (CMs) carrying different mutations.
Methods: We established *in vitro* models for LQT1 caused by two mutations (G589D or ivs7-2A>G). LQT1 specific CMs were derived from patient specific iPSCs and characterized for their electrophysiology using a current clamp and Ca^{2+}-imaging. Their mechanical beating characteristics were analyzed with video-image analysis method.
Results and conclusions: Both LQT1-CM-types showed prolonged repolarization, but only those with G589D presented early after-depolarizations at baseline. Increased amounts of abnormal Ca^{2+} transients were detected in both types of LQT1-CMs. Surprisingly, also the mechanical beating behavior demonstrated clear abnormalities and additionally the abnormalities were different with the two mutations: prolonged contraction was seen in G589D-CMs while impaired relaxation was observed in ivs7-2A>G-CMs.
The CMs carrying two different LQT1 specific mutations (G589D or ivs7-2A>G) presented clear differences in their electrical properties as well as in their mechanical beating behavior. Results from different methods correlated well with each other suggesting that simply mechanical beating behavior of CMs could be used for screening of diseased CMs and possibly for diagnostic purposes in the future.

1. Introduction

Long QT syndrome (LQTS) is an electric disorder of the heart that predisposes patients to arrhythmias and sudden cardiac death. The arrhythmias related to LQTS are distinctive ventricular arrhythmias called Torsades de Pointes (TdP) [1]. LQTS type 1 (LQT1) is the most prevalent subtype of the disease. It is caused by mutations in *KCNQ1* gene encoding the α-subunit of the channel responsible for the slow component of the delayed rectifier potassium current (I_{Ks}) [2,3]. The inadequate I_{Ks} current leads to prolongation of repolarization time of action potentials (APs) in single CMs and to prolonged QT interval seen in electrocardiogram (ECG). Various mutations in *KCNQ1* have been identified to cause LQT1 possibly with varying clinical phenotypes [4,5].

Currently different LQTS subtypes are diagnosed with gene mutations in particular genes. However, there is a huge spectrum of mutations in each gene and the severity of the disease has been observed to be more dramatic due to mutations in some genetic regions compared to others [4,6]. Also in cell culture studies with transfected cells, different mutations in the same gene have had different effects on the electrical properties of the cells [7,8]. While some mutations (*e.g.* G589D) seem to have rather mild and recessive effect on the I_{Ks} current [8], other mutations (*e.g.* ivs7-2A>G) cause a complete loss-of-function of the I_{Ks} channel in a dominant negative fashion [7]. Little is known about the mechanisms of the ivs7-2A>G to cause the loss-of-function effect on I_{Ks} current while G589D mutation seems to be a clear trafficking mutation with normal functioning of the channel but with hindered transportation to the plasma membrane [9].

With induced pluripotent stem cell (iPSC) technology, it is possible to generate genetically defined stem cell lines [10,11] and differentiate

---

* Corresponding author at: Biokatu 12, FI-33014, University of Tampere, Finland. Tel.: +358 40 190 1765; fax: +358 3 3641501.
E-mail address: anna.kiviaho@uta.fi (A.L. Kiviaho).

[1] This author takes responsibility for all aspects of the reliability and freedom from bias of the data presented and their discussed interpretation.

http://dx.doi.org/10.1016/j.ijcha.2015.04.008
2352-9067/

these into any cell type of interest. Thereby, *e.g.* LQTS-specific CMs can be generated and studied *in vitro* [12–18]. Traditionally the functionality of CMs in cell culture is determined by electrical or optical analysis, such as patch clamp-technique and microelectrode array (MEA) or calcium (Ca^{2+})-imaging and voltage sensitive probes. However, all these methods have some limitations. Patch clamp-technique is time consuming as well as invasive and cells die after measurements. Voltage sensitive dyes and the tracers used in Ca^{2+}-imaging may alter the electrophysiological properties of CMs and the cells may also be damaged by photo-toxicity [19] or compartmentalization [20] and cells die after analysis. MEA can efficiently be used for cell clusters but due to the physical dimensions of the electrodes and limitations in the sensitivity, it is not suitable with single cells. In addition, these methods detect only ion fluxes that obviously are important but some other, currently even unknown factors influencing the beating of CMs may be neglected. The analysis of mechanical beating properties could reveal additional information beyond the electrical phenomena and this analysis is neither invasive nor toxic and cells can be monitored for a long time.

In this study we present the electromechanical properties of LQT1-CMs having different mutations in the *KCNQ1* gene (G589D or ivs7-2A>G). The electrical and mechanical behavior of the cells was analyzed using a single cell current clamp, Ca^{2+}-imaging and light microscopy video-image analysis. CMs with either of the LQT1-genotypes had significantly prolonged APs, but only CMs with G589D mutation had spontaneous early afterdepolarizations (EADs) at baseline. Additionally, also abnormal Ca^{2+} transients were observed in LQT1-CMs. We also demonstrate that the mechanical beating behavior of the CMs with different *KCNQ1* genotypes has distinct mutation-specific features. This is the first published work where mechanical beating properties of LQTS are studied at the single cell level and the first evidence that LQTS can be detected by monitoring the mechanical beating of the cells.

2. Methods

The study was approved by the ethical committee of Pirkanmaa Hospital District (R08070) and written consent was obtained from all fibroblast donors.

2.1. Clinical information

LQT1 patient carrying G589D mutation is a 46-year-old female with corrected QT interval (QTc) of 464 ms. She has been suffering from syncopal spells. The other LQT1 patient is a 51-year-old female carrying ivs7-2A>G in *KCNQ1*. She has suffered from dizziness, darkening of vision and episodes of unconsciousness. Her QTc is 489 ms. Both of these patient are on β-blocker medication. Control iPSCs were generated from a healthy female, 55 years of age with QTc of 406 ms. The patients with LQT1 were on beta blockers and no irregularities in the QTc were found in the resting condition (Fig. 3 A–C).

2.2. Cell culture conditions

Primary fibroblasts from the skin biopsy were cultured under fibroblast culturing conditions using Dulbecco's modified Eagle medium (DMEM, Lonza, Basel, Switzerland) with 10% FBS (Lonza), 2 mM glutamax (Life Technologies Ltd, Paisley, UK) and 50 U/ml penicillin/streptomycin (Lonza). 293FT-cells (Life Technologies Ltd) were cultured in the same conditions with 1% nonessential amino acids (NEAA, Cambrex, East Rutherford, NJ, USA). Plat-E-cells (Cell Biolabs, San Diego, CA, USA) and irradiated/mitomycin C (Sigma-Aldrich, St. Louis, MO, USA) treated mouse embryonic fibroblasts (MEF) (Millipore, Billerica, MA, USA) were maintained similarly but without antibiotics. iPSCs were sustained together with MEF feeder cells in KSR-medium containing knockout (KO)-DMEM (Life Technologies Ltd), 20% KO-serum replacement (KO-SR, Life Technologies Ltd), NEAA, glutamax, penicillin/streptomycin, 0.1 mM β-mercaptoethanol (Life Technologies Ltd), and 4 ng/ml basic fibroblast growth factor (bFGF, R&D Systems Inc., Minneapolis, MN, USA). All the cells were grown at 37 °C and 5% CO_2 and the medium was changed every other day for iPSCs and two times a week for all the other cells.

2.3. Generation and characterization of iPSC lines

The LQT1 patients carried either the G589D mutation of *KCNQ1* (*KCNQ1*-FinA) or the ivs7-2A>G mutation in *KCNQ1* (*KCNQ1*-FinB) [21]. Skin biopsies from the donors were cultured in 0.2% gelatin (Sigma-Aldrich)-coated flasks under fibroblast culturing conditions. iPSC lines were established using lentivirus infection followed by retrovirus infection. The full protocol has been described by Takahashi and colleagues[10]. Cells, plasmids and reagents used in this protocol include: 293FT cells, Plat-E cells, pLenti6/UbC/mSlc7a1-vector (Addgene, Cambridge, MA, USA), ViraPower™ Packaging Mix (Life Technologies Ltd), Lipofectamine™ 2000 (Life Technologies Ltd), Fugene 6 (Roche Diagnostics, Mannheim, Germany), and pMX retroviral vectors (hOCT3/4, hSOX2, hKLF4 and hc-MYC, all from Addgene). Several lines were established from both patients and from control individual and two from each were selected for further characterization. Studied cell lines were UTA.00208.LQT1 and UTA.00211.LQT1 generated from *KCNQ1* patient with G589D mutation, UTA.00102.LQT1 and UTA.00118.LQT1 generated from *KCNQ1* patient with ivs7-2A>G mutation, and UTA.04602.WT and UTA.04607.WT generated from healthy control individuals.

Characterization of control iPSC lines is described in detail by Ahola and colleagues [22]. LQT1 specific iPSCs were characterized similarly by RT-PCR, immunocytochemistry, embryoid body (EB) and teratoma formation. Teratomas were generated from one control iPSC line (UTA.04602.WT) and two LQT1-lines one carrying G589D mutation and the other ivs7-2A>G in *KCNQ1*. In addition, the karyotypes of all the lines were analyzed. The lines were also assayed with PCR and restriction reactions to detect the correct mutations of *KCNQ1* from the genomic DNA and the control iPSC line was verified not to carry these mutations. DNA was isolated using DNA Tissue XS-kit (Macherey-Nagel GmbH & Co., Düren, Germany) and multiplied with AmpliTaq 360 Polymerase (Life Technologies Ltd) with 100 ng of template, 2 mM of $MgCl_2$, 200 μM of NTPs, 0.5 μM of primers (G589D forward: ttg act ctc agc tac ctc cc, reverse: tgc agg agc ttc acg ttc ac, ivs7-2A>G forward: ggg gag ctg tag ctt cca ta, reverse: agc caa atg cat ggt gag at, Biomers.net GmbH, Ulm, Germany), and 1 U/ μl of enzyme in total volume of 40 μl. Reaction conditions: 96 °C for 10 min (96 °C for 30 s, 60 °C for 30 s, 72 °C for 2 min), 35 cycles, 72 °C for 5 min. Digestion for *KCNQ1*-G589D was done with HIN6I (Thermo Fisher Scientific, Inc., Waltham, MA, USA) with Tango Buffer (Thermo Fisher Scientific, Inc.), and for *KCNQ1*-ivs7-2A>G with Dde1 (Thermo Fisher Scientific, Inc.) using FastDigest Buffer (Thermo Fisher Scientific, Inc.) both with 10 μl from PCR in total volume of 20 μl at 37 °C over night. Products were run on 4% agarose gel (EuroClone S.p.A., Milano, Italy): wild type (WT) for G589D (G589D-WT) generates product sizes 146, 82 and 39 bp, heterozygote (Hez) for G589D (G589D-Hez) generates an extra fragment of 185 bp, ivs7-2A>G-WT produces sizes 228, 39 and 33 bp and ivs7-2A>G-Hez an extra product with size of 261 bp. Extra fragments are caused by vanishing of the cleavage sites due to the mutations (G589D: $146 + 39 = 185$, ivs7-2A>G: $228 + 33 = 261$) (Fig. 2).

2.4. Cardiac differentiation and immunocytochemical characterization of CMs

CM differentiation was accomplished by co-culturing iPSCs with END-2 cells (a gift from Prof. Mummery, Humbrecht Institute, Utrecht, The Netherlands). END-2 cells were cultured as described by Mummery and colleagues [23]. Differentiation was initiated by dissecting the undifferentiated iPSC colonies mechanically into aggregates containing a few hundred cells. These cells were then plated onto mitomycin

C-treated END-2 cells in KSR medium without serum, serum replacement, or basic fibroblast growth factor but with 2.92 mg/ml of ascorbic acid [4] (Sigma-Aldrich). The cell colonies were monitored daily by microscopy, and the medium was changed after 5, 8, and 12 days. After 14 days of culturing, 10% serum replacement was added to the ascorbic acid free medium.

For immunocytochemical staining the beating areas of the cell colonies were cut with a scalpel and treated with collagenase A (Roche Diagnostics, Mannheim, Germany). Dissociated cells were plated on 0.1% gelatin-coated 24-well plate wells in KO-DMEM containing 20% FBS. A maximum of seven days after dissociation, beating cells were fixed with 4% paraformaldehyde (PFA, Sigma-Aldrich) for immunostaining with cardiac markers: anti-cardiac-troponin-T (1:1500, Abcam, Cambridge, MA, USA), anti-α-actinin (1:1500, Sigma-Aldrich), anti-myosin-heavy-chain (MHC, 1:100, Millipore), anti-ventricular-myosin-light-chain (MLC2v, 1:150, Abcam) and anti-atrial-myosin-light-chain (MLC2a, 1:300, Abcam). The secondary antibodies were Alexa-Fluor-568-donkey-anti-goat-IgG, Alexa-Fluor-568-goat-anti-mouse-IgG, Alexa-Fluor-488-donkey-anti-rabbit-IgG, and Alexa-Fluor-488-donkey-anti-mouse-IgG (all 1:800, all from Life Technologies Ltd).

2.5. Video recording

For the video recordings CM aggregates were dissociated in the same way as for immunocytochemical analysis (see above). Videos were recorded within a week from dissociation using video microscopy (Nikon Eclipse TS100, Nikon Corporation, Tokyo, Japan) with a video camera Optika DIGI-12 (Optika Microscopes, Ponteranica, Italy). 30–60 second long monochrome videos were recorded with 720 × 480 resolution and 30 frames per second. Beating was determined as normal if the rhythm was regular and the phases of contraction and relaxation followed each other without any delay or additional movement of the cell. Any deviation from that was considered as abnormal beating.

2.6. Beating analysis

In total 58 videos (13 controls, 24 LQT1-G589D (FinA)-specific and 25 LQT1-ivs7-2A>G (FinB)-specific) were analyzed using digital image correlation (DIC) based analysis method, as described by Ahola et al. [22]. In brief, the velocity vector fields representing video image gray level changes in pixel level were calculated from subsequent video frames using a minimum quadratic difference based DIC method. For each CM, the beating focus point was visually determined and the CM was divided into 8 sectors, each comprising of 45° sector, around the beating focus point. With each selection, motion towards the beating focus point was determined as radial, and perpendicular motion as tangential movement. The sum radial and tangential components were computed for each sector.

Out of the 16 possible signals obtained from a CM 3 signals were selected based on the signal quality. From these signals the average parameters of beating were defined: (1) duration of the contraction, (2) time when contracted, (3) duration of the relaxation, (4) incomplete relaxation time and (5) time when relaxed.

2.7. Allelic imbalance

Allelic discrimination between the WT and mutated *KCNQ1* alleles in CMs derived from different iPSC lines was done by qPCR using standard curves. In order to establish a *KCNQ1* allelic standard curves, the plasmid with WT *KCNQ1* and the plasmid containing the mutant allele were combined with following ratios: 1:0, 8:1, 4:1, 2:1, 1:1, 1:2, 1:4, 1:8 and 0:1, respectively, for the qPCR reactions [12]. The standard curves were done similarly for both mutations (G589D and ivs7-2A>G) addressed in this study. Plasmids used for the curve preparation were pBluescript SK+ plasmids (Addgene) with the inserted gene at the BamHI/NotI-site. The standard curves were plotted $\log_2$ of WT/mutant ratios of plasmids *versus* corresponding ΔCt values. The ΔCt values were defined by subtracting Ct value of WT allele from Ct value of the allele with the mutation. In standard curves, ΔCt values for plasmid ratios are represented in statistical form of mean ± standard deviation ($n = 3$) [18].

In addition, ΔCt values were defined for *KCNQ1* mutations and those were used for locate spots of *KCNQ1* mutated samples on plasmid-derived standard curves. The location of spot defines allelic imbalance of mutation when compared to nearby plasmid ratios.

To determine the allelic imbalance of *KCNQ1* in CMs originated from different mutation specific cell lines (UTA.00208.LQT1 with G589D, and UTA.00118.LQT1 containing ivs7-2A>G) the clusters of beating areas were first cut using a scalpel and total RNA was purified from the cell clusters with a NucleoSpin® RNA II Kit (Macherey-Nagel GmbH & Co.) according to the manufacturer's protocol. The isolated RNA was converted into cDNAs using a High Capacity cDNA Reverse Transcription Kit (Life Technologies Ltd). For allelic discrimination the primers and probes were designed by Custom TaqMan® SNP Genotyping Assay service (Life Technologies Ltd). qPCR reactions were done using 7.5 μl 2× TaqMan® Universal PCR Master Mix, 0.375 μl Custom TaqMan® SNP Genotyping Assay, and 2.125 μl sterile water with total volumes of 12 μl and 3 μl of cDNA or plasmid DNA added into the reaction. The program was initiated with 2 min at 50 °C and 10 min at 95 °C following 40 cycles of 15 s at 95 °C and 1 min at 60 °C.

2.8. Current clamp-measurements

2.8.1. Potassium channel blockers

Rapid delayed rectifying potassium (I_{Kr} or hERG) channel blocker, N-[4-[[1-[2-(6-methyl-2-pyridinyl)ethyl]-4-piperidinyl]carbonyl]phenyl] methanesulfonamide dihydrochloride (E-4031 [24] Sigma-Aldrich) was dissolved in H_2O (stock 2.11 mM) and stored at −20 °C. I_{Ks} blocker, 2-(4-chlorophenoxy)-2-methyl-N-[5 [(methylsulfonyl)amino]tricyclo [3.3.1.13,7]dec-2-yl]-propanamide (JNJ303 [25] Tocris Bioscience, Bristol, United Kingdom) was dissolved in DMSO (stock 25 mM) and stored at −20 °C. Experimental HEPES based perfusate with E-4031 and JNJ303 was freshly prepared on the day of use by dissolving the stocks to final concentrations of 100 nM and 300 nM (DMSO 0.03%), respectively. Action potentials (APs) were unaffected by a 0.03% DMSO vehicle tested in 5/5 CMs.

2.8.2. Measurement of action potentials

APs were recorded from spontaneously beating CMs in current-clamp mode using the perforated patch configuration [26] The HEPES based extracellular perfusate consisted of (in mM): 143 NaCl, 4.8 KCl, 1.8 $CaCl_2$, 1.2 $MgCl_2$, 5 glucose, and 10 HEPES, pH was adjusted to 7.4 with NaOH (at room temperature) and the osmolarity set to 308 ± 2 mOsm with sucrose (Gonotec, Osmomat 030, Labo Line Oy, Helsinki, Finland). The intracellular solution consisted of (in mM): 122 $KMeSO_4$, 30 KCl, 1 $MgCl_2$, and 10 HEPES. KOH was used to set pH to 7.15 and the osmolarity was set to 302 ± 2 mOsm. Amphotericin B (Sigma-Aldrich) was used as a membrane perforation agent and dissolved in DMSO to a final concentration in the patch pipette of 0.24 mg/ml. Dissociation of the spontaneously beating CMs was done similarly as for immunocytochemical staining and for video recordings but the cells were plated onto 0.1% gelatin-coated cover glasses of 5 mmø for patch clamp-measurements. The CMs were recorded on days 6–7 after plating. Coverglasses with CMs were fast transferred to a preheated 36 ± 1 °C fast RC-24N perfusion chamber (Warner Instruments LLC, Hamden, CT, USA). An SH-27B inline heater (Warner Instruments LLC) was used to preheat the perfusate. Cells were rested in the extracellular perfusate for more than 10 min prior to patching. Patch electrodes (model PG150T, Harvard Apparatus, Holliston, MA, USA) were pulled with a PC-10 puller (Narishige International Limited, London, UK) and flame polished with microforge MF-900 (Narishige International Limited) to a resistance of 3.0–3.5 MΩ measured in the bath perfusate. Drugs

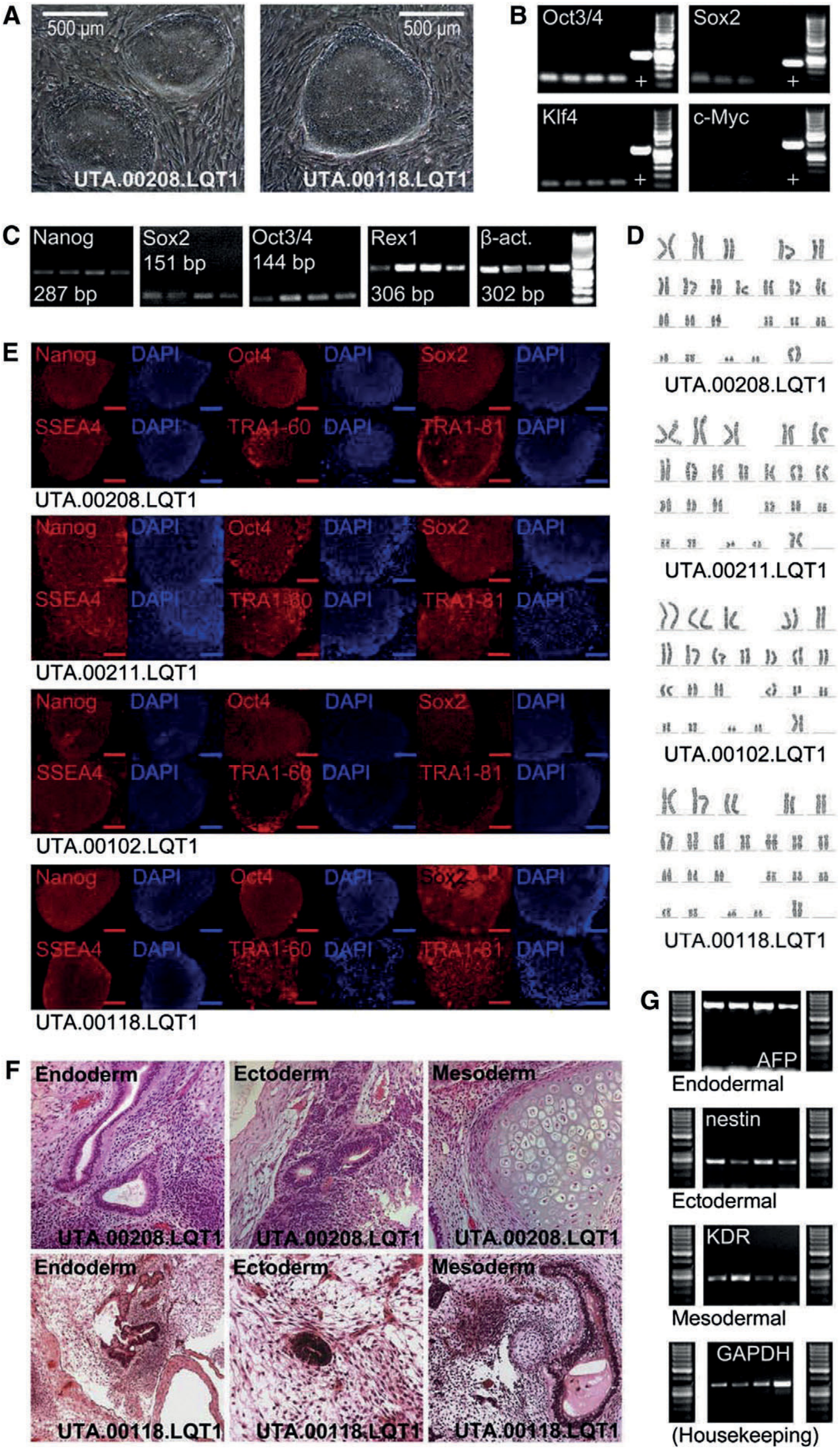
A
500 µm
UTA.00208.LQT1
500 µm
UTA.00118.LQT1
B
Oct3/4
+
Sox2
+
Klf4
+
c-Myc
+
C
Nanog
287 bp
Sox2
151 bp
Oct3/4
144 bp
Rex1
306 bp
β-act.
302 bp
D
UTA.00208.LQT1
UTA.00211.LQT1
UTA.00102.LQT1
UTA.00118.LQT1
E
Nanog
DAPI
Oct4
DAPI
Sox2
DAPI
SSEA4
DAPI
TRA1-60
DAPI
TRA1-81
DAPI
UTA.00208.LQT1
UTA.00211.LQT1
UTA.00102.LQT1
UTA.00118.LQT1
F
Endoderm
Ectoderm
Mesoderm
UTA.00208.LQT1
UTA.00118.LQT1
G
AFP
Endodermal
nestin
Ectodermal
KDR
Mesodermal
GAPDH
(Housekeeping)

were applied using a gravity controlled VC3 perfusion system (ALA Scientific Instruments, Farmingdale, NY, USA). APs were recorded in gap-free mode with pClamp 10.2 using the Axopatch 200B patch clamp amplifier connected to an acquisition computer *via* AD/DA Digidata 1440 (Molecular devices LLC). Current-clamp recordings were digitally sampled at 20 kHz and filtered at 5 kHz using the low pass Bessel filter on the recording amplifier. Numbers of CMs measured (n) are presented in the Tables 2A and 2B, and Tables 3A and 3B.

2.8.3. Extraction of action potential characteristics

Following stabilization of the spontaneously generated APs in current-clamp mode, a baseline of minimum of 2 min was acquired before drug application. Gap-free traces of individual CM recordings were then imported into Microcal Origin™ 8.6 or 9.0 and processed by an automated script. Beats per minute (BPM), AP duration at 50% and 90% of repolarization (APD_{50} and APD_{90}), AP amplitude (APA), and maximum diastolic potential (MDP) were extracted. dV/dT (V_{max}, maximal upstroke velocity) was extracted from the differentiated time course traces as peak values corresponding to each single AP. Single AP characteristics were then plotted as a function of time for evaluation and a series of minimum of 15 APs were averaged for each CM and used in the statistical analysis. Ventricular-like CMs were defined by $APD_{90}/APD_{50} < 1.3$ and APA>95 mV, atrial-like by $APD_{90}/APD_{50} > 1.3$ and APA>95 mV and finally nodal-like were defined by $APD_{90}/APD_{50} > 1.3$ and APA < 95 mV.

2.9. Combined current clamp-measurements and video analysis

APs from a CM of each cell line (control, G589D and ivs7-2A>G) were recorded using a current clamp. During the current clamp-measurement, a concurrent video was recorded using an inverted IX71 microscope (Olympus Corporation, Hamburg, Germany) and an ANDOR iXon 885 CCD camera (Andor Technology, Belfast, Northern Ireland). The video recordings were then analyzed using the previously described method [22]. A good quality beating motion signal was selected, and the AP and the motion signal for each cell line were synchronized.

2.10. Calcium imaging

CMs were dissociated as described in the section about immunocytochemical staining and plated onto 0.1% gelatin-coated 13 mm cover slips. 6–8 days after dissociation the cells were loaded with 4 μM Fura-2 AM (Life Technologies Ltd) for 30 min in HEPES based medium at 37 °C. After incubation the cover slips were moved to an RC-25 recording chamber (Warner Instruments LLC) and perfused with 36 ± 1 °C HEPES based solution (in mM): 137 NaCl, 5 KCl, 0.44 KH_2PO_4, 20 HEPES, 4.2 $NaHCO_3$, 5 D-glucose, 2 $CaCl_2$, 1.2 $MgCl_2$ and 1 Na-pyruvate with pH adjusted to 7.4 with NaOH. Ca^{2+}-measurements were done with an inverted IX71 microscope and UApo/340 ×20 air objective (Olympus Corporation). Images were acquired with an ANDOR iXon 885 CCD camera (Andor Technology). A Polychrome V light source (15 nm bandwidth) and the camera were synchronized by an external DSP controller (TILL Photonics, Munich, Germany). TILLvisION software was used to acquire image data (TILL Photonics). Fura-2 in spontaneously beating cells was exited at 340 nm and 380 nm light and emission was detected at 505 nm and the data presented as ratios. The Ca^{2+} handling was extracted for 15 s sweeps of spontaneous baseline beating and categorized into different rhythm categories based on the types of abnormalities observed: normal beating with stable amplitude (N), arrhythmias with double or more Ca^{2+} peaks (AD), and arrhythmias with small amplitude Ca^{2+} events between the stable amplitude Ca^{2+} spikes (AS). A criterion for the AD group was a Ca^{2+} spike with double or several peaks which do not reach the baseline. For the AS group the presence of a small amplitude Ca^{2+} event of at least 10% of the preceding Ca^{2+} spike amplitude was required. Numbers (n) of CMs measured were: for G589D specific cells the n = 87, for 7-2A>G mutated the n = 80, and for control CMs the n = 45.

2.11. Statistical analysis

The variance between two experiments or more was calculated in Microcal Origin™ 9.0. Variance between two individual experiments was accessed using the two sample *t*-test and between more than two individual experiments the one-way ANOVA-test was used and followed by a Scheffe's post hoc-test. In drug experiments, the baseline and drug effect were compared using paired sample *t*-test. $p < 0.05$ was considered significantly different and levels of significance are represented as (*) $p < 0.05$ and (**) $p < 0.01$. Data is shown as mean ± S.E.M. if not otherwise stated.

3. Results

3.1. Pluripotency of the iPSCs

All the iPSC lines used in this study were verified for their pluripotency (control iPSCs have been characterized earlier [22]). Both control and LQT1-specific lines formed colonies typical for human pluripotent stem cells (Fig. 1 A). The iPSCs also expressed markers for pluripotent state shown both by RT-PCT and immunocytochemistry (Fig. 1 C and E), and the transgenes were silenced (Fig. 1 B). *In vitro* pluripotency was shown by embryoid body (EB) formation (Fig. 1 G) and *in vivo* by teratoma forming assay (Fig. 1 F). All the lines were also verified for the normal karyotype (Fig. 1 D).

3.2. Biochemical and genetic analysis of iPSC derived CMs

The expression pattern of spontaneously single beating cells was typical for CMs exhibiting troponin T, α-actinin, myosin heavy chain (MHC), atrial specific myosin light chain (MLC2a) and ventricular myosin light chain (MLC2v). Fig. 2 A–C depicts representative immunostainings of control (Fig. 2 A), G589D (Fig. 2 B) and ivs7-2A>G (Fig. 2 C) specific cell lines.

The LQT1-specific lines were found to carry the correct mutations and these mutations were not found in control lines. This was determined by RT-PCR analysis and restriction enzyme digestion (Fig. 2 D–F).

3.3. Mechanical properties of LQT1-specific CMs

We first visually analyzed the beating behavior of single CMs in videos obtained from the two control lines, the two G589D specific lines and the two ivs7-2A>G specific lines. Control CMs used in the video analysis had a normal beating pattern (marginal irregularities, see below) with only contraction and relaxation phases following each other. However, with our two G589D specific lines we also observed a large proportion of abnormally beating cells with a prolonged phase of contracted state before relaxation. The two ivs7-2A>G lines were also having a prolonged contraction/relaxation cycle. These cells typically had normal contraction but the relaxation phase was prolonged having vacillation before cells fully relaxed (see Supplementary videos 1–3).

Fig. 1. Pluripotency of iPSC lines. A: All the iPSC lines formed colonies typical for pluripotent stem cells. B and C: All the exogenous transgenes (Oct3/4, Sox2, Klf4 and c-Myc) were silenced (B) and endogenous markers for pluripotent state (Nanog, Sox2, Oct3/4 and Rex1) were expressed (C). β-Actin was used as a housekeeping gene. D: All the iPS cell lines had normal karyotype. E: Immunocytochemistry demonstrated the expression of pluripotency markers. F: Cell types derived from all three germ layers were found in teratomas. G: The expression of markers for the three germ layers was detected from EBs by RT-PCR.

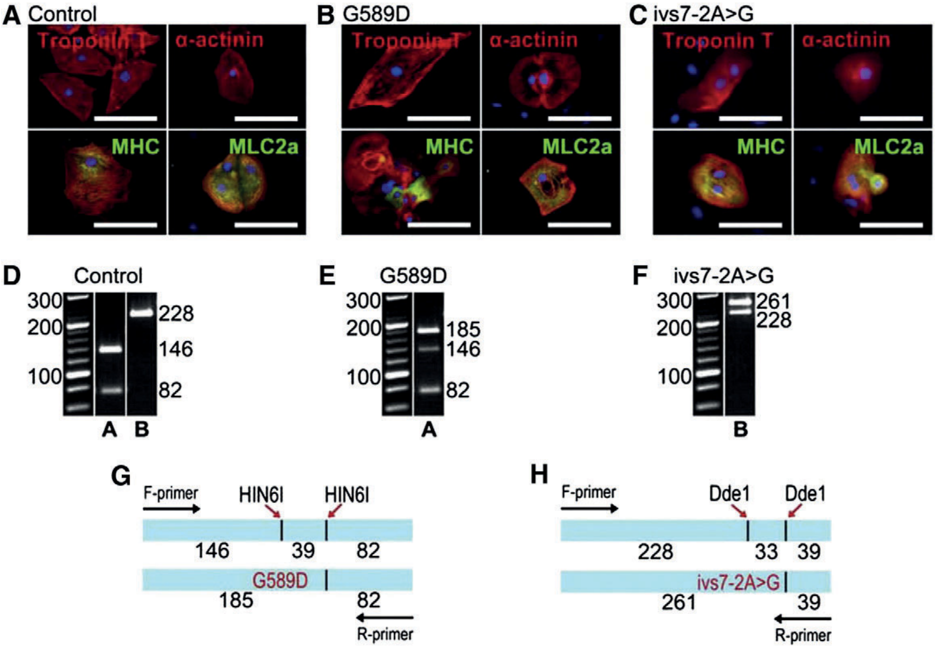

Fig. 2. Characterization of iPSC derived CMs. A–C: The CMs expressed cardiac-specific proteins. The scale bars refer to 100 μm. D–F: The LQT1-specific lines carried the correct mutations while no G589D or ivs7-2A>G mutations were found in control cell lines. "A" in the figure refers to G589D mutation and "B" to ivs7-2A>G. Control CMs produced products of 146 and 82 bp (and 39 bp, not shown in the figure) for G589D, and 228 bp-product (also fragments of 39 and 33 bp, not shown in the figure) for the region corresponding ivs7-2A>G mutation (D). Heterozygous G589D specific lines (one shown in E) created an extra product of 185 bp and heterozygous ivs7-2A>G lines had an extra product with the size of 261 bp (one in F). G and H illustrate the cleavage sites for the restriction enzymes used, their disappearance due to the mutations and the sizes of the products from the reactions for G589D (G) and ivs7-2A>G (H).

Videos from control as well as LQT1-CMs with either of the mutations were analyzed in detail according to the displacement model illustrated in Fig. 4 A (see also the Methods section). Representative signals from single CMs from both LQT1-specific cell lines (G589D or ivs7-2A>G) as well as from control CM are presented in Fig. 3 D–F. Normally beating control CMs ($n = 13$) comprised only of the phases 1 (contraction), 3 (relaxation) and 5 (relaxed) (Fig. 4 B). However, in 17/24 CMs with G589D mutation, a prolonged contraction time was observed: They exhibited an additional phase 2 between contraction and relaxation phases, and during that phase the CMs stayed contracted. In a minor proportion (2/17) of G589D-CMs, a phase 4 (incomplete relaxation) was also found (Table 1, Fig. 4 C). CMs carrying the ivs7-2A>G mutation also exhibited a prolonged contraction (phase 2, in 17/25), but the duration of the phase 2 was not as prominent as in G589D-CMs. Instead, ivs7-2A>G-CMs typically had rather normal contraction, but the relaxation was abnormal and prolonged (in 15/17 CMs) due to vacillation (incomplete relaxation, phase 4, Table 1, Fig. 4 D). The time durations of different phases in control CMs and in CMs with the two LQT1 specific mutations are summarized in Table 1. There was some overlap in the abnormal beating behavior between the two mutations: However, only 12% (2/17) of the cells with G589D failed to relax normally, but 88% (15/17) of the cells with ivs7-2A>G demonstrated some prolongation in the contraction phase (phase 2). Beating patterns comparable to controls were also observed in CMs with G589D ($n = 7/24$, 29%) or ivs7-2A>G ($n = 8/25$, 32%).

When the absolute time of contraction (phases 1 and 2), relaxation (phases 3 and 5) and incomplete relaxation (phase 4) was plotted against the beating frequency the contraction time for the control cell population (Fig. 4 E) stayed at the range of 0.25–0.5 s corresponding the contraction time of human heart [27]. The relaxation time increased with a decreased beating rate also resembling the behavior of human heart. The abnormally beating LQT1-CMs presented contraction times of up to 0.75 s, while the contraction times of the control cells were less than 0.5 s (a not statistically significant difference, one-way ANOVA). If incomplete relaxation (phase 4) was added to the contraction time, the total times when the cells were not relaxed, were even more different from the times observed in normally beating cells although the difference was still not statistically significant (Fig. 4 F and G). The normally beating LQT1-CMs resembled control CMs regarding their contraction-relaxation properties (Supplementary Fig. 1).

3.4. Allelic imbalance in patient specific cells

The allelic discriminations between the WT and mutated *KCNQ1* alleles in CMs specific for either G589D or ivs7-2A>G mutation were determined. The expression ratio between the WT and the G589D-*KCNQ1* was found to be 4:1 (WT:mutated) in both LQT1-G589D cell lines (Supplementary Fig. 2). For the *KCNQ1*-ivs7-2A>G mutation the discovered ratio was 3:1 (WT:mutated) (Supplementary Fig. 2).

3.5. Electrical properties of LQTS-specific CMs

3.5.1. Baseline characteristics

Representative APs from ventricular CMs (both G589D and ivs7-2A>G-specific) as well as from control CM are presented in Fig. 3 G–I. The majority of the CMs recorded were ventricular-like and only a marginal proportion was nodal-like (Table 2A). As expected, the APDs were significantly prolonged in nodal-, atrial- and ventricular-like LQT1-CMs compared to the control CMs (Fig. 5 D, ANOVA, $p < 0.05$). MDPs for atrial- and ventricular-like CMs were recorded from −65 mV to −82 mV with overshoots of around +40 mV. In contrast, nodal-like CMs were more depolarized and around −66 mV with overshoots less than +25 mV (Table 2A).

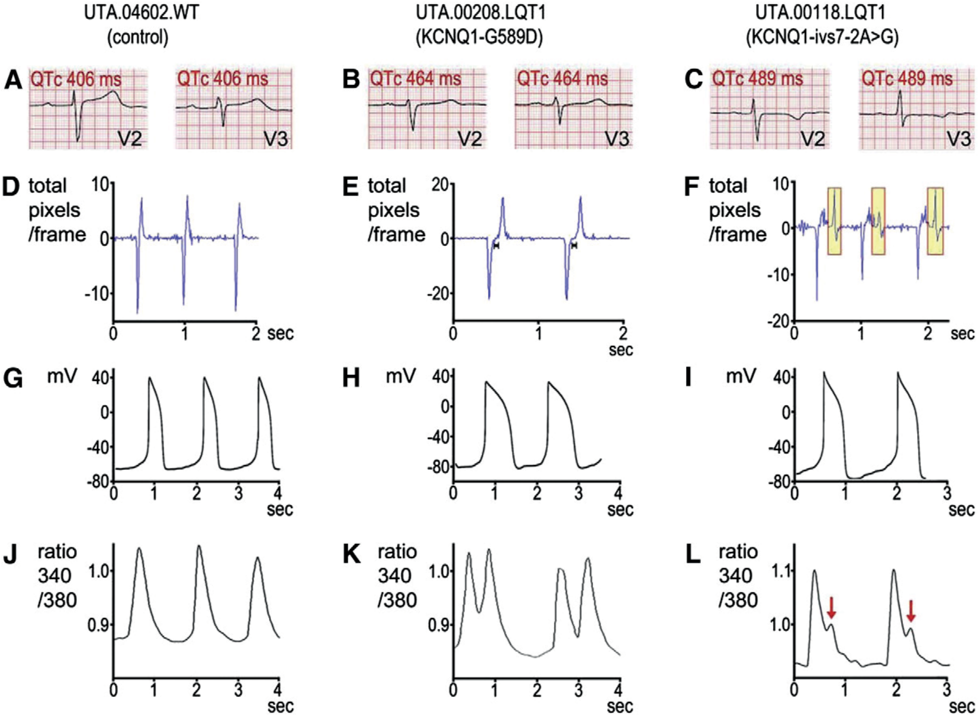

Fig. 3. ECGs of the donors and functionality of iPSC derived CMs. A–C: ECGs from the primary cell donors. D–F: Video recording analysis of control (D), G589D (E) and ivs7-2A>G (F)-specific CMs. Contraction is indicated with downward peak and the upward peak refers to relaxation. Bars (E) indicate the phase 2 (see Fig. 4 A) and show the time when the CMs stayed contracted and the highlighted areas (F) refer to the time of incomplete relaxation (phase 4 in Fig. 4 A). G–I: Ventricular APs from control CMs (G) and LQT1-specific CMs carrying G589D (H) or ivs7-2A>G (I). J–L: Ca^{2+}-imaging signals from control (J) and LQT1-specific CMs (K, L). The most prevalent type of abnormal Ca^{2+} transients in ivs7-2A>G-specific CMs was additional small Ca^{2+} transients (AS) (L, extra peaks marked with arrows) but in G589D CMs double or more Ca^{2+} peaks (AD) (K) in addition to AS were seen.

In the G589D-specific CMs, but not in controls or in ivs7-2A>G-specific CMs, spontaneous baseline early afterdepolarizations (EADs) were observed in 16.7% (5/30) of ventricular-like CMs (Fig. 5 E, Table 2B). These CMs with baseline EADs were not used in the drug studies. Nevertheless, in these cells with spontaneous EADs we found a consistent elevation of the APD_{90}/APD_{50} ratios (>1.8) compared to baseline ratios without EADs (<1.3). The ratio prolongation is due to the presence of EADs evoking around −25 mV, and thereby prolonging only the APD_{90} value (see Fig. 5 E).

3.5.2. Effect of JNJ303 and E-4031

Ventricular-like CMs were exposed to the I_{Ks} blocker, JNJ303 (300 nM) and APs from the baseline, in the presence of JNJ303 and after wash out was extracted (Fig. 5 F). In control CMs (n = 10), JNJ303 significantly prolonged APD_{50} and APD_{90} by a similar proportion of 31% and 28%, respectively, but other AP characteristics were unaffected (Table 3A). However, the effect of JNJ303 was only marginal on the APD_{50} and APD_{90} in G589D-specific cells (prolongation of 7.7% and 8.7%, respectively, Fig. 5 F, middle panel), and in ivs7-2A>G-specific CMs no effects were observed (Table 3A, Fig. 5 F, lower panel). The effect of JNJ303 was fully reversible following the wash out, and the beating frequency was not significantly affected. In a few cells from each group the JNJ303 block was verified by a consecutive application, which always was similar to the first (Fig. 5 F, LQT1-G589D). The APD_{90}/APD_{50} ratios for the control, G589D-specific- and ivs7-2A>G-specific CMs at baselines and in the presence of JNJ303 were similar and found to be between 1.19–1.27.

To evaluate our I_{Ks} findings we also applied the I_{Kr} (hERG) blocker, E-4031 (100 nM) on ventricular-like CMs. The effect of E-4031 from three representative current-clamp recordings is shown in Fig. 5 G. In control cells the APD_{50} and APD_{90} were prolonged by E-4031 (30% and 74%, respectively), and the APD_{90}/APD_{50} ratio was now increased from 1.21 (baseline) to 1.67 (E-4031) but no EADs were evoked (Fig. 5 G, upper panel, Table 3B). In contrast, all ventricular-like CMs in the G589D-specific group (5 cells) and in the ivs7-2A>G-specific group (7 cells) exhibited EADs when exposed to E-4031 (Fig. 5 G, middle and lower panel, respectively). The G589D-CMs had APD_{50} and APD_{90} significantly prolonged by 70% and 318% (paired sample *t*-test), respectively, and ADP_{90}/APD_{50} ratios were found to be increased from 1.16 (baseline) to 2.18 (E-4031). In the CMs with ivs7-2A>G, APD_{50} and APD_{90} were even more significantly prolonged by 412% and 771% (paired sample *t*-test), respectively, and ADP_{90}/APD_{50} ratios were found to be increased from 1.14 (baseline) to 2.09 (E-4031). In contrast to the effects of JNJ303, E-4031 decreased the beating frequency of all CMs (paired sample *t*-test). All CMs tested with E-4031 became significantly depolarized during exposure (paired sample *t*-test), but the overshoot (peak) was not affected by E-4031 (Fig. 5 G, Table 3B). Even though APDs nearly recovered following wash out the, MDPs recovered only partially (Fig. 5 G, right panels) after exposure to E-4031. In line with this, the beating frequency increased following the wash out (data not shown).

3.6. Comparison of the electrical and mechanical phenotypes

The mechanical analysis was also conducted together with the current clamp-measurements (Fig. 6). Thereby the mechanical and electrophysiological phenotypes could be compared and the timing of the electrical activity and the contraction/relaxation of the cells could be evaluated. In both cell types, control CMs (Fig. 6 A) and LQT1 specific

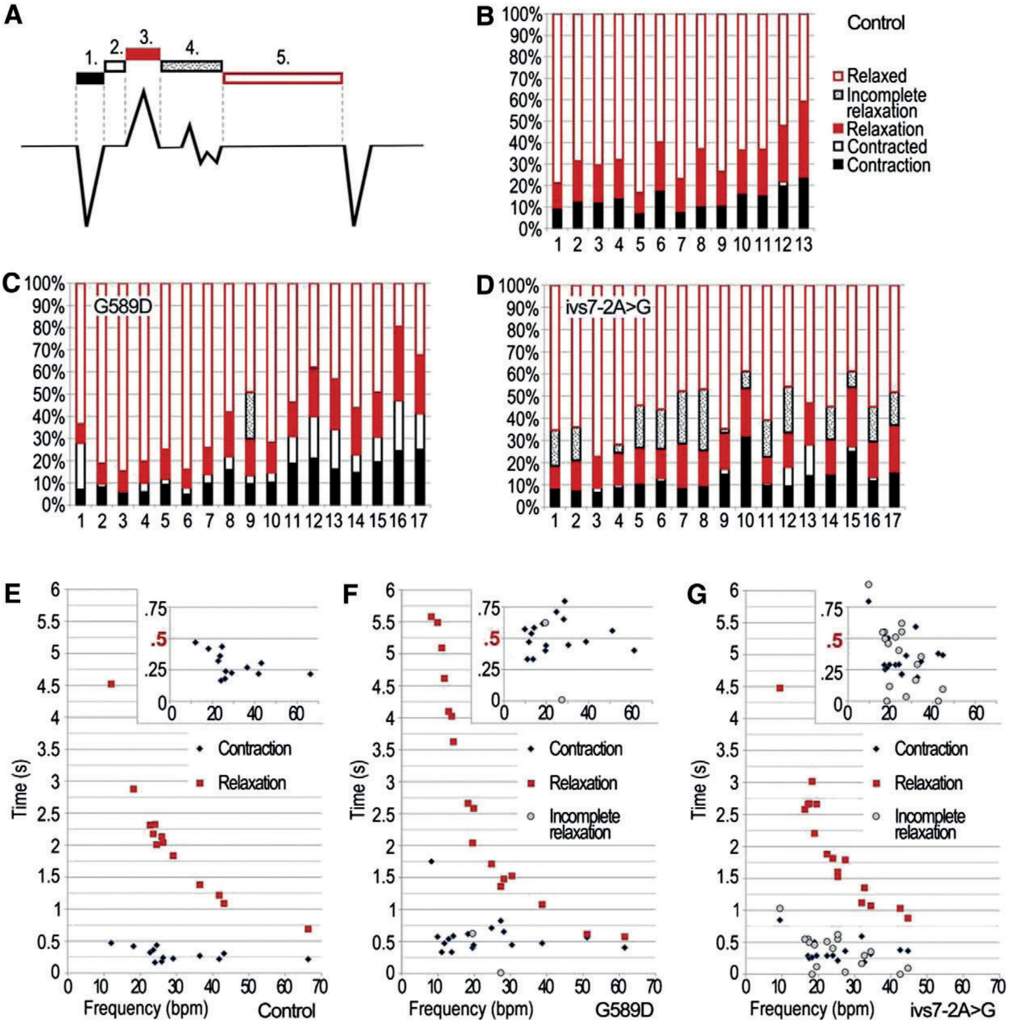

Fig. 4. Analysis of LQT1-CMs using digital image correlation. A: An artificial illustration of a beating signal. 1: time of contraction (phase 1), 2: time in contracted state (phase 2), 3: time of relaxation (phase 3), 4: time of incomplete relaxation (phase 4), and 5: time in relaxed state (phase 5) (see phases also in Table 1). The same colors and patterns are used in panels B–G. B: Beating pattern of control CMs. C: Beating pattern of G589D-CMs. D: Beating pattern of ivs7-2A>G-CMs. The cells are presented in order of beating rate: control CMs: 12–66 beats/min, G589D-CMs: 8–62 beats/min and ivs7-2A>G-CMs: 9–45 beats/min. E–G: The time duration from the beginning of contraction to the beginning of relaxation and from the beginning of relaxation to the beginning of contraction are presented. Contraction time was in the range of 0.25–0.5 s in control CMs (E). In LQT1-CMs the contraction time was longer or incomplete relaxation was present (F and G). The points for contraction time are enlarged to highlight the differences in the contraction times between control CMs and LQT1 specific CMs (a point with a value of 1.75 ms in G589D-figure is not included).

CMs (Fig. 6 B), the AP was immediately followed by the contraction. In LQT1 specific CMs the APD was clearly prolonged and the mechanical abnormality correlated nicely with this prolongation (Fig. 6 B). Also, the mechanical activity of the LQT1 specific cells seemed to continue longer after the electrical activity had already stopped when compared to control CMs.

3.7. Ca^{2+} handling of LQT1-specific CMs

To further study the functionality of LQT1 specific CMs, Ca^{2+} transients were measured during spontaneous baseline beating. In G589D and ivs7-2A>G specific as well as in controls three major responses were found. A robust beating pattern with stable Ca^{2+} amplitude and frequency were characteristic for the majority of the control CMs (N), while arrhythmias with double or more Ca^{2+} peaks (AD) or arrhythmias with small amplitude Ca^{2+} events between the stable amplitude Ca^{2+} spikes (AS) were frequently seen in G589D and ivs7-2A>G CMs (Fig. 7 A, Supplementary Table 1). Both types of arrhythmias (AD and AS) were seen in all cell types though the Ca^{2+} transient abnormalities were more prevalent in both LQT1 specific cell lines compared to control CMs (Fig. 7 B). The cells with G589D had the highest proportion of ADs (23%). The duration of the calcium elevation was significantly longer in CMs with G589D exhibiting ADs compared to those showing AS type of arrhythmia or normal beating ($p < 0.01$, one-way ANOVA). AS-arrhythmia were also more pronounced in CMs with G589D resulting in significantly lower beating frequency ($p < 0.02$, one-way ANOVA).

Table 1

The average times (ms) and standard mean errors for each individual beating phase and the total sum of the phases. Phase 1 is the time of contraction, phase 2 refers to the time when the cells stay contracted, phase 3 is the relaxation time, and phase 4 indicates the time of incomplete relaxation. The time when the cells are relaxed (phase 5) is not displayed in the table. (*) indicates $p < 0.05$ and (***) indicates $p < 0.001$ (one-way ANOVA) for abnormal G589D-CMs vs. control CMs and vs. abnormal ivs7-2A>G-CMs concerning the phase 2. For abnormal ivs7-2A>G-CMs vs. abnormal G589D-CMs (two sample t-test) in the case of the phase 4 (*) also indicates $p < 0.05$ and (***) indicates $p < 0.001$. Data is presented as mean ± S.E.M. The abnormal behavior of the cells is highlighted with bold.

	BPM	Phase 1	Phase 2	Phase 3	Phase 4	Sum P 1–4
Control						
Normal n = 11	$29.3 \pm 4.4^{**}$	294.3 ± 31.9	4.7 ± 1.9	426.0 ± 41.9	N/A	725.0 ± 70.2
Abnormal n = 0	N/A	N/A	N/A	N/A	N/A	N/A
G589D						
Normal n = 7	33.2 ± 6.5	275.9 ± 19.2	15.5 ± 5.7	362.0 ± 19.3	0.0 ± 0	653.4 ± 27.5
Abnormal n = 17	23.6 ± 3.6	285.2 ± 26.3	$\mathbf{180.8 \pm 28.8}^{*}$ (n = 17/17)	365.1 ± 29.1	$\mathbf{37.3 \pm 36.7}$ (n = 2/17)	868 ± 74.8
ivs7-2A>G						
Normal n = 8	30.6 ± 5.7	248.2 ± 31.1	5.0 ± 2.9	383.0 ± 48.0	0.0 ± 0	636.3 ± 79.0
Abnormal n = 17	25.2 ± 2.3	318.7 ± 39.9	$\mathbf{46.3 \pm 13.6}$ (n = 15/17)	424.8 ± 44.4	$\mathbf{366.7 \pm 66.9}^{***}$ (n = 17/17)	1156.4 ± 123.0

Representative Ca^{2+} signals from single CMs from both LQT1-specific cell lines (G589D or ivs7-2A>G) as well as from control CM are shown in Fig. 3 J–L.

4. Discussion

In the present study we analyzed LQT1-specific CMs carrying either G589D or ivs7-2A>G mutation in the *KCNQ1* gene. The LQT1-CMs with either mutation had prolonged AP durations. EADs were spontaneously present only in CMs with G589D mutation but not with ivs7-2A>G mutation. However, EADs could be evoked pharmacologically in CMs with either mutation. In control CMs EADs were absent at baseline and they could not be induced with I_{Ks} or I_{Kr} blockers. Ca^{2+} transients were also aberrant in both types (G589D and ivs7-2A>G) of LQT1-CMs having large double spikes or extra spikes with small amplitude. In control CMs contraction and relaxation happened fast with no pause in-between. However, this beating behavior in LQT1-CMs was clearly abnormal. Using video recording analysis, LQT1-specific CMs were found to exhibit two distinct forms of abnormal mechanical beating behavior: CMs carrying G589D mutation typically stayed contracted for prolonged time while CMs with ivs7-2A>G mutation showed an incomplete relaxation phase.

Our current clamp data demonstrates that the APDs measured from LQT1-CMs with either of the mutations (G589D or ivs7-2A>G) were significantly prolonged. Heterozygous expression of the G589D and ivs7-2A>G mutations in non-cardiac cells has earlier shown that both mutations have a dominant negative effect in gene expression systems [7,28], although the expression of G589D mutation did not lead to altered current density, the cAMP induced up-regulation of I_{Ks} was abolished by the mutation [28]. The ivs7-2A>G mutation on the other hand, almost completely abolished the I_{Ks} current when transiently expressed in non-cardiac cells [7]. The lack of I_{Ks} reduction in the G589D transfected non-cardiac cells may be due to trafficking problems caused by G589D: the mutated protein does not reach the cell surface [9]. The effect of G589D in LQTS has also been explained by disrupted β-adrenergic activation of I_{Ks} [29] but this study clearly shows that the disease phenotype caused by G589D is not solely dependent on central nervous system and activation of β-adrenergic receptor since it is present also in single dissociated CMs.

As mentioned, baseline-APDs were significantly prolonged in LQT1-CMs compared to the control CMs. With LQT1-CM we could further detect that ventricular-like CMs were only marginally affected or completely unaffected by I_{Ks} blockage. The lack of effect of I_{Ks} blockade in our LQT1-CMs is in accordance with the previous observation that the baseline I_{Ks} current is decreased by about 75% in LQT1-CMs [18]. In our study, G589D-CMs had longer baseline-APD_{90} than ivs7-2A>G-CMs and spontaneous EADs were observed only in G589D-CMs, but none in CMs with ivs7-2A>G nor in control CMs. However, the APD prolongation with I_{Kr} blockage always evoked EADs in both types of LQT1-specific CMs but not in control CMs. The I_{Kr} block also induced a depolarization of the baseline as previously shown [30].

CMs carrying either one of the LQT1 mutations demonstrated abnormalities in intracellular Ca^{2+} transients, but the abnormal features were more common in G589D mutated CMs similarly as these CMs had more severe abnormalities in current clamp analysis. Abnormal Ca^{2+} transients could be occasionally observed also in control CMs (6% of the cells), but at least third of the LQT1-CMs presented Ca^{2+} abnormalities. In LQTS-CMs, EADs have been thought to result from late membrane-

Table 2A

Baseline characteristics of spontaneous action potentials (APs) from control cardiomyocytes (CMs) as well as from LQT1-G589D- and LQT1-ivs7-2A>G-specific CMs. (*) indicates significance levels of $p < 0.05$ and (**) $p < 0.01$. Significance levels were obtained by one-way ANOVA of grouped data from nodal, atrial and ventricular CMs, respectively. Data is presented as mean ± S.E.M. CMs with baseline arrhythmia are not included (see Table 2B).

	Number of cells [n (%)]	BPM	APD_{50} (ms)	APD_{90} (ms)	APA (mV)	MDP (mV)	V_{max} (dV/dT)
Control							
Nodal-like	2 (6.7)	75.7 ± 4.4	104.4 ± 2.1	159.1 ± 0.4	88.7 ± 0.6	-66.0 ± 0.3	8.70 ± 2.3
Atrial-like	4 (13.3)	61.5 ± 8.5	132.6 ± 13.6	189.1 ± 32.2	100.4 ± 3.0	-71.6 ± 3.4	26.1 ± 17.9
Ventricular-like	24 (80.0)	55.6 ± 3.4	291.8 ± 21.5	349.6 ± 22.9	110.2 ± 2.4	-69.6 ± 1.5	19.5 ± 4.7
LQT1 (G589D)							
Nodal-like	2 (5.1)	54.5 ± 4.1	$164.5 \pm 6.2^{*}$	$309.2 \pm 39.7^{*}$	83.4 ± 3.7	-63.6 ± 1.7	4.2 ± 7.1
Atrial-like	12 (30.8)	38.9 ± 4.5	$335.7 \pm 36.2^{**}$	$477.7 \pm 51.4^{**}$	106.4 ± 2.8	-70.5 ± 2.0	23.9 ± 6.9
Ventricular-like	25 (64.1)	$37.7 \pm 4.6^{*}$	$458.5 \pm 57.4^{**}$	$545.3 \pm 62.6^{**}$	109.0 ± 3.1	-73.6 ± 1.6	14.8 ± 1.8
LQT1 (ivs7-2A>G)							
Nodal-like	2 (6.1)	69.4 ± 6.0	170.5 ± 17.3	$232.1 \pm 7.7^{*}$	93.0 ± 1.3	-61.0 ± 9.6	9.5 ± 1.5
Atrial-like	6 (18.2)	50.9 ± 9.9	$187.8 \pm 15.0^{*}$	$287.8 \pm 18.5^{*}$	101.2 ± 2.2	-66.0 ± 2.6	16.3 ± 4.2
Ventricular-like	25 (75.7)	$45.6 \pm 2.8^{*}$	$416.1 \pm 22.1^{**}$	$481.5 \pm 23.6^{**}$	115.1 ± 1.3	-72.3 ± 1.0	16.2 ± 2.4

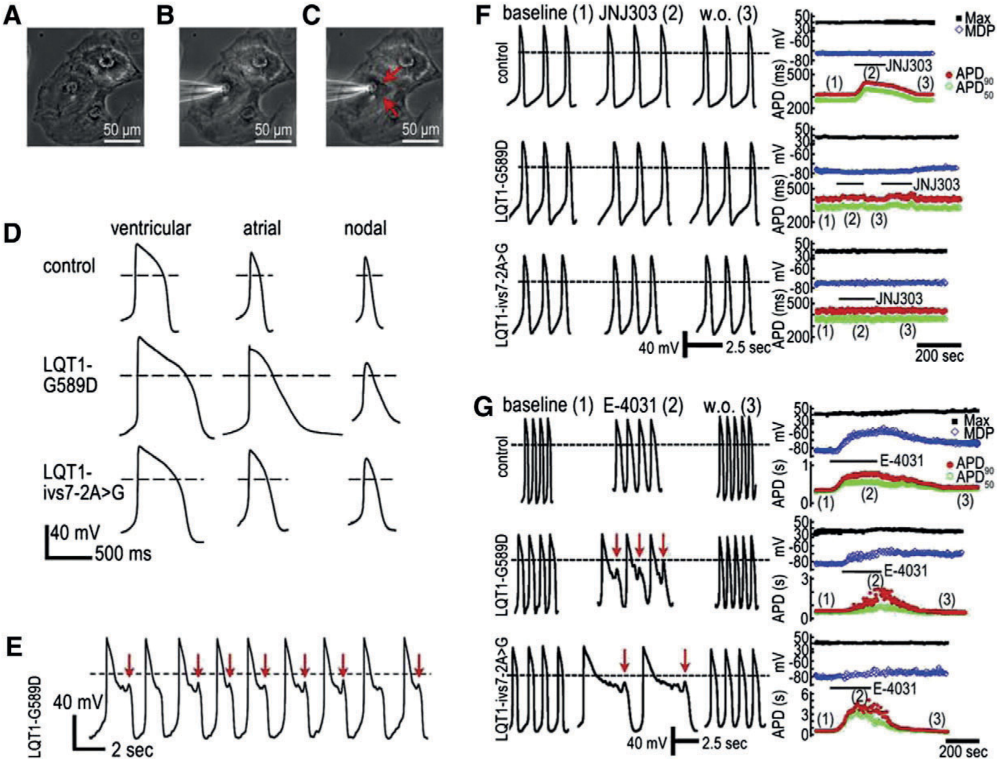

Fig. 5. Current clamp-recordings from control and LQT1-CMs carrying either G589D or ivs7-2A>G. Beating CMs un-patched (A), patched in relaxed phase (B), and patched in contracted phase (C). Arrows indicate the positions where the contraction can be seen (C). D: Current clamp-recordings of ventricular-, atrial- and nodal-like APs are depicted for control (upper panel), G589D (middle panel) and ivs7-2A>G (lower panel)-CMs. E: Baseline characteristics of spontaneous APs with early after depolarizations (EADs) in G589D-specific CMs: dashed line represents 0 mV and arrows indicate EADs. The effects of JNJ303 (F), and E-4031 (G) are shown for ventricular-like AP recordings from controls, as well as from G589D and ivs7-2A>G-CMs. Baseline (1), (2) effect of I_{Ks} (JNJ303) or I_{Ks} (E-4031) blocker, and (3) wash out measurement which fully recovers the effect of JNJ303 but only partially reverses the baseline AP characteristics after the E-4031 treatment. Arrows indicate EADs. The right panels show the time courses for the overshoot (Max), MDP, APD_{90} and APD_{50}. Marks (1), (2) and (3) indicate the times of AP extraction, and the bar represents the exposure of the cells for JNJ303 or E-4031.

Table 2B
Baseline characteristics for G589D-CMs with EADs. Data is presented as mean ± S.E.M.

	Number of cells (n)	BPM	APD_{50} (ms)	APD_{90} (ms)	APA (mV)	MDP (mV)	V_{max} (dV/dT)
LQT1 (G589D)							
Ventricular-like	5	30.1 ± 4.4	820.3 ± 93.1	1559.6 ± 407.1	112.8 ± 3.8	−71.5 ± 2.7	12.7 ± 2.3

inward currents, such as the spontaneous reactivation of the L-type Ca^{2+}-channel during prolonged action potential duration [31]. Therefore it can be assumed that abnormalities in Ca^{2+} transients shown in this study may correspond to EADs and lead to severe arrhythmias. A similar finding has been also earlier observed and demonstrated combining patch clamp and Ca^{2+}-imaging methods [32]. Further studies

Table 3A
Effect of I_{Ks} block on ventricular-like cardiomyocytes (CMs). Statistical difference of *paired sample t-test* is indicated by (*) $p < 0.05$ and (**) $p < 0.01$. Data is presented as mean ± S.E.M.

	Number of cells (n)	BPM	APD_{50} (ms)	APD_{90} (ms)	APA (mV)	MDP (mV)	V_{max} (dV/dT)
Control							
Baseline	10	48.3 ± 8.4	264.7 ± 47.0	334.0 ± 30.1	103.6 ± 3.9	−69.0 ± 2.5	25.3 ± 10.4
300 nM JNJ303		42.8 ± 7.6*	346.6 ± 68.0**	428.2 ± 79.9**	106.3 ± 4.6	−69.7 ± 2.6	27.8 ± 12.3
LQT1 (G589D)							
Baseline	9	44.7 ± 5.5	393.0 ± 57.8	500.4 ± 76.0	108.3 ± 3.1	−71.9 ± 2.6	11.6 ± 2.6
300 nM JNJ303		38.7 ± 5.2	423.6 ± 64.4	544.0 ± 86.0	106.9 ± 2.8	−70.8 ± 2.3	10.9 ± 2.1
LQT1 (ivs7-2A>G)							
Baseline	6	44.5 ± 3.2	387.0 ± 49.3	458.1 ± 51.6	112.4 ± 4.2	−74.2 ± 2.6	9.8 ± 1.9
300 nM JNJ303		43.1 ± 4.6	386.0 ± 36.0	452.0 ± 37.9	111.1 ± 3.6	−72.0 ± 3.1	9.8 ± 1.9

Table 3B

Effect of I_{Kr} block on ventricular-like CMs. Ventricular-like LQT1-specific CMs all showed early after-depolarizations (EADs) in the presence of E-4031. Statistical difference of *paired sample t-test* is indicated by (*) $p < 0.05$, (**) $p < 0.01$ and (***) $p < 0.001$. Data is presented as mean ± S.E.M.

	Number of cells (n)	BPM	APD_{50} (ms)	APD_{90} (ms)	APA (mV)	MDP (mV)	V_{max} (dV/dT)
Control −EADs							
Baseline	5	68.8 ± 4.3	256.8 ± 30.4	308.0 ± 30.1	111.4 ± 3.5	-74.6 ± 3.6	10.1 ± 1.4
100 nM E-4031		60.2 ± 7.6	332.4 ± 82.5	$535.3 \pm 102.9^{*}$	$83.3 \pm 7.5^{**}$	$-52.1 \pm 1.5^{**}$	6.2 ± 1.8
LQT1 (G589D) + EADs							
Baseline	5	43.2 ± 3.5	458.6 ± 25.1	536.0 ± 33.8	114.6 ± 0.4	-81.1 ± 0.9	13.7 ± 2.9
100 nM E-4031		$23.5 \pm 4.4^{*}$	$781.7 \pm 16.2^{***}$	$1703.8 \pm 100.8^{**}$	$103.6 \pm 1.7^{*}$	$-70.7 \pm 2.9^{*}$	$9.3 \pm 1.5^{*}$
LQT1 (ivs7-2A>G) + EADs							
Baseline	7	42.5 ± 3.4	464.7 ± 49.3	526.1 ± 53.6	117.5 ± 1.4	-73.6 ± 1.8	14.1 ± 0.9
100 nM E-4031		$13.8 \pm 2.6^{***}$	$1915.7 \pm 468.8^{*}$	$4055.8 \pm 1173.1^{*}$	$109.7 \pm 2.6^{**}$	$-64.1 \pm 2.7^{**}$	$11.3 \pm 1.0^{**}$

are needed to clarify the mechanism of the different Ca^{2+} transients observed in our study and their correlation with the EADs as well as with the motion abnormalities observed with the two different LQT1 related mutations.

In addition to conventional methods (patch clamp and Ca^{2+}-imaging), we also analyzed the mechanical beating behavior of single LQT1-specific CMs by video imaging and this analysis revealed either prolonged contraction (G589D) or disturbed relaxation (ivs7-2A>G) of the cells. This abnormality has not been reported earlier in iPSC-derived LQTS specific CMs, but the observation is in line with a clinical observation of prolonged contraction duration in LQTS mutation carriers compared to healthy individuals [33]. In this study, combined current clamp-measurements and video analysis of the mechanical behavior demonstrated the correlation between the prolonged APD and abnormal mechanical phenotype also in single LQT1 specific CMs.

The two patients of this study are both heterozygous for the LQT1-mutations and the allelic discrimination study revealed an imbalance in the expression of the WT and mutated forms of *KCNQ1*. The ratio of expression (WT:mutated) for G589D was found to be 4:1 and for ivs7-2A>G the ratio was 3:1. It was reported earlier that LQT1-CMs with R190Q mutation exhibited equal expression of wild type and mutant alleles [18]. With the expression ratios observed in our study, the probability that one or more mutated α-subunits are participating in forming the tetrameric I_{Ks} channel is about 70%. This is in accordance with the functional abnormalities observed in the videos recorded from our CMs. Ca^{2+}-imaging also revealed abnormal Ca^{2+} transients in LQT1 CMs but the proportions of abnormal CMs were slightly lower than those obtained with video imaging. The presence of spontaneous EADs were, however, considerably lower than other abnormalities. It is possible that there are compensatory mechanisms involved in

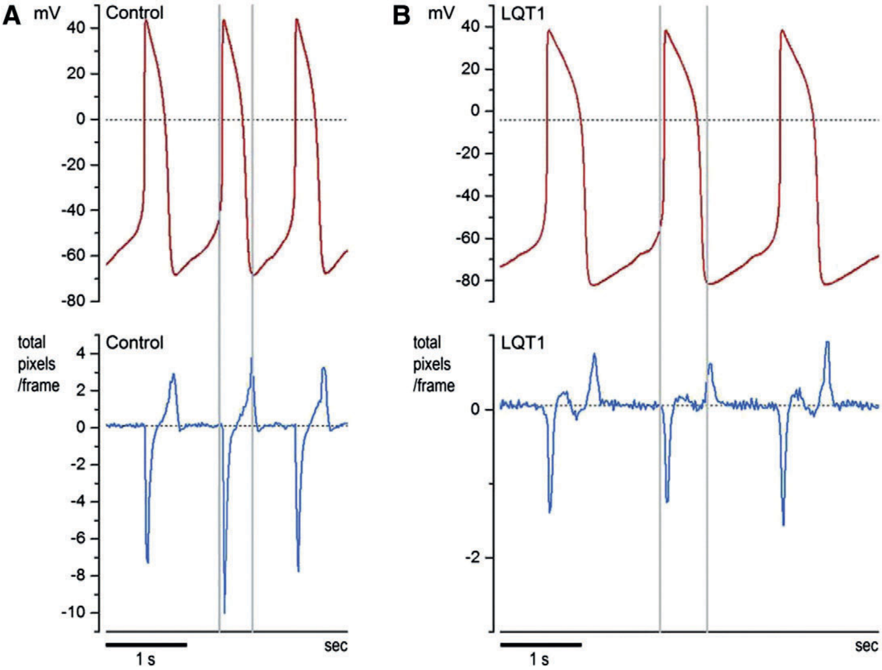

Fig. 6. Combined current clamp-measurements and video analysis. Control CMs (A) as well as the LQT1 specific CMs (B) showed a nice correlation in timing of the contraction and the AP: Contraction followed immediately after the initiation of AP. In LQT1 specific CMs the APD was clearly prolonged compared to the control cells and the mechanical abnormality observed by video analysis correlated with the prolongation of the APD (B).

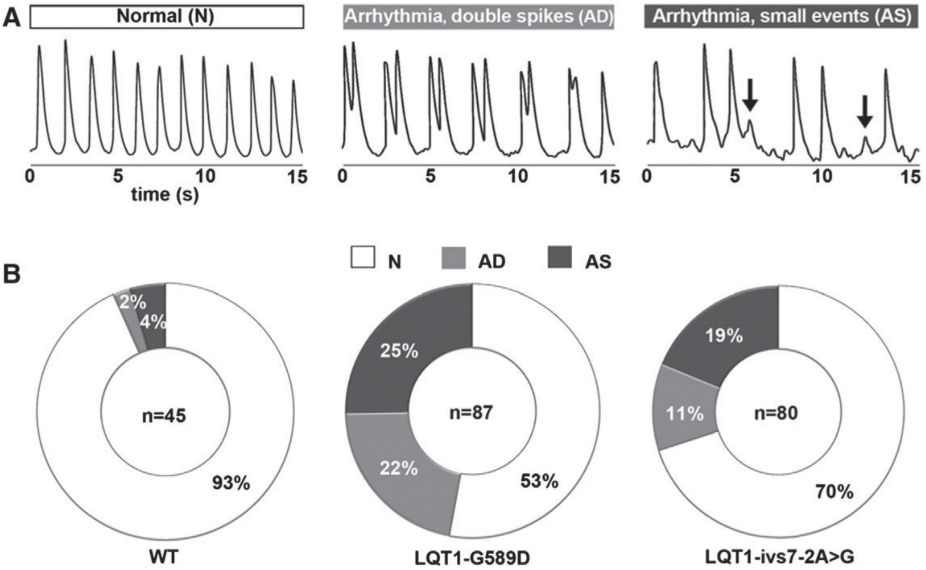

Fig. 7. Analysis of Ca^{2+} transients of control and LQT1 specific CMs. (A) Three different transient categories: normal transients with stable amplitude (N), arrhythmias with double or more Ca^{2+} peaks (AD), and small amplitude Ca^{2+} events (arrows) (AS) were found. (B) Doughnut charts indicate the percentage of the control and LQT1 specific CMs under each transient category (N, AD and AS).

electrical data obtained by patch clamp, resulting in a lower frequency of abnormalities compared to other methods. It is also important to point out that the ratios obtained by allelic imbalance measurements reflect the situation at mRNA level and do not accurately depict the proportions of the two alleles expressed at protein level since the transcripts may be alternatively processed before translation into proteins. Further, there is a possibility that the expression ratio of the WT and mutated allele may vary from cell to cell. It is also possible that the cells with different beating properties could represent also a particular CM subpopulation (ventricular, atrial or nodal).

Our findings support the previous studies [4,6] suggesting that mutations in different parts of the *KCNQ1* gene are associated with different clinical outcomes. However, no clinically distinct differences between the patient groups carrying the two mutations presented in this study have been reported. QTc of G589D-carriers has been reported to be 462 ± 38 if recorded from patients without any medication at the time of ECG recording. For the ivs7-2A>G the corresponding QTc value has been reported to be 470 ± 31 [21]. Both patients investigated here were symptomatic. G589D-patient, 46-year-old female has been suffering from syncopal spells. The other patient, 51-year-old female carrying ivs7-2A>G in *KCNQ1*, has suffered from dizziness, darkening of vision and more recently also from episodes of unconsciousness. On cell level G589D-CMs demonstrated more severely prolonged APDs which could be visualized as prolonged contracted state in beating CMs. The ivs7-2A>G-CMs had less severe APD prolongation at baseline, but they were more sensitive to agents blocking other ion channels. Additionally their beating behavior presented problems in relaxation phase suggesting other, currently unknown problems in repolarization currents in these cells. Since the patients present clinically similar phenotypes, it is most likely that there are some compensatory elements influencing the intact heart which moderate the clinical outcome. The highly organized transverse (t)-tubule structures in ventricular myocardium might partially balance the abnormalities in the Ca^{2+} transients of G589D and ivs7-2A>G-CMs [34]. At the same time, it is also possible that the typical abnormality that we observed in G589D-cells, namely prolonged contraction time, could actually generate more severe symptoms due to a shortened relaxation time.

This is the first time that two different LQTS related mutations in the same gene are reported to result in differences in functional properties of the patient specific CMs. Additionally, this is the first report to demonstrate abnormal mechanical beating properties of LQTS-specific single CMs. Earlier, the mechanical abnormalities with increased diastolic phase have been reported at the level of a whole heart of LQTS patients [33] but the abnormal mechanical phenotype in LQTS specific single cells is a novel and rather unexpected finding. Here we demonstrate that the disease specific beating of the cells can be distinguished from the normal behavior of single CMs just by analyzing the mechanical features of the beating. This novel method for characterization of CMs may generate additional detailed information from the beating of the cells and also from LQTS in general. In addition, this simple detection method allows developing it further for high through-put screening for LQTS specific – and also other cardiac disease specific – CMs.

5. Conclusion

CMs derived from two symptomatic LQT1 patients carrying two different *KCNQ1* mutations presented different manifestations when their electrical or mechanical beating properties were analyzed. APDs were significantly prolonged in both types of LQT1-CMs, but spontaneous EADs were present only in G589D-CMs. Mechanical beating behavior of G589D-CMs presented mostly prolonged contraction phase while inv7-2A>G-CMs had a fairly normal contraction time, but failed to relax properly. These results also demonstrate that simply by analyzing the mechanical beating behavior of the cells, the diseased CMs can be distinguished from the normal ones, providing a simple platform for diagnostic applications using iPSC derived CMs in the future.

Supplementary data to this article can be found online at http://dx.doi.org/10.1016/j.ijcha.2015.04.008.

Conflicts of interest

None.

Acknowledgments

We thank Merja Lehtinen and Markus Haponen for technical support (University of Tampere, BioMediTech and School of Medicine, Tampere, Finland). Christine Mummery (Department of Anatomy and Embryology, Leiden University Medical Center, Leiden, The Netherlands) is acknowledged for providing END-2 cells.

Acknowledgement of grant support: The study was funded by the Finnish Funding Agency for Technology and Innovation (40345/11), Finnish Cardiovascular Foundation, Pirkanmaa Hospital District, Finnish Cultural Foundation Pirkanmaa Regional Fund and Tampere Graduate Program in Biomedicine and Biotechnology.

References

[1] Hedley PL, Jørgensen P, Schlamowitz S, Wangari R, Moolman-Smook J, Brink PA, et al. The genetic basis of long QT and short QT syndromes: a mutation update. Hum Mutat 2009;30(11):1486–511.
[2] Barhanin J, Lesage F, Guillemare E, Fink M, Lazdunski M, Romey G. KvLQT1 and IsK (minK) proteins associate to form the I_{Ks} cardiac potassium current. Nature 1996; 384(6604):78–80.
[3] Sanguinetti MC, Curran ME, Zou A, Shen J, Specter PS, Atkinson DL, et al. Coassembly of KvLQT1 and minK (IsK) proteins to form cardiac I_{Ks} potassium channel. Nature 1996;384(6604):80–3.
[4] Laksman ZWM, Hamilton RM, Chockalingam P, Ballantyne E, Stephenson EA, Gross GJ, et al. Mutation location effect on severity of phenotype during exercise testing in type 1 long-QT syndrome: impact of transmembrane and c-loop location. J Cardiovasc Electrophysiol 2013;24(9):1015–20.
[5] Splawski I, Shen J, Timothy KW, Lehmann MH, Priori S, Robinson JL, et al. Spectrum of mutations in long-QT syndrome genes: KVLQT1, HERG, SCN5A, KCNE1, and KCNE2. Circulation 2000;102(10):1178–85.
[6] Barsheshet A, Goldenberg I, O-Uchi J, Moss AJ, Jons C, Shimizu W, et al. Mutations in cytoplasmic loops of the KCNQ1 channel and the risk of life-threatening events: implications for mutation-specific response to Î^2-blocker therapy in type 1 long-QT syndrome. Circulation 2012;125(16):1988–96.
[7] Fodstad H, Bendahhou S, Rougier J, Laitinen-Forsblom P, Barhanin J, Abriel H, et al. Molecular characterization of two founder mutations causing long QT syndrome and identification of compound heterozygous patients. Ann Med 2006;38(4): 294–304.
[8] Piippo K, Swan H, Pasternack M, Chapman H, Paavonen K, Viitasalo M, et al. A founder mutation of the potassium channel KCNQ1 in long QT syndrome: implications for estimation of disease prevalence and molecular diagnostics. J Am Coll Cardiol 2001;37(2):562–8.
[9] Aromolaran AS, Subramanyam P, Chang DD, Kobertz WR, Colecraft HM. LQT1 mutations in KCNQ1 C-terminus assembly domain suppress IKs using different mechanisms. Cardiovasc Res 2014;104:501–11.
[10] Takahashi K, Tanabe K, Ohnuki M, Narita M, Ichisaka T, Tomoda K, et al. Induction of pluripotent stem cells from adult human fibroblasts by defined factors. Cell 2007; 131(5):861–72.
[11] Yu J, Vodyanik MA, Smuga-Otto K, Antosiewicz-Bourget J, Frane JL, Tian S, et al. Induced pluripotent stem cell lines derived from human somatic cells. Science 2007; 318(5858):1917–20.
[12] Davis RP, Casini S, van den Berg CW, Hoekstra M, Remme CA, Dambrot C, et al. Cardiomyocytes derived from pluripotent stem cells recapitulate electrophysiological characteristics of an overlap syndrome of cardiac sodium channel disease. Circulation 2012;125(25):3079–91.
[13] Egashira T, Yuasa S, Suzuki T, Aizawa Y, Yamakawa H, Matsuhashi T, et al. Disease characterization using LQTS-specific induced pluripotent stem cells. Cardiovasc Res 2012;95(4):419–29.
[14] Itzhaki I, Maizels L, Huber I, Zwi-Dantsis L, Caspi O, Winterstern A, et al. Modelling the long QT syndrome with induced pluripotent stem cells. Nature 2011; 471(7337):225–9.
[15] Lahti AL, Kujala VJ, Chapman H, Koivisto A-P, Pekkanen-Mattila M, Kerkelä E, et al. Model for long QT syndrome type 2 using human iPS cells demonstrates arrhythmogenic characteristics in cell culture. Dis Model Mech 2012;5(2):220–30.
[16] Malan D, Friedrichs S, Fleischmann BK, Sasse P. Cardiomyocytes obtained from induced pluripotent stem cells with long-QT syndrome 3 recapitulate typical disease-specific features in vitro. Circ Res 2011;109(8):841–7.
[17] Matsa E, Rajamohan D, Dick E, Young L, Mellor I, Staniforth A, et al. Drug evaluation in cardiomyocytes derived from human induced pluripotent stem cells carrying a long QT syndrome type 2 mutation. Eur Heart J 2011;32(8):952–62.
[18] Moretti A, Bellin M, Welling A, Jung CB, Lam JT, Bott-Flügel L, et al. Patient-specific induced pluripotent stem-cell models for long-QT syndrome. NEJM 2010;363(15): 1397–409.
[19] Hoebe RA, Van Der Voort HTM, Stap J, Van Noorden CJF, Manders EMM. Quantitative determination of the reduction of phototoxicity and photobleaching by controlled light exposure microscopy. J Microsc 2008;231(1):9–20.
[20] Paredes RM, Etzler JC, Watts LT, Zheng W, Lechleiter JD. Chemical calcium indicators. Methods 2008;46(3):143–51.
[21] Fodstad H, Swan H, Laitinen P, Piippo K, Paavonen K, Viitasalo M, et al. Four potassium channel mutations account for 73% of the genetic spectrum underlying long-QT syndrome (LQTS) and provide evidence for a strong founder effect in Finland. Ann Med 2004;36(1):53–63.
[22] Ahola A, Kiviaho AL, Larsson K, Honkanen M, Aalto-Setälä K, Hyttinen J. Video image based analysis of single human induced pluripotent stem cell derived cardiomyocyte beating dynamics using digital image correlation. Biomed Eng Online 2014;7:13–39.
[23] Mummery C, Ward-van Oostwaard D, Doevendans P, Spijker R, van den Brink S, Hassink R, et al. Differentiation of human embryonic stem cells to cardiomyocytes: role of coculture with visceral endoderm-like cells. Circulation 2003;107(21): 2733–40.
[24] Wettwer E, Scholtysik G, Schaad A, Himmel H, Ravens U. Effects of the new class III antiarrhythmic drug E-4031 on myocardial contractility and electrophysiological parameters. J Cardiovasc Pharmacol 1991;17(3):480–7.
[25] Towart R, Linders JTM, Hermans AN, Rohrbacher J, van der Linde HJ, Ercken M, et al. Blockade of the I_{Ks} potassium channel: an overlooked cardiovascular liability in drug safety screening? J Pharmacol Toxicol Methods 2009;60(1):1–10.
[26] Rae J, Cooper K, Gates P, Watsky M. Low access resistance perforated patch recordings using amphotericin B. J Neurosci Methods 1991;37(1):15–26.
[27] Bombardini T, Gemignani V, Bianchini E, Venneri L, Petersen C, Pasanisi E, et al. Diastolic time–frequency relation in the stress echo lab: filling timing and flow at different heart rates. Cardiovasc Ultrasound 2008;6(15).
[28] Heijman J, Spätjens RL, Seyen SR, Lentink V, Kuijpers HJ, Boulet IR, et al. Dominant-negative control of cAMP-dependent I_{Ks} upregulation in human long-QT syndrome type 1. Circ Res 2012;110(2):211–9.
[29] Marx SO, Kurokawa J, Reiken S, Motoike H, D'Armiento J, Marks AR, et al. Requirement of a macromolecular signaling complex for beta adrenergic receptor modulation of the KCNQ1–KCNE1 potassium channel. Science 2002;295(5554):496–9.
[30] Doss M, Di Diego J, Goodrow R, Wu Y, Cordeiro J, Nesterenko V, et al. Maximum diastolic potential of human induced pluripotent stem cell-derived cardiomyocytes depends critically on I_{Kr}. PLoS One 2012;7(7):e40288.
[31] January CT, Moscucci A. Cellular mechanisms of early after depolarizations. Ann NY Acad Sci 1992;644(1):23–32.
[32] Spencer CI, Baba S, Nakamura K, Hua EA, Sears MAF, Fu C, et al. Calcium transients closely reflect prolonged action potentials in iPSC models of inherited cardiac arrhythmia. Stem Cell Rep 2014;3(2):269–81.
[33] Haugaa KH, Amlie JP, Berge KE, Leren TP, Smiseth OA, Edvardsen T. Transmural differences in myocardial contraction in long-QT syndrome: mechanical consequences of ion channel dysfunction. Circulation 2010;122(14):1355–63.
[34] Ferrantini C, Crocini C, Coppini R, Vanzi F, Tesi C, Cerbai E, et al. The transverse-axial tubular system of cardiomyocytes. Cell Mol Life Sci 2013;70(24):4695–710.

PUBLICATION
IV

Simultaneous Measurement of Contraction and Calcium Transients in Stem Cell Derived Cardiomyocytes

Ahola, A., Pölönen, R.-P., Aalto-Setälä, K. & Hyttinen, J.

Annals of Biomedical Engineering (2018), 46:148
https://doi.org/10.1007/s10439-017-1933-2

Annals of Biomedical Engineering, Vol. 46, No. 1, January 2018 (*© 2017*) pp. 148–158
DOI: 10.1007/s10439-017-1933-2

Simultaneous Measurement of Contraction and Calcium Transients in Stem Cell Derived Cardiomyocytes

A. AHOLA,[1] R.-P. PÖLÖNEN,[2] K. AALTO-SETÄLÄ,[2,3] and J. HYTTINEN[1]

[1]BioMediTech Institute and Faculty of Biomedical Sciences and Engineering, Tampere University of Technology, Korkeakoulunkatu 10, 33720 Tampere, Finland; [2]BioMediTech Institute and Faculty of Medicine and Life Sciences, University of Tampere, Tampere, Finland; and [3]Heart Hospital, Tampere University Hospital, Tampere, Finland

(Received 29 June 2017; accepted 19 September 2017; published online 3 October 2017)

Associate Editor Smadar Cohen oversaw the review of this article.

Abstract—Induced pluripotent stem cell derived cardiomyocytes (iPSC-CM) provide a powerful platform for disease modeling and drug development *in vitro*. Traditionally, electrophysiological methods or fluorescent dyes (e.g. calcium) have been used in their functional characterization. Recently, video microscopy has enabled non-invasive analysis of CM contractile motion. Simultaneous assessments of motion and calcium transients have not been generally conducted, as motion detection methods are affected by changing pixel intensities in calcium imaging. Here, we present for the first time a protocol for simultaneous video-based measurement of contraction and calcium with fluorescent dye Fluo-4 videos without corrections, providing data on both ionic and mechanic activity. The method and its accuracy are assessed by measuring the effect of fluorescence and background light on transient widths and contraction velocity amplitudes. We demonstrate the method by showing the contraction-calcium relation and measuring the transient time intervals in catecholaminergic polymorphic ventricular tachycardia patient specific iPSC-CMs and healthy controls. Our validation shows that the simultaneous method provides comparable data to combined individual measurements, providing a new tool for measuring CM biomechanics and calcium simultaneously. Our results with calcium sensitive dyes suggest the method could be expanded to use with other fluorescent reporters as well.

Keywords—Biomechanics, Fluorescence, Motion analysis, Calcium-contraction coupling.

ABBREVIATIONS

CaPIV	Calcium particle image velocimetry
CD	Contraction duration
CM	Cardiomyocyte
CPVT	Catecholaminergic polymorphic ventricular tachycardia
CTD	Calcium transient duration
hiPSC	Human induced pluripotent stem cell
iPSC	Induced pluripotent stem cell
iPSC-CM	Induced pluripotent stem cell derived cardiomyocyte
PIV	Particle image velocimetry
RYR	Cardiac ryanodine receptor
MQD	Minimum quadratic difference
WT	Wild type

INTRODUCTION

Cardiovascular diseases represent the leading cause of death globally. Additionally, adverse effects of cardioactive and non-cardiac drugs remain the most common reason for market withdrawal. Induced pluripotent stem cell derived cardiomyocytes (iPSC-CM) have presented a promising platform for both disease modeling and drug development with healthy and patient specific cells. These studies have been traditionally done using electrical measurements, while methods for measuring mechanical function of cells without extensive instrumentation have only recently been emerging. High throughput methods for drug screening with iPSC-CMs are needed, as the large variability in electrophysiological results regarding iPSC-CM bring about the need for a greater number of experiments.[15] These methods could be used in addition for development of personalized therapy for genetic cardiac diseases, such as catecholaminergic polymorphic ventricular tachycardia (CPVT).[10]

Address correspondence to A. Ahola, BioMediTech Institute and Faculty of Biomedical Sciences and Engineering, Tampere University of Technology, Korkeakoulunkatu 10, 33720 Tampere, Finland. Electronic mail: antti.l.ahola@tut.fi

The commonly used methods for analyzing electrophysiological functions of cardiomyocytes (CM) include calcium imaging,[18] patch clamping[8,11] and microelectrode array[11] studies. However, these measurements often require manual operation by trained personnel and thus are not well suited towards high-throughput applications. In addition, while the ionic function they measure control the mechanical function of the CMs, the resulting signals do not relate directly to the resulting biomechanics that is the actual CM functional aspect. CM biomechanics has traditionally been measured *in vitro* using atomic force microscopy,[19] mechanical transduction with microposts[4,22] and traction force microscopy.[21] Video-based methods have been developed and studied by us[1,2,9] and by several other groups.[6,7,14] As the method is non-invasive and has easy to use instrumentation, video analysis has good high-throughput capabilities.

Calcium imaging can be used as a powerful tool for high throughput profiling of drug responses *in vitro*. In CMs, calcium plays a key role as a second messenger of excitation contraction coupling. Drug effects are reflected as changes in calcium transient profile. With fluorescent calcium reporter dyes, either small molecule or genetically encoded, it is possible to visualize and record calcium fluxes inside CMs. Special high throughput imaging apparatuses, for example Hamamatsu FDSS,[3] allow simultaneous reading of calcium transients from up to hundreds of samples. These platforms can be used to study several disease models and drugs in a short time period compared to conventional microscopes. High content screening produces large amount of data, which require automated software for handling and analyzing the massive amounts of data.[17]

The major benefit of human iPSC (hiPSC) in CM studies is their power to provide CMs from specific phenotypes. Here CPVT cells was selected as targeted application example for our novel methodology. CPVT is a rare but severe inherited cardiac disease in structurally normal hearts, which may lead to sudden cardiac death. CPVT patients experience arrhythmias during mental or physical stress. CPVT is associated with mutations in *RYR2* gene, coding for cardiac ryanodine receptor (RYR), among few other disease-associated genes. Therapy includes drug treatment with beta-blockers, implantable cardiac defibrillators or left cardiac sympathetic denervation.[23] The calcium abnormalities arising from mutations in RYR2 reflect to contractile motion of CMs. Therefore, CPVT specific iPSC-CMs are interesting platform to study not only calcium kinetics but also the contractile motion simultaneously.

So far, the ionic and mechanical functions have been studied simultaneously using specific platforms, such as on microposts.[4,22] Video-based measurements, however, do not require such systems: microscopes and video cameras are typical laboratory instruments, which as such enable video-based measurements. Methods to provide combined ionic and biomechanic assessment of the CMs could offer novel avenues to look into disease mechanisms and drug effects. Previously, it has not been able to track motion in bright field microscopy simultaneously with fluorescent reporters due to the effects of fluorescent induced changes in pixel intensity on the motion detection methods. In previous studies the fluorescence background has been subtracted from images with mixed phase-contrast and fluorescence.[6] In another study, calcium reporter GCaMP6f –gene was used and simultaneous measurement was conducted with computed local intensity normalization in each interrogation window to counteract the effect of the intensity changes.[7]

In this study, we combine concurrent calcium imaging with our previously developed video analysis method, which uses minimum quadratic difference (MQD) based particle image velocimetry (PIV) and assess biomechanical and ionic function simultaneously from videos of fluorescent calcium imaging. As in the MQD method we used[1] sets equal weight to all image pixels,[5] we hypothesized that the method could work also in calcium imaging by increasing background lighting conditions to make motion more visible. To verify our hypothesis, consecutive frames with fluorescent calcium dye excitation and transmission channels were measured with two background light levels. We validated the method by comparing contraction and calcium transient widths as well as PIV amplitudes from frames with and without the fluorescent excitation, and with and without background light. We demonstrated the method by measuring the relation of contraction and calcium in wild type (WT) and CPVT cells, and calculated the time interval between the maximum signal onset and offset rates of change in both signals.

MATERIALS AND METHODS

Patient-Specific Human iPSC Lines

Details on hiPSC culturing and CM differentiation are available in supplements.

In this study both normal control CMs and diseased CMs prone to arrhythmias were used. The diseased CPVT cells were derived from patients having mutations in *RYR2* gene, associated with structural changes in RYR, resulting in abnormal release of Ca^{2+} from sarcoplasmic reticulum and increased ventricular arrhythmias when heart rate increases. Two CPVT patient specific hiPSC lines were used: UTA.05605.CPVT carrying exon 3 deletion and UTA.05404.CPVT carrying V4563F mutation in *RYR2* gene (referred to as CPVTa and CPVTb respectively). UTA.04602.WT cell line was used as a control. The collection of biopsies for generating patient specific hiPSC lines was approved by the ethical committee of Pirkanmaa Hospital District (Aalto-Setälä R08070) and written informed consent was obtained from all the donors.

Imaging Protocol

Details on imaging protocol are available in supplements.

CMs plated on glass coverslips were loaded with Fluo-4 AM. Imaging was done using Olympus IX71 inverted microscope with Polychrome V and TH4-200 light sources and Andor iXon 885 EMCCD camera. Cells were perfused with warmed (37 °C) perfusate medium. Two channels were recorded consecutively: the Olympus light source was turned on to obtain video image while still being able to discern Ca^{2+} fluctuations. The recording process is illustrated in Fig. 1a. In total, 25 videos were recorded: 7 CPVTa, 5 CPVTb and 13 WT videos. The recordings were all baseline measurements.

Video Data Processing

The obtained recordings, consisting of video imaging and calcium imaging data with light source off and on, were categorized and processed. The region of interest for each recording was selected based on both intensity of the calcium fluctuations and observed motion.

MQD based PIV, as described previously,[1,2,9] was used for determining velocity vector fields in the video image series. The process was applied to both transmission and calcium imaging with background light on, resulting in two series of velocity vector fields from which motion signals are calculated: one from the frames with only visible light—traditional PIV measurement—and another from the frames with fluorescent emission of calcium indicator, defined as calcium PIV (CaPIV). Only the frames with light source on were included in these sets. Calcium signals were calculated from the pixel intensity in each frame. With respect to the light source status, two consecutive data series were obtained: calcium with fluorescent light from Polychrome V—Ca (dark)—and calcium with light from both Polychrome V and Olympus TH4-200 (transmission) - Ca (bright). With this method, four signal types were obtained—two from both modalities: calcium and motion. The process is illustrated in Fig. 1a.

Using our previously described method, shortly, the directional motion signals indicating contraction and relaxation velocities were obtained from velocity vector fields by determining a CM beating focus point. The motion directed towards it was defined as radial movement and the perpendicular motion as tangential, resulting in motion signals. As opposed to the previous article, each vector was divided in these components with respect to their location. The same region of interest was used for calcium imaging. Further, contraction signals were calculated from the motion signals by integration with respect to time. Linear detrending was applied to the resulting signals to correct the baseline.

As a non-ratiometric dye was used and absolute contraction amplitude was not assessed, calcium, contraction and motion signals were all normalized to interval [0,1] by linear rescaling for visualization. The motion signal baseline was then set to zero, with contraction being positive and relaxation negative. For calcium and contraction signals, one beat long cross-

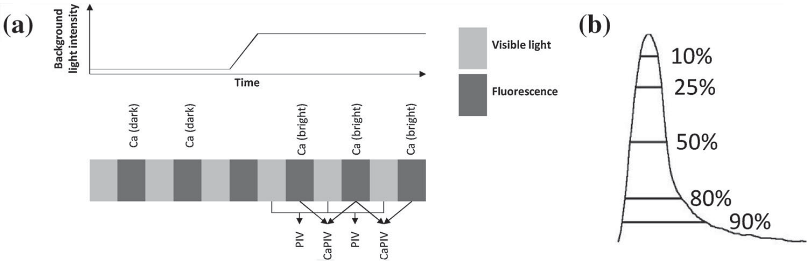

FIGURE 1. Imaging protocol, processing of the video channels and definition of transient duration parameters. (a) Fluorescent calcium and visible light were recorded in consecutive frames. Midway during the recording, light source was turned on to increase the background light intensity, allowing video signal to be captured. Traditional PIV was measured from the frames with only visible light and CaPIV signal was measured from frames with calcium fluorescence present. Calcium signal was categorized based on the background light intensity to Ca (dark) and Ca (bright). (b) Transient duration parameters are defined as percentages from the peak maximum, similarly as when classifying action potentials.

correlation based averaged signal templates were calculated, as described earlier.[2] The averaging was synchronized based on the maximum rate of change during the onset of the contraction or transient. A correlation coefficient of 0.5 was used to exclude only the most abnormal beats.

Signal Comparison

The similarity of the recorded signals was measured by determining parameters describing the waveform widths and amplitudes. The duration of the contraction in the templates was characterized by calculating contraction duration (CD) parameters and the duration of calcium by calcium transient duration (CTD) parameters. The durations at percentages of the maximum peak height were defined as shown in Fig. 1-b—an approach similar to characterization of action potentials. The used parameters were CD10, CD25, CD50, CD80 and CD90, representing the width of the peak at each percentage measured from the peak in each waveform. For calcium, the same CTD parameters were determined, respectively.

Temporal differences between the contraction and calcium transient were measured using the combined signals from the maximum rate of change in the onset and offset of CaPIV and Ca (bright). As the calcium transients may have several peaks of different heights, this approach was selected instead of comparing the time difference between peaks themselves.

Statistics

Mean values and standard deviations of CDs and CTDs, as well as temporal differences between contraction and calcium were calculated. CDs and CTDs were tested against each other using a two-sample *t* test with all combinations of PIV, CaPIV, Ca (dark) and Ca (bright). In addition, durations from WT cell videos ($n = 13$) were tested against those measured from CPVT cell videos (CPVTa $n = 7$, CPVTb $n = 5$) regarding all combinations of signal types from the same modality—calcium and motion. Waveform amplitude similarity was determined by calculating the symmetric mean absolute percentage error of contraction motion velocity magnitudes of each contraction in PIV and CaPIV signals. Linear regression was used to map width parameters against the other signal types, and their similarity was estimated using linear regression R^2 parameter. *P*-values below 0.05 were considered statistically significant. The statistical analysis was performed in MATLAB R2014a, The Mathworks, Inc.

RESULTS

Beating Characteristics

For WT, the average beating rate was 22 beats per min with a ± 10.8 standard deviation. For CPVTa and CPVTb the values were 20.7 ± 12.9 and 12.2 ± 5.6 beats per min, respectively. The number of beats in CPVT videos were lower than in WT videos as some videos only had two beats with the background light on/off.

Representative Signals

Representative signals with synchronized motion (CaPIV) and calcium signals (Ca (bright)) were calculated. For each cell line, both motion and contraction signals are shown with overlaid calcium transients in Fig. 2. In motion signals (left side), an upward peak signifies contractile and downward peak relaxation movement velocity. Motion signal is used for illustrating the fine details of the movement. Contraction signal (right side)—the integral of the motion signal with respect to time—shows displacement during a contraction. The contraction signal enables easier comparison of calcium and contraction. For this illustration, the signals were linearly normalized separately for visualization.

In the visual inspection of the displacement and calcium signals from studied WT cell populations, contraction started only after increase in calcium transient had started. Contraction signals typically had a steeper offset slope than calcium, which had a longer tail, and started to fall slightly earlier. In CPVTa cells, in some signals motion followed the calcium transient with a longer delay than in WT. No evident afterdepolarizations or tailing of calcium was present in the signals. In CPVTb, the contraction signal started to fall slightly later than the calcium transient.

Method Validation

The simultaneous recording method was validated by comparing signals obtained from PIV (motion from videos without fluorescence), CaPIV (motion from videos with fluorescence), Ca (bright) (calcium with background light) and Ca (dark) (without background light) signals. CTD parameters from the two calcium signals, CD parameters from the two contraction signals, and amplitudes from the two motion velocity signals were calculated.

PIV and CaPIV did not show statistically significant differences between the means of CD parameters. This can be seen in Fig. 3, where the overlaid CaPIV (in blue) and PIV (red) show a very similar curve, with

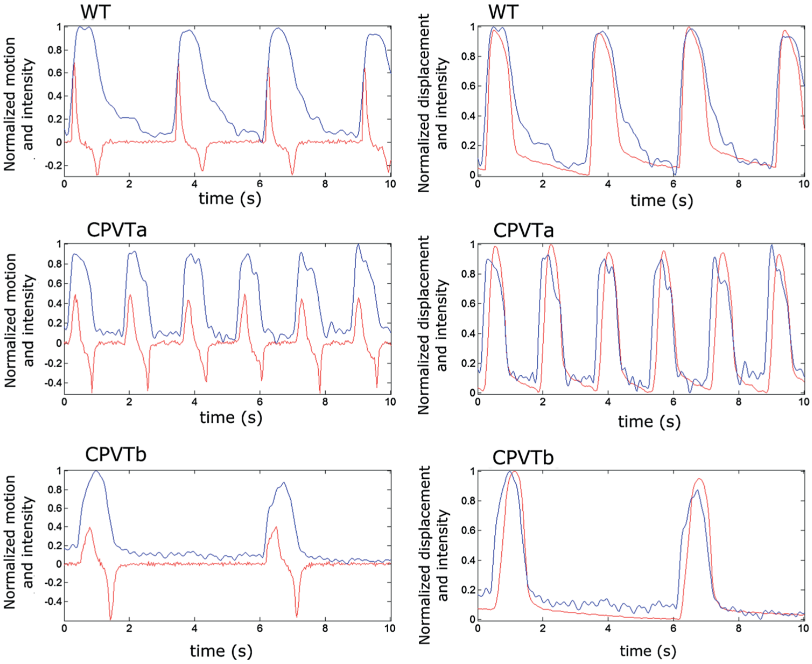

FIGURE 2. **Representative motion (left side) and displacement (right side) signals plotted over calcium transients for the three cell lines. In the motion signals, the contractile movement velocity is represented with and upward peak and the relaxation movement velocity as a downward peak in red, while calcium transient is shown in blue. In the displacement signals (right side), representing the motion velocity signal integral with respect to time, contraction is shown in red and calcium transient in blue. Representative signals are shown for the three cell lines.**

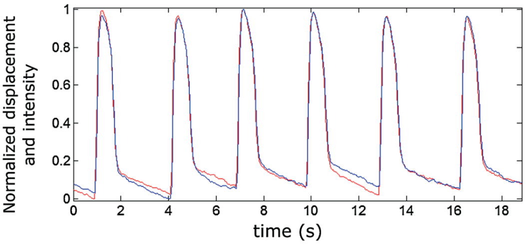

FIGURE 3. **A representative displacement measurement showing overlaid CaPIV (blue) with fluorescence and PIV (shown in red) without fluorescence.**

minor deviations showing near the baseline. Similarly, Ca (bright) and Ca (dark) did not exhibit significant differences in CTD parameters. This indicates that no major differences were induced by the change in lighting to enable the combined signal measurement.

The symmetric mean absolute percentage errors between PIV and CaPIV contraction velocity amplitudes were calculated for the contractions in each recording. The difference was found to be 6.42 ± 3.44% in WT, 4.11 ± 5.01% in CPVTa and 2.73 ± 1.57% in CPVTb. The total error for all recordings was 5.04 ± 3.87%.

Assessment of Cell Line Functions Using Simultaneous Contraction and Calcium

Contraction and Calcium Signal Characteristics

The widths of the contraction peak in CaPIV and the calcium transient Ca (bright) in the simultaneous measurement were characterized by parameters indicating their duration at percentages of the peak maximum height. The CD- and CTD-parameters were calculated at signal levels 10, 25, 50, 80 and 90 and shown in Table 1.

In both CD and CTD parameters, the standard deviation was very high indicating high variance within the cell lines.

Similarity of Signals Between Modalities

Linear regressions between pairs of contraction/calcium transient durations for the four different signals were calculated. The results are shown in Table 2. Pairs of the same modality (leftmost tables)

TABLE 1. Calcium and contraction signal characterization.

	CD10	CD25	CD50	CD80	CD90	CTD10	CTD25	CTD50	CTD80	CTD90
WT	229 ± 77 ms	343 ± 118 ms	475 ± 165 ms	684 ± 206 ms	888 ± 391 ms	328 ± 104 ms	513 ± 148 ms	797 ± 227 ms	1315 ± 420 ms	1663 ± 570 ms
CPVTa	317 ± 185 ms	436 ± 200 ms	590 ± 266 ms	888 ± 250 ms	1340 ± 651 ms	356 ± 150 ms	581 ± 236 ms	797 ± 305 ms	1057 ± 330 ms	1283 ± 414 ms
CPVTb	255 ± 175 ms	379 ± 181 ms	515 ± 202 ms	714 ± 190 ms	919 ± 301 ms	273 ± 150 ms	413 ± 244 ms	589 ± 268 ms	788 ± 296 ms	905 ± 415 ms

The characterization of contraction and calcium in the simultaneous measurement. The parameters CD10–CD90 refer to contraction peak widths and CTD10–CTD90 to calcium transient widths at percentages of maximum peak height.

show high R^2 values: PIV exhibits very high coefficient of determination (R^2) values with CaPIV in both WT and CPVT cells. Only in CD90 the value of CPVTb R^2 was below 0.9. Likewise, high R^2 values were obtained from regression between Ca (bright) and Ca (dark) even though the signals were not concurrent like motion signals. In calcium, R^2 values below 0.9 were seen in CPVTa CTD25 and CTD90, and a relatively low value in CTD10 of CPVTb. Low R^2 values were typically seen in cross-modality pairs near the baseline (CD/CTD80 and CD/CTD90), especially in CPVTa. These results indicate the simultaneous measurement works well—the signals of the same modality are indeed very similar in shape. Further, the simultaneous motion and calcium measurements show a disconnection of calcium and motion in CPVT lines—especially CPVTa—which is not evident in calcium measurements.

Calcium-Motion Coupling

The concurrent calcium-contraction measurement allows the measurement of synchronicity in calcium and motion dynamics. Here, we looked at the temporal differences between these signals by calculating the time points of maximum rate of change in the onsets and offsets of calcium transient and motion from Ca (bright) and CaPIV, respectively. The obtained values are shown in Table 3.

Positive time values in onset and offset indicate that motion signal is following the calcium transient. Some negative values in offset were obtained indicating that motion reached its peak relaxation velocity before maximum calcium decline velocity. In Table 3 this is indicated by large standard deviation compared to the offset value especially for CPVTa. Although CPVTa shows a higher onset and CPVTb a higher offset in mean times, the findings are not statistically significant due to the large variability. Also these results reveal that CPVTa and CPVTb show different contraction-calcium coupling dynamics from WT but also different from each other.

The difference between the means of motion and calcium signal parameters was statistically significant in WT in all parameters ($p < 0.05$ in CD/CTD10, $p < 0.01$ in the remaining parameters), but not in CPVTa or CPVTb. This finding shows that measurements of motion and calcium provide complementary information and insight on the Ca^{2+} and contraction coupling dynamics.

When comparing the cell lines, the motion modalities PIV and CaPIV did not exhibit significant differences between the contraction durations of WT and CPVT cell lines. However, calcium modalities Ca (bright) and Ca (dark) showed significant differences

TABLE 2. Linear regression of CD and CTD parameters.

	PIV/CaPIV			PIV/Ca (bright)			CaPIV/Ca (bright)		
	WT	CPVTa	CPVTb	WT	CPVTa	CPVTb	WT	CPVTa	CPVTb
10	0.983	0.997	0.975	0.663	0.128	0.430	0.698	0.136	0.511
25	0.943	0.997	0.996	0.737	0.540	0.897	0.698	0.537	0.888
50	0.965	0.997	0.995	0.637	0.731	0.732	0.612	0.684	0.752
80	0.967	0.991	0.976	0.640	0.129	0.451	0.630	0.091	0.384
90	0.966	0.989	0.817	0.710	0.000	0.186	0.724	0.003	0.057
	Ca (bright)/Ca (dark)			PIV/Ca (dark)			CaPIV/Ca (dark)		
	WT	CPVTa	CPVTb	WT	CPVTa	CPVTb	WT	CPVTa	CPVTb
10	0.914	0.913	0.567	0.518	0.138	0.958	0.525	0.150	0.945
25	0.939	0.753	0.859	0.685	0.605	0.834	0.612	0.616	0.793
50	0.951	0.970	0.991	0.552	0.741	0.742	0.507	0.702	0.760
80	0.968	0.946	0.992	0.573	0.155	0.539	0.564	0.119	0.473
90	0.950	0.778	0.961	0.686	0.070	0.274	0.685	0.111	0.082

Linear regression between the contraction (CD)/calcium transient durations (CTD) at percentages of the maximum peak height (10, 25, 50, 80 and 90) for each pair of measured signals.

TABLE 3. Time intervals between calcium and contraction.

	WT	CPVTa	CPVTb
Ca (bright) and CaPIV difference on onset	163 ± 132 ms	238 ± 136 ms	126 ± 102 ms
Ca (bright) and CaPIV difference on offset	40 ± 91 ms	24 ± 142 ms	113 ± 75 ms

Mean time differences and standard deviations between the calcium transient and contraction in different cell lines, in milliseconds. The differences between cell lines are not statistically significant.

between means of WT and CPVTb in CTD80 and CTD90. Neither calcium nor motion modalities displayed significant differences between WT and CPVTa.

DISCUSSION

We developed and demonstrated a method for simultaneous CM motion and calcium transient recording from fluorescent videos. The method uses simultaneous application of both transmission and fluorescent light source. In traditional methods the calcium based fluorescent signal could represent a source of error for PIV analysis and further, the brightfield imaging could affect the calcium imaging transients. We tested the method susceptibility to both error sources by separating these factors with interlacing brightfield and fluorescent video frames and observed that a simultaneous measurement of calcium and contraction is feasible.

We recorded consecutive frames of brightfield imaging and calcium fluorescent imaging in iPSC-CMs on video, with background light on and off. Four different signals were obtained: motion from brightfield video (PIV), motion from video with fluorescence (CaPIV), calcium imaging without background light (Ca (dark)) and calcium imaging with background light (Ca (bright)). We characterized the signals for both validation and demonstration of the method. With this procedure, we aimed to demonstrate that CM contraction could be quantified reliably while running a simultaneous fluorescent measurement.

Further, we demonstrated the usefulness of the simultaneous measurement by comparing the calcium and contraction signals, calculating time intervals between calcium and motion, and analyzing the differences between WT and two different CPVT cell lines.

Effect of Fluorescent Light on Motion Analysis

Previously, the intensity changes caused by fluorescence have prevented simultaneous motion measurements. MQD, however, does not put emphasis on bright pixels thus making it a plausible method for the task. Our results show that the intensity fluctuation effect by fluorescent light is negligible to both timing and magnitude of the motion signal. This is the first time such measurement and assessment of accuracy have been done without using corrections with a fluorescent dye.

Our results indicate that MQD based analysis of CM motion is minimally affected by the presence of a fluorescence based measurement. In t-tests, there were no significant differences between the means of measured CD parameters. The R^2 values in linear regression studies between normal brightfield PIV and CaPIV with fluorescence were very high in all three cell lines indicating the very low impact of fluorescence presence. There were small differences in the lower parts of the peaks as well as a minor 5% difference in magnitudes of contraction velocities. We believe this measurement setup allows measuring of motion with a variety of different fluorescent indicators, as long as movement is present. Determining a sufficient level of lighting for the measurements may be a key factor in the acquisition of two simultaneous high quality recordings.

Effect of Bright Light on Calcium Imaging

Applying transmission light had only small effect on the calcium imaging waveforms. In linear regression analysis, high R^2 values were obtained between Ca (bright) and Ca (dark), in all three cell lines. However, in CPVT some lower regression values were obtained due to a number of possible factors: calcium transients Ca (bright) and Ca (dark) were not from the same beats, the number of recorded cells in CPVT lines was low and as the beating rate was lower, the number of beats in each signal was smaller than in WT. As illustrated in the CPVTa signals shown in Fig. 2, the calcium transients could have multiple small peaks (i.e. arrhythmias/abnormal transients) making the direct comparison of peak width parameters difficult. For WT cells, the peaks were more regular and Ca (bright) and Ca (dark) were both capable of characterizing the cell lines similarly, as shown in t-tests. Ca (dark) and Ca (bright) amplitudes were not compared, as the comparison would not have been valid due to the bleaching of fluorescent dye during the measurement. Moreover, it is evident that increased background light increases the background noise level in fluorescence measurement. However, sufficient transmission light or constant fluorescent light is needed for detection of motion signal from the video. At the same time, the fluorescent emission of the dye should be strong enough to be detected while the transmission video is acquired. Increasing the light intensity or exposure time of the sample may not be the best solutions since they result in higher photobleaching of fluorophores and slower frame rates.

Ratiometric dyes have different emission spectra for bound and unbound states with the indicated ion, for example with Fura-2. Therefore, it takes two consecutive channel recordings to capture the ratio between these states, which takes longer and results in lower frame rates in acquisition. In this case, as an additional channel for brightfield video is measured, non-ratiometric dyes, such as Fluo-4, are better since their emission needs to be recorded only on one wavelength rather than ratiometric dyes. The results indicate that in calcium studies, with a focus on the waveforms instead of absolute Ca^{2+} concentration, it is feasible to apply also the brightfield light to obtain additional information on the mechanical activity without affecting the calcium measurement.

Cell Line Differences

There was no statistically significant differences in *t*-tests between motion in WT and CPVT cell lines when considering PIV or CaPIV. CPVT cells typically present arrhythmias under adrenergic stimulation, but as only the baseline beating is analyzed here, the motion signals correspond to those of WT. These results would indicate that the CPVT cells do not directly exhibit beating phenotypes different from WT cells at baseline conditions. Earlier, using PIV we have found differing beating phenotypes in LQT cells, but of course also the clinical presentation of the diseases are different.[9]

Ca (bright) and Ca (dark) showed statistically significant differences between WT and CPVTb in CTD80 and CTD90, but not between WT and CPVTa. These differences could be caused by a higher variation in diastolic calcium levels in CPVTb caused by a leakage of calcium through RYRs in the cells. However, the amplitude of these diastolic events is so low compared to the actual calcium peak so there were no differences in the parameters associated with the higher parts of the peak (i.e. CTD10).

The combination of motion and calcium measurements showed a varying disconnection of the two, as shown by the R^2 values (Table 2) especially for CPVTa. The most prevalent cause for CPVT lies in mutations in RYR2 gene coding for RYR.[20] It is located at the membrane of sarcoplasmic reticulum in CMs and acts as a channel releasing calcium from sarcoplasmic reticulum to cytosol. Mutations in RYR2 cause spontaneous calcium leakage through the channel and altered calcium transients inside CMs.[13] In CPVTb population, which carries a V4653F mutation in RYR, the substituted amino acid is located in the channel domain of the protein.[16] It is thought to be a gain-of-function point mutation, as most of the RYR mutations, and alter the channels sensitivity or permeability to calcium ions.[23] CPVTa population, which carries an exon 3 deletion, has the structural defect on the cytosolic part of the protein in the N-terminal domain and is associated with more severe clinical outcome.[12] The difference in the nature of these two mutations could explain the differences in our results. The disconnection between calcium and beating motion could be related to the earlier finding by Tang *et al.* where the exon 3 deletion was found to be resulting in an abnormal termination of calcium release through the RYR.[24]

Simultaneous Calcium and Motion Measurements

The combined simultaneous recording of motion and calcium as shown here provides new tools for studying the CM contraction mechanism. In t-tests between motion and calcium modalities, statistical differences were seen in WT cell lines, but not in CPVTa/CPVTb. The lack of statistical difference between motion and calcium in CPVT was surprising and it may again be caused by the low number of recorded cells or more heterogeneous beating patterns and calcium transients. In linear regression analysis of motion and calcium modalities, represented in Table 2, CPVTa had lower R^2 values than WT and CPVTb: there was practically no relation between the measurements in peak parameters characterizing the low amplitudes.

Mean time differences of signal onset and offset rate of change maxima did not show statistically significant differences between the cell lines due to high variability and low number of cells measured. However, CPVTa did show indication of longer time intervals between calcium and motion in onset, and CPVTb in offset.

Overall, the results indicate that calcium and motion go hand in hand as is expected, but one cannot directly be deduced from the other. Although the low correlation values in CPTVa may be caused by the low number of samples, high correlation values were not present for WT either where the sample number was higher. This reinforces the idea that even if Ca^{2+} is the driving force in CM contraction, calcium measurement alone cannot be used to describe the mechanical function in full detail. Further, motion alone does not necessarily reflect the ionic functions, emphasizing the need for the combined method suggested here as a new tool for CM analysis.

Method Advantages

Video-based measurements are minimally invasive and have low instrumentation requirements. These aspects make them a feasible candidate for high-throughput studies. For laboratories, this method can be used in conjunction with other studies, as microscopes and video cameras are mainstay laboratory equipment. The threshold for including contraction measurements in studies is lower than measurements with other methods, because no additional equipment is needed. Combining the method with fluorescent beads, substrate deformation and thus contraction force could be measured as well. While here we have considered individual cells and small clusters, the method should be applicable for larger samples of cardiac tissue, as long as 2-dimensional approach is still feasible. As we have shown here, the possibility of measuring CM contraction from calcium imaging data also enables revisiting previous studies and expanding on their results.

Study Limitations and Sources of Error

To validate the method we used interlaced video. The time difference between PIV and CaPIV videos—by being consecutive frames and the relatively low frame rate—must be taken into account when estimating their differences and similarities. The frame interlacing produces intrinsic time differences of 21.7 and 8.8 ms for our minimum frame rate 46 and maximum frame rate 114, respectively. A higher frame rate with slow beating cells would give a more accurate reading. However, the observed differences between normal brightfield PIV and fluorescence CaPIV were small, indicating that MQD-based motion measurements are minimally obstructed by fluorescence signals. We have previously explored waveform averaging in brief,[2] suggesting a frame rate of 60. Further studies with a higher frame rate and more beats per video would better quantify the difference in amplitudes for measurements where absolute precision of magnitude is required. Due to the low number of recordings, the findings related to the disconnection between calcium and motion in CPVT cells should be considered tentative. A study focusing on calcium-motion coupling in CPVT cells is required for reliability.

In this study, CMs were cultured on glass coverslips where their morphology is different from mature human CMs. Therefore, results may be different using i.e. patterned CMs. However, our method should be applicable to those studies also.

Our method uses simultaneous optimized transmission and fluorescent light sources. The results showed that the added light source had very small effect on the detected fluorescent signal. However, the method is producing additional light load to the fluorescent dye and cells and thus photobleaching of the dye and phototoxicity should be considered. As our method uses no fluorescent signal background correction, it is straightforward to compute and free from possible correction errors.

CONCLUSION

We have developed and evaluated a protocol for simultaneous calcium and motion signal measurement. By measuring the same motion from videos with and without fluorescence, we were able to validate and quantify the accuracy of a simultaneous measurement. Our results show that MQD based PIV is minimally affected by fluorescence. Furthermore, by measuring the calcium transients with and without background light, we showed that simultaneous brightfield imaging causes minimal interference to the calcium measurement. This is the first time simultaneous measurements of video-based CM motion with fluorescent dye based calcium transients are conducted without fluorescent video background corrections. It opens a new avenue to study the simultaneous ionic and biomechanical functions and the differences in their dynamics.

Our demonstration of simultaneous measurement implies that combined imaging is applicable also with other fluorescent reporters. Combining the measurement of motion would provide an additional layer of information for fluorescence studies. All these will open a new door to greater understanding of electromechanical coupling in CM contraction, disease mechanisms and drug effects.

ELECTRONIC SUPPLEMENTARY MATERIAL

The online version of this article (doi: 10.1007/s10439-017-1933-2) contains supplementary material, which is available to authorized users.

ACKNOWLEDGMENTS

We would like to thank Kim Larsson (BioMediTech Institute and Faculty of Medicine and Life Sciences, University of Tampere, Tampere, Finland) for technical support. The study was funded partly by personal research grants from Finnish Cultural Foundation Pirkanmaa regional fund and Paavo Nurmi Foundation, and Human Spare Parts project funded by Finnish Funding Agency for Technology and Innovation (TEKES).

OPEN ACCESS

REFERENCES

[1] Ahola, A., A. L. Kiviaho, K. Larsson, M. Honkanen, K. Aalto-Setälä, and J. Hyttinen. Video image-based analysis of single human induced pluripotent stem cell derived cardiomyocyte beating dynamics using digital image correlation. *Biomed. Eng. Online* 13:39, 2014.

[2] Ahola, A., P. Pradhapan, E. Laurila, K. Aalto-setälä, and J. Hyttinen. Motion Analysis method for determining cardiomyocyte beating properties based on digital image correlation and templates. In Computing in Cardiology Conference (CinC), 2014, pp. 1137–1140, 2014.

[3] Bedut, S., C. Seminatore-Nole, V. Lamamy, S. Caignard, J. A. Boutin, O. Nosjean, J.-P. Stephan, and F. Coge. High-throughput drug profiling with voltage- and calcium-sensitive fluorescent probes in human iPSC-derived cardiomyocytes. *Am. J. Physiol. Heart Circ. Physiol.* 311:H44–53, 2016.

[4] Grespan, E., S. Martewicz, E. Serena, V. Le Houerou, J. Rühe, and N. Elvassore. Analysis of calcium transients and uniaxial contraction force in single human embryonic stem cell-derived cardiomyocytes on microstructured elastic substrate with spatially controlled surface chemistries. *Langmuir* 32:12190–12201, 2016.

[5] Gui, L. C., and W. Merzkirch. A method of tracking ensembles of particle images. *Exp. Fluids* 21:465–468, 1996.

[6] Hayakawa, T., T. Kunihiro, S. Dowaki, H. Uno, E. Matsui, M. Uchida, S. Kobayashi, A. Yasuda, T. Shimizu, and T. Okano. Noninvasive evaluation of contractile behavior of cardiomyocyte monolayers based on motion vector analysis. *Tissue Eng. Part C Methods* 18:21–32, 2012.

[7] Huebsch, N., P. Loskill, M. A. Mandegar, N. C. Marks, A. S. Sheehan, Z. Ma, A. Mathur, T. N. Nguyen, J. C. Yoo, L. M. Judge, C. I. Spencer, A. C. Chukka, C. R. Russell, P.-L. So, B. R. Conklin, and K. E. Healy. Automated video-based analysis of contractility and calcium flux in human-induced pluripotent stem cell-derived cardiomyocytes cultured over different spatial scales. *Tissue Eng. Part C. Methods* 21:467–479, 2015.

[8] Hwang, H. S., D. O. Kryshtal, T. K. Feaster, V. Sánchez-Freire, J. Zhang, T. J. Kamp, C. C. Hong, J. C. Wu, and B. C. Knollmann. Comparable calcium handling of human iPSC-derived cardiomyocytes generated by multiple laboratories. *J. Mol. Cell. Cardiol.* 85:79–88, 2015.

[9] Kiviaho, A. L., A. Ahola, K. Larsson, K. Penttinen, H. Swan, M. Pekkanen-Mattila, H. Venäläinen, K. Paavola, J. Hyttinen, and K. Aalto-Setälä. Distinct electrophysiological and mechanical beating phenotypes of long QT syndrome type 1-specific cardiomyocytes carrying different mutations. *IJC Hear. Vasc.* 8:19–31, 2015.

[10] Kujala, K., J. Paavola, A. Lahti, K. Larsson, M. Pekkanen-Mattila, M. Viitasalo, A. M. Lahtinen, L. Toivonen, K. Kontula, H. Swan, M. Laine, O. Silvennoinen, and K. Aalto-Setala. Cell model of catecholaminergic polymorphic ventricular tachycardia reveals early and delayed afterdepolarizations. *PLoS ONE* 7:e44660, 2012.

[11] Lahti, A. L., V. J. Kujala, H. Chapman, A.-P. Koivisto, M. Pekkanen-Mattila, E. Kerkelä, J. Hyttinen, K. Kontula, H. Swan, B. R. Conklin, S. Yamanaka, O. Silvennoinen, and

K. Aalto-Setälä. Model for long QT syndrome type 2 using human iPS cells demonstrates arrhythmogenic characteristics in cell culture. *Dis. Models Mech.* 5:220–230, 2012.

[12]Lobo, P. A., L. Kimlicka, C.-C. Tung, and F. Van Petegem. The deletion of exon 3 in the cardiac ryanodine receptor is rescued by beta strand switching. *Structure* 19:790–798, 2011.

[13]MacLennan, D. H., and S. R. W. Chen. Store overload-induced Ca(2+) release as a triggering mechanism for CPVT and MH episodes caused by mutations in RYR and CASQ genes. *J. Physiol.* 587:3113–3115, 2009.

[14]Maddah, M., J. D. Heidmann, M. A. Mandegar, C. D. Walker, S. Bolouki, B. R. Conklin, and K. E. Loewke. A non-invasive platform for functional characterization of stem-cell-derived cardiomyocytes with applications in cardiotoxicity testing. *Stem Cell Rep.* 4:621–631, 2015.

[15]Paci, M., E. Passini, S. Severi, J. Hyttinen, and B. Rodriguez. A population of in silico models to face the variability of human induced pluripotent stem cell-derived cardiomyocytes: The hERG block case study. In Computing in Cardiology Conference (CinC), pp. 1189–1192, 2016.

[16]Peng, W., H. Shen, J. Wu, W. Guo, X. Pan, X. Wang, S. R. W. Chen, and N. Yan. Structural basis for the gating mechanism of the type 2 ryanodine receptor RyR2. *Science* 2016. doi:10.1126/science.aah5324.

[17]Penttinen, K., H. Siirtola, J. Àvalos-Salguero, T. Vainio, M. Juhola, and K. Aalto-Setälä. Novel analysis software for detecting and classifying Ca^{2+} transient abnormalities in stem cell-derived cardiomyocytes. *PLoS ONE* 10:e0135806, 2015.

[18]Penttinen, K., H. Swan, S. Vanninen, J. Paavola, A. M. Lahtinen, K. Kontula, and K. Aalto-Setälä. Antiarrhythmic effects of dantrolene in patients with catecholaminergic polymorphic ventricular tachycardia and replication of the responses using iPSC models. *PLoS ONE* 10:e0125366, 2015.

[19]Pesl, M., J. Pribyl, I. Acimovic, A. Vilotic, S. Jelinkova, A. Salykin, A. Lacampagne, P. Dvorak, A. C. Meli, P. Skladal, and V. Rotrekl. Atomic force microscopy combined with human pluripotent stem cell derived cardiomyocytes for biomechanical sensing. *Biosens. Bioelectron.* 85:751–757, 2016.

[20]Priori, S. G., C. Napolitano, N. Tiso, M. Memmi, G. Vignati, R. Bloise, V. Sorrentino, and G. A. Danieli. Mutations in the cardiac ryanodine receptor gene (hRyR2) underlie catecholaminergic polymorphic ventricular tachycardia. *Circulation* 103:196–200, 2001.

[21]Ribeiro, M. C., L. G. Tertoolen, J. A. Guadix, M. Bellin, G. Kosmidis, C. D'Aniello, J. Monshouwer-Kloots, M.-J. Goumans, Y. Wang, A. W. Feinberg, C. L. Mummery, and R. Passier. Functional maturation of human pluripotent stem cell derived cardiomyocytes *in vitro*—Correlation between contraction force and electrophysiology. *Biomaterials* 51:138–150, 2015.

[22]Rodriguez, A. G., S. J. Han, M. Regnier, and N. J. Sniadecki. Substrate stiffness increases twitch power of neonatal cardiomyocytes in correlation with changes in myofibril structure and intracellular calcium. *Biophys. J.* 101:2455–2464, 2011.

[23]Roston, T. M., F. Van Petegem, and S. Sanatani. Catecholaminergic polymorphic ventricular tachycardia: a model for genotype-specific therapy. *Curr. Opin. Cardiol.* 32:78–85, 2017.

[24]Tang, Y., X. Tian, R. Wang, M. Fill, and S. R. W. Chen. Abnormal termination of Ca^{2+} release is a common defect of RyR2 mutations associated with cardiomyopathies. *Circ. Res.* 110:968–977, 2012.